Optimization of spherical proportional counter backgrounds and response for low mass dark matter search

Alexis Brossard

Thèse de doctorat

NNT : 2020UPASS041

Optimization of spherical proportional counter backgrounds and response for low mass dark matter search

Thèse de doctorat de l'Université Paris-Saclay et de Queen's University

École doctorale n° 576, Particules, Hadrons, Énergie, Noyau, Instrumentation, Imagerie, Cosmos et Simulation, (PHENIICS)
Spécialité de doctorat : astroparticules et cosmologie
Unité de recherche : Université Paris-Saclay, CEA, Département d'Electronique des Détecteurs et d'Informatique pour la Physique, 91191, Gif-sur-Yvette, France.
Référent : Faculté des sciences d'Orsay

Thèse présentée et soutenue à Kingston (Canada), le 13 février 2020, par

Alexis BROSSARD

Composition du jury :

Guillaume GIROUX Professeur assistant, Queen's University	Président
Silvia SCORZA Professeure associée, Laurentian Univerisity	Rapporteur et Examinatrice
Viktor ZACEK Professeur, Université de Montreal	Rapporteur et Examinateur
Alexander WRIGHT Professeur assistant, Queen's University	Examinateur
Paul COLAS Docteur, CEA Paris-Saclay	Examinateur
Étienne AUGE Professeur des universités, Université Paris-Saclay	Examinateur
Gilles GERBIER Professeur, Canada Excellence Research Chair (CERC), Queen's University	Directeur
Ioannis GIOMATARIS Docteur, CEA Paris-Saclay	Codirecteur

To my grandparents.

Abstract

The NEWS-G collaboration uses Spherical Proportional Counters to search for Weakly Interacting Massive Particles (WIMP). The first detector, SEDINE, developed for this goal is a 60 cm diameter sphere installed at the Laboratoire Souterrain de Modane in France. In 2015, the collaboration took a run with neon as the target material for an exposure of 9.7 $\mathrm{kg} \cdot \mathrm{days}$. This run allowed new limits to be set on the spin-independent WIMP-nucleon cross-sections with 90% confidence upper limit of $\sigma_{\mathrm{SI}} < 4.4 \times 10^{-37}\mathrm{cm}^2$ for a $0.5\,\mathrm{GeV/c}^2$ WIMP. The study of the background events observed during this run shows that it is dominated by the presence of the ^{210}Pb decay chain in the different materials composing the detector, its shielding, and on the inner surface of the sphere. The experience acquired in running the detector SEDINE and the analysis of its data allowed procedures to be developed to mitigate radioactive contaminations and the resulting background events in the experiment. For the next detector a more stringent selection of radio-pure materials surrounding the detector is carried out. The radioactive background affecting the experimental set up is then estimated via the measurements of material radioactive contaminations and the simulation of the different components. The development of new sensors allows a better homogeneity of the detector response and improved data acquisition in a larger detector. The new detector is a 140 cm diameter copper sphere, to be

installed at SNOLAB in Canada in 2020. Its performances will be also enhanced by the development of new methods of signal characterisation and energy calibration.

Résumé

Les compteurs proportionnels sphériques sont utilisés pour la recherche de matière noire par la collaboration NEWS-G depuis 2013 avec le détecteur SEDINE installé au Laboratoire Souterrain de Modane. Ce premier détecteur a permis d'établir une nouvelle limite de la section efficace d'interaction WIMP-nucléon pour des WIMPs (Weakly Interactive Massive Particles) de masse inférieure à 0.6 GeV/c^2. Depuis, la collaboration travaille à la mise au point d'un nouveau détecteur. Cette thèse se concentre sur deux aspects de l'expérience, la réduction du bruit de fond radioactif et le développement de nouvelles anodes permettant de réduire le seuil en énergie du détecteur jusqu'à la détection d'électrons uniques afin de garantir les meilleurs performances pour le prochain détecteur. Le premier chapitre est une introduction à l'ensemble de la thèse.

Le second chapitre se concentre sur le problème de la matière noire. L'existence de matière noire a été postulée au cours du vingtième siècle par plusieurs observations à différentes échelles. Le premier indice vint de l'astronome Fritz Zwicky qui postula l'existence d'une forme de matière inconnue en observant la vitesse des galaxies au sein de l'amas de Coma. Au cours des années 70, Vera Rubin, observa que la matière lumineuse présente dans les galaxies n'apportait pas une masse suffisante pour expliquer la vitesse de rotation des étoiles. Plus récemment, l'étude du bruit de fond

cosmologique confirma que environ 26% de l'Univers est composé de matière noire. Plusieurs hypothèses on été formulées afin d'expliquer ces observations. L'existence d'objets macroscopiques tels que des trous noirs et des naines brunes ou des modifications des lois de la gravité ont été évoquées mais mises en défaut par plusieurs observations. L'hypothèse la plus populaire est l'existence de WIMP. Ces particules massives et interagissant faiblement pourraient être détectées via leur diffusion élastique avec les noyaux de matériaux cibles de détecteurs présents sur terre. Les WIMPs sont la classe de particule principalement recherchée par la collaboration NEWS-G. La collaboration est spécialisée dans la recherche de matière noire légère, d'une masse inférieure à quelques GeV/c^2. Cette spécificité impose d'utiliser des noyaux cibles légers tels que l'hydrogène ou l'hélium et d'avoir un seuil de détection en énergie le plus faible possible, jusqu'à la détection d'électrons uniques. Le fait que ces particules interagissent faiblement impose d'avoir un bruit de fond le plus bas possible. Cette particularité pour la détection des WIMPs est commune à toutes les expériences. Plusieurs autres expériences, utilisant d'autres technologies ainsi que d'autres matériaux cibles tels que l'argon ou le germanium recherchent la matière noire. En conclusion, ce chapitre présente un état de l'art de la recherche de WIMP.

Le chapitre suivant présente la technologie des compteurs proportionnels sphériques utilisée par la collaboration NEWS-G pour la recherche de matière noire. Ce détecteur consiste en une sphère de cuivre remplie de gaz. La sphère est reliée à la masse et une tension est appliquée sur une anode placée en son centre. Le détecteur offre alors un large volume de gaz baigné par un champ électrique. Lorsqu'une particule interagit avec un atome du gaz, elle dépose de l'énergie qui se traduit par une ionisation et l'émission d'électrons primaires. Sous l'influence du champ électrique, les électrons

primaires dérivent vers l'anode au centre de la sphère. Lorsque qu'un électron est proche de l'anode, à moins de 100 μm, sous l'effet du champ électrique suffisamment intense, il acquiert une énergie cinétique supérieure au potentiel d'ionisation du gaz et déclenche une avalanche qui crée plusieurs milliers de paires électrons-ions secondaires. Le signal est alors induit par le mouvement des ions secondaires en direction de la sphère. Ce courant électrique est intégré par un pré-amplificateur puis digitalisé. L'étude de la forme des impulsions mesurés permet d'identifier la nature des dépôts d'énergie. L'amplitude des impulsions est liée à l'énergie déposée et leur temps de montée est lié à la distribution spatiale du dépôt. La discrimination de la forme des pulses permet d'identifier les dépôts d'énergie ponctuels. Ce type de détecteur offre plusieurs avantages. D'abord il est possible d'utiliser plusieurs matériaux cibles et de comparer la compatibilité d'un éventuel excès avec l'hypothèse d'un signal de matière noire. La géométrie du détecteur lui confère une faible capacité électrique qui ne dépend que de la taille de l'anode centrale. Cette faible capacité procure un très faible bruit électronique intrinsèque et donc un seuil en énergie faible. Finalement, la discrimination de la forme des pulses permet d'identifier les dépôts ponctuels et donc le dépôts attendus résultant de la diffusion élastique des WIMPs.

Le quatrième chapitre se focalise sur le détecteur SEDINE. Ce détecteur est une sphère de cuivre de 60 cm de diamètre installée au Laboratoire Souterrain Modane (LSM) en France. La sphère est placée dans un blindage fait de 5 à 7 cm de cuivre, 10 à 15 cm de plomb et finalement 30 cm de polyéthylène. En 2015, SEDINE a été utilisée avec un mélange de gaz composé de 99.3% de néon et 0.7% et méthane. Les données prises durant cette acquisition permirent de définir une nouvelle limite de la section efficace d'interaction WIMP-nucléon. L'analyse de ces données permit de définir

plusieurs points faibles du détecteur à améliorer pour le suivant. La calibration du détecteur faite avec de l'Argon-37 permit de mettre en évidence la non-homogénéité de la réponse du détecteur du fait de l'utilisation d'une anode simple ainsi que l'impact de la contamination en oxygène du gaz. Ces deux aspects ont été intégrés à la simulation de la réponse du détecteur. Une fois qu'une simulation correcte du détecteur fut mise en place, les différents bruits de fond radioactifs ont été étudiés. Une première analyse mit en lumière le fait que les contaminations des différents matériaux composants le détecteur, son blindage et la roche du laboratoire en Uranium-238, Thorium-232 et Potassium-40 de l'ordre de quelques dizaines ou centaines de μBq/kg, ne pouvaient expliquer le bruit de fond observé. En 2017, une nouvelle méthode de mesure de la contamination de Plomb-210 dans le cuivre fut publiée et montra que l'hypothèse de l'équilibre de la chaine de l'Uranium-238 était incorrect et que l'activité de Plomb-210 est de l'ordre de plusieurs dizaines de mBq/kg. Une seconde étude prenant en compte de tel niveau d'activité de Plomb-210 dans les différents matériaux composant le détecteur ainsi que sa surface interne permit de montrer que, à basse énergie, la chaine du Plomb-210 est responsable de 85% du bruit de fond observé.

Le cinquième chapitre présente l'étude menée afin de réduire le bruit de fond du prochain détecteur qui sera installé à SNOLAB au Canada. Ce détecteur est plus gros avec un diamètre de 140 cm, et fait de meilleurs matériaux. Le blindage est composé d'une coquille de 25 cm de plomb dont les 3 cm les plus proches de la sphère sont faits de plomb archéologique. Cette coquille est finalement entourée de 40 cm de polyéthylène. Plusieurs techniques ont été développées afin de réduire les différents bruits de fond. Premièrement, le temps d'exposition du cuivre utilisé pour la fabrication de la sphère aux rayons cosmiques a été limité à trois mois afin de réduire

l'accumulation principalement d'isotopes de cobalt radioactif. Une boite à gants a été installée au dessus de la sphère afin de pouvoir manipuler les différents composants sans exposer la surface interne du détecteur à l'air du laboratoire contaminé par du Radon-222. Finalement, 500 μm de cuivre pur ont été plaqués sur la surface interne du détecteur afin de réduire le bruit de fond induit par la présence de la chaine de désintégration du Plomb-210 dans le cuivre.

Le dernier chapitre se concentre sur le développement de senseur. Le senseur est un paramètre clé du détecteur. L'utilisation de senseur simple tel que celui utilisé avec SEDINE limite les performances du détecteur. La tension pouvant être appliquée sur la bille est limitée par les décharges pouvant se produire avec la canne la supportant. La présence du fil reliant la bille déforme le champ électrique et induit une non-homogénéité de la réponse du détecteur. Ces deux faiblesses peuvent être corrigées en appliquant une seconde tension sur un "parapluie" fait d'un matériel résistif placé autour du fil et proche de la bille. Ces senseurs avec parapluie résistif ont montré leur capacité à avoir des seuils de détection très bas, jusqu'à la détection d'électrons uniques. Finalement, pour les détecteurs larges tels que celui qui sera utilisé à SNOLAB, des senseurs de type "Achinos" (oursin) ont été développés. Ces senseurs sont composés d'un corps central sur lequel est appliqué un matériel résistif et onze billes. Ce type de senseur a montré ses capacités à détecter des électrons uniques dans de grands volumes ($1m^3$).

Pour conclure, cette thèse présente des améliorations de la technologie des compteurs proportionnels sphériques pour la recherche de matière noire. La réduction du bruit de fond ainsi que le développement de nouveaux senseurs offrant un seuil de détection d'un électron unique vont améliorer la sensibilité de l'expérience pour des

WIMPs de moins de 1 GeV/c^2.

Acknowledgments

I would like first to thanks my supervisor Gilles Gerbier for bringing me to Canada to live this great adventure. Acquiring knowledge from all your wise advice and discussions is a great honour. Thanks for your trust and your kindness. Working with you during these years elevated me both in term of my scientific knowledge and as a human being. I greatly thanks my co-supervisor Ioannis Giomataris for welcoming me on France. Working with you was very rewarding and I am glad to have acquired some of your invaluable knowledge of gas detectors.

I want to thank my fellows student at Queen's University Marie Vidal, George Savvidis, and a special mention for Paco Vazquez de Sola Fernandez who shared the past five years with me. You are a great co-worker, I wish you all best in your future post-doc, I will miss you and your invaluable math skills. Many thanks to the most brilliant student Daniel Durnford, the P.I. of the next dark matter experiment which will discover dark matter if NEWS-G has not already done so.

All my thanks to the great people who paved my way during this adventure. Thanks to Sabine Roth and Alvine Kamaha. Many thanks to Ali Dastgheibi-Fard, for all your advice and the knowledge acquired and your welcome at the LSM. Thanks a lot to Jean-François Caron who reviewed this manuscript, thanks too your good eyes and your precisions. Your help was extremely precious. An enormous thanks to

Quentin Arnaud, the best of all. Never has having a beer and a cigarette been so instructive. I wish you all best for you great coming career. Thanks to the best lab chief Philippe Gros. Thank you for your time, your kindness, for all you taught to me. All the time we have spend together was extremely valuable.

I want to address a warm thanks to all members of the NEWS-G collaboration. Many thanks to Julie McDonald for her kindness and all the time she gave me. Thanks to Ioannis Katisoulas and Michel Gros for welcoming me two times in Saclay. Thanks to Michel Zampaolo for welcoming me in Modane and Thierry Zampieri for the hiking with me in the beautiful 'Vallée de la Maurienne'. Thanks a lot to the members in Grenoble, and particularity to Jean-François Muraz for his kindness and patience allowing me for understand all the details of his amazing Comimac. A great thanks to the members from Royal Military College of Canada for the ^{37}Ar supply, without which the sensor development at Queen's would not have been possible. Many thanks to Eric Hoppe for the invaluable skill of electroplating. Last but not least, a great thanks to Maurice Chapellier. Working with you is a real pleasure. My knowledge about radioactivity and electronics would not be the same without you.

I want to thanks all the roommates I met over these years. You are awesome dudes and have been a familly. Thanks to Rango, Florie, August, Ginnie, Eydis, Ethan, Kyle, Joabe, Ivan and all that I may forget. Also a great thanks to Chanpreet Amole who is the best officemate, see you soon under the sun.

Merci beaucoup à ma famille, mes parents Catherine et Charles qui m'ont toujours soutenu et épaulé depuis tout petit et durant toutes mes années d'études. Si j'en suis là aujourd'hui c'est grâce à vous. Un énorme merci à mon frère Thibaut qui a été le meilleur compagnon de route depuis le berçeau, sa femme Noémie et leurs enfants

Zoé et Louis. Je suis très impatient de rentrer vous retrouver en France.

Et pour finir, un grand merci à mes meilleurs amis Alexis et Alexandra. Grandir avec vous durant toutes ces années a été la plus incroyable des expériences. Je vous dis à bientôt pour venir rencontrer votre petite qui arrive.

Contents

List of Tables

List of Figures

Chapter 1

Introduction

Astrophysical observations, from galactic to cosmological scales show that a significant part of the Universe is made of invisible or "dark" matter [1]. None of the particles described in the standard model of particle physics or a combination of them have characteristics allowing a description of this invisible matter [2]. Thus, identifying a particle responsible for this amount of unknown mass is a challenge benefiting for both our understanding of the Universe and the incomplete Standard Model of particle physics. Several candidates were postulated to solve the dark matter issue. The most relevant one is weakly interacting massive particles (WIMPs). WIMPs are assumed to have a weak scale interaction cross-section with standard model particles [2]. Three ways of detection are used to look for WIMPs. The indirect detection, where particle detectors are used to search for an excess of events due to the self-annihilation of WIMPs [3]. The production, where detectors surrounding particle accelerators are used to search for missing transverse energy, a possible signature of WIMP production [4]. And finally the direct detection, where detectors are used to search for WIMPs scattering on target nuclei. The WIMP mass being unknown, different detector technologies covering a large range of targets from hydrogen to xenon

are exploring the possible accessible masses. Exploring the mass and cross-section parameters implies several challenges. First, low cross-section requires a very low background environment. Any interaction of γ, β, μ or neutron can mimic a WIMP pulse, reducing the sensitivity of the experiment. The NEWS-G collaboration with Spherical Proportional Counters (SPC) [5] is exploring the lower part of the mass range with a WIMP mass region of interest lying below 1 GeV/c^2. This specificity implies a second challenge, having a very low energy threshold down to single-electron detection. The goal of this work is to improve and optimize the SPC technology to meet the criteria of low background experiment and low energy threshold. The optimization of the background is done through the selection and simulation of the materials composing the experiment. Optimization of the detector response relies on the development of sensors sensitive enough to ensure a single electron detection. Chapter 2 will describe the different dark matter evidences, candidates, and methods of detection. Chapter 3 presents the main interactions of radiation with matter followed by a general description of gaseous proportional counters and properties of electron drift under an electric field. The remainder of the chapter will focus on the specificities of the SPC and the pulse formation under a spherical electric field. The characteristics of the electric pulses, their amplitude and rise time, allow for determining some properties of the interacting particle such as the energy it deposited or the spatial distribution of this deposition. Then, a description of the pulse treatment and their shape discrimination is given, to finally present the tools and methods used for the detector simulation. In 2015, the NEWS-G collaboration set a new limit for WIMP masses lower than 0.5 GeV/c^2 at a cross-section of 4.4×10^{-37}cm^2 with a 60

cm detector filled with a neon and methane mixture at 3.1 bar placed at the Laboratoire Souterrain de Modane in France for 41 days of data acquisition. This result will be briefly described in chapter 4 followed by the description of the background recorded during the WIMP search run. This description relies on the estimation of radioactive contamination of the detector materials and the environment where it takes place. Chapter 5 will describe the optimization of the background of the next-generation detector: a 140 cm copper sphere to be installed in SNOLAB in Canada in 2020. The promising results obtained with the first detector will be strongly improved by an intensive material selection and background mitigation. The method used for radio-purity measurement in all materials composing the detector, its shield and the different methods to reduce their contributions to the background budget, and an estimation of the remaining background and its impact on the experiment sensitivity will be presented in this chapter. Chapter 6 will present improvement of the detector technology, specifically on the sensor, done to achieve low energy detection in a large SPC, in addition to the calibration method developed to ensure a good understanding of the detector behaviour at such low threshold.

Chapter 2

Dark matter

2.1 Introduction

Decades of astronomical observation brought strong evidence that our universe contains a large amount of invisible or "dark" matter. These observations were done on different scales from the galaxy to the cosmological scale. It is estimated that $70.4 \pm 0.6\%$ of the total matter content of the observable universe is in the form of non-relativistic, non-baryonic matter [6] at the cosmological scale. The first section of this chapter will describe the different observations which brought this intuition of dark matter. Following the evidence of invisible matter, theorists postulated several objects of different nature and size, micro or macroscopic, able to provide a significant amount of mass without producing light. The second part of this chapter will review some of the most popular candidates postulated during the past decades. As mentioned in the introduction chapter, the most popular candidate is WIMPs. The last section of this chapter will focus on WIMP detection. The three approaches to WIMP detection will be described with more details the direct detection approach used by the NEWS-G collaboration.

2.2 Evidence for dark matter

Evidence for dark matter existence has arisen from several astrophysical and cosmological observations. Astrophysical observations include velocity dispersion of stars in galaxies, galaxy cluster dynamics and large scale object mass measurement by gravitational lensing. Anisotropies in the cosmic microwave background have brought evidence that at a very large scale, the Universe is made of more than only baryonic matter.

2.2.1 Velocity of galaxies in the Coma cluster

In 1933, the Swiss astrophysicist Fritz Zwicky [7] used the virial theorem to postulate the existence of an unseen matter. The total kinetic energy E of a system of N self-gravitating objects of average mass m and orbital velocity v is given by:

$$E = \frac{1}{2}Nmv^2 \tag{2.1}$$

With an average separation of r between the N objects of the cluster, the potential energy of the $N(N-1)/2$ pairings is:

$$U = -\frac{1}{2}N(N-1)\frac{Gm^2}{r} \tag{2.2}$$

The virial theorem states that for such a cluster:

$$E = -\frac{U}{2} \tag{2.3}$$

The mass of the cluster M can be estimated from the measurements of v and r

$$M = Nm = \frac{2rv^2}{G} \tag{2.4}$$

While measuring radial velocities of galaxies in the Coma cluster and its radius, Zwicky estimated the average mass of the galaxies within the cluster and obtained a value about two orders of magnitude greater than expected from their luminosity. To explain the difference between the visible mass of the Coma cluster and the mass measured from the galaxies‘ velocities in the cluster, Zwicky postulated a new type of non-visible matter which only contributes to the cluster dynamic by the gravitational effect. He named this matter ‘Dark Matter‘.

2.2.2 Rotation curve of galaxies

During the 1970s, Vera Rubin observed the circular velocity of stars and gas inside spiral galaxies. In such a system, stars and gas rotate around the galactic center on almost circular orbits. For a circular velocity v at a radius r from the galactic center, the condition for the stability of the orbit is that the centrifugal acceleration is equal to the gravitational acceleration:

$$\frac{v}{r} = \frac{GM(r)}{r^2} \tag{2.5}$$

Where $M(r)$ is the mass inside the orbit of radius r. Then, the radial dependence of v would be expected to follow Kepler’s Law:

$$v = \sqrt{\frac{GM(r)}{r}} \tag{2.6}$$

Rubin's measurements showed a different behaviour. The galaxy rotation-curves do not follow this law but stay almost constant after attaining a maximum of around 5 kpc as shown in Fig 2.1. The solution to this is that in addition to stars and gas, the galaxies are made of a diffuse halo of dark matter, $M(r)$ proportional to r, leading to $v(r) \approx$ constant.

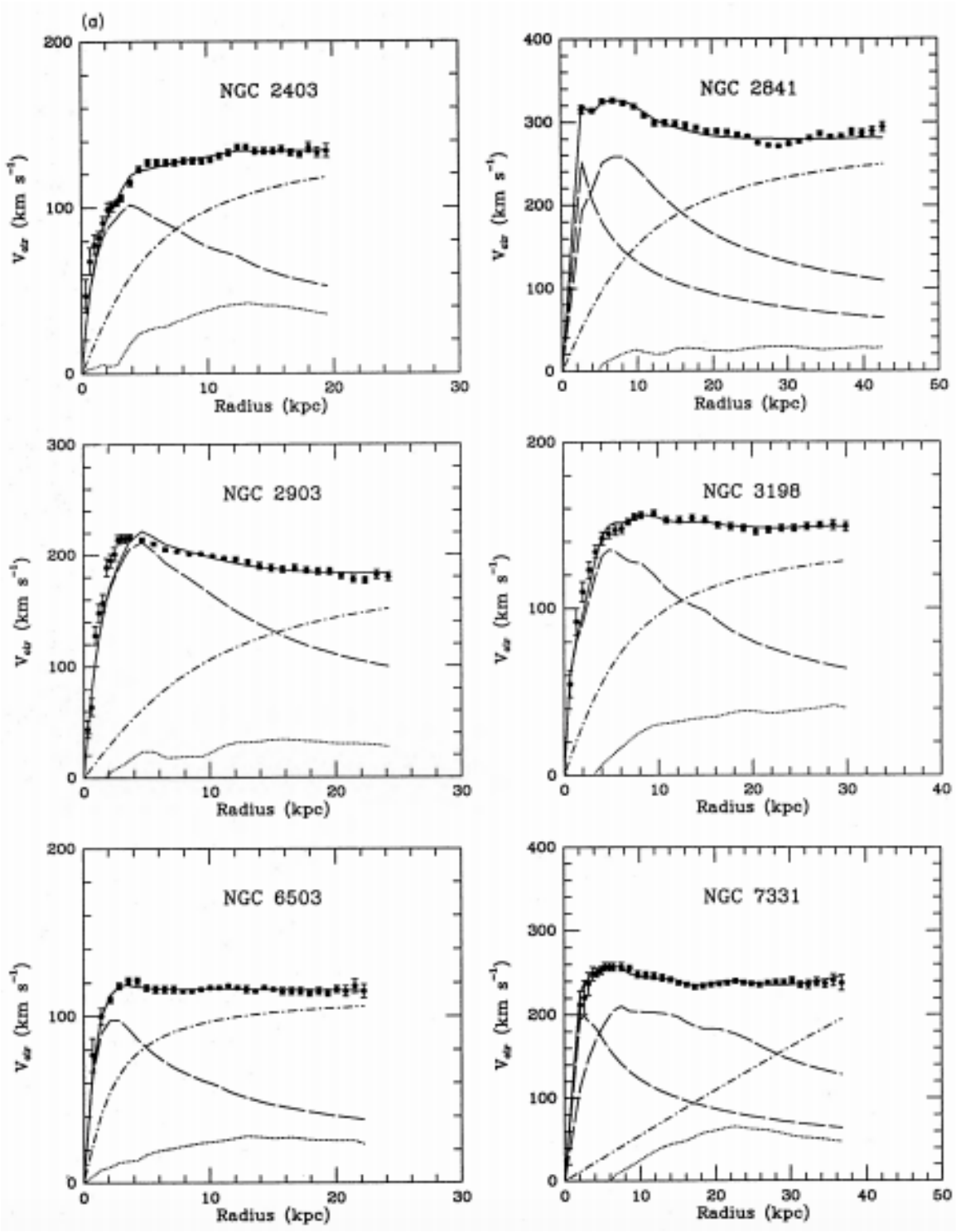

Figure 2.1: Rotation curve of few galaxies, showing the necessary contribution from a dark matter halo (dash-dot) in addition to the contributions of the gas (dot) and disk (dash) to produce the observed velocity distribution [8]

2.2.3 Galaxy cluster merging

A photon in a gravitational field moves as if it has mass and light rays bend around gravitating masses. It is possible to construct a map of the gravitational potential of a massive object by measuring the distortion of the images of background galaxies. On the other hand, it is possible to construct a map of the baryonic matter distribution by observing typical photons that it emits. Clowe et al. [9] observed the Bullet cluster, a unique object formed by the merging of two galaxy clusters. In such a collision, galaxies behave as collisionless particles, while the gas cloud that composes most of the cluster mass experiences pressure. Figure 2.2 shows the gravitational potential (green line) and the distribution of interstellar gas (color gradient). The discrepancy of the two maps is direct proof of the existence of dark matter.

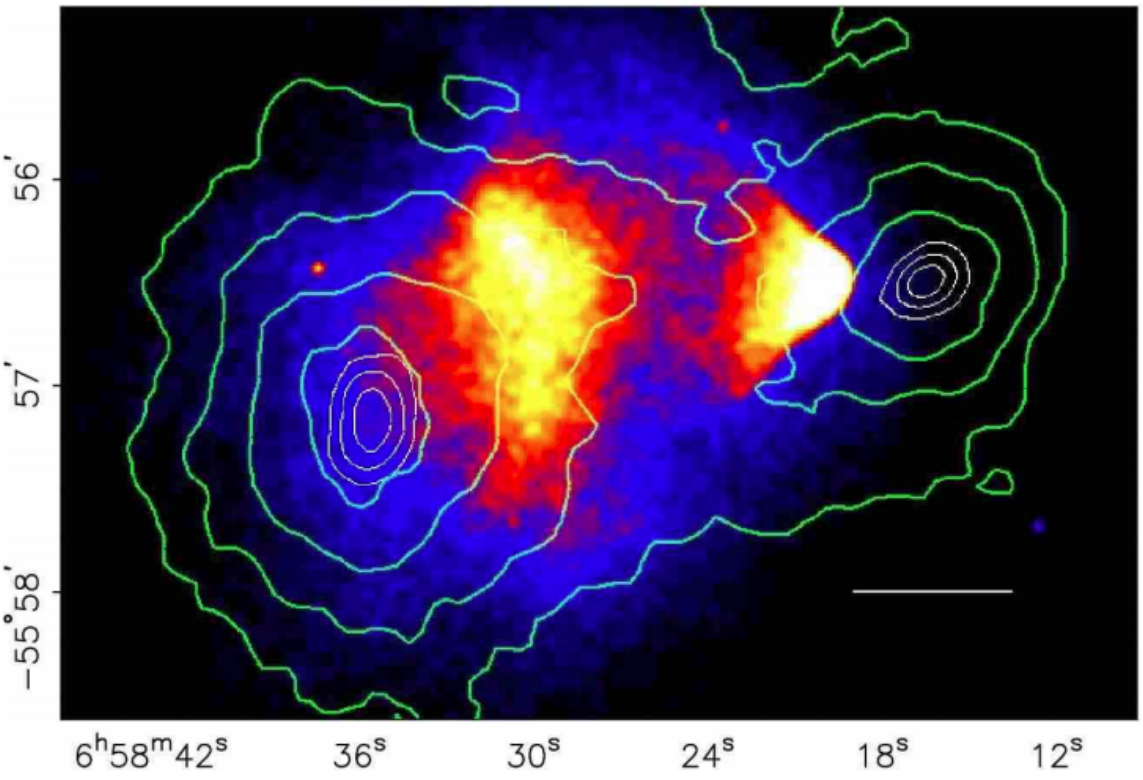

Figure 2.2: The Bullet cluster. The green contours are the gravitational potential. The colors indicate the X-ray temperature of the plasma which corresponds with the distribution of baryonic matter. [9] .

2.2.4 Cosmic microwave background anisotropy

The Cosmic Microwave Background (CMB) is the photons emitted during radiation-matter decoupling. Before decoupling, the early Universe consisted of a plasma of free electrons and light nuclei. The CMB was coupled to this plasma via Thomson scattering from the free electrons. Then, when the universe was ≈ 300000 years old, electrons and nuclei combined to form atoms. At this point, photons ceased to interact and travelled toward us. These photons composing the CMB contain information on the state of the universe at the time of the decoupling. Several experiments have

observed the CMB. The latest map of the CMB was obtained by the Planck mission (Fig 2.3) and published in 2015.

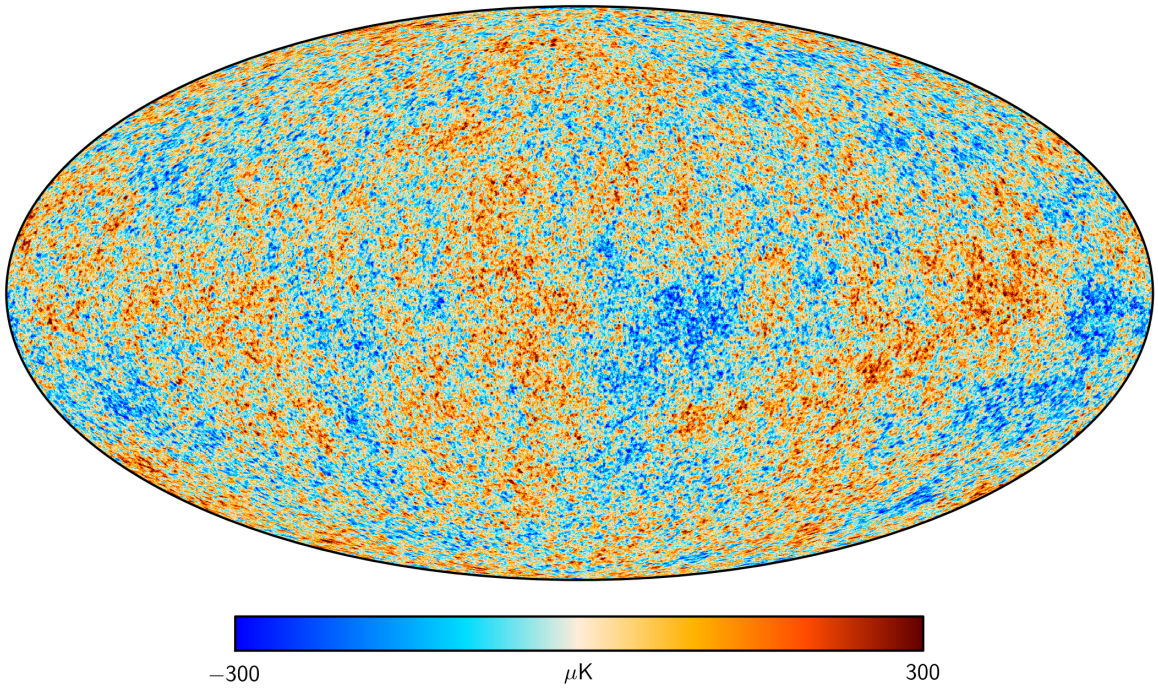

Figure 2.3: Cosmic Microwave Background measured by the Planck spacecraft. The color scale indicates the fluctuation of the temperature [10].

When emitted, these photons were in thermal equilibrium with the electron-nuclei plasma at a temperature of T $\approx$ 3000K. The CMB has a today mean measured temperature of $T = 2.725 \pm 0.001$ K due to the expansion of the Universe. Figure 2.3 shows a non-uniform universe. The coolest parts of the CMB correspond to higher density because photons are red-shifted as they escape the gravitational potential wells. We can extract from this mapping a relationship between anisotropy and angular scale.

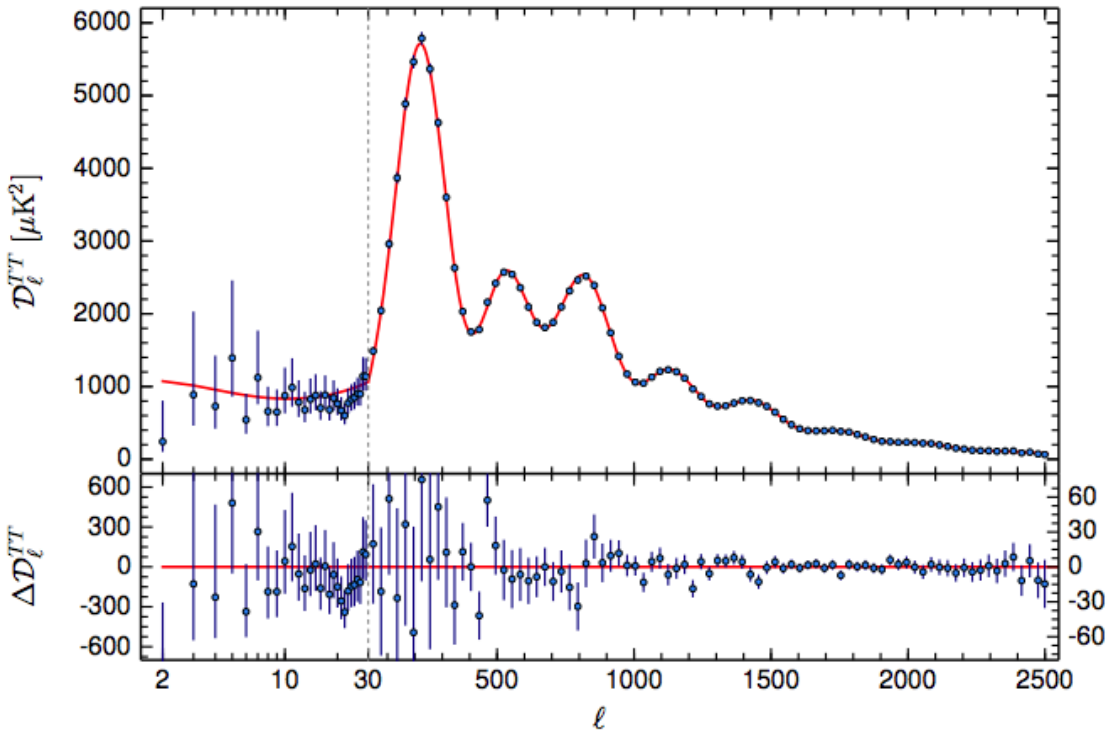

Figure 2.4: Fluctuation of the CMB with regards to the angular scale. The red curve is obtained with the theoretical ΛCDM model with free parameters adjusted by maximum likelihood [11].

The fit of the spectral fluctuation of the CMB allows us to extract several pieces of information about the universe [11]. More specifically, three parameters describing the energetic content of the universe can be obtained, Ω_b the baryon density parameter, Ω_c the dark matter density parameter and Ω_Λ the dark energy density parameter. These three parameters have been estimated to:

- $\Omega_b = 0.0486 \pm 0.0010$
- $\Omega_c = 0.2589 \pm 0.0057$
- $\Omega_\Lambda = 0.6911 \pm 0.0062$

This latest evidence brought the remarkable results that the energy content of our universe is made of an unknown form called 'dark energy'. Secondly, the baryonic matter described by the standard model of particle physics forms only 4% of the universe. The remaining 26% of the content of the universe is made of non-baryonic dark matter.

2.3 Dark matter candidates

Several hypotheses have been formulated during the past decades to explain the observations described in the previous section. These hypotheses can be divided into three categories: a new theory of gravitation, a large amount of mass brought by macroscopic objects, and finally the possibility of the existence of some unknown elementary particle. The three hypotheses will be discussed with particular attention on the last one, investigated by the NEWS-G collaboration.

2.3.1 MOND

The MOdified Newtonian Dynamics (MOND) [12] model attempts to explain the flatness of the rotation curve of galaxies by modifying the acceleration due to gravity for very low acceleration, $a_0 \approx 10^{-10} ms^{-2}$. The MOND model assumes a force of gravity given by $F = m\mu(a/a_0)a$ instead of the well known $F = ma$ described by Newton's second law, μ is a function of the acceleration and assumes the value of $\mu \approx 1$ for $a/a_0 >> 1$ and $\mu \approx \frac{a}{a_0}$ for $a/a_0 << 1$. This model allows for a constant orbital velocity at very large radii and very low acceleration and is consistent with the observations done by Vera Rubin. However, the model is not consistent with other astronomical

observations such as the Bullet cluster mass distribution and cosmological observation supported by the ΛCDM model claiming the existence of a non-baryonic form of matter.

2.3.2 MACHOS

Another alternative to explain the excess of mass in the universe consists of Massive Compact Halo Objects or MACHOS. MACHOS consist of undetected astronomical objects such as black holes, neutrons stars, white or brown dwarfs or planets. The search for such objects in sufficient quantity to explain the astronomical observations did not succeed [13]. Also, MACHOs are composed of baryonic matter, and it is known from the CMB measurements that the amount of baryonic matter is not enough to form a large fraction of the dark matter.

2.3.3 Non-baryonic dark matter

The standard model (SM) of particle physics describes all known particles. The model was developed during the 20th century and showed its strength at multiple times. The experimental confirmation of the existence of quarks, neutrinos, and gauge bosons during the past century brought strong evidence of the validity of the standard model [14]. The discovery of the Higgs boson in 2012 by the Large Hadron Collider (LHC) at the CERN in Geneva magnified its solidity [15] [16]. However, it is well known that the standard model is limited and is not sufficient to describe all observations, such as the neutrino mass. Additionally, the Standard Model does not give any description of gravity. These last considerations pave the way for a

new physics, 'beyond the standard model' potentially providing new massive candidates able to explain the observations. Candidates for non-baryonic dark matter must satisfy several conditions. They must be stable on the cosmological scale, they must interact weakly with electromagnetic radiation, and they must have the right density [17].

Neutrinos

Neutrinos are a natural candidate for dark matter because they are non-baryonic, massive, and weakly interacting. Although they are abundant in the universe, their low mass leads to an insignificant contribution to the total dark matter estimated in the universe. The analysis of the cosmic microwave background allows setting an upper limit to the neutrino density parameter, $\Omega_\nu \leq 0.014$ [18]. Thus, is it possible that neutrinos contribute some amount of dark matter but they can not provide the $\Omega_c = 0.2589 \pm 0.0057$ alone.

Axions

Originally introduced by the Peccei-Quinn theory in 1977 to resolve the strong CP problem in Quantum Chromodynamics (QCD), axion particles are viable Dark Matter candidates. The strong CP problem is due to the observed conservation of the Charge Parity symmetry in QCD while this symmetry is expected to be violated in the frame of the Standard Model. Peccei and Quinn introduced a new symmetry whose spontaneous breaking leads to the CP conservation by the creation of a pseudo-Nambu-Goldstone boson called the axion. Cosmological and astrophysical observations require axions to be very light with a mass in the range $10^{-6} \leq m_a \leq 10^{-3}\,\mathrm{eV/c^2}$.

Axions could be detected via axion-photon interactions.

WIMPs

Weakly Interacting Massive Particles (indicated by χ) are particles with masses roughly from GeV/c^2 to TeV/c^2. In the early universe, right after the period of inflation, WIMPs are supposed to have been in thermal and chemical equilibrium with the hot 'soup' of Standard Model particles. The high temperature of the universe allows for the creation of particle - anti-particle pairs, including WIMPs. These creations were counter-balanced by the annihilation of these pairs of particle and anti-particle. As the universe cooled down the production rate of pair of particles decreased. However, they could still annihilate, and the WIMP density decreased exponentially. However, as the universe kept expanding, the WIMP annihilation rate decreased and became negligible due to their small interaction probability. This point is known as the 'freeze-out' point. The WIMP density in the universe became roughly constant with that measured today, this is known as the WIMP relic density and has been approximated to be [2]:

$$\Omega_\chi h^2 \approx \frac{3 \times 10^{-27} \mathrm{cm}^3 \mathrm{s}^{-1}}{< \sigma_{\chi\chi} v >} \tag{2.7}$$

where $\sigma_{\chi\chi}$ is the annihilation cross-section and v the velocity. If we assume the annihilation cross-section of WIMPs to be weak-scale, in the order of $\sigma \mathrm{v} \approx 10^{-26} \mathrm{cm}^3 \mathrm{s}^{-1}$ (where v is the relative velocity between the annihilating particles) [19], their estimated relic abundance is found to be of the same order of magnitude as suggested by the cosmological observations of dark matter density. This fact is known as the 'WIMP miracle'. In addition to this miracle, WIMPs are a good candidate for dark

matter because several theories beyond the Standard Model propose massive particles with the property to be weakly interacting. The most prominent example of such a theory is supersymmetry (SUSY). The symmetry of SUSY relates particles with the same strong, weak and electromagnetic quantum numbers and with spins differing by 1/2 unit [20]. As partners of the quarks and leptons, we introduce new spin 0 squarks and sleptons, and as partners of the vector bosons, we introduce spin 1/2 gauginos. SUSY requires a new discrete symmetry that makes its lightest new particle stable. Such particle is called the neutralino and is notated $\bar{\chi}^0$. The neutralino satisfies all of the primary requirements of the WIMP model.

2.4 Search for WIMPs

The search for WIMPs is done in three different ways. High energy collisions of Standard Model particles can produce WIMPs, and this possibility is under investigation at the Large Hadron Collider in the form of a search for supersymmetric particles. The second possibility is the indirect search for WIMPs. Indirect detection experiments aim to detect the daughter products of possible WIMP self-annihilation into Standard Model particles. Finally, direct detection relies on the scattering of WIMPs on nuclei of target material on earth. This last possibility is the one explored by the NEWS-G collaboration.

2.4.1 Production

A neutralino pair may be produced in a particle accelerator which is operated at energy higher than twice the neutralino mass. The search for neutralino is done by looking at missing transverse energy. Once produced by a collision of standard

model particles, neutralino particles could leave the detector surrounding the collision point without interacting. The reconstruction of transverse momentum would be unbalanced, highlighting the presence of an undetected particle. To date, no WIMP production has been reported by experiments at any of the colliders, (LHC, Tevatron, LEP,...) [21]. Results from the Run-I LHC dataset recorded by the Atlas and CMS experiments are consistent with SM background expectation, limits have been set on different models, emphasizing the complementary nature of collider and direct detection searches. Collider searches can constrain the low WIMP mass region where direct detection suffers a lack of sensitivity. Figure 2.5 illustrates the complementarity of both methods where detection is more sensitive for dark matter masses higher than $10\,\mathrm{GeV/c^2}$ and collider production is more efficient at lower masses. We emphasize that the exclusion regions obtained in this way will depend strongly on the assumptions of the model. The extrapolations are done with full knowledge that the simplified model is merely a crude guess, and one must be careful not to overgeneralise [21].

2.4.2 Indirect detection

The indirect detection of dark matter relies on the detection of WIMP annihilation or decay products which are SM particles [22]. These particles include neutrinos, gamma rays, positrons, antiprotons, and antinuclei. WIMPs can be slowed down, captured and trapped in celestial objects like earth or the sun, thus enhancing their density and their probability of annihilation [17]. The product of such annihilations could be muons neutrinos which can interact in the earth. Incoming muons could be detected in large neutrino telescopes such as SuperKamiokande [23] or IceCube [24].

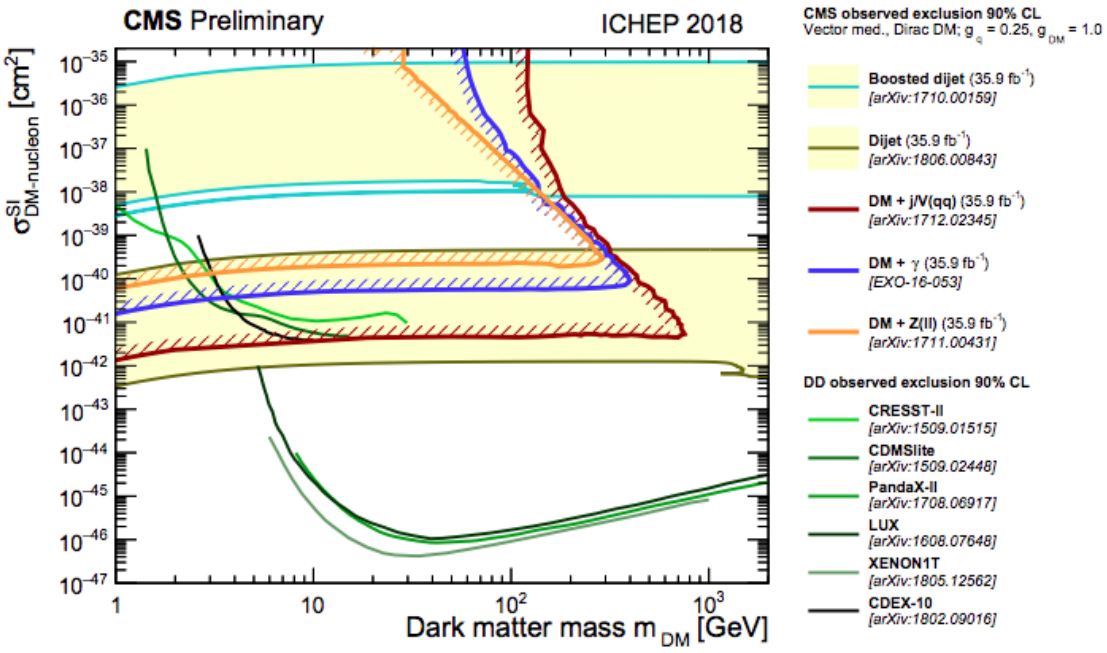

Figure 2.5: The $90\% - \mathrm{CL}$ constraints from the CMS experiment m_{DM}-spin-independent DM–nucleon plane for a vector mediator, Dirac DM, and benchmark couplings $g_{DM} = 0.25$ and $g_{DM} = 1.0$ [21]

Another indirect detection method relies on the gamma-ray spectrum in the galaxy. Galactic models can be used to derive the total gamma flux and their spectrum. WIMP annihilation in the galactic halo would lead to a deviation from these models. This signal would strongly depend on the size of the halo but is expected to be most prominent near the galactic center. Interesting results from such a search come from the FERMI/LAT satellite experiment which detected an excess of ≈ 133 GeV photons from the galactic center. However, the detailed analysis set a global significance estimated to 1.6 standard deviations [25]. In addition to the gamma spectrum, galactic models predict a spectrum for positrons, antiprotons, anti-deuterium, and anti-helium. Satellite-based experiments such as PAMELA [26] or AMS02 [27] can measure this spectrum. Both experiments detected a rise of the positron fraction in

cosmic rays. The possibility that annihilating dark matter might be responsible for this signal generated a great interest. However, it was pointed out that nearby pulsars or the acceleration of secondary positrons in supernova remnants could potentially account for the excess positrons. The combined data from PAMELA, AMS02, and Fermi show that for dark matter to generate this signal, the particle would have to be heavy,$\approx 1 - 3\text{TeV/c}^2$ [22]. Similarly to the electron/positron ratio, AMS02 observed an excess of antiprotons at energies between 10 and 20 GeV. This excess has no simple explanation and has been interpreted as a possible signal of annihilating dark matter. However, systematic uncertainties related to the antiproton production cross-section, solar modulation and cosmic-ray transport make the significance of this feature difficult to assess at this time [22]. This excess is a suggestion for dark matter masses between 60 and 80 GeV/c^2.

2.4.3 Direct detection

The direct detection of WIMPs relies on the detection of nuclear recoils induced by the elastic scattering of WIMPs on a target material. Due to the assumed weak-scale interaction cross-section between WIMPs and standard model particles, detecting such interaction demands large detectors placed in a low background environment. This section will summarize the theory of such detection, the interaction cross-section, expected differential recoil energy spectrum and characteristics of a WIMP signal and will be concluded by a summary of the current detection limits.

Cross sections

The WIMP-nucleus cross section may be written in terms of a spin-independent and a spin-dependent term. The spin independent is given by:

$$\sigma^{SI} = \frac{4\mu_A^2}{\pi}\left[Zf_p + (A-Z)f_n\right]^2 \tag{2.8}$$

and the spin dependent by:

$$\sigma^{SD} = \frac{32G_F^2\mu_A^2}{\pi}\frac{J+1}{J}\left(a_p\langle S_p\rangle + a_n\langle S_n\rangle\right)^2 \tag{2.9}$$

where $\mu_A = M_\chi M_A/(M_\chi + M_A)$ is the WIMP-nucleus reduced mass, with M_χ the mass of the WIMP and M_A the mass of the nucleus. Z is the atomic number of the nucleus, J is the total nuclear spin and G_F is the Fermi constant. f_p, a_p, f_n and a_n are the effective spin-independent and spin-dependent couplings of the WIMP to the proton and neutron. $\langle S_n\rangle$ is the expectation values of the proton and neutron spins within the nucleus [28]. The total WIMP-nucleus cross section is the sum of equations 2.8 and 2.9. For many spin-independent models, $f_p \approx f_n$, so the spin-independent WIMP-nucleus cross-section can be rewritten as:

$$\sigma_{0WN}^{SI} = \sigma_{SI}\frac{\mu_A^2}{\mu_n^2}A^2 \tag{2.10}$$

where the dependence on the target material may be factored as:

$$\sigma_{SI} = \frac{4\mu_n^2 f_n^2}{\pi} \tag{2.11}$$

is the spin-independent cross-section of a WIMP on a single nucleon. The spin-independent cross-section with a single nucleon is used in the literature because it is independent of the target nuclei.

For spin-dependent, the contributions of nucleons with opposite spins cancel, so the total spin-dependent cross-section depends on the net spin of the nucleus. Nuclei with even numbers of protons or neutrons have nearly no net proton or neutron spin and have almost no sensitivity to spin-dependent interactions on protons and neutrons respectively. For example, argon is mainly composed of ^{40}Ar and neon is mainly composed of ^{20}Ne, so these targets are insensitive to spin-dependent interactions. Many materials used as WIMP targets such as neon, germanium, silicon or xenon have even numbers of protons and hence are insensitive to spin-dependent interactions on protons, and only a fraction of the isotopes of these targets have a sensitivity to spin-dependent interactions on neutrons. Experiments such as PICO [29] are sensitive to spin-dependent interactions on protons by using fluorine as a target material. NEWS-G can also be sensitive to spin-dependent interactions on protons using hydrogen in the form of CH_4 as a target.

Recoil energy spectrum

Due to their low velocity in the galactic frame, around 220 km/s, WIMPs will interact with the nucleus as a single target by elastic scattering. The recoil energy E_r given to a nucleus of mass m_A is then:

$$E_r = E_i r \frac{1 - \cos\theta}{2} \tag{2.12}$$

where E_i is the WIMPs initial kinetic energy, $E_i = M_\chi v^2/2$, θ is the scattering angle and r is a dimensionless parameter defined by:

$$r = \frac{4M_\chi M_A}{(M_\chi + M_A)^2} \tag{2.13}$$

The energy momentum transfer is maximum for $r = 1$ meaning $M_\chi = M_A$. Which means that the average recoil energy from a WIMP interaction is largest when the target mass is similar to the WIMP mass.

The differential interaction rate per kilogram of detector is then defined by the product of the number of interaction per nucleon with the number of nuclei per kilogram of material:

$$dR = \frac{N_0}{A} n_0 f(\vec{v} + \vec{v_E}) \sigma v d^3\vec{v} \tag{2.14}$$

where N_0 is Avogadro's number, so that N_0/A is the number of nuclei per kilogram of material and σ is the cross section. n_0 is the local WIMP number density $n_0 = \rho_\chi/M_\chi$ where ρ_χ is the mass density of WIMPs in the galaxy. ρ_χ is estimated from galactic dynamics to be about $0.3\,\mathrm{GeV}/(\mathrm{c}^2\mathrm{cm3})$, or roughly a third of a proton mass per cubic centimetre [30]. σ is the WIMP-nucleus cross section.

We can reasonably assume that the WIMP velocities in the frame of the Galaxy follow the Maxwellian distribution:

$$f(\vec{v} + \vec{v_E}) = \frac{e^{(-\vec{v}+\vec{V}_E)/v_0^2}}{k} \tag{2.15}$$

where k is a normalisation factor and $v_0 = 220 \pm 20\,\mathrm{km/s}$ is the local circular velocity [28]. Considering the simplified case ignoring the earth velocity ($v_E = 0$) and the

galaxy's escape velocity ($v_{\text{esc}} = \infty$), we get:

$$\frac{dR}{dE_R}(E_R) = \int_{E_R/r}^{\infty} \frac{1}{\left(\frac{1}{2}M_\chi v^2\right) r} \frac{R_0}{2\pi v_0^4} v e^{\frac{-v^2}{v_0^2}} \left(4\pi v^2 dv\right) = \frac{R_0}{E_0 r} e^{\frac{-E_R}{E_0 r}} \tag{2.16}$$

where

$$R_0 = \frac{2}{\sqrt{\pi}} \frac{N_0}{A} n_0 \sigma v \tag{2.17}$$

and $E_0 = M_\chi v_0^2/2$ is the most probable WIMP incident energy. The equation (2.16) gives a good approximation of the expected recoil energy spectrum. Figures 2.6 and 2.7 were produced assuming a velocity of the earth in the WIMP halo to be $v = 220\,\text{km/s}$ and a nucleon cross section on the order of the weak scale, $\sigma = 1\,\text{pb} = 10^{-36}\text{cm}^2$.

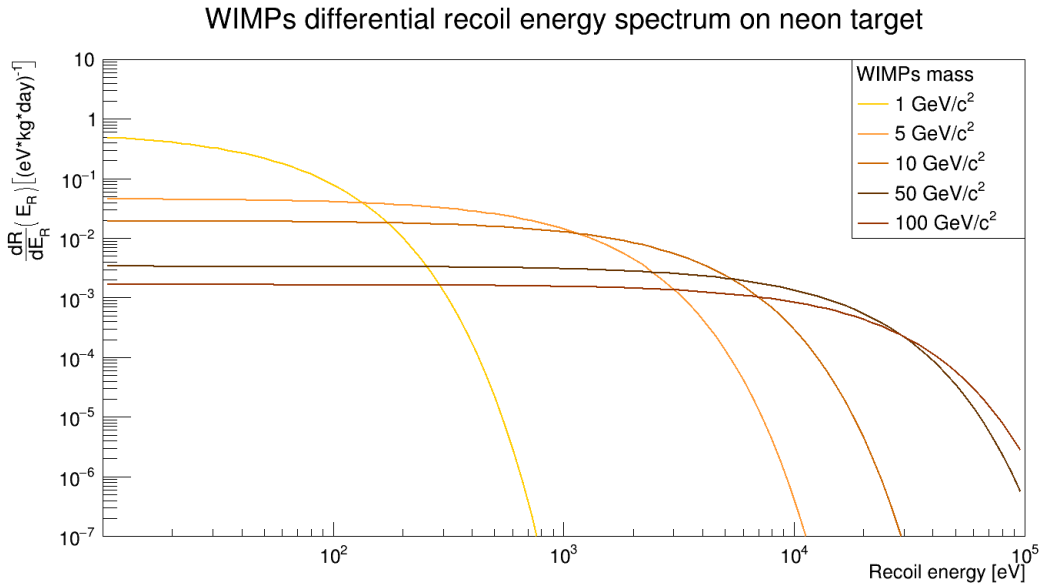

Figure 2.6: Recoil energy spectrum of WIMPs with different masses on a neon target.

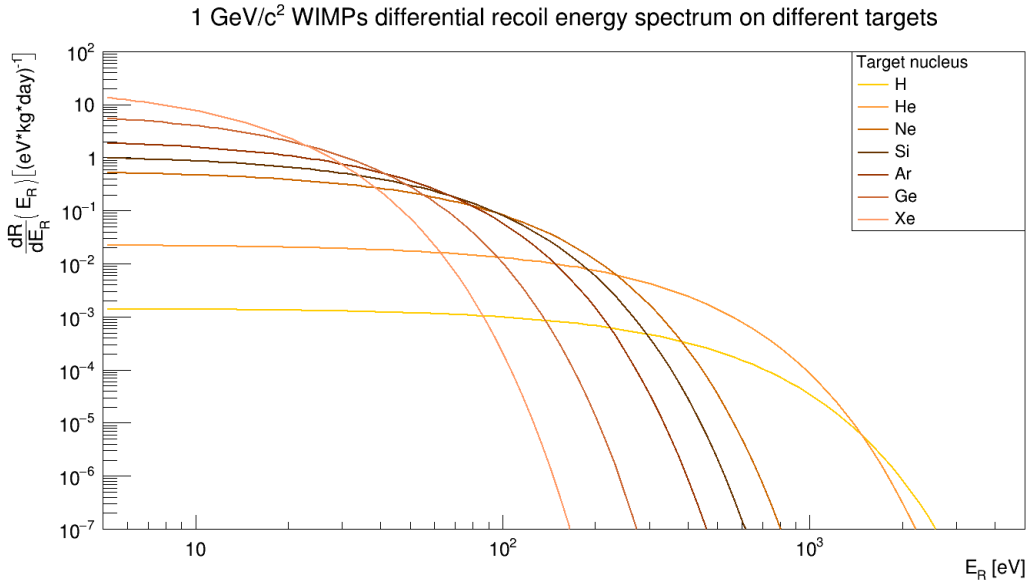

Figure 2.7: Recoil energy spectrum of 1 Gev/c^2 WIMP on different target mass

We can derive two main facts from fig 2.6 and 2.7. Due to the kinematics of the interaction, light WIMPs produce a recoil spectrum that drops earlier compare to the larger masses. Secondly, the recoil energy spectrum of light WIMPs ($M_\chi \approx 1\,\text{Gev/c}^2$) is extended by using light target masses. This fact is of particular interest to the NEWS-G collaboration. Using gases with low A, such as neon or hydrogen, enhances its sensitivity to light WIMP candidate below 1 GeV/c^2. At the present time, using a detector filled with methane, NEWS-G is the only experiment able to look for WIMP scattering on a hydrogen target.

Exclusion curve

Dark matter experiments count events. The number of events N expected for a given cross section σ and exposure follows a Poisson distribution. Without good knowledge of the background, we can assume that all detected events are dark matter candidates.

The excluded cross section at 90% confidence σ_{ex} is then the one that would have 10% probability of giving the number of events observed or more. This cross section is given by:

$$\sigma_{\mathrm{ex}} = \frac{\sigma \times N_{\mathrm{ex}}}{N_{\sigma}} \tag{2.18}$$

where N_{σ} is the integral of the differential recoil energy spectrum for a given WIMP mass M_{χ} and cross section σ. N_{ex} is the upper limit on the number of events that the experiment should observe if the cross section is σ_{ex} and is given by:

$$\mathrm{N}_{\mathrm{ex}} = \frac{1}{2} F^{-1}_{\chi^2}(0.9; 2(N+1)) \tag{2.19}$$

where $\mathrm{F}^{-1}_{\chi^2}$ is the quantile of the chi-square distribution [17] and N the number of events observed. If 0 (1, 2, 3) event is observed, 2.3 (3.89, 5.32, 6.68) events can be excluded at 90%. It is instructive to compare the effect of the different characteristics of detectors on the exclusion curve, determined on a range of M_{χ}. First, we can compare the exclusion curves for different target masses. Figure 2.8 shows the WIMP exclusion curves for different target masses, where the recoil energy spectrum was determined with formula 2.16 in a range E_{nr} from 0.1 to 500 keV, assuming $\mathrm{v}_0 = 220\,\mathrm{km/s}$, 100 kg·day of exposure and no events detected. Although the exclusion is strongly related to the energy range and other parameters, the assumptions used allow us to clearly identify the advantages of each target. We can remark that the best sensitivity occurs for WIMP masses close to the mass of the target. At lower masses, the excluded cross section rises rapidly as the cut-off of the recoil spectrum approaches, and then reaches the energy threshold of the experiment. At higher masses, the excluded cross-section increases as the number of expected WIMP events decreases due to the fixed mass

density of WIMPs. This figure shows clearly that to search for light WIMPs, we have to use light targets.

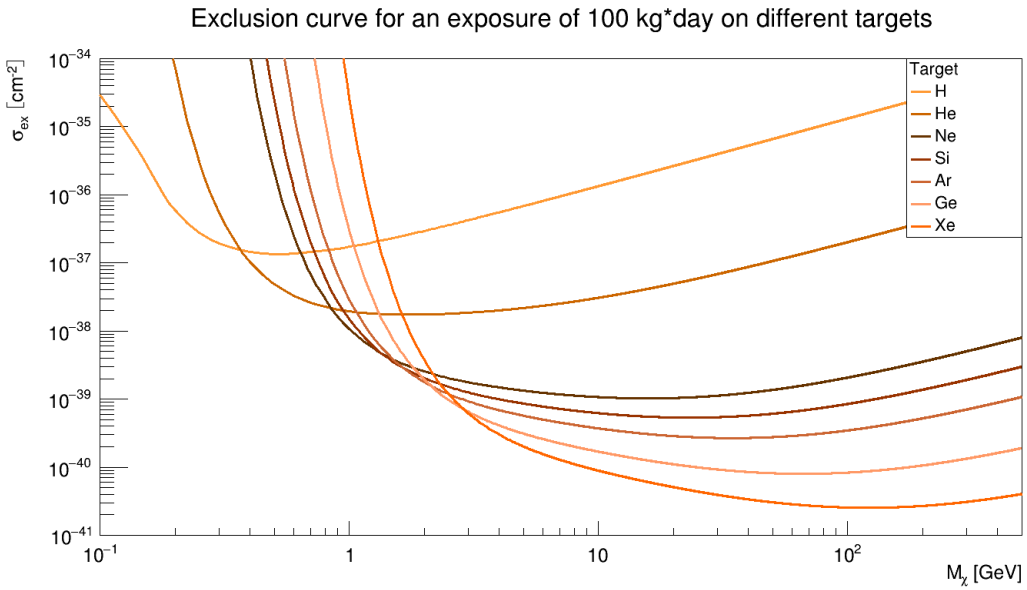

Figure 2.8: WIMP exclusion curve for different target, assuming an exposure of 100 kg·day, a threshold of recoil energy range in [0.1;500] keV and no events detected.

Secondly, we can study the WIMP exclusion curves for different energy thresholds. Figure 2.9 shows the exclusion curves on a neon target with different energy thresholds for exposure of 100 kg·days and the same other assumptions as for the previous figure. The exclusion curves rise as the WIMP mass reaches the energy threshold, so it fundamental to keep the threshold as low as possible, typically down to the ionization potential of the target material used.

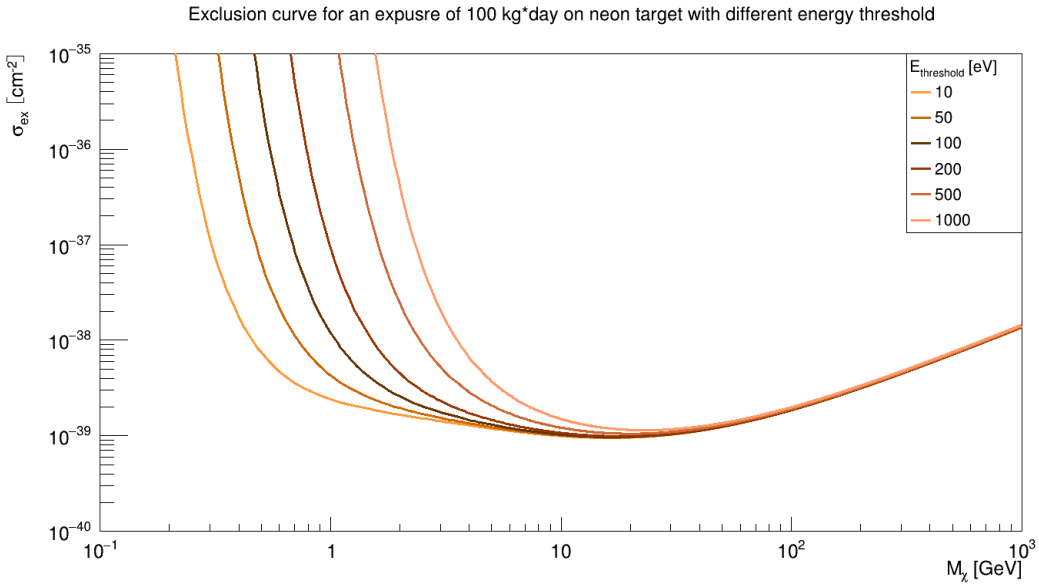

Figure 2.9: WIMP exclusion curve for different energy threshold, assuming an exposure of 100 kg·day on a neon target.

Finally, we can compare the effect of the number of events detected on the limits, assuming that without any possibility to distinguish if an event is from a WIMP interaction or background radiation, all are considered as WIMP candidate. Figure 2.10 shows the effect of the background on the exclusion curve for exposure of 100 kg·day on a neon target. The exclusion curve is strongly related to the number of events observed and the limit roughly scales with it. It is crucial to keep the background as low as possible to be able to set a competitive limit on the dark matter cross section. This is true for all dark matter search experiments and more generally for rare event detection experiments such as neutrinoless double beta decay.

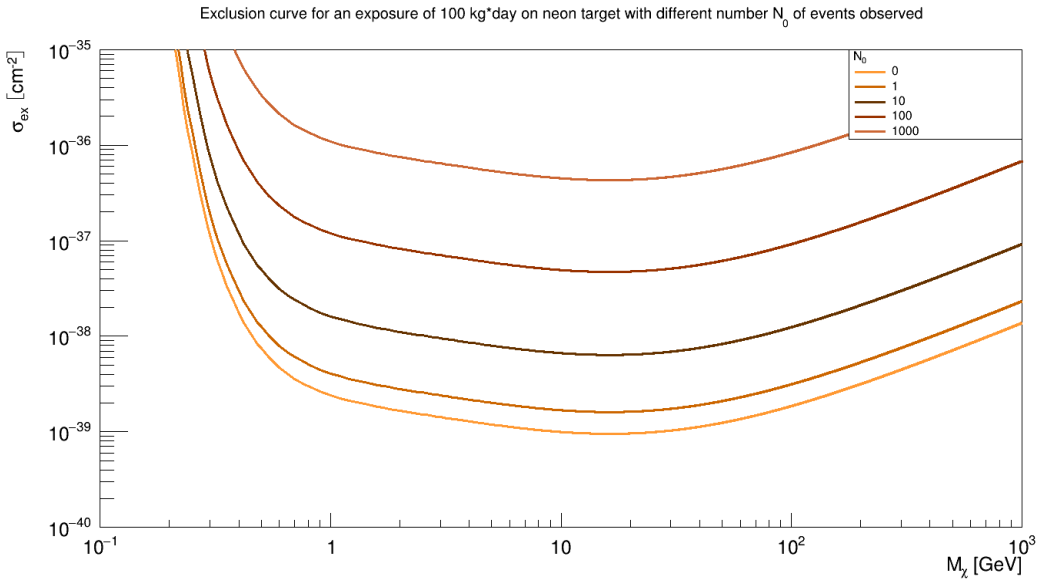

Figure 2.10: WIMP exclusion curve for different number of events detected, assuming an exposure of 100 kg·day on neon target and a threshold at 22 eV.

The three preceding plots explain the challenges to be overcome to detect WIMPs and especially sub-GeV WIMPs. We need to have a detector made of low A target masses (H, He, Ne), with an energy threshold as low as possible, to ensure a single electron detection and with the lowest background radiation possible. This thesis gives an optimization of these requirements, chapters 4 and 5 focus on the background, and chapter 6 on the hardware needed for single-electron detection.

Annual modulation

Due to the rotation of the earth around the sun, its speed in the galactic frame of reference is given by [28]:

$$v_E(t) \approx 232 + 15 \cos\left(2\pi \frac{t - 152.5}{365.25}\right) \text{ km/s} \tag{2.20}$$

where t is the day of the year and with maximum occurring at $t = 152.5$ days, or June 2. Due to this change of velocity during the year, the expected WIMP interaction rate is expected to modulate with a variation of roughly 3% between its maximum in June and its minimum in December. This annual modulation in the expected WIMP event rate is a unique characteristic, and it allows one to validate WIMPs as the source of the signal.

WIMP experiments

There are a variety of different experimental approaches to detect dark matter directly. All the different technologies rely on the detection of the energy deposited by the scattering of a dark matter particle on a nucleus. We can classify experiments in three main categories: detection of charges, light, and heat or a combination of two of them. Figure 2.11 illustrates the different techniques used for direct detection.

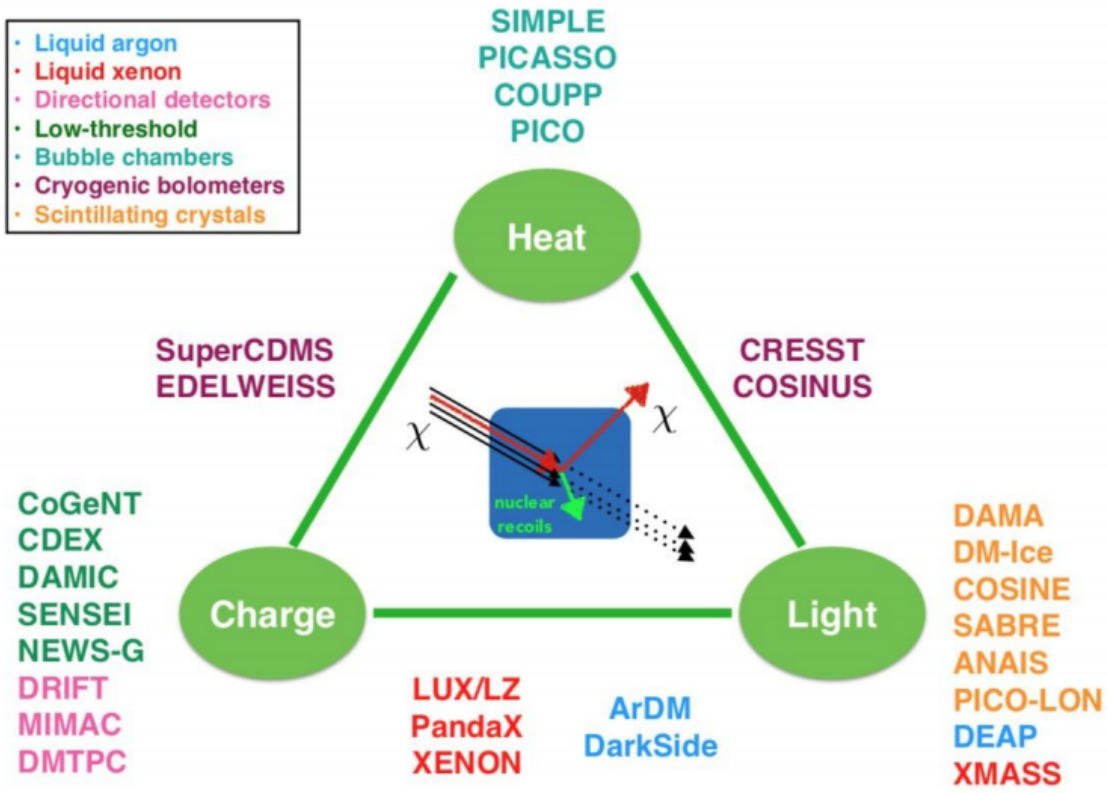

Figure 2.11: Summary of direct detection experiments [31]. The names correspond to experiments and they are related to the searched signal, heat, charge, light, and combination of two of them.

Light detection The detection of light in noble gas can be used for WIMP detection and is employed by the DEAP-3600 collaboration [32] installed at SNOLAB. The detector consists of an 85 cm radius acrylic vessel capable of holding up to 3600 kg of liquid argon (LAr). 255 photomultiplier tubes (PMTs) surround the vessel. A particle interaction in the LAr produces 128 nm scintillation light detected by the PMTs after being shifted to visible light. A powerful pulse shape discrimination mitigates the background. LAr excitation can form singlet or triplet states with lifetimes of 6 and 1300 ns respectively. Particles interacting with different linear

energy transfer populate these states differently. Nuclear recoils populate mostly singlet states and electronic recoils populate mostly triplet states. In 2017, DEAP-3600 set a leading limit on the WIMP-nucleon spin-independent cross-section on argon of $\sigma < 1.2 \times 10^{-44}\text{cm}^2$ for a 100 GeV/c^2 WIMP mass (90%C.L.) [33]. Solid crystals made of NaI and CsI coupled to PMTs are also used for the detection of light. Solid crystals used by DAMA [34] or COSINE-100 [35] also have a powerful pulse shape discrimination. The most famous experiment using this technique is DAMA that claimed the observation of an annual modulation of the signal to be evidence of a dark matter detection. The results are controversial and will be discussed in the 'state of art section'.

Heat detection Heat detection is used by superheated bubble chambers such as PICO [29] where the nuclear recoil causes a phase change of the liquid into a gas which produce a bubble. This technique has the tremendous advantage to be insensitive to β and γ radiation giving a low background composed of neutrons and α. Acoustic sensors allow for α rejection. In addition, combining an external neutron shield and a careful selection of the material provides a practically background free detector.

Charge detection Several collaborations search for dark matter through charge detection using three different targets. DAMIC [36] uses charge-coupled devices (CDDs) where WIMP signal results in a silicon nucleus recoil. The CCD's low electronic noise allows for a low energy threshold of a few tens of eV and its high spatial resolution and the excellent energy response results in very effective background identification techniques. CoGenT [37] use P-type high purity germanium detectors. With their low energy threshold and ability to reject surface backgrounds, this type of detector

allows for exploring 10 GeV/c^2 WIMP candidates. Other experiments using germanium detectors can detect both charge and heat and will be discussed in the next section. Finally, the charge detection can be done using gas as a target. We can first mention NEWS-G; this technology will be discussed throughout this thesis. Other gaseous WIMPs detectors rely on large gas volumes coupled to bulk micromegas [38] producing electron multiplication in a very tiny gap. This method is used by the MIMAC collaboration [39]. Running at low enough pressure, the MIMAC collaboration aims to perform directional WIMP detection at the Laboratoire Souterrain de Modane. The TREX-DM [40] collaboration uses a similar method with a 20 litre cylindrical chamber that can hold pressurized gas up to 10 bar, enclosed in a micromegas readout plane. The advantage of a gaseous detector is to combine the use of light elements and a low energy threshold.

Heat and charge detection Heat and charge detection is done using a Ge or Si cryogenic detector. Energy deposition in the crystal results in the production of two signals. The primary ionization produces both charges and phonons. During their drift toward the anode, primary charges generate secondary phonons with a total energy proportional to the potential difference traversed. This is known as the Neganov-Luke effect [41]. The recoil energy E_r is reconstructed from the total phonon energy E_P by subtracting a term proportional to the ionization-derived recoil energy E_q to account for the Neganov-Luke effect [42].

$$E_r = E_p - \frac{eV}{\epsilon} E_q \tag{2.21}$$

where e is the elementary charge, V is the absolute value of the operating potential and ϵ the average electron-hole pair creation energy. This effect allows for powerful discrimination of nuclear and electronic recoil using the ionization yield. The ionization yield is defined as the ratio of the ionization energy to recoil energy (E_q/E_r). A nuclear recoil produces less ionization than an electronic recoil. Lastly, position reconstruction of the energy deposition allows for the suppression of surface events that dominate the background. Using such technology, in 2105 the CDMS collaboration set a new limit of $1.8 \times 10^{-44}\,\mathrm{cm}^2$ and $1.18 \times 10^{-41}\mathrm{cm}^2$ at 90% confidence for 60 and 8.6 GeV/c^2, respectively. In 2016, the EDELWEISS collaboration set limit of $9.4 \times 10^{-44}\mathrm{cm}^2$ and $4.3 \times 10^{-40}\mathrm{cm}^2$ at 90% confidence for 20 and 5 GeV/c^2 respectively [43].

Charge and light detection Charge and light detection are done in large Time Projection Chambers (TPC) filled with a liquid noble gas, usually argon or xenon. Under the influence of an electric field, charges drift toward the anode. The anode is placed on top of the TPC where the target material is in the gaseous phase allowing for signal amplification. The light is detected by PMTs placed below and above the target material. A first prompt scintillation signal (S1) generated in the liquid phase is recorded by the PMTs followed by a second signal (S2) induced by the ionization electrons. This technology benefits from a strong background suppression by the charge to light ratio (S2/S1) and the multiplicity of the S2 signal [44]. In addition, a spatial reconstruction of the events is possible. The relative amount of light in the different PMTs allows for the xy reconstruction of the energy deposition, and the z is constructed based on the time difference between S1 and S2. This allows for the rejection of surface events. Using this technique, the Xenon-1T collaboration

based at the Laboratori Nazionali del Gran Sasso (LNGS) in Italy set a limit of $7.7 \times 10^{-47}\text{cm}^2$ for 35 GeV/c^2 and PandaX-II [45] set a limit of $8.6 \times 10^{-47}\text{cm}^2$ for 40 GeV/c^2, both in 2017. Using large dual-phase TPCs filled with xenon is the most competitive technique for spin-independent dark matter searches with masses above 10 GeV/c^2. This technology also shows competitive results at lower masses when filled with argon. The DarkSide-50 collaboration used an argon TPC to set the most stringent limit on the spin-independent dark matter with masses down to 1.8 GeV/c^2.

Light and heat detection The detection of both light and head is done with scintillating crystals. The CRESST-III collaboration used $CaWO_4$ crystals as cryogenic calorimeters [46]. Each interaction in the $CaWO_4$ crystal produces a phonon signal and a light signal measured by a second calorimeter. The light signal allows for the discrimination of nuclear and electronic recoil. The CRESST-III collaboration set the most stringent limit for WIMP masses below 1 GeV/c^2.

2.5 State of the art of WIMP direct detection

After decades of searching for WIMPs, there has not yet been any conclusive observation. Figures 2.12 and 2.13 show the current limits on WIMP masses and nucleon cross-sections in a mass range 0.5 to 10^3 GeV/c^2 and 0.2 to 20 GeV/c^2.

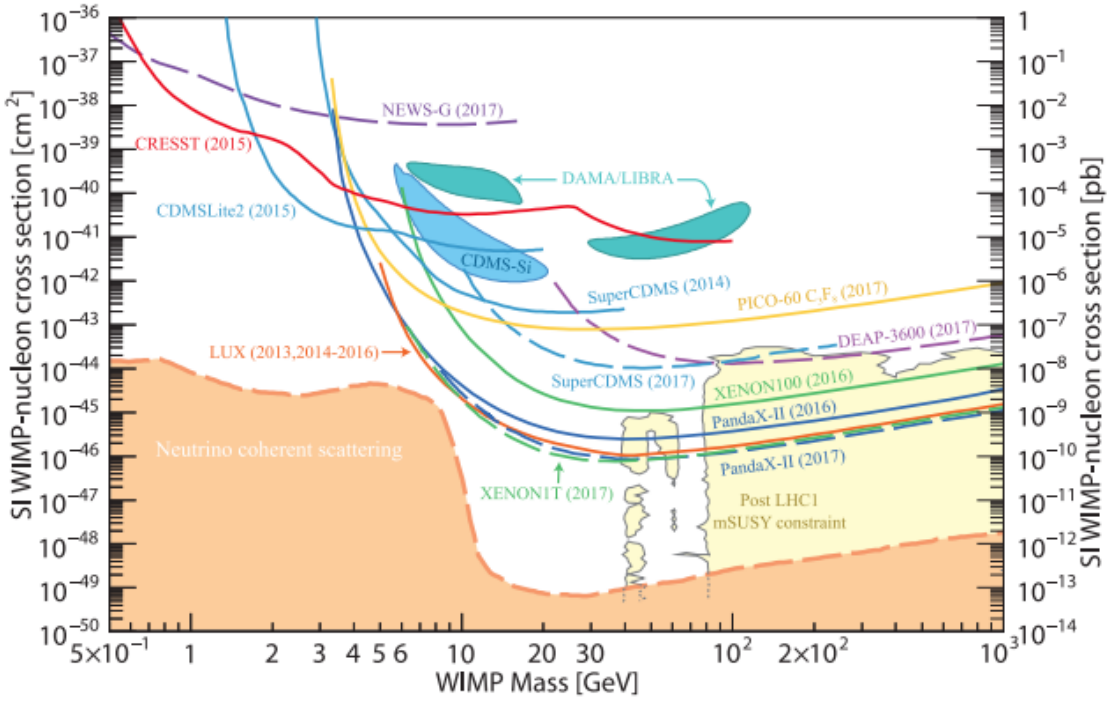

Figure 2.12: Parameter space for elastic spin-independent dark matter-nucleon scattering [17]. The DAMA/LIBRA and CDMS-Si enclosed areas are regions of interest from possible signal events. The NEWS-G results are indicated by the purple dashed line [47].

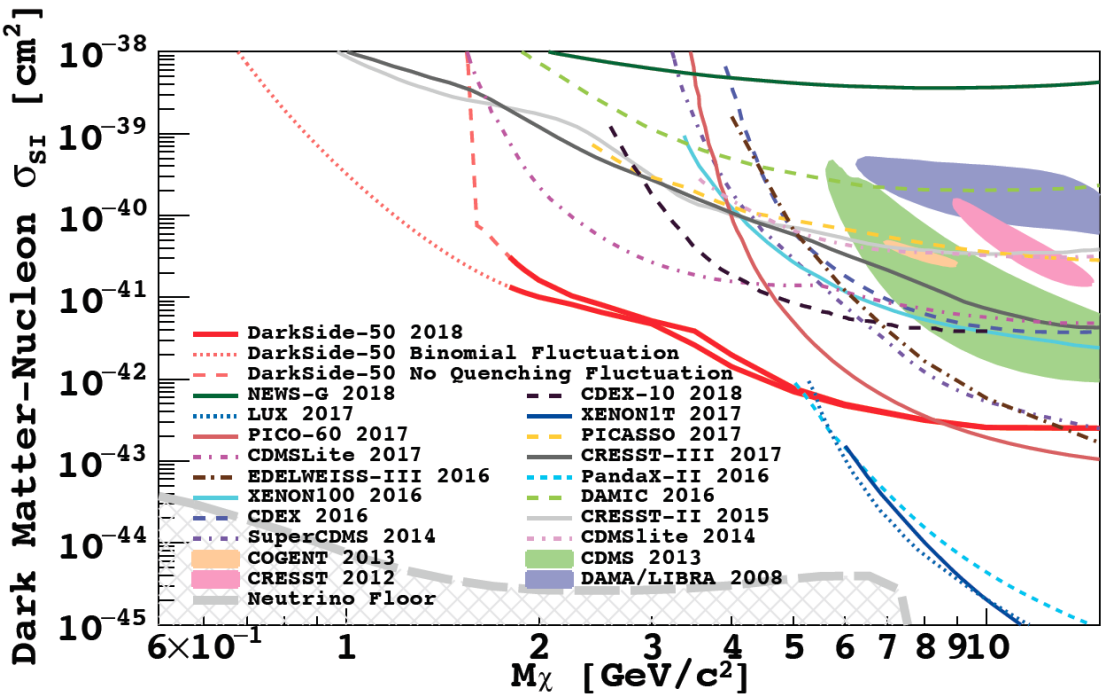

Figure 2.13: Parameter space for elastic spin-independent dark matter-nucleon scattering zoomed in the low mass region. Between 2 and 6 GeV/c^2, the most stringent limit is from the Dark-Side 50 collaboration (red curves) [48] . The solid dark grey curve show the current most stringent limit for sub-GeV WIMPs from the CRESST-III collaboration [46]

Figure 2.12 shows two coloured areas. The purple one shows the space parameters where the DAMA/LIBRA claimed a detection [34] by measuring the expected annual modulation of the WIMP event rate. However, the region of WIMP parameter space tagged by DAMA/LIBRA has been excluded by multiple other experiments. This lack of evidence from other experiments throws the DAMA/LIBRA results into doubt. The green area shows the space parameters where CDMS reported having observed events with a Si detector [49] although they do not claim this as an evidence for dark matter detection. Figure 2.13 shows the parameter space where NEWS-G will be competitive. The current most stringent limit for sub-GeV WIMPs is about

$\approx 10^{-38}\text{cm}^2$ and was set by the CRESST-III experiment in 2017.

2.6 Discussion

WIMPs are investigated in three ways: production, and direct and indirect detection. Today, after decades of investigation, a tremendous investment of thousands of physicists around the world, no non-ambiguous signal of a dark matter signature can be claimed. The direct detection of WIMPs is an intensive field of research and employs a variety of detection techniques. Exploring the possible mass range of the WIMPs candidates is challenging. For masses higher than a few GeV/c^2, dual-phase TPCs set the most stringent limits. The low mass part of the range is currently explored by cryogenic and gaseous detectors. The NEWS-G collaboration explores this part of the spectrum. The NEWS-G detectors are particularly effective in this parameter space because of their low energy threshold and the possibility to use low A target nuclei such as hydrogen. The next chapter will detail the SPC technology.

Chapter 3

The spherical proportional counter

Gaseous particle detectors have been developed for a century. The single-wire proportional counter was invented in 1908 by E. Rutherford and H. Geiger [50]. Several technologies involving different geometry, size, gas pressure, and electric field are used in many areas from particle physics to industry and medicine. Gaseous detector can be divided into three categories: the ionization chamber, which uses low electric fields, where the signal is induced by ions and electrons from the primary ionization; the Geiger counter, which uses a strong electric field and where all pulses are of the same amplitude regardless of the number of original ion-electron pairs that initiated the process [51]; and, the proportional counter which uses intermediate electric fields. In such a device, the signal from primary ionization is amplified inducing pulses considerably larger than for an ionization chamber. However, the amplification is much smaller than in a Geiger counter: the pulses are proportional to the initial number of primary electron-ion pairs, allowing for energy discrimination. The NEWS-G SPCs operate as a proportional counters.

Spherical proportional counters consist of a grounded spherical vessel with a sensor placed in its center. Under the influence of the electric field, electrons from a primary

ionization drift toward the center of the sphere. Close to the anode, an avalanche occurs, creating a large number of secondary ion-electron pairs. The motions of the secondary ions then induces the signal. This chapter describes the functioning of an SPC, from the energy deposition to the signal treatment. The next chapters are based on simulations of the detector. These simulations are done using several software packages, each reproducing a specific interaction and detector function. These software packages will be presented at the appropriate step along with the chapter. The first section describes the interaction of particles with matter, producing the primary ionization. The second section focuses on the properties of the signal common to all proportional counters and will be followed by the specificities of the spherical proportional counter. The penultimate section focuses on the sensor, one of the critical points of the detector to ensure the best working conditions. The last part will then link all the properties described previously to the search for dark matter.

3.1 Interaction of particles with matter

Particles crossing the detector are detected by the ionization produced during their journey through the gas volume. Depending on their charges, masses, and energies, different particles produce characteristic deposition. Charged particles such as electrons or muons deposit energy all along their path and neutral particles such as neutrons or photons ionize matter at a particular point of interaction. This section describes the different mechanisms of energy loss proper to each type of particle.

3.1.1 Charged particles

When charged particles pass through gas within the detector, they interact with the electrons of the gas molecules and lose energy. These interactions lead to excitation and ionization of the gaseous medium. Other interactions such as Bremsstrahlung, Cerenkov, or transition radiation are of little importance for the gaseous proportional counter.

Heavy ions

The general class of heavy ions includes all charged particles more massive than electrons. It includes pions, muons, or alphas. The energy loss is due to the effect of the Coulomb force between the charged particle and the electron cloud of the atoms constituting the medium being traversed. Although interactions of the particles with the gas nuclei are possible, they are rare and not significant for gaseous detectors. The average energy loss in an absorber with respect to the path length is called the linear stopping power:

$$S_e = -\frac{dE}{dx} \tag{3.1}$$

The formalism of this phenomenon was described by Bethe using relativistic quantum mechanics. The electronic stopping power is given by the Bethe-Bloch formula [51]:

$$-\frac{dE}{dx} = \frac{4\pi e^4 z^2}{m_0 v^2} Z \left[\ln\left(\frac{2m_0 v^2}{I}\right) - \ln\left(1-\beta^2\right) - \beta^2 \right] \tag{3.2}$$

where v and ze are the velocity and charge of the incident particle, N and Z are the number density and atomic number and, I is the ionization potential of the target

material. m_0 is the electron rest mass, e is the electronic charge, and $\beta = v/c$.

Fast electrons

Due to their low mass, the behaviour of electrons differs from heavy ions. Because their mass is the same as the electron in the atomic cloud, they lose much more energy per interaction. Each interaction is able to change the trajectory of the incoming electron abruptly. Electrons also differ from heavy charged particles in that energy may be lost by radiative processes as well as Coulomb interactions. The stopping power in then the sum of a collisional and radiative component:

$$\frac{dE}{dx} = \left(\frac{dE}{dx}\right)_c + \left(\frac{dE}{dx}\right)_r \tag{3.3}$$

A similar equation to Equation 3.2 was derivated by Bethe to describe the specific loss due to ionization and excitation for fast electrons:

$$-\left(\frac{dE}{dx}\right)_c = \frac{2\pi e^4 NZ}{m_0 v^2}[\ln\left(\frac{m_0 v^2 E}{2I^2(1-\beta^2)}\right) - \ln(2)\left(2\sqrt{1-\beta^2} - 1 + \beta^2\right) + \left(1-\beta^2\right) + \frac{1}{8}\left(1-\sqrt{1-\beta^2}\right)^2] \tag{3.4}$$

where the symbols have the same meaning as in Equation 3.2. The radiative losses take the form of Bremsstrahlung radiation. The linear specific energy loss through this radiative process is:

$$-\left(\frac{dE}{dx}\right)_r = \frac{NEZ(Z+1)e^4}{137 m_0^2 c^4}\left(4\ln\frac{2E}{m_0 c^2} - \frac{4}{3}\right) \tag{3.5}$$

It is of some interest to remark that the ratio of the two energy loss mechanisms is roughly equal to:

$$\frac{(dE/dx)_r}{(dE/dx)_c} \approx \frac{EZ}{700} \tag{3.6}$$

where E is in MeV. With an SPC filled with a low A gas (low Z) the radiative loss from Compton scattered or δ electron is negligible. However, the detector shell is made of copper and surrounded by lead, and high energy β decay in these materials produces a large quantity of Bremsstrahlung γ. Gamma rays can cross a much more substantial thickness of material than electrons, so Bremsstrahlung γ produced in the copper and the lead are an important source of background for the experiment. This is discussed in the next chapter.

Energy loss distribution

The Bethe-Bloch formula gives a mean value of the energy loss of an incident particle per ionization or excitation of the traversed medium. However, when the medium is thin enough or made of gas at low enough pressure, there are few collisions. The the energy deposition thus depends on fluctuations due to δ electrons. The energy loss distribution shows significant fluctuations and is approximated by the strongly asymmetric Landau distribution as shown on Fig 3.1, which can be approximated by:

$$F(\lambda) = \frac{1}{\sqrt{2\pi}} \exp\left(-\frac{1}{2}(\lambda + e^{-\lambda})\right) \tag{3.7}$$

Where:

$$\lambda = \frac{\Delta E - \Delta E_0}{\chi} \tag{3.8}$$

Here ΔE is the energy loss, ΔE_0 is the most probable energy loss and χ is the mean energy loss within a thickness x of traversed matter.

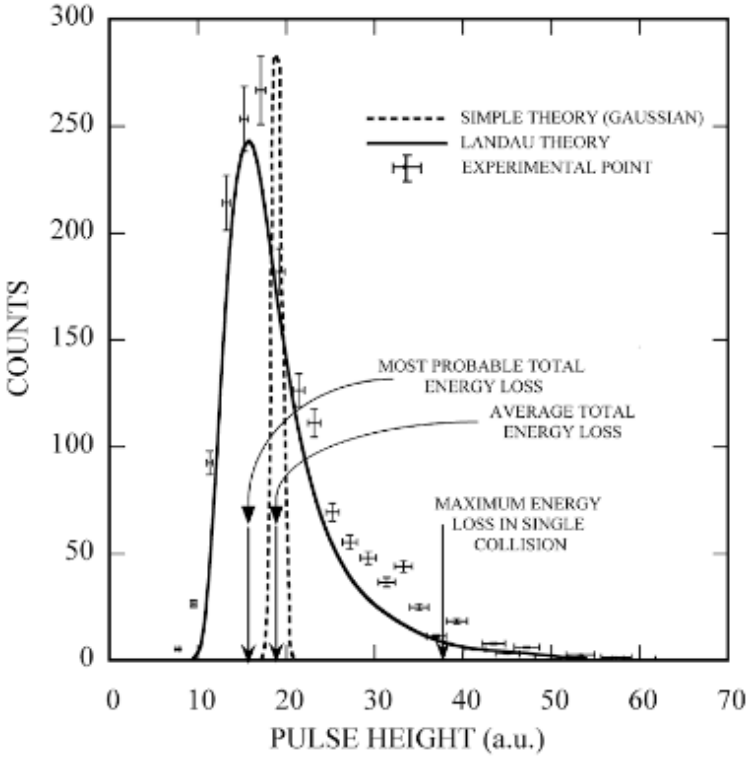

Figure 3.1: Experimentally measured energy loss distribution in an argon carbon dioxide counter, compared to the corresponding Landau and Gaussian distributions [52].

3.1.2 Photons

Photons are neutral electromagnetic radiation. They do not lose energy via Coulomb interaction as charged particles do. They interact with matter by three mechanisms, the photoelectric effect, Compton scattering, and pair production. These interactions lead to a partial or total energy transfer to the electrons. These electrons are the particles which then deposit their energy to the medium and allow the photon to be detected. Figure 3.2 shows the predominance of each process with respect to the

energy of the incident photon and the atomic number of the medium.

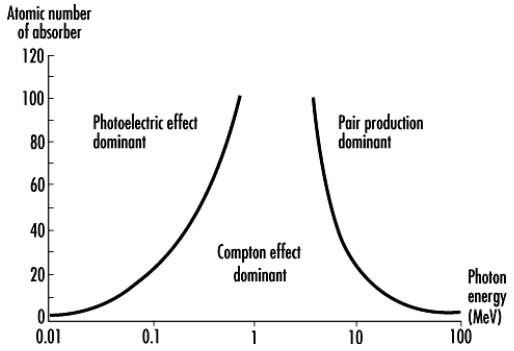

Figure 3.2: The relative importance of the three types of interaction of gamma rays with matter.

Photoelectric effect

This effect leads to the absorption of a photon with energy E_γ by an atomic electron with the subsequent ejection of the electron from the atomic cloud. The energy of the outgoing electron is then:

$$E_{e^-} = E_\gamma - E_B \tag{3.9}$$

where E_B is the binding energy of the electron. For photon energies above the K-shell, the photo-absorption cross section can be approximated by [53]:

$$\Phi = 4\alpha^4\sqrt{2}Z^5\Phi_0\left(\frac{m_e c^2}{E_\gamma}\right)^{\frac{7}{2}} \tag{3.10}$$

where α is the fine structure constant $\alpha \approx \frac{1}{137}$, and $\Phi_0 = 8\pi\frac{r_e^2}{3} \approx 6.651 \times 10^{-25}\text{cm}^2$. The Z^5 dependency of the cross section makes atoms with high Z value interesting for detection of photons. This interaction will leave the atom in excited state. De-excitation can occur by emission of X-ray photons or an Auger electron (Fig 3.3)

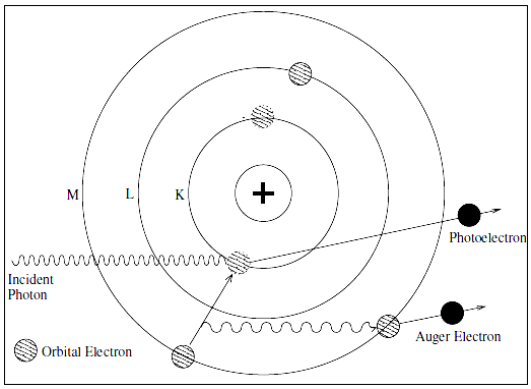

Figure 3.3: Graphical illustration of the phenomena taking place during the photoelectric scattering process.

Compton scattering

Compton scattering is one of the best-understood type of photon interaction. It is the scattering of photons on free electrons. Of course, in matter, the electrons are bound. However, if the photon energy is high compared to the binding energy of the electron, this binding energy can be neglected and the electrons can be considered as free.

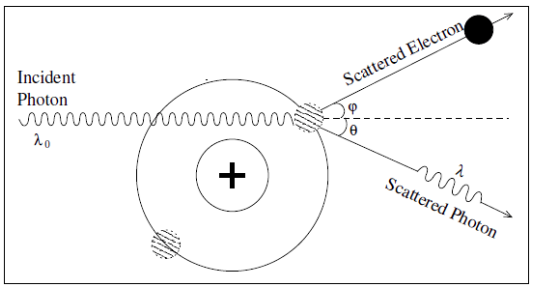

Figure 3.4: Compton scattering.

Applying energy and momentum conservation, the following relations can be obtained: the energy of the scattered photon is

$$h\nu' = \frac{h\nu}{1 + \gamma(1 - \cos\theta)} \tag{3.11}$$

and the energy transferred to the electron is

$$T = h\nu - h\nu' = h\nu \frac{\gamma(1 - \cos\theta)}{1 + \gamma(1 - \cos\theta)} \tag{3.12}$$

Where $\gamma = h\nu/m_e c^2$, $h\nu$ is the energy of the incoming photon and $h\nu'$ is the energy of the scattered photon. From the above equation, we can determine the maximum energy that can be transferred to the electron. It occurs when $\theta = 180\,\text{deg}$. In this case, the photon is back scattered and the electron acquires an energy $T_{\max}$:

$$T_{\max} = h\nu \left(1 - \frac{1}{1 + \frac{2h\nu}{m_e c^2}} \right) \tag{3.13}$$

Pair production

In the presence of a Coulomb field, like the one from the nucleus of an atom, a photon can produce an electron-positron pair like shown in Fig 3.5.

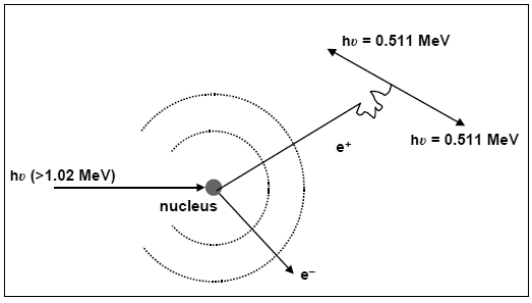

Figure 3.5: Graphical illustration of the pair production process.

The process has a threshold of 1.022 MeV which is the sum of the masses of the electron and the positron. The electron and positron created will split the excess energy of the incoming photon.

$$E_{e^-} + E_{e^+} = h\nu - 1022\,keV \tag{3.14}$$

The probability to have pair production is a function of the photon energy and the atomic number Z of the absorbing medium.

Gamma detection with an SPC

Figure 3.6 shows the mass attenuation coefficient of gamma rays in a gas mixture made of 98% of argon and 2% of methane for energies between 1 and 100 keV. At low energy, the photoelectric effect is dominant but its influence decreases and Compton scattering becomes dominant for gammas with energy higher than ≈ 75 keV.

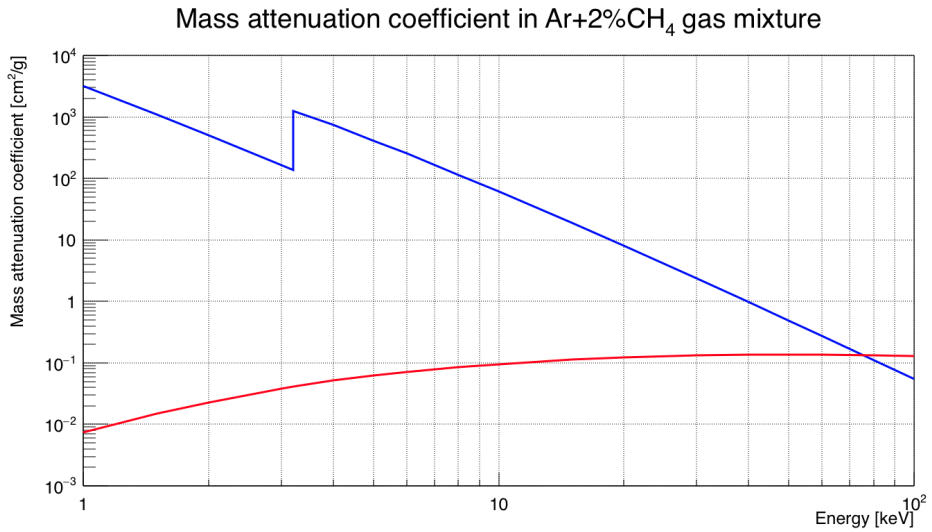

Figure 3.6: Mass attenuation coefficient of gamma in a gas mixture made of 98% of argon and 2% of methane. The red curve shows the Compton scattering and the blue curve show the photoelectric effect.

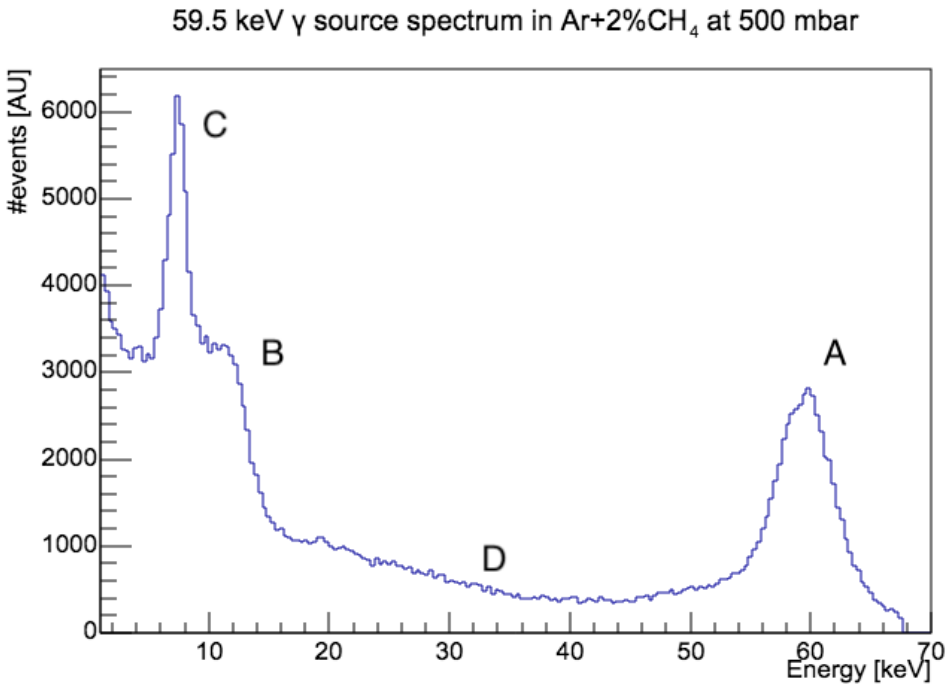

Figure 3.7: Spectrum of a 59.5 keV gamma source recorded with an SPC filled with 98% argon and 2% methane.

Figure 3.7 shows the spectrum recorded by placing a 59.5 keV gamma source (^{241}Am) closed to a 30 cm diameter SPC filled with a gas mixture made of 98% argon and 2% methane at 500 mbar. The peak A is due to the photoelectric effect. The initial energy of the gamma is fully transferred to an electron, and the energy is fully reconstructed. Figure 3.6 shows that at this energy the probability of Compton scattering is roughly half than for the photoelectric effect. The Compton scatterings are clearly identified by the flat component dropping around 12 keV (B). For 59.5 keV gamma ray, the Compton edge corresponding to the maximum energy transferred to an electron is at 11.2 keV. The peak C is due to X-rays coming from the sphere itself. The sphere is made of stainless steal, so mainly iron. The interaction of photons occurring within the metal shell excite atoms which de-excite by the emission of a 6.4 keV X-ray. This characteristic X-ray is proper to each atom. For example, copper de-excitation produces 8.1 keV X-rays which are useful calibration, and are discussed in the next chapters. Finally, the continuous spectrum between the peaks is due to cosmic muon and surface electrons coming from the inner surface of the sphere.

3.1.3 Neutrons

Like photons, neutrons carry no charge and therefore cannot interact in matter through the Coulomb force. The interaction of neutrons with matter is only through the strong nuclear force. Neutrons must come within $\approx 10^{-13}$ cm of the nucleus before any interaction can happen. This makes neutrons very penetrating particles. They can travel several centimeters inside a medium without interacting, making them almost undetectable in a detector of comparable size. When a neutron interacts, it may happen through a variety of nuclear processes depending on its energy [53]:

- Elastic scattering from nuclei $A(n,n)A$: This is the principal mechanism of energy loss for neutrons in the MeV region. During the process a part of the kinetic energy of the neutron is transferred to the nucleus and the velocity and direction of the neutron changes. The average energy loss will be $2E_nA/(A+1)^2$ where E_n is the initial kinetic energy of the neutron and A the mass number of the nucleus. This means that to reduce the kinetic energy of neutrons, material rich in hydrogen $A = 1$ like polyethylene are the most efficient with a mean energy loss of $E_n/2$ per collision.

- Inelastic scattering $A(n,n')A*$,$A(n,2n')B$, etc: In this reaction, the nucleus is left in an excited state which may later decay by gamma-ray or some other form of radiative emission.

- Neutron capture $n+(Z,A) \rightarrow \gamma+(Z,A+1)$,$(n/p)$, (n,d), (n,α), (n,t), $(n,\alpha p)$, etc.: In general, the cross section for neutron capture goes approximately as $1/v$. Where v is the velocity of the neutron. Absorption is most likely at low energies.

- Fission (n,f) Again this is most likely at thermal energies.

- High energy hadron shower production. This occurs only for very high energy neutrons with $E_n > 100\,\mathrm{MeV}$.

3.1.4 Ionization yield

The ionization yield is defined as the fraction of the energy released by a recoil in a medium through ionization compared with its total kinetic energy.

$$QF = \frac{E_{eVee}}{E_{eVnr}} \tag{3.15}$$

Where QF corresponds to the ionization yield (Quenching Factor), E_{eVee} the energy released through ionization and E_{eVnr} the total energy of the nuclear recoil ($E_{eVnr} > E_{eVee}$). Knowing the ionization yield of a detector is a key parameter to determine the energy deposited by the elastic scattering of a WIMP on a target nuclei and convert the energy measurement in electron equivalent recoil (eVee) to nuclear recoil (eVnr). This measurement is being done using the COMIMAC [54] ion beam or a neutron produced by a TANDEM accelerator.

Geant4 for simulation of energy deposition

Simulation of the detector starts with the simulation of the energy deposition of particles crossing the detector. It is done with Monte Carlo methods handled by the software Geant4. Monte Carlo methods are numerical techniques for calculating probabilities and related quantities by using sequences of random numbers [55]. These methods are often used to solve a problem with no analytical or very complex solutions. GEometry ANd Tracking (Geant4) [56] is an open-source toolkit developed by an international collaboration of laboratories and research institutes. The software is developed in the C++ object-oriented programming language. It allows for the simulation of the propagation of different particles through the geometry of

a detector. In a Geant4 simulation, primary particles are produced one by one and transported through the various regions of the geometry by a series of steps. The length of a step is determined by the physics process. At the beginning of each step, the different processes registered for this particle type suggest a step length and the shortest suggested length is taken. If a process involves energy loss, the energy is deposited at that point. If a process produces secondary particles, they are simulated if their expected range in the given material is at least the minimum required range; otherwise, their energy is deposited. All particles are tracked until they have no more kinetic energy, disappear by a reaction or leave the detector geometry. To save time and make the simulation more efficient, the information given by Geant4 is saved only for steps occurring in a given volume of interest. In the case of the SPC, the sensitive volume is given by the volume of gas enclosed in the copper sphere. There is no standardized output format with Geant4. Several options are possible such as ROOT or ASCII files. For the simulation done in the context of this thesis work, the raw output from Geant4 was printed in ASCII files before being treated with ROOT programs. For each step inside the gas volume, information (such as the position, the energy deposited, the particle kinetic energies...) are printed in the output file.

Geant4 requires at least three inputs: a description of the geometry of the detector (*G4VUserDetectorConstruction*), a list of the particles and physics processes (*G4VUserPhysicsList*), and a primary particle generator (*G4VUserPrimaryGeneratorAction*). In addition to these three classes, a class based on step (*G4VUserSteppingAction*) is used to print the results of the simulation for each step.

There is no fixed set of physical processes that are automatically included in a Geant4 simulation. The user has to select all types of particles and processes involved in the simulation. One way is to build a class selecting all particles and processes. Another way is to select one of the pre-defined reference physics lists. For the NEWS-G experiment, we used the pre-defined *Shielding Physics List*. The different particles and processes taken into account are described below [57]:

-Photon:

e^-/e^+ pair production is implemented by the Bethe-Heitler model with the LPM effect at high energies and Compton scattering is implemented by the Klein-Nishina model. The photo-electric effect and Rayleigh scattering are both handled by the Livermore models.

-Electrons and Positrons:

Multiple Coulomb scattering is handled by the Urban model from 0 to 100 MeV and by the WentzelVI model from 100 MeV to 100 TeV. This is combined with the single Coulomb scattering model, which is applied for large-angle scattering. Bremsstrahlung is implemented by the eBremSB model and the eBremLPM model, which takes into account the LPM effect at high energies. The Moller-Bhabha formulation models ionization, and positron annihilation is implemented by the eplus2gg model.

-Muons:

Multiple Coulomb scattering is handled by the WentzelVI model combined with the

single scattering model at all energies, and by the eCoulombScattering model at all energies. The MuBrem model handles Bremsstrahlung. Ionization is implemented by several models depending on energy and particle type. From 0 to 200 keV, the Bragg model is used for μ^+ and the ICRU73Q0 parameterization is used for μ^-. Between 200 keV and 1 GeV, the BetheBloch model is used for both μ^+ and μ^-, and from 1 GeV to 100 TeV, the MuBetheBloch model is used for both μ^+ and μ^-. The muPair-Production model handlese^+/e^- pair production caused by either μ^+ or μ^-.

-Alpha and Ions:

Only two EM processes are applied. Multiple Coulomb scattering is implemented by the Urban model at all energies. For alphas Bragg ionization is performed below 7.9 MeV and BetheBloch ionization above. For generic ions, Bragg is used below 2 MeV and BetheBloch above.

-Neutrons:

Neutrons of 20 MeV and lower use the High Precision neutron models and cross-sections to describe elastic scattering, inelastic scattering, capture and fission.

3.2 Gaseous proportional counter

Section 3.2 presents the functioning of the proportional counter. All properties mentioned in this section are common to all proportional counters independently of their geometries. The functioning of the detector is briefly illustrated by figure 3.8.

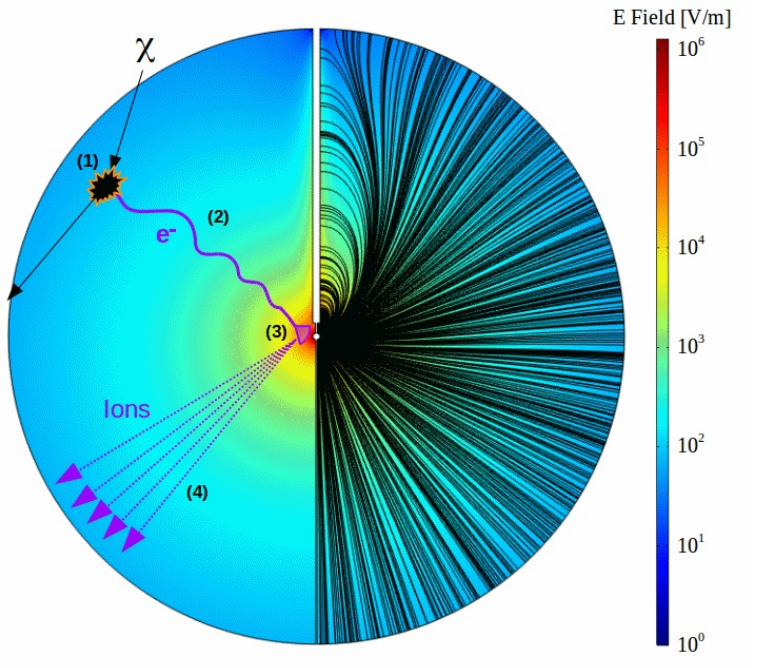

Figure 3.8: Schematic view of the spherical proportional counter and detection principle.

When particles interact in the gas volume, they ionize some gas, inducing the emission of a primary electron (1). The number of primary electrons produced depends on the gas properties: its ionization potential and the mean energy to create one ion-electron pair (W-value). Under the influence of the electric field, the primary electrons drift toward the anode at the center of the sphere (2). During the drift, they diffuse such that they reach the sensor at different times. Typical drift times vary from μs to ms depending on gas pressure and composition. When primary electrons reach the amplification region, within $\approx 100 \mu m$ around the anode, the strong electric field gives them sufficient kinetic energy to produce secondary ion-electron pairs, creating a charge avalanche (3). The signal is then induced by the motion of the secondary ions toward the cathode (4).

3.2.1 Primary ionization

When a particle passes through the detector, it dissipates energy and produces electron-ion pairs inside the gas by the processes described in the previous sections. These primary electrons can be energetic enough to ionize other gas molecules. By summing all their contributions, we recover the total energy deposited and then the total number of ion-electron pairs. This number is related to the mean ionization potential of gas molecules composing the medium:

$$W = \frac{\Delta E}{n_t(\Delta E)} \tag{3.16}$$

W is the mean energy to create one ion-electron pair, ΔE is the total energy deposited in the medium and $n_t(\Delta E)$ the number of ion-electron pairs produced. The W value is always greater than the ionization potential I of a gas. It is because not all the energy dissipated goes to ionization, but also other mechanisms, such as excitation. The W value increases with decreasing ionizing particle energy due to the fact that in low energy region, the ratio of the ionizing cross-section to the cross-section for the non-ionizing process becomes smaller. The W-value also depends on the kind of ionizing particle due to the different cross-section ratio between ionizing and non-ionizing interactions for every particle type inside a certain medium.

	First ionization potential [eV]	W-Value [eV/ion pair]	
Gas		Fast electrons	Alpha particles
Ar	15.7	26.4	26.3
He	24.5	41.3	42.7
H_2	15.6	36.5	36.4
N_2	15.5	34.8	36.4
O_2	12.5	30.8	32.2
CH_4	14.5	27.3	29.1

Table 3.1: W values for different gases for electrons and alpha particles [58].

In addition to the mean number of ion-electrons pairs formed by each incident particle, the fluctuation in their number for incident particles of identical energy is also interesting. These fluctuations set a fundamental limit on the energy resolution that can be achieved in any detector based on ionization. In the simplest model, the formation of each ion-electron pair can be considered as a Poisson process. Therefore, the total number of pairs formed should be subject to fluctuation, characterized by a standard deviation equal to the square root of the average number of pairs formed.

3.2.2 Thermal diffusion of charged particles

In the absence of an external electric field, ions and electrons released in a gas behave like neutral molecules. The properties of particles under such conditions are described by the classic kinetic theory of gases. The probability for a particle of energy ϵ at the

absolute temperature T, is given by the Maxwell-Boltzmann law:

$$F(\epsilon) = 2\sqrt{\frac{\epsilon}{\pi\,(kT)^3}}e^{\frac{-\epsilon}{kT}} \tag{3.17}$$

where k is Boltzmann's constant. The Maxwell-Boltzmann law is shown on figure 3.9

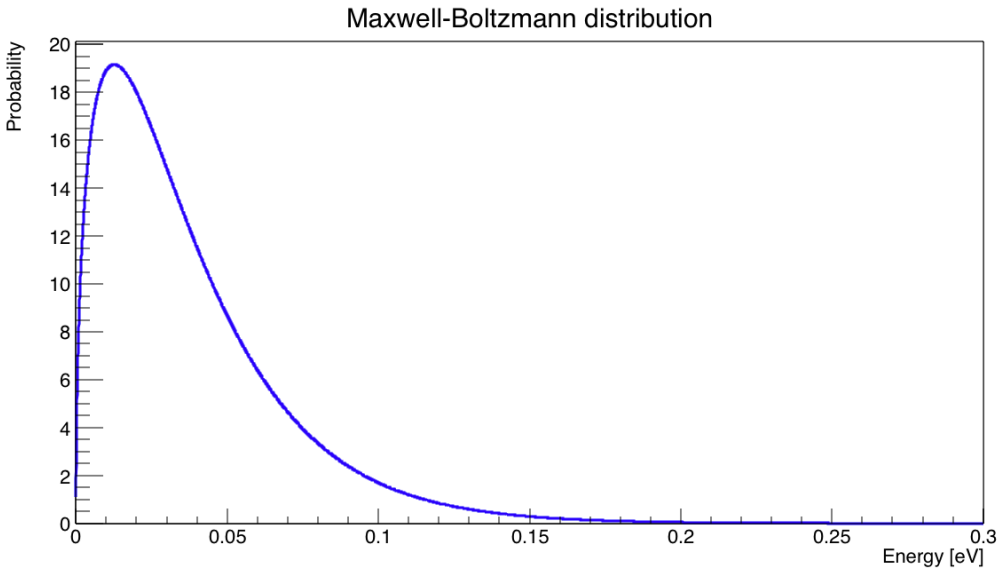

Figure 3.9: Energy distribution of ions and electrons at normal conditions ($T = 293.15\,\mathrm{K}$)

The average thermal energy is obtained by integration over the distribution $\overline{\epsilon}_T = kT$. Under normal conditions, $\overline{\epsilon}_T \approx 0.025\,\mathrm{eV}$. The corresponding distribution of velocities v for a particle of mass m is:

$$f(v) = 4\pi\left(\frac{m}{2\pi kT}\right)^{\frac{3}{2}} v^2 e^{-\frac{mv^2}{2kT}} \tag{3.18}$$

The average value of v is then given by:

$$\overline{v} = \sqrt{\frac{8kT}{\pi m}} \tag{3.19}$$

and its most probable value by:

$$v_{\mathrm{MP}} = \sqrt{\frac{2kT}{m}} \tag{3.20}$$

A localized charge distribution diffuses symmetrically by multiple collisions following a Gaussian distribution:

$$\frac{dN}{dx} = \frac{N}{\sqrt{4\pi Dt}} e^{\frac{-x^2}{4Dt}} \tag{3.21}$$

where x is the distance from the creation point, t the time elapsed and D the diffusion coefficient. The standard deviation of this distribution is given by:

$$\sigma_x = \sqrt{2Dt} \tag{3.22}$$

3.2.3 Drift and diffusion of ions in an electric field

Under the action of an electric field E, ions acquire a net motion along the direction of the field. Along their path, ions are subject to elastic scattering. Because of their high mass, their diffusion is very weak. As a result of a large number of collisions, the drift velocity of ions is quickly saturated. The average velocity v_d of this slow motion is proportional to the electric field or to the reduced electric field E/P where P is the gas pressure, up to a very high value of E (Fig 3.10). We call this constant factor the ion mobility:

$$\mu = \frac{v_d}{E} \tag{3.23}$$

The value of the mobility is specific to each ion moving in a given gas, values for several gases are summarized in table 3.2. It is proportional to the temperature and inversely proportional to the gas pressure through the expression:

$$\mu(P,T) = \frac{T}{T_0}\frac{P_0}{P}\mu(P_0,T_0) \tag{3.24}$$

A constant mobility is the direct consequence of the fact that, up to high fields, the average energy of ions is almost unmodified.

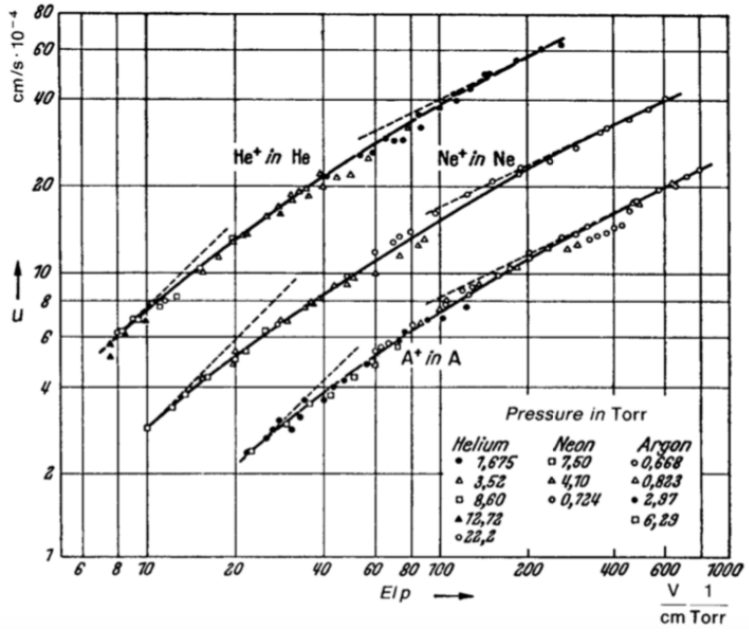

Figure 3.10: Drift velocity of several ions in their own gas as a function of the reduced electric field [52].

Gas	Ions	Mobility [$cm^2V^{-1}s^{-1}$]
He	He^+	10.40 ± 0.10
Ne	Ne^+	4.14 ± 0.2
Ar	Ar^+	1.535 ± 0.007
Kr	Kr^+	0.96 ± 0.09
Xe	Xe^+	0.57 ± 0.05

Table 3.2: Mobilities of various noble gas ions in their parent gas [59].

The relationship between mobility and diffusion coefficient is given by the Nernst-Townsend formula [52]:

$$\frac{D}{\mu} = \frac{kT}{e} \tag{3.25}$$

Ions drifting for a time t over a length x diffuse with a probability distribution given by equation 3.22 with a linear standard deviation along the drift direction:

$$\sigma_x = \sqrt{\frac{2kT}{e}\frac{x}{E}} \tag{3.26}$$

3.2.4 Drift and diffusion of electrons in an electric field

On the microscopic scale, electrons drifting through a gas are scattered on the molecules so that their direction is randomized in each collision. Under the action of an electric field E, between two collisions, in addition to their instantaneous velocity v_i, the electrons acquire a net motion in the direction of the field with a drift velocity v_d equal to its acceleration along the field, multiplied by the average time that has elapsed since the last collision [60]:

$$v_d = \frac{eE}{m_e}\tau \tag{3.27}$$

where τ is average time between two collisions. The drift velocity v_d is much smaller than the instantaneous velocity v_i. This extra energy, on average is lost during collision. There is a balance between the picked up and the energy lost during collision. For a drift distance x the mean number of collisions n is given by:

$$n = \frac{x}{v_d}\frac{1}{\tau} \tag{3.28}$$

The energy balance along the path of length x is given by:

$$nf(\epsilon)\epsilon = eEx \tag{3.29}$$

where $f(\epsilon)$ is the average fractional energy loss per collision. The average time between collision τ can be expressed in term of cross section σ and the number density N:

$$\frac{1}{\tau} = N\sigma(\epsilon)v_i \tag{3.30}$$

Here v_i is related to the total energy of the drifting electron by:

$$\epsilon = \frac{1}{2}m_e v_i^2 \tag{3.31}$$

From these considerations, we can derive the two equilibrium velocities:

$$v_d^2 = \frac{eE}{m_e N\sigma(\epsilon)}\sqrt{\frac{f(\epsilon)}{2}} \tag{3.32}$$

$$v_i^2 = \frac{eE}{m_e N\sigma(\epsilon)}\sqrt{\frac{2}{f(\epsilon)}} \tag{3.33}$$

As long as ϵ is below the excitation levels of the gas molecules, the scattering is elastic and $f(\epsilon)$ is approximately equal to twice the mass ratio of the collision partners. It is on the order of 10^{-4} for electrons. In a gas mixture composed of several components i, the effective cross-section and fractional energy loss per collision have to be calculated from the properties of individual component:

$$\begin{aligned} \sigma(\epsilon) &= \Sigma n_i \sigma_i(\epsilon)/N \\ \sigma(\epsilon)\lambda(\epsilon) &= \Sigma n_i \lambda_i(\epsilon)\sigma_i(\epsilon)/N \\ N &= \Sigma n_i \end{aligned} \tag{3.34}$$

As a result of multiple collisions with gas molecules giving a randomly oriented velocity, electrons diffuse spreading the initially localized charge cloud. The size of the cloud depends on the gas and also strongly on E due to the increase of the electron energy. To take this into account, the Nernst-Townsend formula can be modified by introducing the phenomenological characteristic energy ϵ_k, name defined by:

$$\epsilon_k = \frac{eED(\epsilon)}{v_d(E)} \tag{3.35}$$

Then, the linear space diffusion over the drift distance x can be written as:

$$\sigma_x = \sqrt{\frac{2\epsilon_k}{e}\frac{x}{E}} \tag{3.36}$$

3.2.5 Electron loss effect

Two phenomena can lead to a loss of electrons and, therefore, a degradation of the signal. First, when a positive ion and a negative electron collide, they might recombine

to form a neutral atom releasing a low energy photon. The recombination rate can be written as:

$$R_c = \frac{dn^+}{dt} = \frac{dn^-}{dt} = \alpha n^+ n^- \tag{3.37}$$

with n^+ and n^- respectively the ion and electron concentration and alpha the recombination coefficient. Recombination is not a critical effect under the influence of an electric field, because the charges are strongly separated by the field.

The second and more problematic cause of electron loss is the electron capture by a molecule having electron affinity creating a negative ion.

$$e^- + M \rightarrow M^- \tag{3.38}$$

Assuming p the fraction of electronegative pollutant in the gas and λ the electron mean free path, the number of collisions per unit time of an electron with the electronegative molecules is $v_d p/\lambda$ and the probability of attachment is:

$$\frac{h v_i p}{\lambda v_d} = \frac{1}{\lambda_c} \tag{3.39}$$

where λ_c is the mean free path for capture defined by:

$$\lambda_c = \sqrt{\frac{m}{2\epsilon}} \frac{v_d}{N h p \sigma \epsilon} \tag{3.40}$$

and h the probability of attachment per collision. The loss of electrons along a drift distance x is then:

$$\frac{n}{n_0} = e^{-x/\lambda_c} \tag{3.41}$$

Our primary concern is the contamination of oxygen and water vapor. Figure 3.11 shows the fraction of electrons surviving after 20 cm drift in two gas mixtures as a function of the oxygen content. The value of h, frequency of collision, and average attachment time for these two contaminants at normal conditions are given in Tab 3.3.

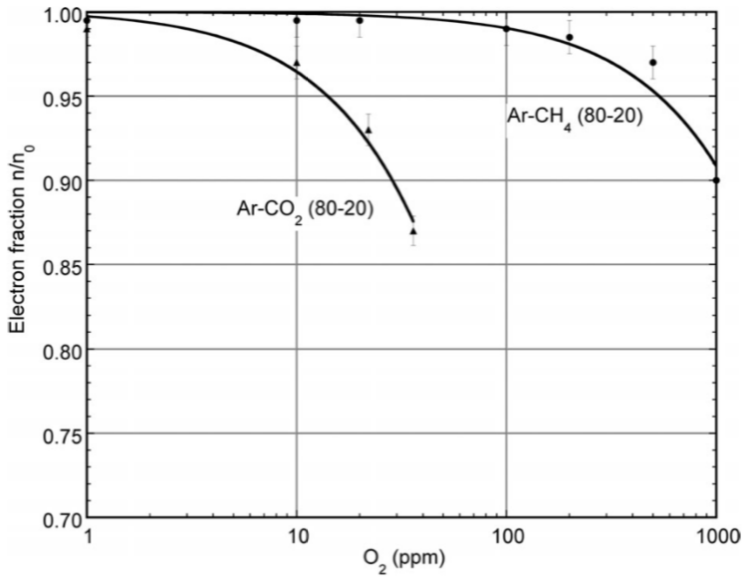

Figure 3.11: Fraction of electrons surviving after 20 cm drift in two gas mixtures, as a function of the oxygen contamination. ($E = 200\,\mathrm{V/cm}$) [52]

Gas	h	N [s^{-1}]	t_h [s]
O_2	2.5×10^{-5}	2.1×10^{11}	1.9×10^{-7}
H_2O	2.5×10^{-5}	2.8×10^{11}	1.4×10^{-7}

Table 3.3: Electron attachment probability, frequency of collisions and average attachment time for oxygen and water vapour at normal condition [52]

3.2.6 Charge multiplication

When the energy of a drifting electron exceeds the ionization potential of an atom or molecule of the medium, bound electrons can be ejected producing an ion/electron pair while the ionizing electron continues its path. Then, both primary and secondary electrons can ionize more gas molecules leading to an exponential increase of ion/electron pairs known as a Townsend avalanche. λ is the average distance an electron has to travel before having an ionizing collision; its inverse, $\alpha = 1/\lambda$, is known as the first Townsend coefficient and represents the number of ion/electron pairs produced per unit length. It is related to the ionization cross-section through the expression:

$$\alpha = N\sigma \tag{3.42}$$

where N is the number of molecules per unit volume. The Townsend avalanche results in charge amplification. The amplification process occurs at high electric field, close to the anode. Figure 3.12 shows the dependency of the Townsend coefficient with the strength of the electric field, and Fig 3.13 shows where the secondary ion-electron pairs are created. The avalanche starts roughly at 100 μm around the anode and the number of pairs created rises exponentially as we approach its surface.

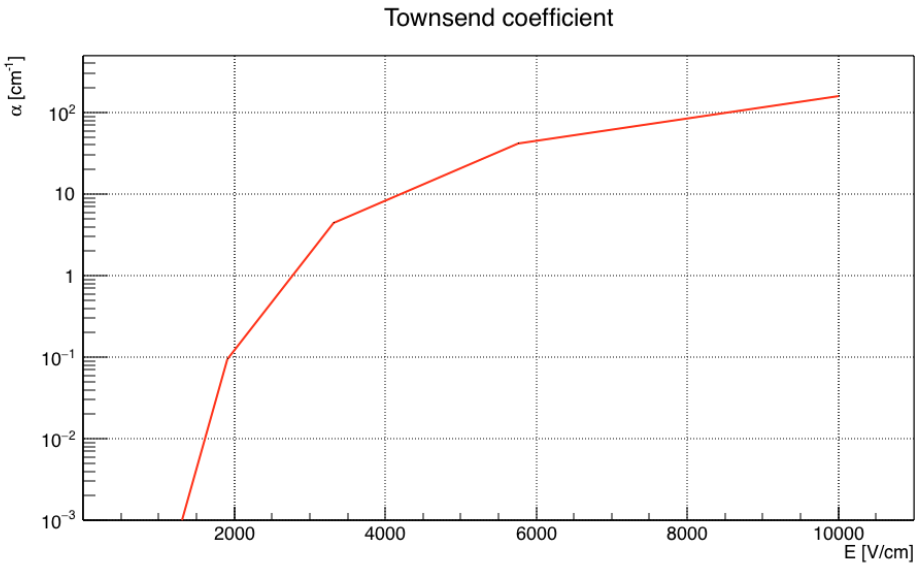

Figure 3.12: Simulation of the Townsend coefficient. The detector is a 60 cm diameter sphere filled with Ne + 0.7%CH_4 at 3.1 bar with a 6 mm diameter sensor biased at 2520 V.

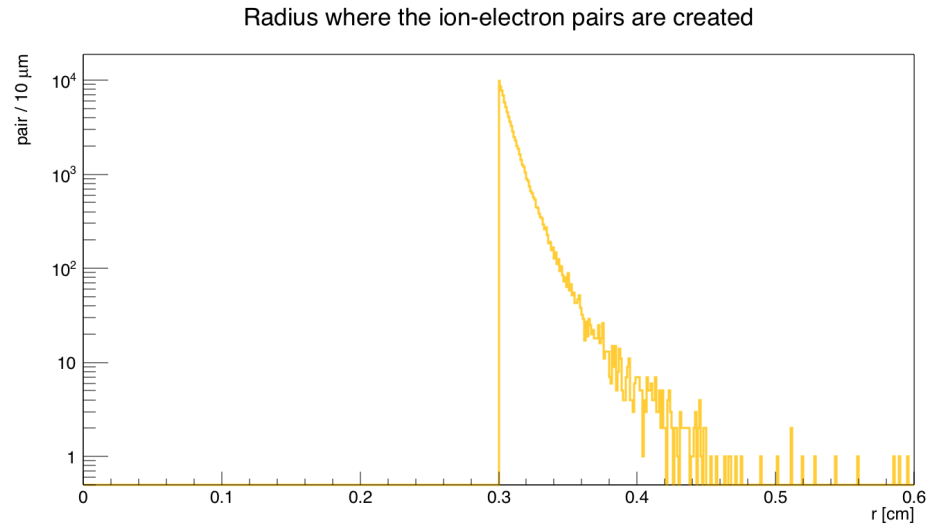

Figure 3.13: Simulation of the radius where secondary ion-electron pairs are created by 50 primary electrons reaching the sensor. The detector is a 60 cm diameter sphere filled with Ne + 0.7%CH_4 at 3.1 bar with a 6 mm diameter sensor biased at 2520 V.

Consider one electron released in a uniform electric field. After a path $1/\alpha$, one ion/electron pair will be produced. The two electrons continue to drift, and after another mean free path $1/\alpha$, they create two more ion/electron pairs and so on. If n_0 electrons initiate an avalanche, the number of ion/electron pairs after a path dx is given by:

$$dn = n_0 \alpha dx \tag{3.43}$$

Integrating over a path length x:

$$n = n_0 e^{\alpha x} \tag{3.44}$$

The ratio

$$G = \frac{n}{n_0} = e^{\alpha x} \tag{3.45}$$

represents the charge multiplication factor and is also called the 'gas gain'. In the general case of a non-uniform electric field, α is a function of the position. The multiplication factor along a path between coordinate x_1 and x_2 can be obtained as follows:

$$G = e^{\int_{x_1}^{x_2} \alpha(x) dx} \tag{3.46}$$

A simple approximation of the parameter α is given by [52]:

$$\frac{\alpha}{P} = A e^{-B\frac{P}{E}} \tag{3.47}$$

where A and B are constants depending only on the gas mixture. This formula shows the dependence of α on the electric field and the pressure explicitly.

Gain fluctuations can be caused by many different processes such as pressure variation,

geometrical imperfection or attachment. If we want to determine the mean number N of ions in the total avalanche, we sum over the probability $P(n)$ of getting n electrons in the individual small avalanches.

$$N = n_1 + n_2 + n_3 + ... + n_k \tag{3.48}$$

where each of the independent variables n_i has a distribution function P_n. If the number k of initiating electrons is large, the central limit theorem of statistics applies. If the mean of $P(n)$ is called $\overline{n}$ and the variance is σ^2, the central-limit theorem states that in the limit $k \to +\infty$, $P(N)$ is Gaussian:

$$P(N) = \frac{1}{\sigma\sqrt{2\pi}} \exp\left[(N - \overline{N})^2/2\sigma^2\right] \tag{3.49}$$

For a large number of primary electron k, the exact shape of $P(n)$ is not needed for the distributions of avalanches. For low energy events, and especially single-electron events, $P(n)$ is defined by the Polya distribution [61]

$$P\left(\frac{n}{\overline{n}}\right) = \frac{(\theta+1)^{\theta+1}}{\Gamma(\theta+1)} \left(\frac{n}{\overline{n}}\right)^{\theta} e^{[-(\theta+1)n/\overline{n}]} \tag{3.50}$$

The variance of the Polya distribution is given by:

$$\sigma^2 = \frac{1}{\theta+1} \tag{3.51}$$

The shape of the Polya distribution is driven by the value of the parameter θ (Figure 3.14), from an exponential distribution for $\theta = 0$ to a Gaussian distribution for $\theta \gg 1$.

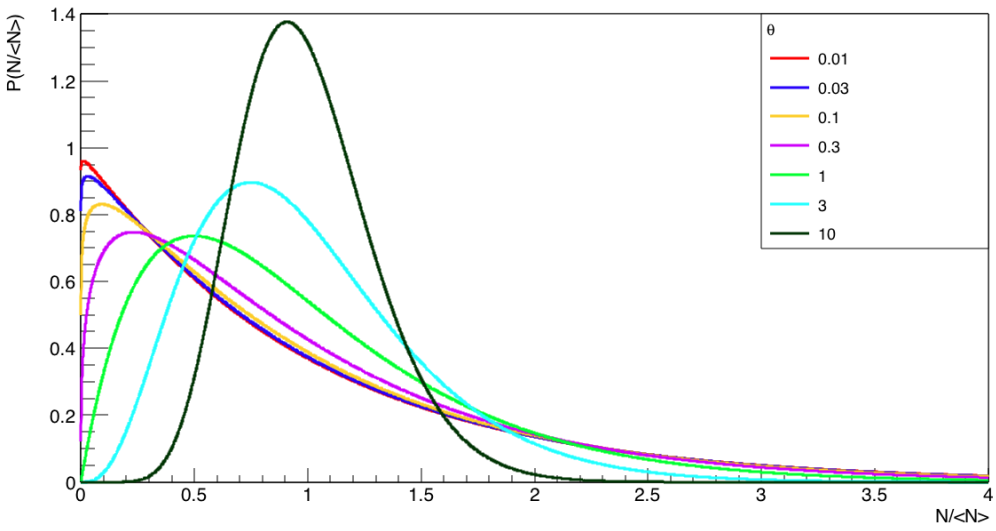

Figure 3.14: Polya distribution for different values of the parameter θ

The probability distribution function of secondary electrons created by N primary electrons is given by the N^{th} convolution of the Polya distribution [62]

$$P^{N}_{\text{polya}}\left(\frac{n}{\overline{n}}|\theta\right) = \left(\frac{(1+\theta)^{(1+\theta)}}{\Gamma(1+\theta)}\right)^{N} \left(\frac{n}{\overline{n}}\right)^{(N\theta+N-1)} e^{-(1+\theta)\frac{n}{\overline{n}}} \times \prod_{i=1}^{N-1}\left[\frac{\Gamma(i+i\theta)\Gamma(1+\theta)}{\Gamma(i+1+(i+1)\theta)}\right] \tag{3.52}$$

As shown on figure 3.15, for large value of N, the Polya distribution tends to a Gaussian distribution.

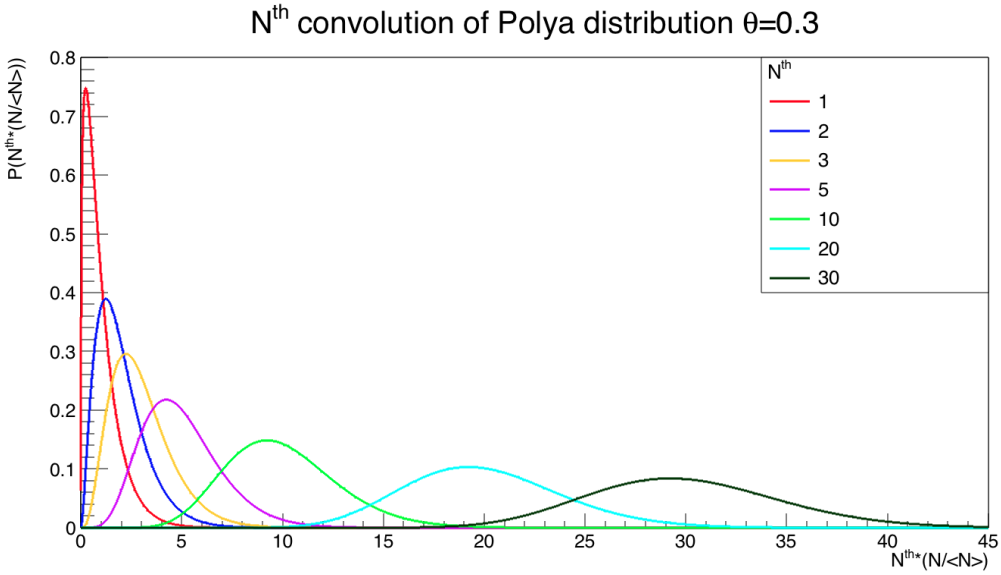

Figure 3.15: N^{th} convolution of the Polya distribution.

In some gas mixture, such like Ne and CH_4, the avalanche is amplified by Penning transfer [63]. This effect occurs when during the avalanche, Ne^* atoms with excitation energy higher than the ionization potential of the CH_4 will ionize it, increasing the number of secondary ion-electron pairs.

3.2.7 Simulation of electron drift

The simulation of the drift of electrons in gas and an electric field relies on two software packages. The first one, COMSOL multiphysics, allows for a detailed description of the electric field within the detector. The second one, Magboltz,models the properties of electron motion such as drift velocity, diffusion and Townsend coefficient at a given electric field.

COMSOL Multiphysics

COMSOL Multiphysics is a general-purpose simulation software for modeling designs, devices, and processes in all fields of engineering, manufacturing, and scientific research [64]. The AC/DC Module add-on of the COMSOL Multiphysics platform provides a wide range of modeling features and numerical methods for investigating the electromagnetic field by solving Maxwell's equations. For our purpose, COMSOL is used to produce a detailed map of the detector's electromagnetic field. Figure 3.16 shows the meshing used by COMSOL to compute the voltage and electromagnetic field in the detector volume, equipotential lines, and the direction of the electric field, determined for a 30 cm diameter detector with a 3 mm diameter sensor biased at 1750 V and supported by a grounded rod.

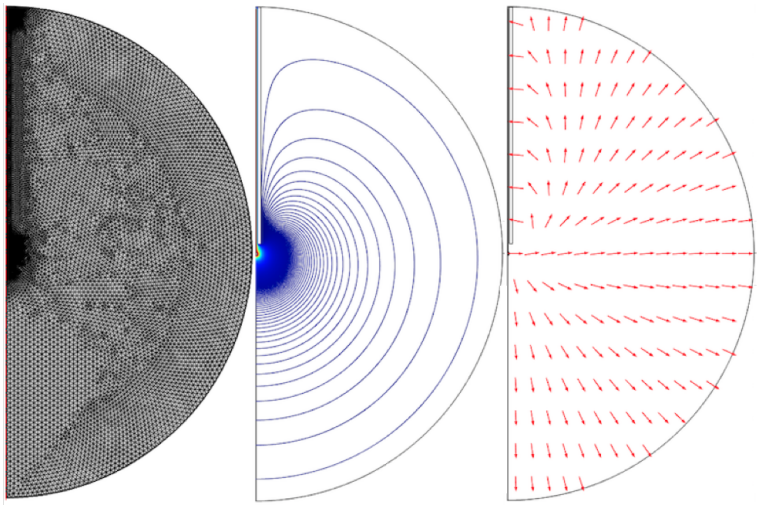

Figure 3.16: Left: Meshing used by COMSOL to compute the voltage and magnetic field in the detector volume. Centre: Equipotential lines. Right: Electric field direction.

Magboltz

Magboltz is a software developed by S.F. Biagi [65]. It models electron transport in gas mixtures. Magboltz allows for the calculation of drift velocity, diffusion, Townsend coefficient, and electron attachment. These parameters are determined by numerically integrating the Boltzmann transport equation, simulating an electron bouncing around inside a gas. After each collision with the gas molecules, the position, energy, and direction of the electron is updated. The solution of the Boltzmann equation converges to equilibrium after 10^7 collisions.

3.3 Specification of the SPC

The Spherical Proportional Counter was developed by Ioannis Giomataris in 2006 [5] at the Commissariat à l'Energie Atomique (CEA) in Saclay, France. The first prototypes were made by converting old Large Electron-Positron Collider (LEP) accelerating cavities (Fig 3.17) into SPCs.

3.3.1 Detector description

The detector consists of a grounded metallic spherical vessel filled with gas. The anode is a small ball made of metallic or resistive material, on which a positive high voltage is applied, placed at the center of the sphere and supported by a grounded metallic rod. The electric field varies with the inverse of the distance from the anode squared ($1/r^2$) and is highly inhomogeneous along the radius. The large variation of the electric field, from the sensor to the sphere, divides the detector volume naturally into two regions. Most of the detector volume is the drift region. Electrons produced in this region drift towards the sensor. Within a few hundreds of μm around the

Figure 3.17: Accelerating cavity from LEP converted into SPC.

anode, electrons enter the amplification region. In this small region, the electric field is strong enough to accelerate electrons above the ionizing potential of the gas, and an avalanche occurs (Sec 3.2.6). Figure 3.8 briefly describes the functioning of the detector.

3.3.2 The ideal electric field

The angular isotropy of the electric field is a crucial parameter for the optimal operation of an SPC. Although the spherical symmetry is broken by the presence of the grounded rod, this section describes the ideal electric field. The effect of the rod on the detector response is discussed later. In the ideal case where a potential V is applied to the anode with radius r_2, and the cathode of radius r_1 is grounded, the anode ball contains an electric charge Q. Gauss' Law can be used to calculate the

electric field inside the detector volume:

$$\oint_S \vec{E} \cdot d\vec{S} = \frac{Q}{\epsilon} \tag{3.53}$$

where ϵ is the gas permittivity, of the order of 0.1 pF/cm. The integration around a sphere of radius r gives:

$$E(r) = \frac{Q}{4\pi\epsilon}\frac{1}{r^2} \tag{3.54}$$

Using $E = -\nabla V$, we have:

$$V(r) = -\int E(r)dr = \frac{Q}{4\pi\epsilon}\int \frac{dr}{r^2} = \frac{Q}{4\pi\epsilon}\frac{1}{r} + C^{st} \tag{3.55}$$

By applying the boundary conditions $V(r_2) = V_0$ and $V(r_1) = 0$, we obtain:

$$V(r) = V_0\rho\left(\frac{1}{r} - \frac{1}{r_1}\right) \tag{3.56}$$

with:

$$\frac{1}{\rho} = \frac{1}{r_2} - \frac{1}{r_1} \tag{3.57}$$

and

$$V_0 = \frac{Q}{4\pi\epsilon\rho} \tag{3.58}$$

We deduce the capacitance of the detector from the previous equation:

$$C = \frac{Q}{V_0} = 4\pi\epsilon\rho \tag{3.59}$$

This capacitance of less than 1 pF, is a remarkable property of the SPC. Notice this value is independent of the size of the spherical vessel, a big difference compared to the parallel plate detectors where the capacitance is proportional to the surface of the detector. Its very low value gives the detector a very low intrinsic noise. Finally, the electric field can written as:

$$E(r) = \frac{V_0}{r^2}\rho \tag{3.60}$$

3.3.3 Response of the detector, induced pulses

Jacques Derré developed the formalism of the pulse formation in 2007 [66]. After the drift of primary electrons, the signal is induced by secondary ion-electron pairs produced during the avalanche. Since the avalanche occurs within a few μm around the anode, the electrons are collected quickly within a few ns. The positive ions travel a longer distance during a much longer time. The induced pulse is then mostly due to the motion of secondary ions; the contribution of electrons is negligible. The signal induced by an avalanche created at a time $t = 0$ can be calculated analytically for the case of the ideal electric field. The ion mobility in the gas μ is taken as independent of the electric field but inversely proportional to the pressure P:

$$\mu = \frac{\mu_0}{P} \tag{3.61}$$

where μ_0 is the mobility at 1 atmosphere and is on the order of $2 \cdot 10^{-6}\mathrm{cm}^2\mathrm{V}^{-1}\mu\mathrm{s}^{-1}$. By definition:

$$\mu = \frac{1}{E(r)}\frac{dr}{dt} \tag{3.62}$$

Replacing $E(r)$ by equation 3.60:

$$r^2 dr = \alpha dt \tag{3.63}$$

with:

$$\alpha = \mu_0 \frac{V_0}{P} \rho \tag{3.64}$$

Integration of equation 3.63 on the drift range gives:

$$\int_{r_2}^{r} u^2 du = \int_0^t \alpha dt \tag{3.65}$$

The ions arrive at the time t at the distance r given by:

$$r(t) = (r_2^3 + 3\alpha t)^{\frac{1}{3}} \tag{3.66}$$

By substituting equation 3.66 into equation 3.56, we can derive the potential at a point where an ion is at t:

$$V(t) = V_0 \rho \left[(3\alpha t + r_2^3)^{-\frac{1}{3}} - \frac{1}{r_1} \right] \tag{3.67}$$

The duration of the ion drift corresponds to $r = r_1$:

$$t_{\max} = \frac{r_1^3 - r_2^3}{3\alpha} \tag{3.68}$$

The ion drift time is long, typically a few seconds. Now we apply the Shockley-Ramo theorem to compute the charge on the anode induced by the motion of ions:

$$\begin{aligned} dQ_{\text{ind}} &= -q_{\text{ions}} dr \frac{E(r)}{V_0} \\ dQ_{\text{ind}} &= -q_{\text{ions}} v_{\text{ions}} dt \frac{E(r)}{V_0} \\ dQ_{\text{ind}} &= -q_{\text{ions}} \mu E dt \frac{\rho}{r^2} \\ dQ_{\text{ind}} &= -q_{\text{ions}} \alpha \rho \frac{dt}{r^4} \\ dQ_{\text{ind}} &= -q_{\text{ions}} \alpha \rho \left(r_2^3 + 3\alpha t\right)^{-\frac{4}{3}} dt \end{aligned} \tag{3.69}$$

By integration over time, we get the charge pulse given by the detector for an avalanche created at time $t_0 = 0$:

$$Q_{\text{ind}} = -q_{\text{ions}} \rho \left[\frac{1}{r_2} - \frac{1}{(r_2^3 + 3\alpha t)^{\frac{1}{3}}} \right] \tag{3.70}$$

We can remark that at the maximum ion drift time $t_{\max}$ given by equation 3.68, which is the duration of the detector pulse, the induced charge is equal to sum of charges on the avalanche:

$$Q_{\text{ind}} = -q_{\text{ions}} \tag{3.71}$$

Now we can derive the expected shape of the induced signal by taking into account the pre-amplifier response. As the transfer function of the pre-amplifier, we can take an exponential:

$$A = e^{-t} \tag{3.72}$$

The electric signal given by an avalanche created at $t = 0$ is then given by the convolution of the detector response by the amplifier transfer function:

$$S(t) = \int_0^t A(t-u)\frac{dQ_{\text{ind}}}{du}(u)du \tag{3.73}$$

$$S(t) = -q_{\text{ind}}\alpha\rho e^{-t/\tau}\int_0^t e^{u/\tau}\left(r_2^3 + 3\alpha u\right)^{-\frac{4}{3}}du \tag{3.74}$$

We can now derive the expected signal for a point-like energy deposition such as from photon conversion. The N primary electrons reach the anode with a temporal dispersion σ due to the longitudinal dispersion the electron cloud during its path in the gas. The total signal S_{tot}, is the convolution of each individual amplified signal and the dispersion σ:

$$S_{\text{tot}} = \sum_{i=1}^{N}\frac{1}{\sqrt{2\pi\sigma}}\int_{-\inf}^{t} S_i(t-u)e^{\frac{u^2}{2\sigma^2}}du \tag{3.75}$$

The signal induced by the motions of charges in the sphere decreases and returns to equilibrium before t_{max}, the time taken to positive ions to reach the cathode due to the time constant τ of the pre-amplifier. t_{max} is on the order of few seconds while τ is on the order of tens of μs. Figure 3.18 shows the induced charge and the output voltage from a single electron. For this example, the detector is a 60 cm diameter sphere filled with 3 bars of neon with a 3 mm radius sensor biased at 2520 V. The signal is read through a pre-amplifier with a time constant of 140 μs. With such conditions, $\text{t}_{\text{max}} \approx 8.5\,\text{s}$, is much larger than the time constant of the pre-amplifier.

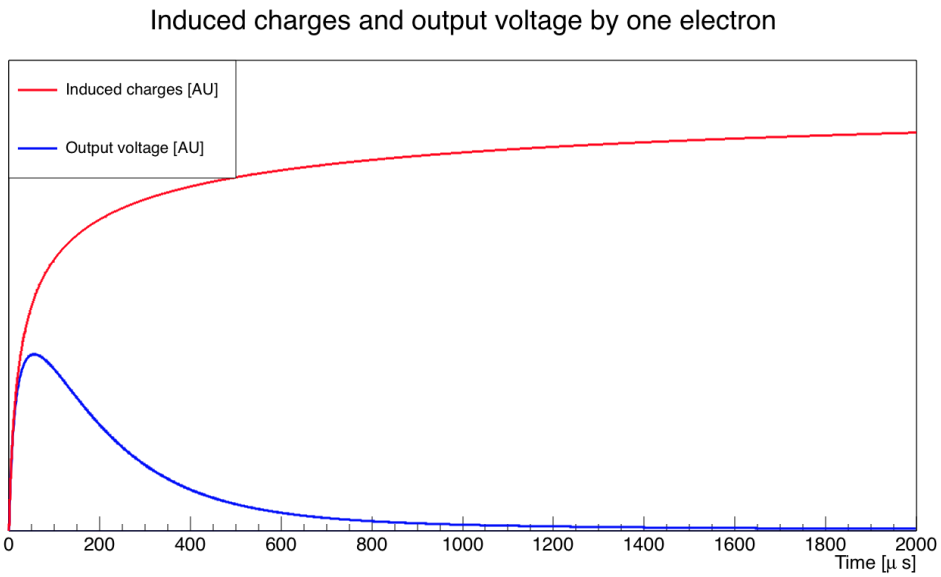

Figure 3.18: Induced charge and output pulse of a single electron.

3.3.4 Charge induced by electrons and ions

The Shockley–Ramo theorem states that in a system of a stationary conductors, the charge induced on a conductor i by a unit charge moving from point A to B is $q_i = V_B - V_A$ where is V is potential assuming 1 V on the conductor i and 0 on the other. Following their creation within a few μm around the anode, electrons experience a small potential difference and induce a negligible charge compared to ions that travel from all along the radius of the sphere, from the potential V_A to the ground. In SPCs, the signal is predominantly induced by the motion of ions. In the example of the simulation of the avalanche in Fig 3.13, 96.9% of the induced charge is from ions and 3.1% from electrons.

3.3.5 Ballistic deficit

The ballistic deficit is the loss of output signal amplitude due to the interplay between the finite charge collection time in a detector and the characteristic time constant of the amplifier [67]. When the time constant of the amplifier is much smaller than the total drift time the ions t_{max}, the amplitude of the output signal does not correspond to the total charge produced during the avalanche. This effect biases the amplitude of the output signal, especially when the signal is induced by several primary electrons reaching the sensor at different times. Figure 3.19 shows the induced charge (red) and output voltage (blue) created by two electrons reaching the sensor with a time difference of 200 μs and producing the same number of secondary ion-electron pairs integrated by a pre-amplifier with a time constant of 140 μs.

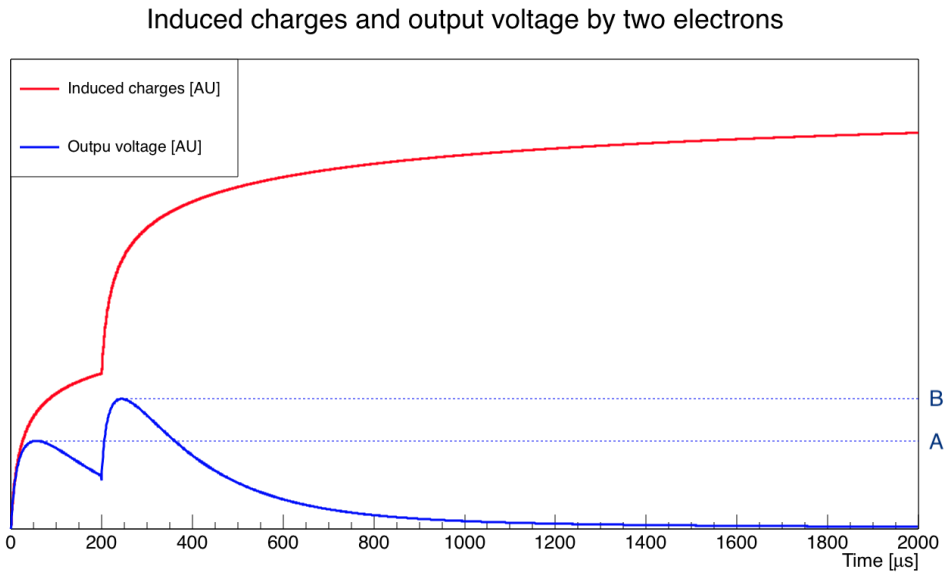

Figure 3.19: Induced charge and output pulse of two electrons.

We see that the total amplitude of the pulse is not simply double the amplitude of the signal induced by one electron (B < 2A). In such conditions, we can not rely on

the amplitude of the pulse to determine the energy deposited in the gas. The pulses need to be treated to obtain a value directly proportional to the energy deposited in the gas.

3.3.6 Pulse treatment

As mentioned in the previous section, the amplitude of the recorded pulses can be biased by the transfer function of the pre-amplifier shorter than the time taken by secondary ions to fully induce the current. The solution is to treat raw pulses to take into account the transfer function of the pre-amplifier and the shape of the current induced by ion motion. The processing of the pulses is shown in Fig 3.20. The example shows a laser-induced pulse where three electrons reach the anode. This event comes from a run taken with a 30 cm diameter sphere filled with 500 mbar of Ar + 2%CH_4. The sensor is a 3 mm ball biased at 1900 V. The raw pulses (upper left) are first smoothed by a trapezoidal filter and then double deconvolved for the pre-amplifier response (upper right) and the shape of the ion-induced (lower left) current with a Fourier deconvolution method [68]. This produces a roughly Dirac delta-shaped signal corresponding to the arrival time of primary electrons. The Dirac delta shapes are then integrated (lower right). Two main parameters can be extracted from the integrated pulses. The amplitude of the event is defined by the height of the integrated pulse which is proportional to the energy deposited. The rise time of the pulse is taken between 10% and 75% of the maximum height, and is related to the spatial distribution of the energy deposition.

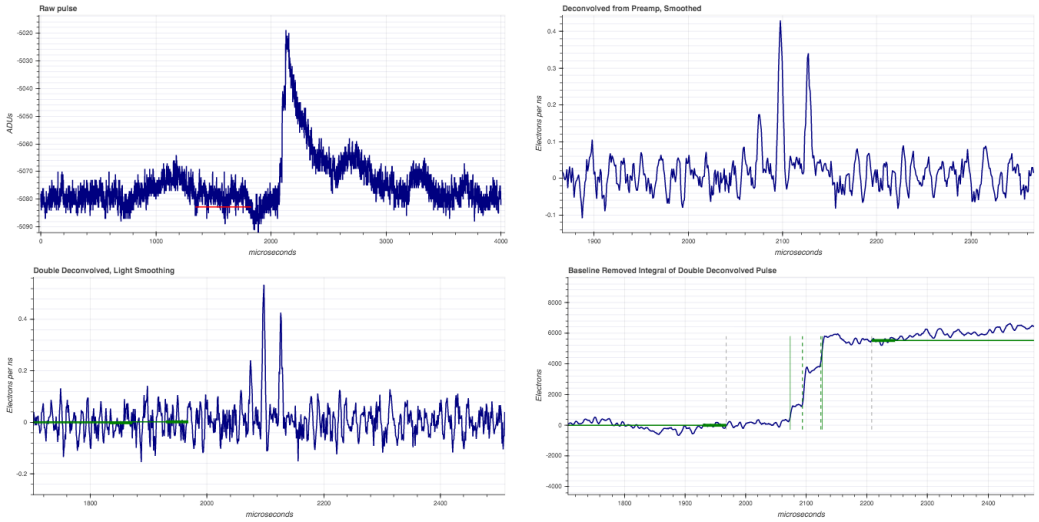

Figure 3.20: (A) upper left: Raw pulse smoothed, (B) upper right: Pulse deconvolved from the amplifier response, (C) lower left: Pulse deconvolved from amplifier response and ion induced current, (D) lower right: Integral of the double deconvolved pulse.

3.3.7 Gain of the detector

The amplitude of the integrated pulses is related to the number of secondary charges produced by the avalanches. This amplitude is expressed in ADU (Analog-to-Digital Unit). The ADU measurements can then be converted to charge using the gain of the pre-amplifier ($G_{\mathrm{P-A}}$) and the gain of the digitizer (G_{DIG}). The gain of the digitizer is estimated by measuring the output signal with a 1 V test signal input. Knowing these two parameters, it is possible possible to estimate the gain of the avalanche using a calibration source. The number of secondary electrons N_{SE} producing a pulse of amplitude A expressed in ADU is:

$$N_{\mathrm{SE^-}} = \frac{A}{\mathrm{G_{P-A}} G_{\mathrm{DIG}}} \tag{3.76}$$

Knowing the energy E that induced the pulses and the W value of the gas mixture, the gain of the avalanche G_{AV} is given by:

$$G_{AV} = \frac{A}{G_{P-A} G_{DIG}} \frac{W}{E} \tag{3.77}$$

3.3.8 Pulse shape discrimination

The combination of the rise time and amplitude allows for a fiducialisation of the detector volume. The amplitude of the integrated pulse is proportional to the energy deposited within the gas volume. The rise time of the pulses is correlated to the spatial distribution of the energy deposition. For point-like energy deposition, the rise time of a pulse is related to the dispersion of the arrival time of primary electrons on the anode. For a point like deposition close to the sensor, the longitudinal diffusion of electrons is smaller than for deposition close to the sphere, producing a pulse with a shorter rise time. The rise time of track-like events is correlated to the difference of drift time between the closest and farthest energy deposition from the sensor. Figure 3.21 shows an example of pulse shape discrimination with the SEDINE detector (Chapter 3.5) filled with 3.1 bar of Ne + 0.7%CH_4 and a 6 mm sensor biased at 2520 V. The events in rectangle A are tracks with a large rise time (high energy β and Compton scattering). Rectangles B and C containe point-like events originating from the inner surface of the detector and the gas volume of the detector volume respectively. A dark matter signal is expected to sit in rectangle C.

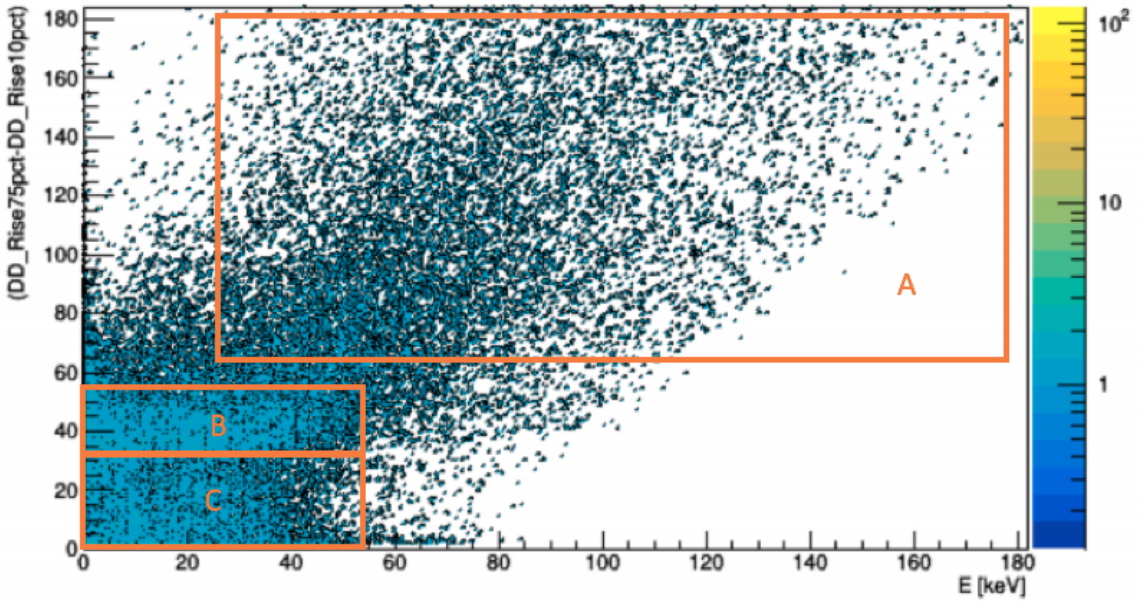

Figure 3.21: Pulse shape discrimination: (A) Track-like events, (B) Point-like events from the surface of the sphere, (C) Point-like events distributed in the gas volume.

3.3.9 Electronic noise

Gas detectors can be seen as a charged capacitor of capacitance C where a voltage V is applied. The charge Q on the anode is then given by $Q = C \times V$. A noise voltage will then induce a charge variation proportional to C. One of the main advantage of the spherical geometry is its natural low capacitance. For such a geometry, the capacitance is given by:

$$C_{\text{sphere}} = 4\pi\epsilon_0\rho \tag{3.78}$$

where $\epsilon = 8.85 \times 10^{-12}\,\text{Fm}^{-1}$ is the vacuum permittivity. A 60 cm diameter sphere with a 3 mm radius sensor has a capacitance of $\text{C}_{\text{sphere}} \approx 0.33\text{pF}$. To compare the

capacitance of a cylindrical and parallel plates detectors are given by:

$$C_{\text{cylinder}} = \frac{2\pi\epsilon_0 L}{\ln\left(\frac{r_{\text{out}}}{r_{\text{in}}}\right)} \tag{3.79}$$

where L is the length of the cylinder, r_{in} the radius of the wire and r_{out} the radius of the cylinder and

$$C_{\text{plates}} = \frac{\epsilon_0 A}{d} \tag{3.80}$$

where A is the surface of the plates and d the distance between them. We can compare detectors with a similar volume of detection. For a sphere, with $r_1 >> r2$, $C_{\text{sphere}} \approx 4\pi\epsilon r_2$ does not depend on the volume but only on the size of the sensor. With a 3 mm radius sensor, SEDINE has capacitance of $\text{C}_{\text{sphere}} \approx 0.33\,\text{pF}$ for volume of $\text{V} \approx 0.1\,\text{m}^3$. A similar volume is obtained with a 1 m^2 parallel-plate detector separated by 10 cm for which the capacitance is $\text{C}_{\text{plates}} \approx 88\,\text{pF}$. A similar volume can be obtained with a 1 m long cylinder with a radius of 56 cm. Assuming the anode is made of 10 μm radius wire, the capacitance of the detector is $\text{C}_{\text{cylinder}} \approx 12\,\text{pF}$. Depending on their dimension, cylindrical and parallel-plate detectorss would have a capacitance two to three orders of magnitude higher than that of a sphere. A similar perturbation external to the detector would have an impact two to three orders of magnitude more important. The low noise level of the detector is clearly visible in Fig 3.20 where the charge induced by a single electron is much higher than the charge induced by the noise.

3.4 Importance of the sensor and electric field corrector

The sensor is one of the key points of the detector. It induces the electric field in the whole volume of the detector allowing for electrons to drift toward it and also creates the high field region within a few tens of micrometers around it, where the signal is amplified. The sensor is made of a tiny ball, from 1 to 6 mm in diameter where a high voltage is applied through an insulated cable. The ball is usually made of iron or silicon. The wire and ball are supported by a grounded rod. The ideal, spherical geometry of the electric field is broken by the presence of the grounded rod as shown in Fig 3.23.

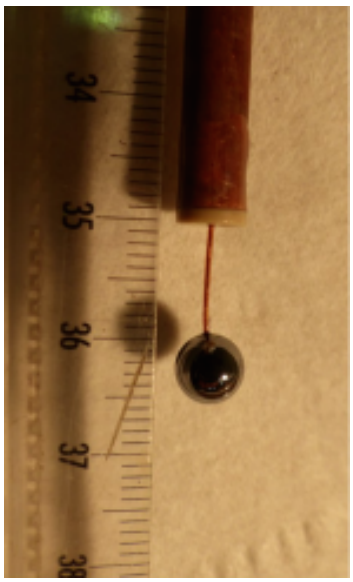

Figure 3.22: The sensor used in SEDINE for the neon WIMP search run.

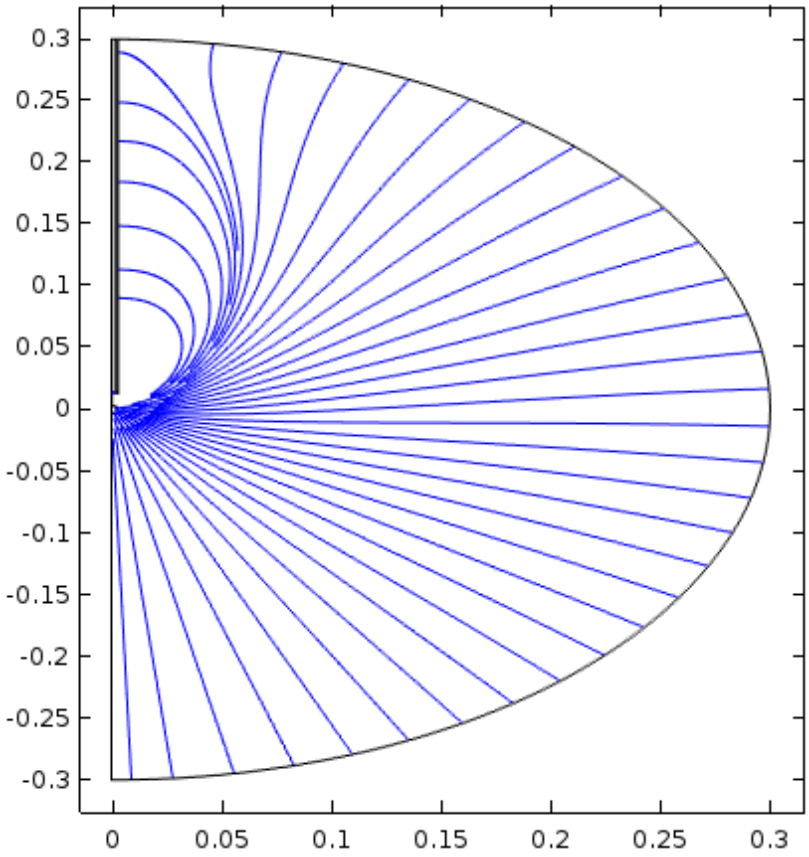

Figure 3.23: Electric field lines in the SEDINE detector with 2520 V applied on a 6 mm sensor.

The anisotropy of the electric field results in a non-linear path for primary electrons. Electrons drifting in the northern hemisphere, the hemisphere containing the rod, have a longer drift time than those drifting in the southern hemisphere. The anisotropy of the electric field close to the sensor (Fig 3.24), where the avalanche occurs produces a gain that depends on the arrival position of the primary electrons on the ball.

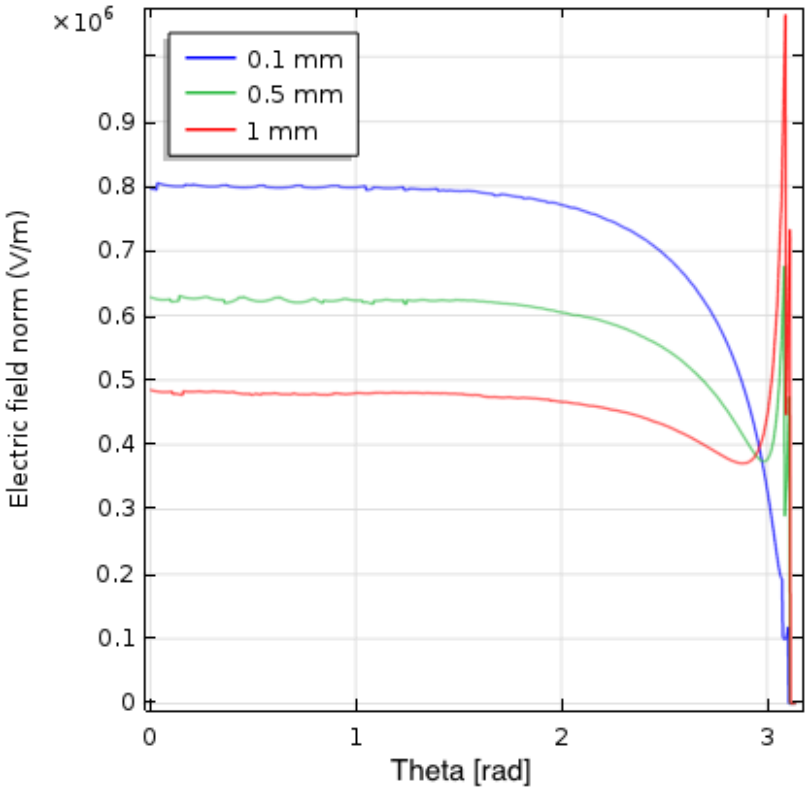

Figure 3.24: Norm of the electric field at 0.1 mm (blue), 0.5 mm (green) and 1 mm (red) form the sensor surface.

The presence of the grounded rod also produces temporal instability. At high voltage, higher than the breakdown voltage of the gas mixture used, a spark between the sensor and the rod can occur. This effect limits the voltage that can be applied to the sensor and consequently, its gain. These different problems can be handled by applying a second voltage on a so-called umbrella. The umbrella first insulates the rod in order to avoid sparks with the ball. Second, applying a second voltage modifies the geometry of the electric field and gives a more homogeneous detector response. The choice of material is crucial. It has to have a large resistivity, to avoid any charge accumulation which could disturb the electric field and induce sparks and to ensure a fast evacuation of positive ions to avoid charge effect that makes the detector response

correlated to the event rate. Several umbrella technologies have been tested. Chapter 5 summarizes results obtained with new sensors.

3.5 Discussion, SPC for dark matter search

The spherical proportional counter has several advantages for the search for dark matter. The combination of the significant amplification from Townsend avalanches and its low natural capacitance and electronic noise allows for a very low energy thresholds allowing the detection of single electron events. The pulse shape discrimination allows for fiducialization of the detector volume, also allowing for the discrimination of point-like and track-like events; WIMP induced signals are expected to be point-like. The detector can be operated with different target material and especially low A targets such as hydrogen. The target materials are affordable and commercially available. The next two chapters focus on the background of SPCs for dark matter searches. These studies rely on the simulation of the detector and the radiation surrounding it. The next chapter shows a comparison of the simulation and data taken with SEDINE at the LSM, and the following presents an estimation of the expected background in the next-generation detector. Chapter 6 finally presents the development of new sensors.

Chapter 4

Background of the SEDINE detector

4.1 Introduction

The SEDINE detector is a 60 cm diameter sphere made of commercially available copper. It has been operated at the Laboratoire Souterrain de Modane in France since 2013. In 2015, the collaboration operated SEDINE for 41 days with a gas mixture made of 99.3% neon and 0.7% methane and set a world-leading limit on WIMPs mass and nucleon cross-sections for WIMP masses below $0.6\,\mathrm{GeV/c^2}$ [47]. A presentation of these results followed a detailed description of the detector and its shield. The purpose of this chapter is to explain the background events observed during this run and the different effects of electron attachment and non-homogeneity of the electric field on pulse formation. During this run, the detector response was not perfect. The rise time and amplitude correlation of the recorded pulses shows an electron loss effect. In addition, the non-gaussianity of the ^{37}Ar is a sign of a non-homogeneity of the detector response (Fig 4.3). The electron attachment effect is simulated with Magboltz, and the effect of the field anisotropy in the amplification region is determined empirically. Once the detector response is known, it is then possible to estimate the

effect of different contaminants in the detector and its surrounding environment on the observed count rate and energy spectrum. These estimations are based on Geant4 simulation [56], and the different contaminations were measured or estimated from the available data. The results of this analysis show a lack of events in the dark matter region of interest. This chapter concludes with a list of possible contamination that could explain the missing events.

4.2 The SEDINE detector

The SEDINE detector is a 60 cm diameter detector made of ultra-pure NOSV copper. It is placed in a cubic shielding made of 5 to 7 cm of copper, 15 cm of lead and finally 30 cm of polyethylene. The experiment is located at the Laboratoire Souterrain de Modane (LSM), under ≈ 1700 m of rock. Figure 4.1 shows the detector inside its shielding seen for the top and a schematic view of the sphere and shielding.

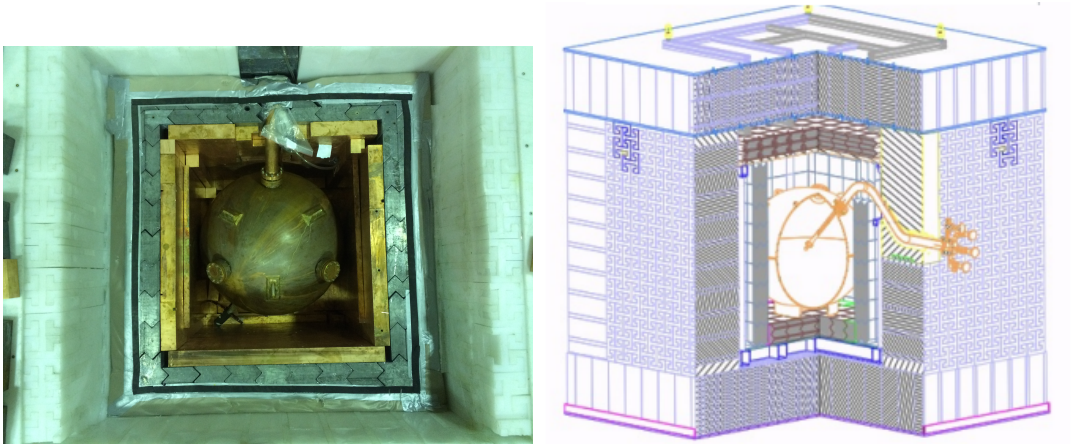

(a) Top view of SEDINE (b) Schematic view of the shielding

Figure 4.1: The SEDINE detector and its shield

4.3 First WIMP search run

In 2015, the detector was operated with a gas mixture made of 99.3% of Ne and 0.7% of CH_4 at 3.1 bar, corresponding to 280 g of target mass, for 42.7 days without interruption. The sensor was made of a 6.3 mm silicon ball biased to 2520 V. A CANBERRA Model 2006 charge sensitive pre-amplifier was used to read-out the signal. A conservative analysis threshold was set at 150 eVee, above the trigger threshold of ~ 36 eVee, to ensure a $\sim 100\%$ trigger efficiency. Further on, a quality cut was applied to reject events within a 4-second window after triggering to remove non-physical events introducing a dead time resulting in 20.1% exposure loss. This cut allows for suppressing spurious "after pulses" sometimes observed after a physical event. After the quality cut, we defined a preliminary Region Of Interest (ROI) in rise time, $10\,\mu s - 32\,\mu s$, and energy $150\,eV - 4000\,eV$. Sideband regions were used to determine the expected backgrounds in the preliminary ROI. The event rate measured in the 4000 eVee − 6000 eVee, energy range was used to extrapolate the expected Compton background down to lower energy, assuming a flat recoil energy spectrum. The sideband region was used together with the simulation to extrapolate the expected number and distribution of surface events leaking in the preliminary ROI. For a total exposure of $9.7\,kg \cdot days$, 1620 events were recorded in the preliminary ROI. The ROI was tuned by using a Boosted Decision Tree (BDT) [69]; a machine learning algorithm which was trained with 10^5 simulated background events and signal events for 8 different WIMP masses (from 0.5 to 16 GeV/c^2). For each WIMP mass, the events were classified as background-like or signal-like using the BDT score (ranging between -1 and 1 respectively), resulting in a WIMP-mass-dependent fine-tuned ROI in the rise time vs energy plane.

For each WIMP mass and considering as candidates all the events observed in the corresponding fine-tuned ROI, a 90% Confidence Level (C.L.) upper limit on the spin-independent WIMP-nucleon scattering cross-section was derived using Poisson statistics. The resulting exclusion limit is presented on Fig 4.2 as a solid red line, setting new constraints on the spin-independent WIMP-nucleon scattering cross-section below $0.6\,\mathrm{GeV/c^2}$ and excluding at 90% C.L. a cross-section of $4.4 \times 10^{-37}\,\mathrm{cm^2}$ for a $0.5\,\mathrm{GeV/c^2}$ light DM candidate mass.

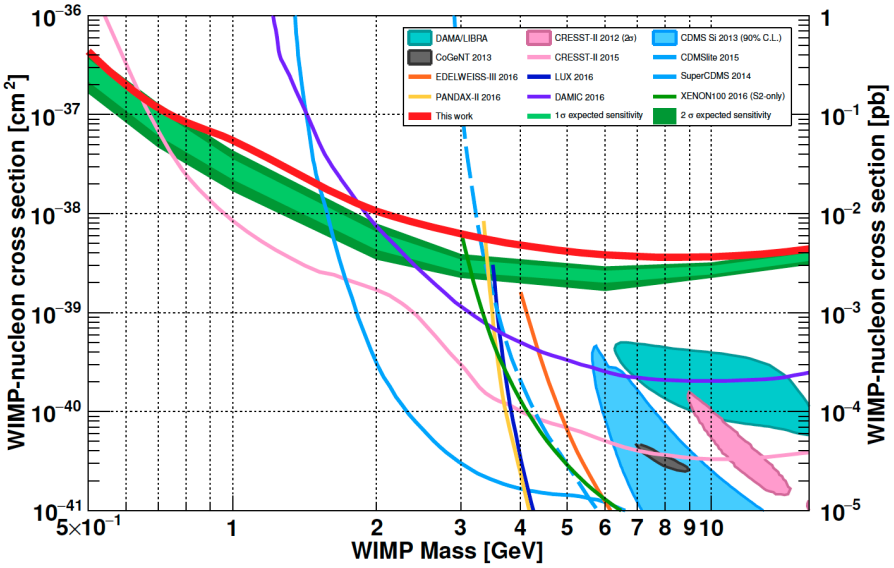

Figure 4.2: Constraints on the spin-independent WIMP-nucleon cross section versus WIMP mass. The result from this analysis is shown as a solid red curve [70].

4.4 Assessing the O_2 contamination and field anisotropy

The rise time and amplitude correlation observed during the ^{37}Ar calibration run shows electron loss effect. Events with large rise times have lower amplitudes than events with low rise times as shown in Fig 4.3. This can be explained by the capture

of electrons by electronegative impurities. A good candidate for electron attachment is oxygen. The possible O_2 concentration is determined by simulating the drift of primary electrons in a gas containing different levels of O_2 (Fig 4.16). This calibration run also shows a non-gaussianity of the response of the detector. This effect is understood to be due to the inhomogeneity of the electric field around the sensor. This non-gaussianity can be simulated by an empirical method. A weighting factor is applied to each simulated pulse depending on the arrival angle on the sensor. This section describes the estimation of these two effects.

4.4.1 O_2 contamination in the gas

After the physics run taken in 2015, we performed a calibration run using ^{37}Ar in the same gas and voltage conditions. This isotope of argon is radioactive and decays by electron capture with a half-life of 35 days. Capture from the K and L-shells release, respectively, 2.82 and 0.270 keV X-rays. The calibration run lasted 16 hours and used the same bias voltage and electronic readout as for the physics run.

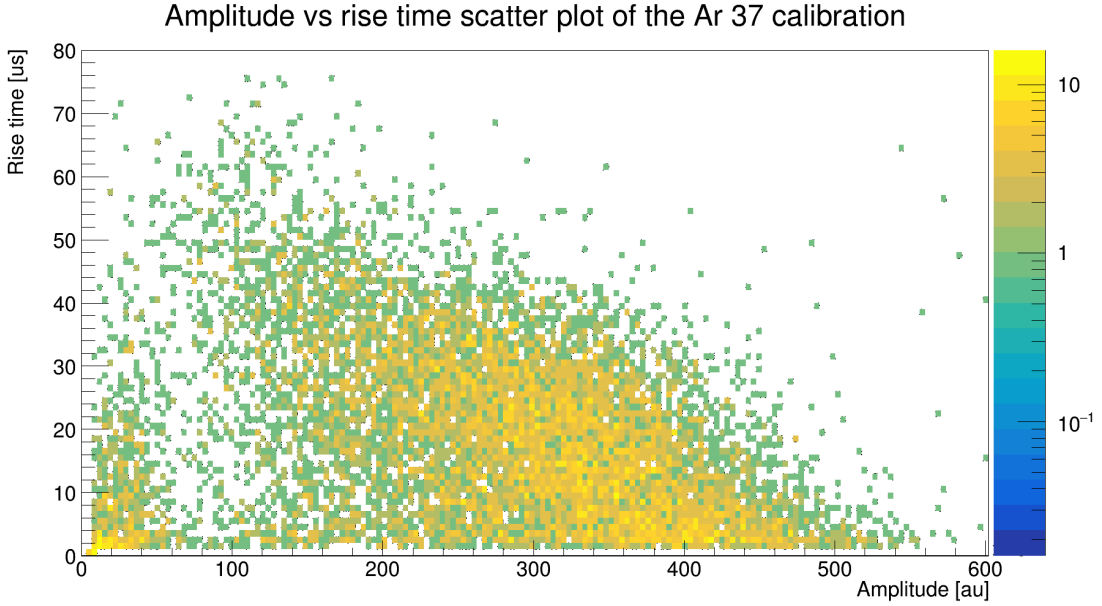

Figure 4.3: 2D histogram rise time vs amplitude of events recorded during the 16-hour run of ^{37}Ar calibration. The strong correlation of lower amplitude for larger rise time shows the presence of impurities in the gas.

Figure 4.3 shows the rise time vs amplitude of the recorded events. It is possible to distinguish the two populations corresponding to the 0.270 and 2.82 keV events. The histogram shows a strong correlation between rise time and amplitude, especially for 2.82 keV events. This correlation can be explained by the presence of an impurity in the gas. Events with longer rise time were induced by decays occurring far from the center of the sphere giving a higher probability for a primary electron to be absorbed by an electro-negative impurity, resulting a pulse with a smaller amplitude. This effect can be reproduced on simulation by adding oxygen contamination to the gas mixture property used by Magboltz.

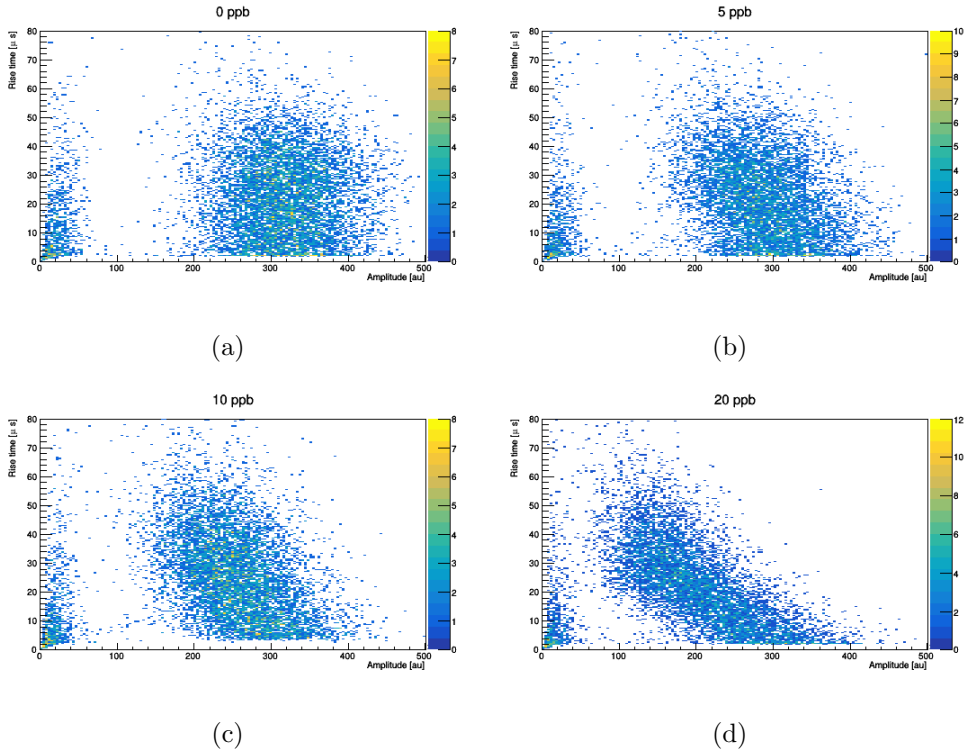

(a) (b)

(c) (d)

Figure 4.4: Effect of the O_2 contamination on the rise time vs amplitude correlation for ^{37}Ar simulation: (a) 0 ppb; (b) 5 ppb; (c) 10 ppb; and, (d) 20 ppb

Figures 4.4 show the effect of oxygen contamination of the gas mixture on simulated ^{37}Ar events. As expected, adding more oxygen increases the rise time vs. amplitude correlation. It is now possible to estimate the oxygen contamination of the gas mixture by measuring the slope of the rise time vs. amplitude correlation. The distributions of amplitudes for different slices of rise-time are fitted with a Gaussian function for which the mean value is represented on Fig 4.5 by black dots. Then, the coordinates of the mean value for each rise time slice are fitted with function $\text{rise time} = a \times \text{amplitude} + b$, the red line on Fig 4.5. The fit parameters obtained are given by $a = -3.3 \pm 0.1 \times 10^2$ and $b = 3.71 \pm 0.03 \times 10^5$.

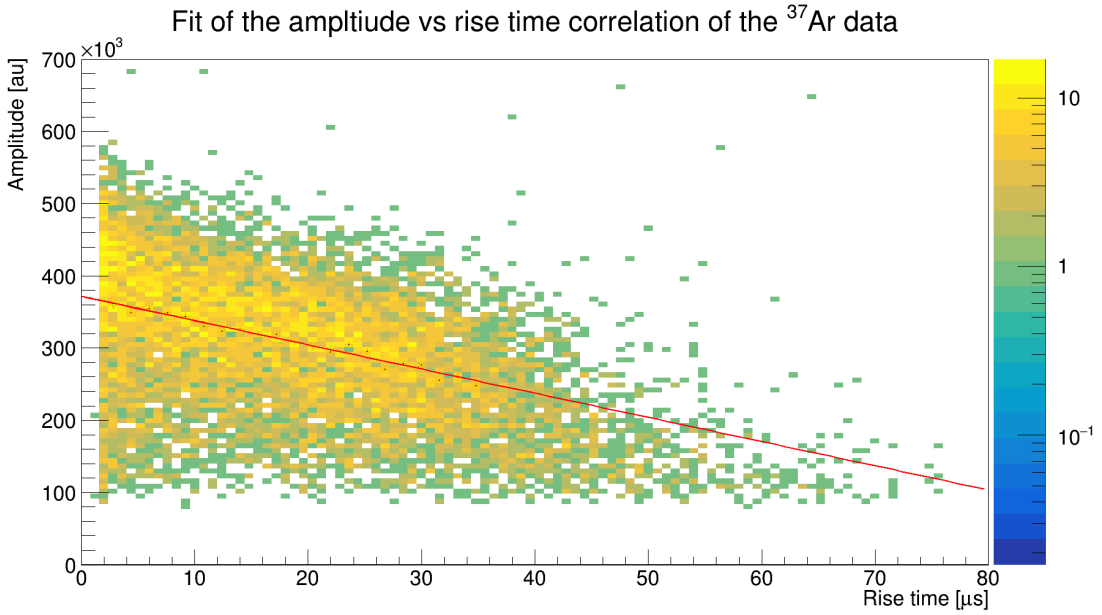

Figure 4.5: Fit of the amplitude vs rise time correlation of the ^{37}Ar data,

The same procedure was applied to simulations with different oxygen contaminations. Figure 4.6 shows the relationship between the slope of the amplitude vs. rise-time correlation and oxygen contamination. The contamination presenting the closest slope to the one observed on the data is 16 ppb. For the next detector, the presence of electronegative impurities will be limited by an Oxy-Sorb filter installed in series with the gas cylinder and monitored with a residual gas analyser.

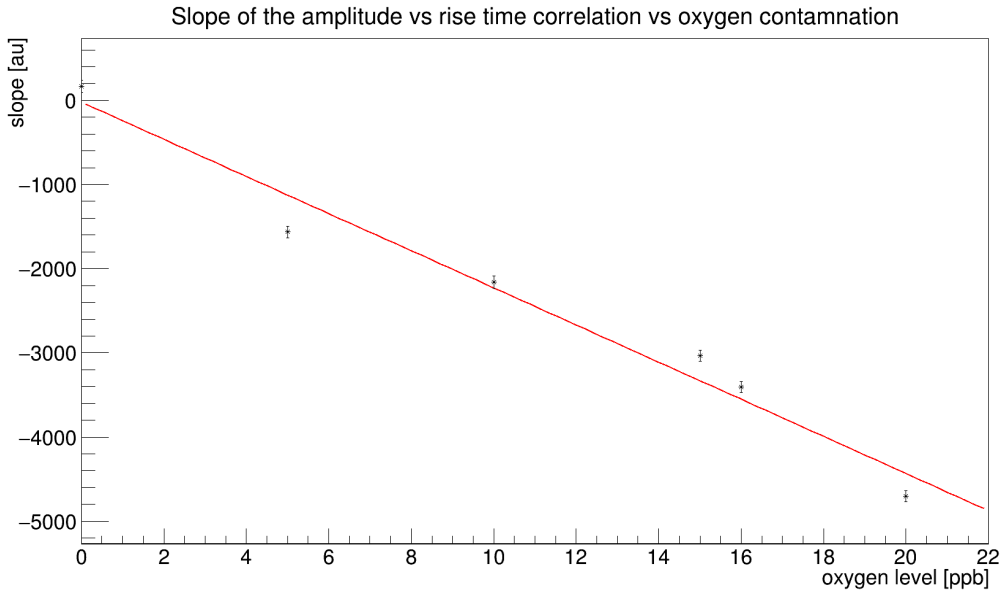

Figure 4.6: Relationship between oxygen contamination and amplitude vs risetime correlation for ^{37}Ar simulation. The oxygen contamination showing the closed slope to the one observed on data is 16 ppb.

4.4.2 Electric field anisotropy in the avalanche region

Another issue affects the amplitude of the recorded pulses. The gain of the detector is driven by the strength of the electric field within less than 1 mm around the anode ball. For the data taken in 2015, the SEDINE detector used a 6.3 mm silicon ball anode (Fig 4.7).

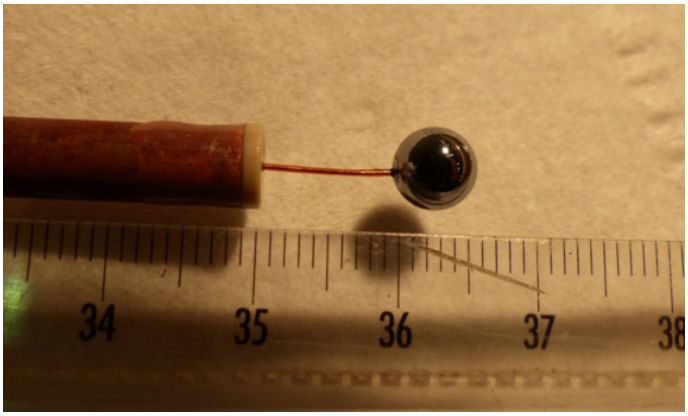

Figure 4.7: 6.3 mm Si sensor used in SEDINE.

Under these conditions the electric field is not homogeneous and isotropic both around the sensor and within the volume of the sphere (Fig 4.8). The electric field is modelled using the finite element software COMSOL.

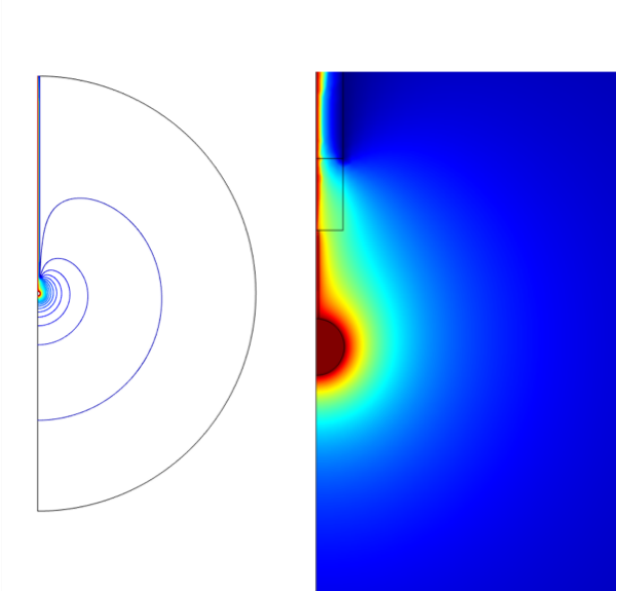

(a) Equipotential in the volume of the detector

(b) Electric field around the sensor

Figure 4.8: The electric field structure of SEDINE.

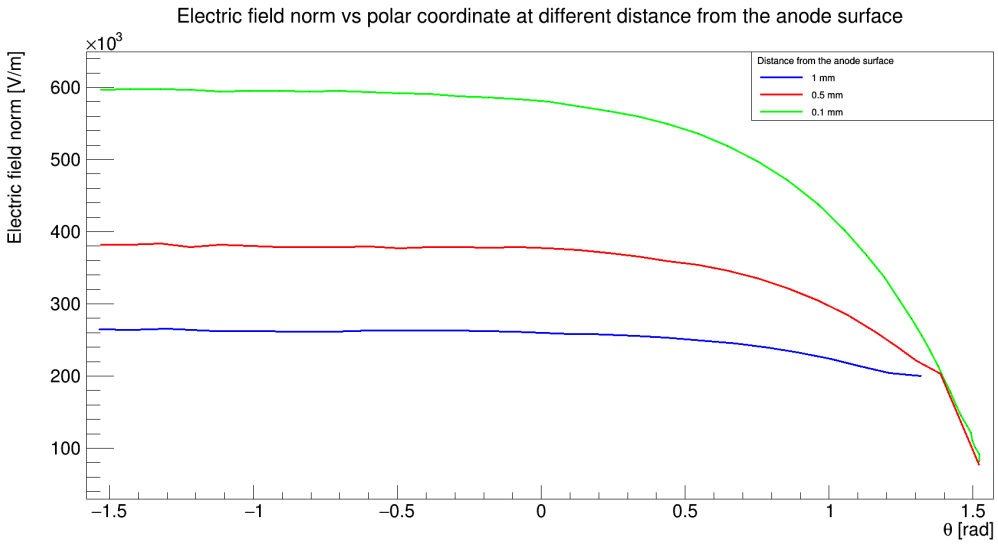

Figure 4.9: Norm of the electric field at 0.1 (green), 0.5 (red) and 1 mm (blue) from the surface of the sensor. $\theta = \pi/2$ corresponds to the direction of the wire.

As shown in Fig 4.9, the electric field is not isotropic around the sensor due to the presence of the wire to support it. The electric field is almost constant in the lower part of the sensor (for θ in $[-\pi/2,0]$) and decreases as we reach the upper half of the avalanche volume (θ in $[0,\pi/2]$). The weaker field affects the gain of the avalanche for primary electrons reaching this upper half of the sensor, producing lower amplitude pulses. This effect has to be taken into account to reproduce the non-gaussianity of the ^{37}Ar spectrum. Although it is difficult to accurately simulate the behavior of electrons in the real electric field, this effect has been modelled by an ad-hoc parametrization of the gain with respect to the angle of arrival of the primary electron. The weighting factor tested is shown in Fig 4.10.

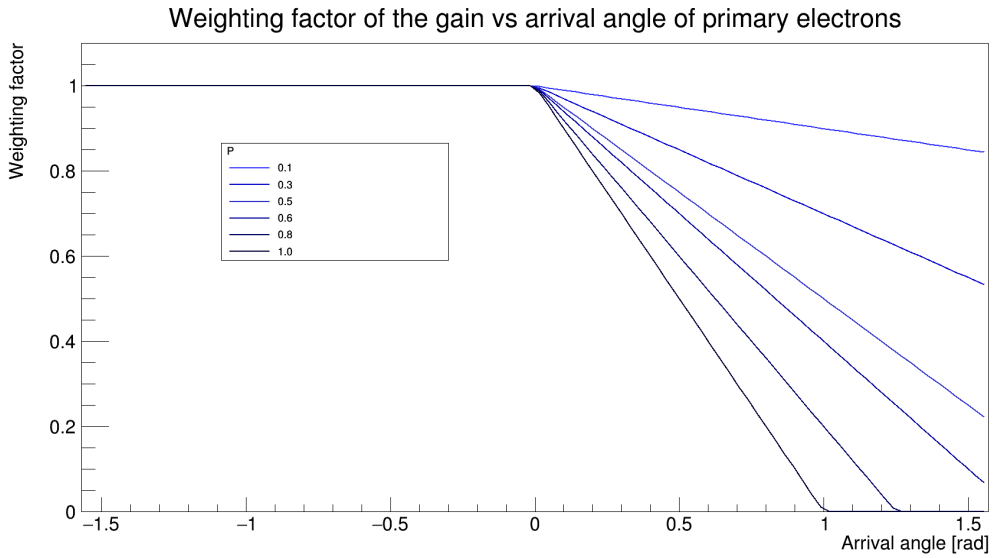

Figure 4.10: Weigthing factor of the gain vs arrival angle of primary electrons.

The weighting factor vs angle of arrival of primary electron are defined by the function

$$WF = Maximum(0, 1 - P \times Maximum(\theta, 0)) \tag{4.1}$$

where P is a parameter driving the slope of the factor for the positive angles of arrival. The correct weighting factor allowing for simulating the anisotropy for the gain is found by comparing the ratio of the Root Mean Square (RMS) by the mean value μ of the energy spectrum of the 2.8 keV peak. The figure 4.11 shows the 2.8 keV energy spectrum of the data, with a ratio RMS/$\mu = 0.33 \pm 0.003$.

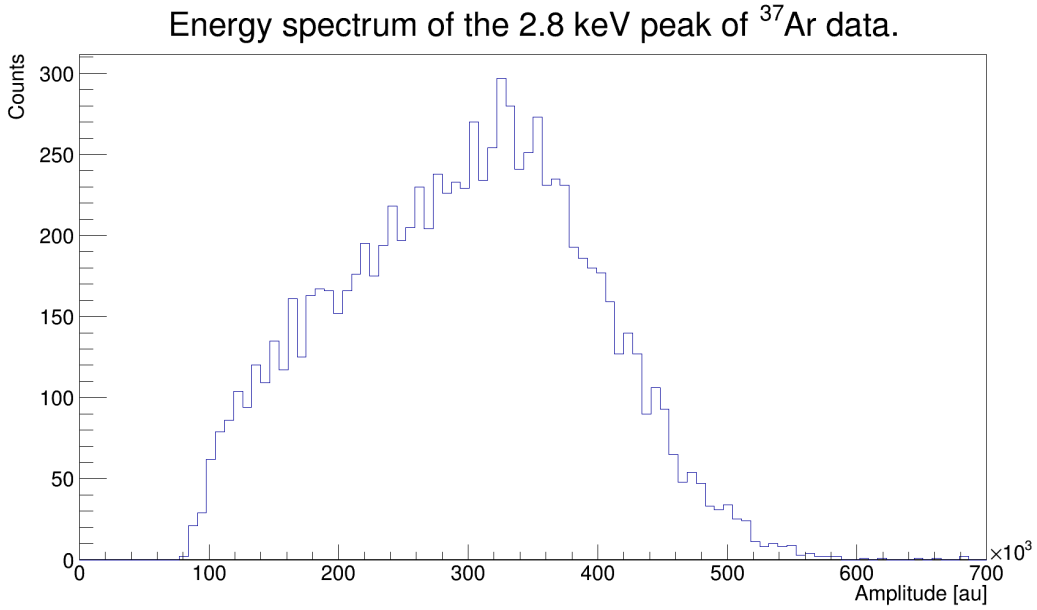

Figure 4.11: 2.8 keV of the ^{37}Ar data with a ratio $RMS/\mu = 0.33 \pm 0.003$

We applied the same procedure to the simulation with different weighting factors defined by the parameter P (Eq 4.1, Fig 4.10). The figure 4.12 presents the ratio RMS/μ as a function of the parameter P. From this figure, we can deduce that for P=0.3, the RMS/μ ratio is equal to 0.33.

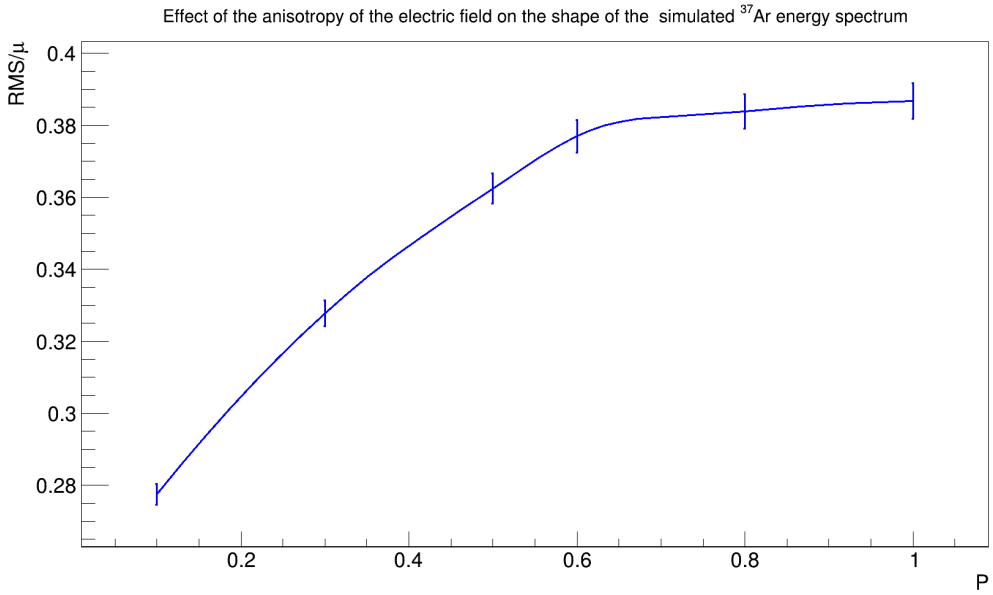

Figure 4.12: Effect of the field anisotropy on the shape of the simulated 2.8 keV peak of the ^{37}Ar.

The purpose of this section was to find the parameters to take into account the possible impurity present in the gas and the inhomogeneity of the electric field. Comparing the slope of amplitude vs. rise-time correlation and the RMS/μ ratio for data and simulation allowed us to deduce an oxygen contamination level and a function that describes the inhomogeneity of the gain.

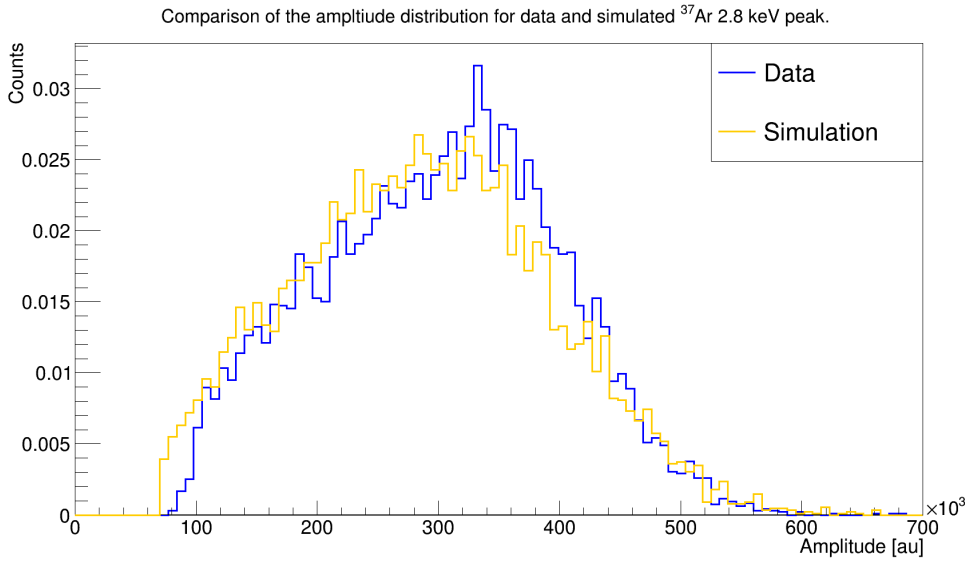

Figure 4.13: Comparison of the amplitude spectrum of data and simulation of the 2.8 keV peak of the ^{37}Ar.

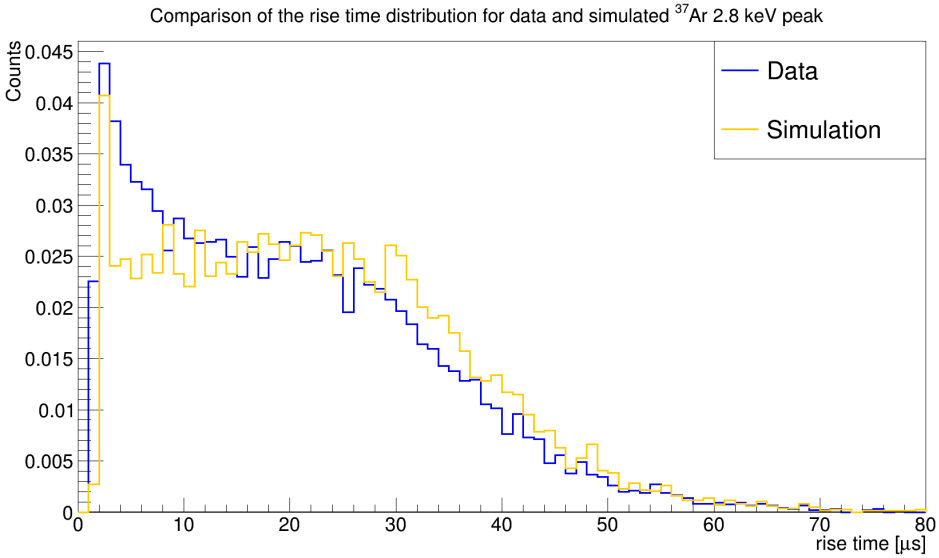

Figure 4.14: Comparison of the rise time spectrum of data and simulation of the 2.8 keV peak of the ^{37}Ar.

The figures 4.13 and 4.14 show the reasonable agreement between data and

simulation both for the rise time and amplitude distribution. The discrepancy at low rise time can be due to the choice of the baseline noise, coming from the background run, added to the simulated pulse. We now know good parameters to add to the simulation to reproduce the data. These parameters are used in the next sections to compare simulation and data.

4.5 ^{22}Na calibration, physical events selection

In addition to the calibration done with ^{37}Ar, we performed a calibration with a ^{22}Na source. ^{22}Na decays by β^+ emission into ^{22}Ne in an excited state. The excited neon decays to the ground state by emitting a 1275 keV γ [71]. This source produces γ induced events from the 1275 keV γ and also from 511 keV γ from the annihilation of the positron with an electron of the surrounding material. Those γ rays are a very useful calibration source because they produce events throughout the whole volume of the detector, with a typical rise time vs. width distribution (where the width of a pulse is define as its width at half height). This distribution is shown in Fig 4.15 left. Physics events have widths between 86 and 500 μs and rise time between 9.6 and 350 μs. Outside this window, the events are electronic noise (Fig 4.16(c)), amplifier response to non-physical current, or physical events on top of a very noisy baseline (Fig 4.16(d)).

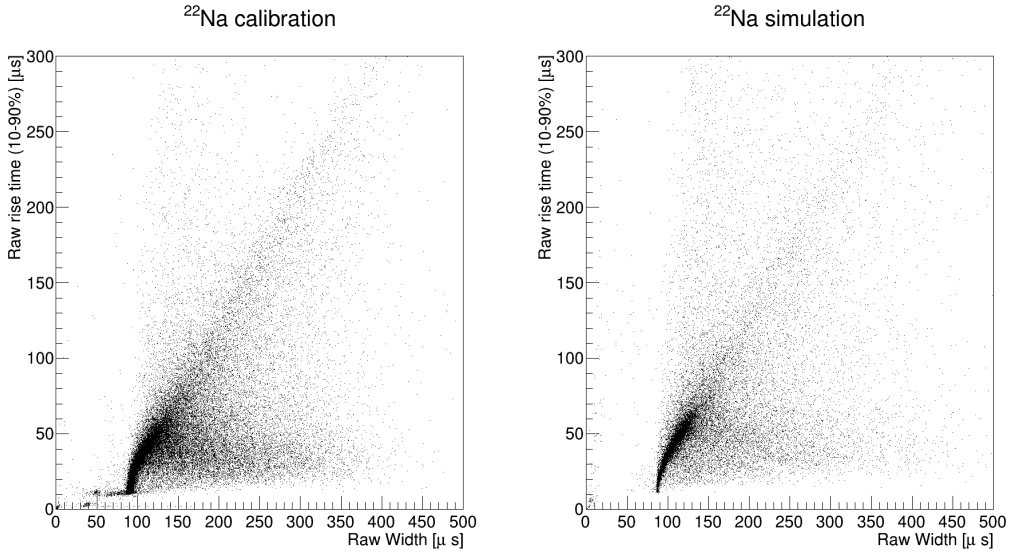

Figure 4.15: Rise time vs. width of the ^{22}Na calibration.

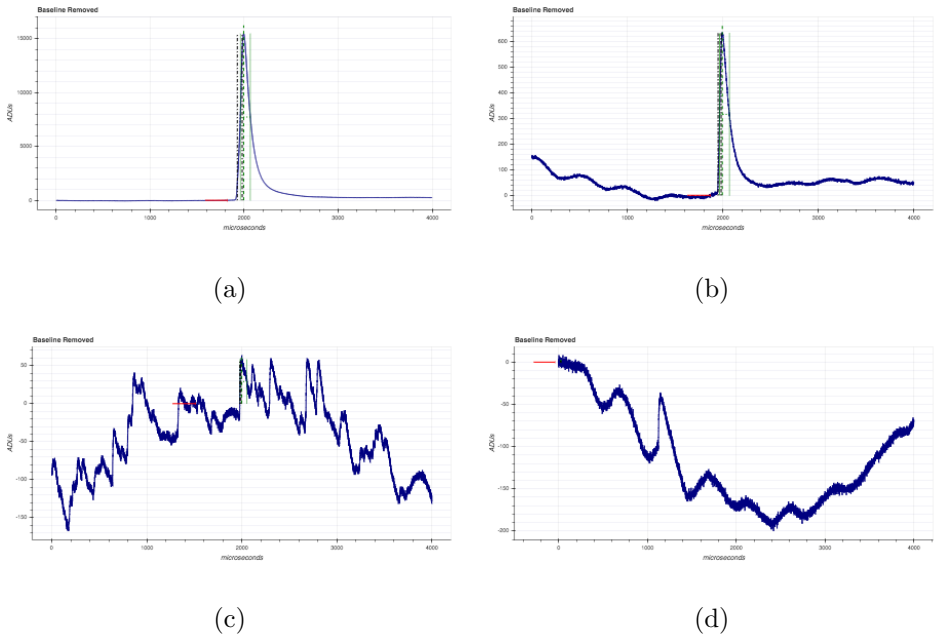

(a) (b)

(c) (d)

Figure 4.16: Example of pulses in different rise time and width windows: (a) physical event; (b) physical event; (c) noise, (d) physical events on noise

Figure 4.15 right shows the simulation of the ^{22}Na calibration. The simulation

reproduces the rise time vs. width distribution.

4.6 Background of the physics run

The purpose of the rest of this chapter is to give an explanation of the events observed during the run used to set the dark matter limit described in Section 4.3 and published in 2017 [47].

4.6.1 Calibration

The run was calibrated using the 8.1 keV X-ray fluorescence of the copper. Selecting volume events, with rise time lower than 30μs, a clear excess of events is visible (Fig 4.17).

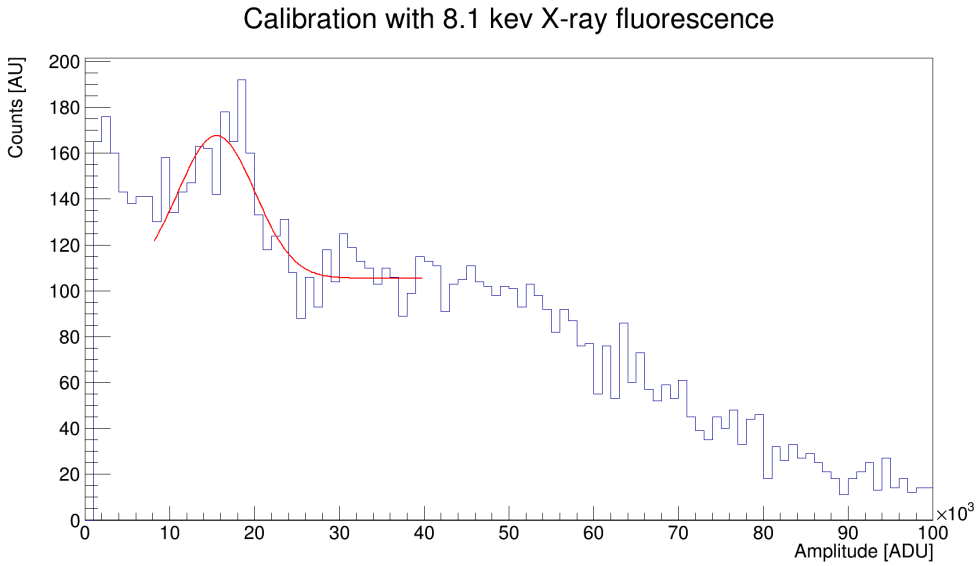

Figure 4.17: Calibration of the physics run with the 8.1 keV X-ray fluorescence.

The fit shown on Fig 4.17 gives a mean value of $1.55 \pm 0.04 \times 10^4$. The W-value of the neon is 36 eV. With a digitizer gain of $G_{DIG} = 48120\,ADU/V$, and a pre-amplifier

gain of $G_{P-A} = 235nV/e^-$ we can estimate the mean gain of the avalanche to be 6090 secondary ion-electron pair per primary electron. The conversion factor for ADU to keV is then 1913 ADU/keV. Figure 4.17 presents a fit of the 8.1 keV peak with a cut for amplitude lower than 1000 ADU. Figure 4.18 shows the volume events without energy threshold cut, scaled by the conversion factor determined previously. The event rate increases by roughly two orders of magnitude for events below 500 eV. No simulation done with Geant4 reproduces this rise of the rate for very low energy events. The rest of this chapter focuses on events with energy above 500 eV.

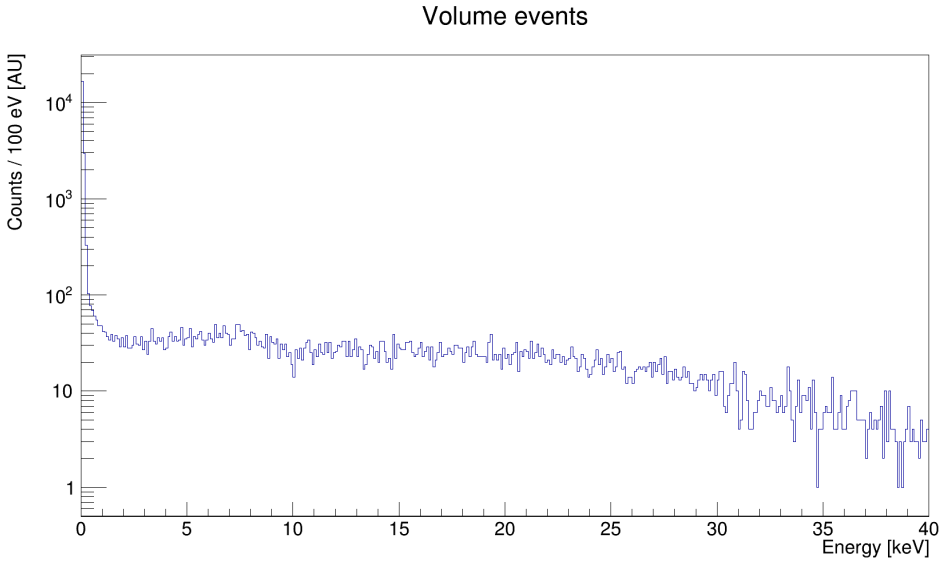

Figure 4.18: Volume events energy spectrum

4.6.2 Copper

The contamination of ^{238}U, ^{232}Th decay chain and ^{40}K in the copper were measured with a high purity germanium detector (HPGe). The upper limit on ^{238}U and ^{232}Th were estimated respectively by counting gamma-rays from ^{228}Ra and ^{228}Th. Such a

method did not give a precise measurement but only the upper limit due to the background of the detector and the low activity of the isotope to be measured. Table 4.1 presents the upper limit of the activity of different elements present in the copper.

Isotope	Activity [mBq/kg]
^{238}U	<0.016
^{232}Th	<0.012
^{40}K	<0.11

Table 4.1: Upper limit on the contamination of the NOSV copper [72]

In addition to the long-lived elements present in the copper, it is activated by exposure to cosmic rays. Neutron interactions in copper produce several isotopes. The main concern is ^{60}Co due to its long half-life of 1925.8 days. The production rate of ^{60}Co at sea level was estimated to be 97.4 atoms/kg/day [73]. Such activation brings a saturation activity of 1.1 mBq/kg. The history of the copper shielding is not well known, but it was stored several for several years underground. In 2015 we can assume its activity to be roughly 25 μBq/kg. This amount corresponds to one year of exposure to cosmic ray followed by ten years of cooling. Similarly, the copper of the sphere itself has not been tracked from its production to the delivery of the sphere underground. To obtain an idea of the impact of its contamination, we estimated 6 months of total exposure of the copper above ground. The sphere was delivered at the Laboratoire Souterrain de Modane in 2012. The physics run was taken in 2015. So, assuming 6 months of activation and 3 years of cooling the ^{60}Co activity during this run was approximately 41 μBq/kg. Similarly, with a production rate of 88.3 atoms/kg/day, 6 months of activation, and 3 years of cooling, the activity of ^{57}Co

in the copper is 9 μBq/kg. Figures 4.19 and 4.20 show a comparison of the event rate of data and simulations of the radioactivity of the copper sphere and copper shielding. We can remark that the contamination of the copper sphere does not bring a substantial contribution to the background rate. The contribution of the copper shielding is strongly dominated by the presence of the ^{60}Co. It could be responsible for approximately 10% of the total event rate. These two figures show clearly that the background is not dominated by the contamination of the copper. Also, it is essential to keep in mind that the activity used to scale the simulation are an upper limit for ^{238}U, ^{232}Th and ^{40}K. Their contributions are likely lower.

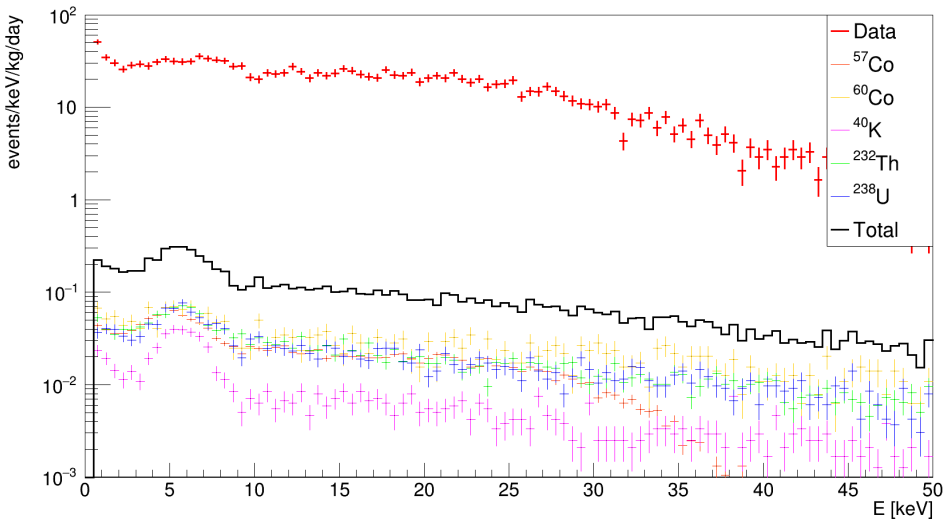

Figure 4.19: Comparison of volume events data and simulation of the copper sphere contamination.

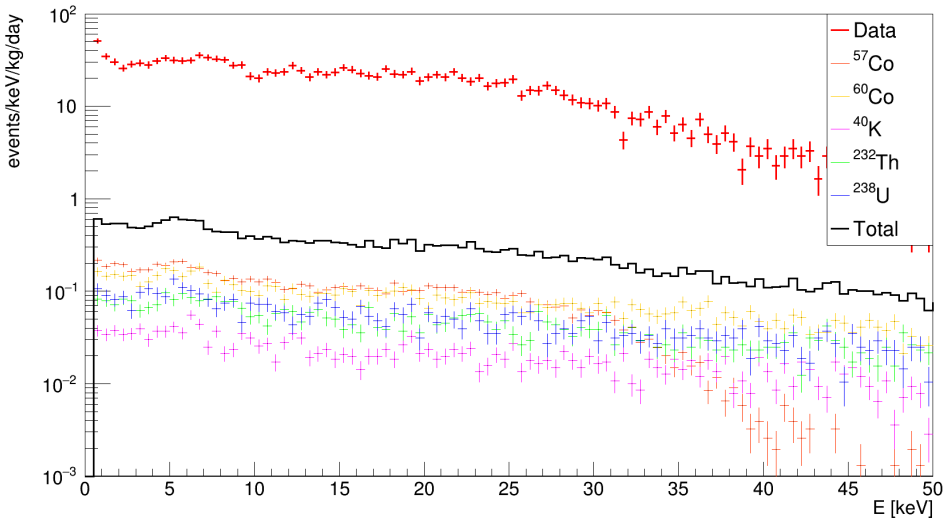

Figure 4.20: Comparison of volume events data and simulation of the copper shielding contamination.

4.6.3 Lead shielding

The sphere and the copper shielding are enclosed in cubic lead shielding. Five walls are 15 cm thick and one 10 cm. The lead composing the lead shielding has not been tested for ^{238}U, ^{232}Th and ^{40}K as the copper. To estimate the impact of its contamination on the background, we used to activity measured on the lead used for the next detector (see next chapter). The results are presented in the following table.

Isotope	Activity [mBq/kg]
^{238}U	0.079
^{232}Th	0.009
^{40}K	<1.46

Table 4.2: Upper limit on the contamination of the lead.

During lead refining, ^{238}U and ^{232}Th are mostly removed, but the lead isotopes are chemically separated and remain in the lead brick at the end of the process. This implies a substantial activity ^{210}Pb, from the ^{238}U chain, in the lead shielding. The ^{210}Pb activity of the lead was measured by a germanium counter at the LSM and is 37.4 ± 4.32 Bq/kg.

Figure 4.21 shows a comparison of the background induced by the contamination of lead shielding and the surrounding gamma flux. The contribution of the lead shielding is strongly dominated by the presence of the ^{210}Pb decay chain.

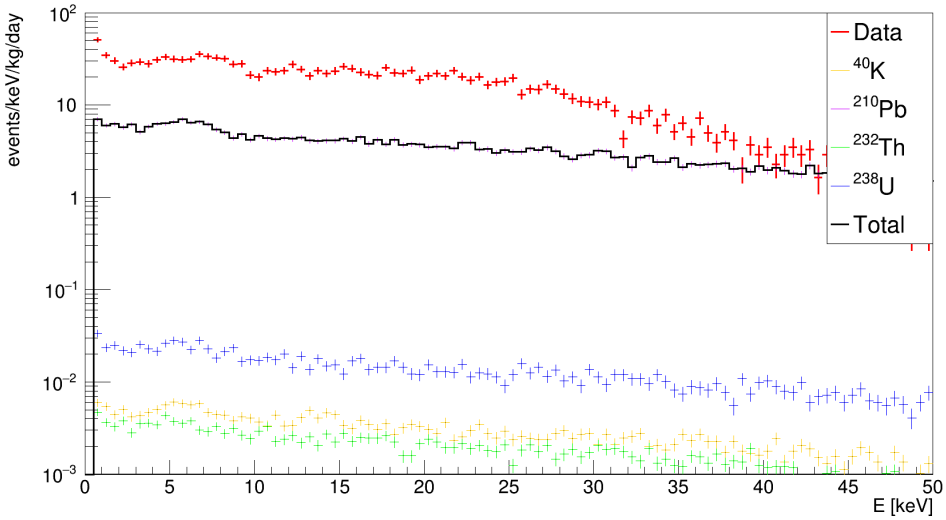

Figure 4.21: Comparison of volume events data and simulation of the lead shielding contamination.

4.6.4 Surrounding rock

Finally, the background estimation takes into account the radioactivity of the rock surrounding the laboratory. The gamma flux from radioactive elements present in the rock was measured to be $125 \pm 4 \times 10^{-3}\gamma$ cm^2 s^{-1} for the 1460 keV γ from ^{40}K and

$42 \pm 7 \times 10^{-3}\gamma$ cm^2 s^{-1} for the 2614 keV γ from ^{208}Tl decay. Figure 4.22 shows the comparison of the background induced by the surrounding gamma flux and the data. The surrounding gamma flux contribute to a few percent of the total background event rate.

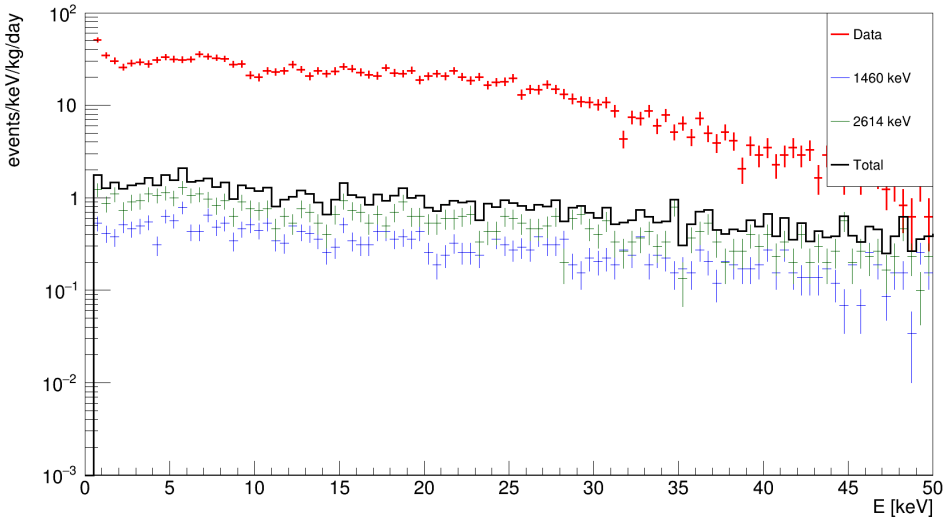

Figure 4.22: Comparison of volume events data and simulation of the surrounding gamma flux.

4.6.5 Summary on first estimation of the background events

The figure 4.23 shows a comparison of the data (red) and the sum of the sources of background described previously (black). The background understood with these simulations is mainly due to the contamination of the lead shielding (gray) followed by the gamma rays form the rock (green), the copper shielding (orange) and finally the copper sphere (blue).

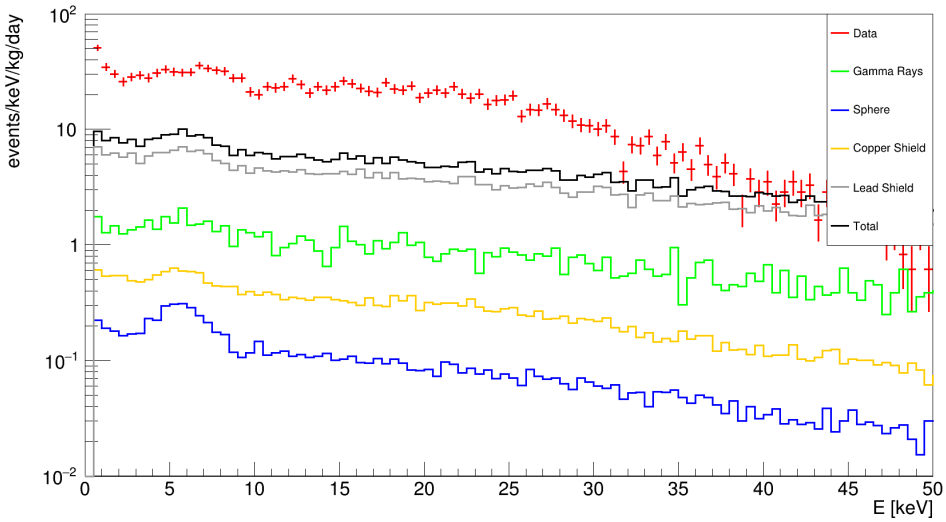

Figure 4.23: Comparison of volume events data and simulation of the lead shielding contamination and surrounding gamma flux.

It is evident that the sources of background listed above only contribute a small fraction of the total background observed. At low energies, between 1 and 5 keV, the average event rate is 29 events/keV/kg/day, where the sum of the simulation is only 8.1. At lower energy, between 500 eV and 1 keV the event rate is 50 events/keV/kg/day where the sum of all the background sources is 9.6. The next section describes other sources of background beyond others already mentioned.

4.7 ^{210}Pb in the copper

In the previous section, we showed that several background sources present in the copper, the lead, and the rock surrounding the detector do not explain the observed background. As daughter of ^{238}U, ^{210}Pb was assumed to be in equilibrium and therefore be a negligible component. Gamma ray spectroscopy using high purity germanium detectors has a limit of 120 mBq/kg for detecting ^{210}Pb by measuring the 46.6

keV de-excitation after its decay to ^{210}Bi. However, in May 2017, K. Kobayashi from the University of Tokyo presented the first measurement of the ^{210}Pb and ^{210}Po activity in bulk copper using a low background alpha particle counter [74]. The result shows that the equilibrium of ^{238}U is highly broken. The ^{210}Pb activity in OFC copper lies between 17 and 40 mBq/kg, three orders of magnitudes higher than the ^{238}U activity. The ^{210}Pb contamination is understood to be a residual of an electrolysis process [75]. As the SEDINE detector is made of copper and surrounded by a copper shielding the ^{210}Pb decay chain in the copper is a promising candidate as a primary source of background. In addition to the contamination in the bulk copper, the surface of the detector is also contaminated with ^{210}Pb from exposure to the air of the laboratory polluted with ^{222}Rn. The following sections first present estimates of ^{210}Pb activity in both the copper bulk and inner surface of the detector and second shows the impact of these contaminations on the background of the experiment.

4.7.1 Assessing the ^{210}Pb contamination

By running the detector at a lower voltage, with a lower gain, it is possible to estimate the alpha rate from the inner surface and the bulk of the copper sphere. Alpha particles from the surface of the detector are fully reconstructed at 5.3 MeV and those coming from the copper bulk are degraded and deposit less energy in the gas (Fig 4.24).

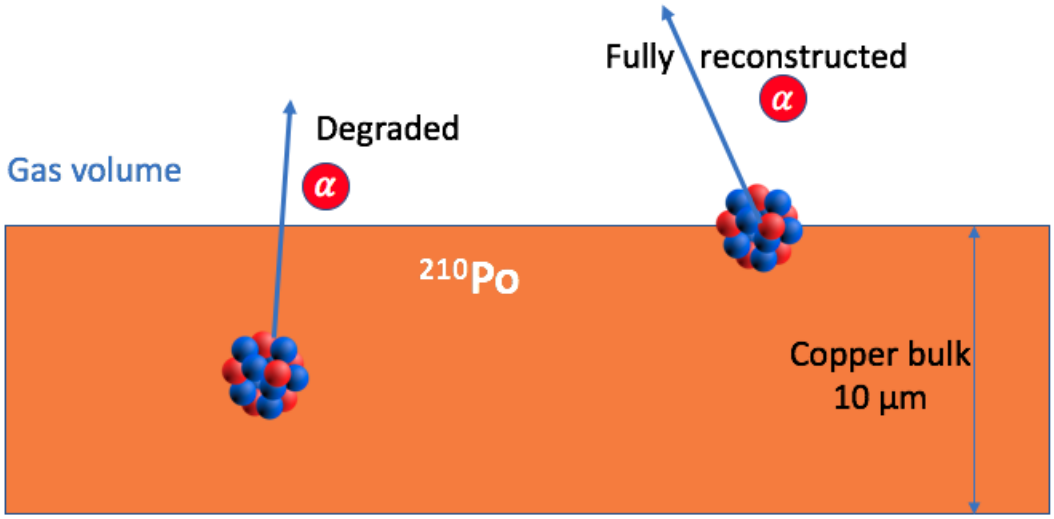

Figure 4.24: Schematic of ^{210}Pb decay in the copper surface and bulk.

Shortly after the physics run, we took another run with the same gas conditions and acquisition but with a lower voltage, 2200 V. Figure 4.25 shows the rise-time vs. amplitude scatter plot where the ballistic deficit and attachment are corrected ad-hoc. The rise time distribution can be divided into two parts, higher and lower than 47 μs. Alpha decay from an isotope fixed on the inner surface of the detector produces events with rise times higher than 47 μs. Events with rise times lower than 47 μs are induced by ^{222}Rn decay in the gas volume (orange ellipse). Events with rise-time higher than 47 μs and amplitude higher than$\approx$ 19000 AU are induced by ^{218}Po (blue ellipse). Finally, the events in the red box are a mixture of ^{222}Rn in the gas and ^{210}Po decay on the inner surface and within the bulk of copper.

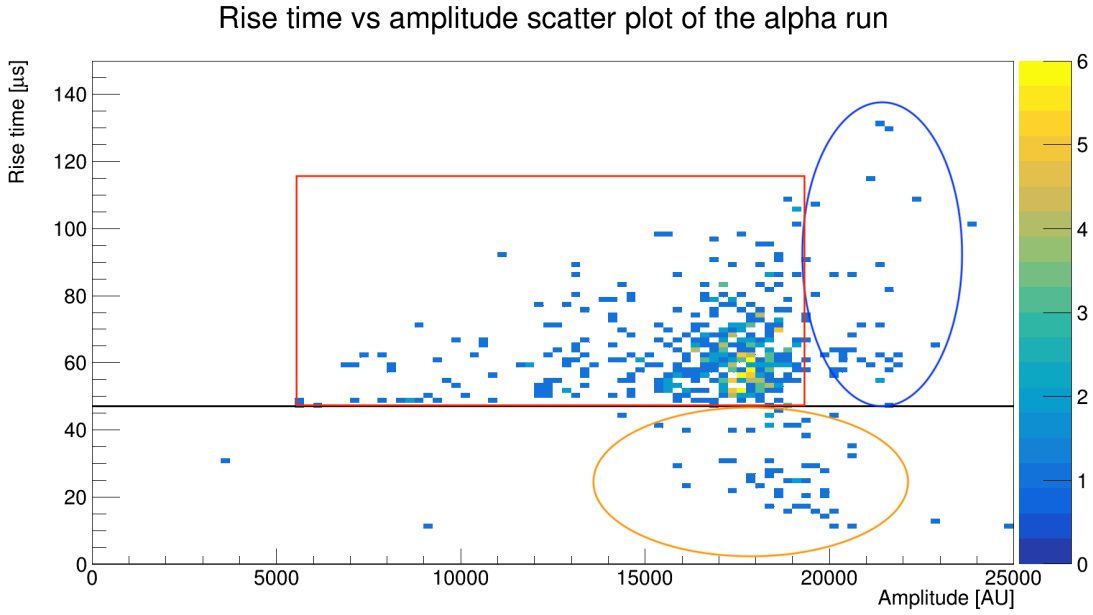

Figure 4.25: Rise time vs, amplitude scatter plot for a low voltage run.

Figure 4.26 shows the spectrum of events with rise time higher than 47 μs (red) and lower than 47 μs (blue). These two distributions can be used to determine the different activities:

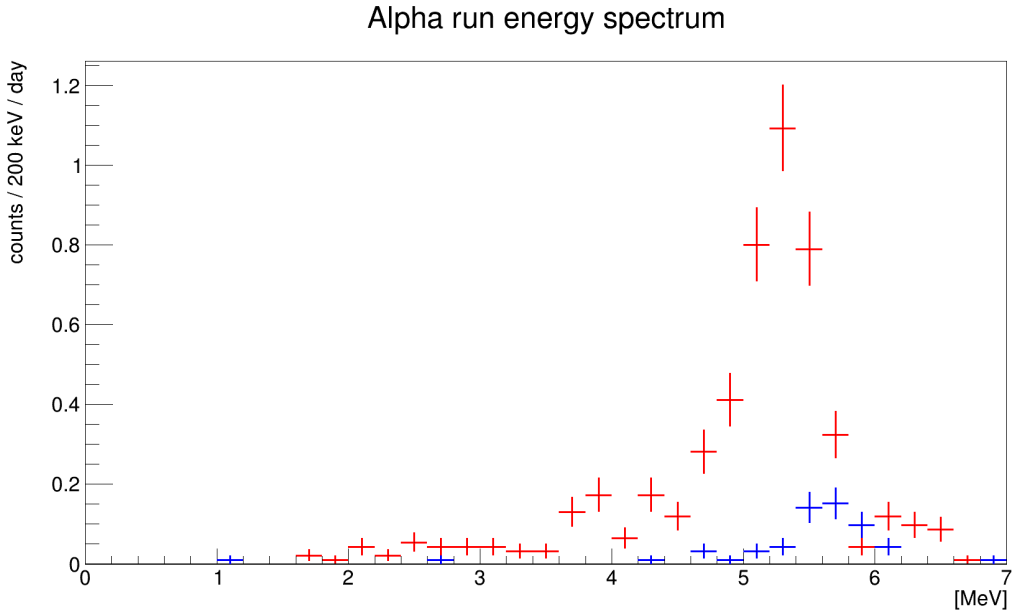

Figure 4.26: Energy distribution of the low-gain run. The blue crosses show the spectrum of ^{222}Rn (events with rise time lower than 47 μs) and the red curve shows events with rise time higher than 47 μs, induced by ^{222}Rn, ^{218}Po and ^{210}Po.

- ^{218}Po: The events induced by the decay of ^{218}Po have energy higher than 5.8 MeV on the red curve of Fig 4.26. During the 92 hour-run, 34 events were detected in this region. We can assume that only half of the ^{218}Po are detected because half of the decays produce alpha particles directed toward the gas, and other half are directed toward the copper sphere. The activity of ^{218}Po is then 0.2 ± 0.04 mBq.

- ^{222}Rn: The events in the orange ellipse in Fig 4.25 are induced by ^{222}Rn. 52 events populate this area. However, due to the short half-life of ^{218}Po compared to ^{222}Rn, both are in secular equilibrium. We should expect 68 events from ^{222}Rn, twice the amount of events from ^{218}Po. However, ^{222}Rn decay occurring

close to the surface and where the alpha particle is emitted along the radius of the sphere produces events with rise-time higher than 47 μs — thus implying that the red box of Fig 4.25 contains 16 events from ^{222}Rn.

- ^{210}Po: We find ^{210}Po on the inner surface and in the bulk of the copper sphere. The activity on the inner surface is estimated by integrating the number of events between 4.8 and 5.8 MeV on the red curve of figure 4.26. Taking into account the 16 events from ^{222}Rn, and the fact that again half of the emitted alpha particles are not detected, the activity of ^{210}Po on the inner surface is 1.8 ± 0.1 mBq. The bulk activity can be estimated by first counting the number of events in a given range and relating this number to activity with the help of a Geant4 simulation. Between 2.5 and 4.8 MeV, the number of alpha particles observed is related to the bulk activity with a conversion of 249 $(\alpha/\mathrm{cm}^2/\mathrm{h})/(\mathrm{Bq/kg})$. Thus, the 107 events observed can be converted to an activity of 26 $\pm$ 3 mBq/kg . This result is in good agreement with the activity measurement by Abe et al [74], however it suffers from large uncertainties. The roughness of the surface of the detector can affect the measurement. The range of a 5.3 MeV alpha particle in copper is about 10 μm. Alpha particles emitted from the surface may deposit energy in a few μm of a copper asperity and be reconstructed with an energy lower than 4.8 MeV and appear to come from the bulk.

4.7.2 Estimation of the impact of the ^{210}Pb contamination

Following the estimation of the ^{210}Pb quantity on the inner surface of the detector and the copper bulk of the sphere, we can estimate the impact on the background of

the detector. We assume the ^{210}Pb activity in the copper of the shielding to be the same as in the copper of the sphere.

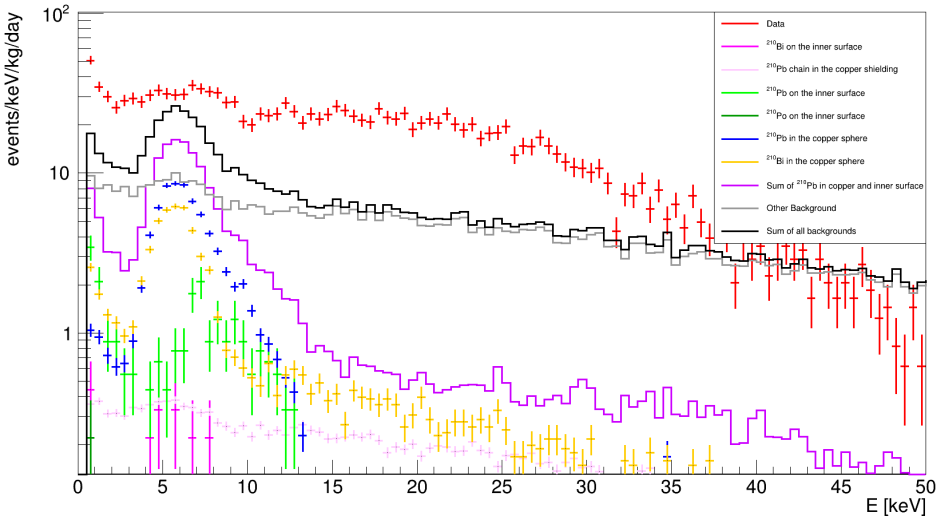

Figure 4.27: Comparison of volume events data and simulation of the ^{210}Pb activity.

Figure 4.27 shows a comparison of the data and simulation of the different contaminations of ^{210}Pb. The violet curve represents the sum of the ^{210}Pb contamination on the inner surface, the copper sphere, and the copper shielding. At low energy, in the 500 eV to 1 keV range the rate is 8.0 ± 1.2 events/keV/kg/day. This total contribution of the ^{210}Pb contamination in the sphere and copper shield is strongly dominated by the activity of the copper sphere (orange for ^{210}Bi, blue for ^{210}Pb) and the ^{210}Pb in the inner surface. Finally, the thick black curve on Fig 4.27 shows the sum of all the contributions listed in the two previous sections. This total contribution does not reproduce the observed background. The simulated background is lower than the observed one. The observed background drops for energy higher than roughly 25 keV where the simulated background continuously decreases. Sevral hypothesis for the

missing background are explored in the next sections.

4.8 ^{222}Rn in the gas mixture

The presence of ^{222}Rn itself in the gas mixture is not a problem because it decay in the volume are fully reconstructed and does not populate the low energy region. However, its daughters ^{218}Pb is left charged and drift toward the sphere to be plated on its surface. Figure 4.28 shows the volume events background induced by the ^{222}Rn daughters. Due to the very short half-life of the ^{214}Po (164.3 μs), it was simulated together with the ^{214}Bi. The 0.2 mBq determined in section 4.7.1 bring a negligible background contribution in volume events compare to other sources.

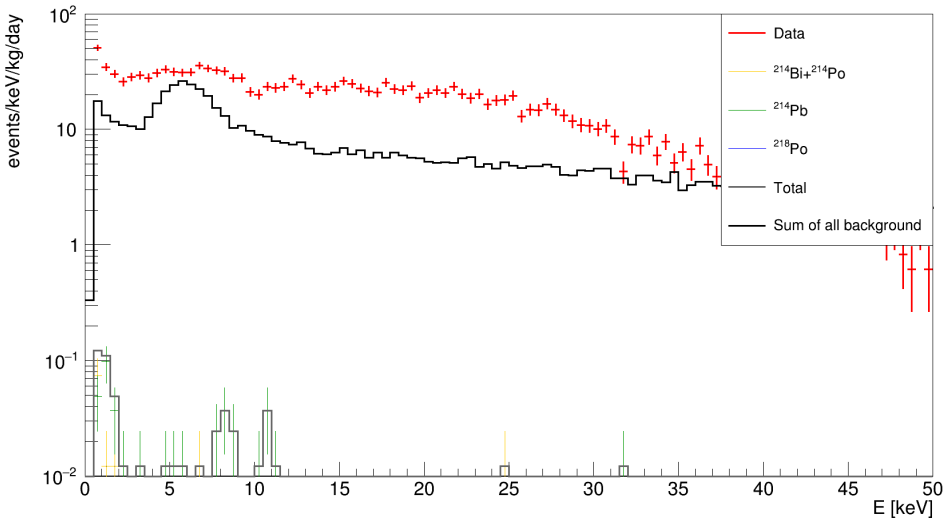

Figure 4.28: Comparison of volume events data and simulation of the ^{222}Rn plated on the inner surface of the sphere.

4.9 Surface events and high energy events

This study of the background focused on volume events with rise times lower than 30 μs. Before trying to figure out what else could induce the observed background, it is useful to look at the other rise time regions to cross-check the validity of the previous simulations.

4.9.1 Surface events

Volume events are mostly induced by Compton interaction distributed in the gas volume. Surface events originate mostly from charged particles coming from the surface of the sphere and the bulk of copper. These charged particles can be created by alpha or beta decay or by the interaction of photons with the copper. Due to their large dE/dx, charged particles deposit their energy close to the surface of the sphere and produce events with large rise time because their primary electrons drift further towards the anode.

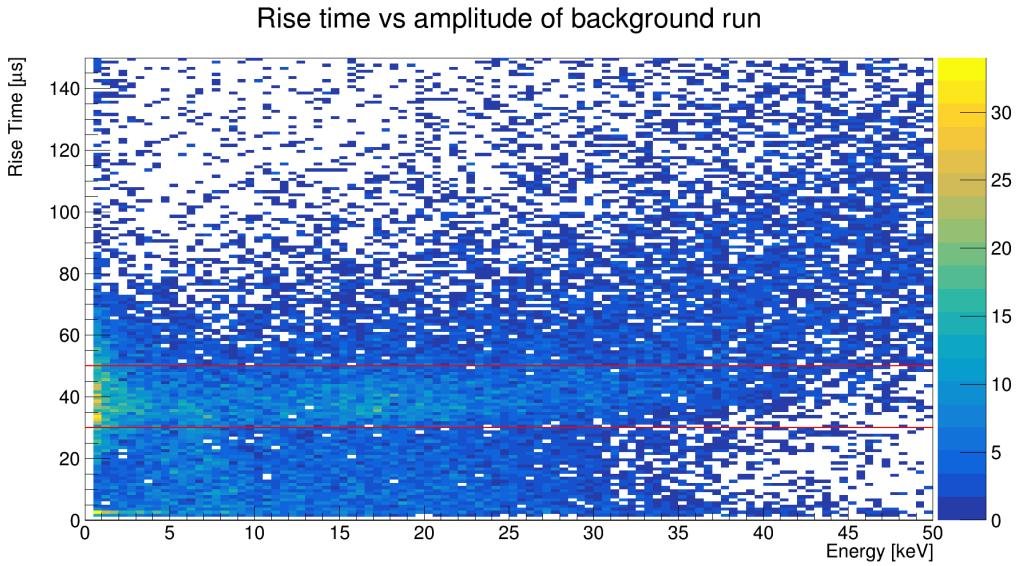

Figure 4.29: Rise time vs. amplitude 2D histogram of the background run. The two lines delimit the surface events region.

Figure 4.29 shows the rise time vs. amplitude 2D histogram of the background run. An apparent accumulation of events appears for rise times between 30 and 50 μs. Figure 4.30 shows a comparison of the spectrum of background surface events and simulations. We can remark that this spectrum is dominated the presence of the ^{210}Pb decay and particularly the ^{210}Pb deposition on the inner surface of the detector (cyan). Between 20 and 26 keV, we can observe an accumulation in the simulation of the ^{210}Po (green) on the inner surface. This accumulation is due to the recoil of ^{206}Pb after an alpha decay. The ^{206}Pb recoils with an energy of 103 keV. However, the deposited energy is affected by the ionization yield. In addition, primary electrons emitted close to the surface travel through the whole detector radius and suffer a large electron capture. The addition of the electron capture and the ionization yield show events much attenuated. The ionization yield was estimated to be 44% with the software SRIM. The recoils of ^{206}Pb should appear around 45 keV. The data

shows an accumulation around 30 keV. The missing energy is correlated to electron capture. The difference between the data and the simulation can be explained by an underestimation of the quenching factor or an overestimation of attachment. Finally, unfortunately, the simulation does not reproduce the rise of events below 2.5 keV.

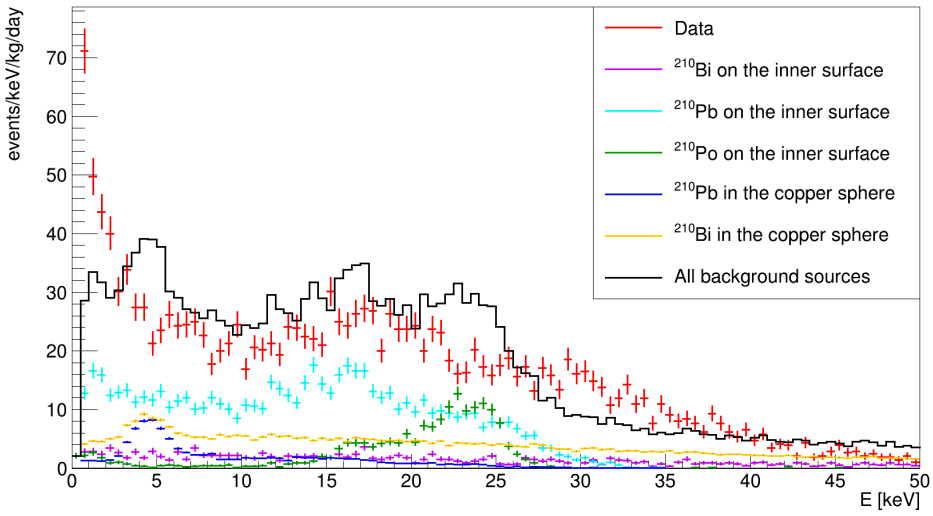

Figure 4.30: Comparison of surface events data and simulation.

4.9.2 High energy events

At energies greater than ≈ 30 keV, an electron from a Compton interaction has a long enough path length to produce track events. The rise time of the events is not dominated by the diffusion of the electrons along their path but the closest and farthest primary electron from the sphere center. Figure 4.31 shows the rise time vs. amplitude 2D histogram of the background run in the whole rise time and energy range. We remark that for high energy events, the detector response is highly non-linear in energy. The accumulation around 130 keV is the alpha particles, mainly from the decay of ^{210}Po on the inner surface of the detector. Those events should

appear at 5.3 MeV.

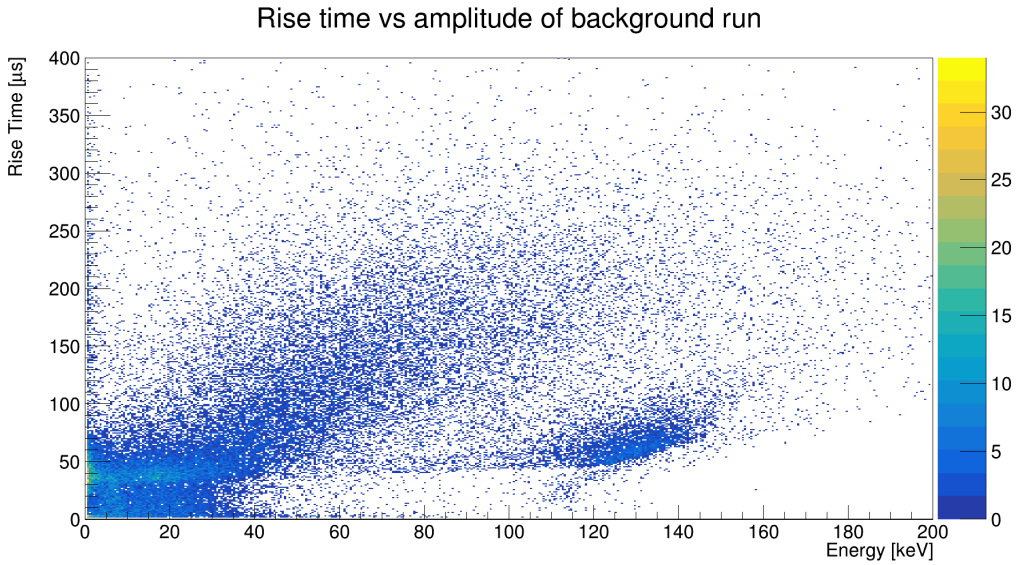

Figure 4.31: Rise time vs. amplitude 2D histogram of the background run extended in the whole energy range.

This non-linearity of the energy response of the detector at high energy is not fully understood. Several factors can cause such behavior such as, electron attachment due to the presence of oxygen. However, an attachment strong enough to attached almost 98% of the primary electrons would have a dramatic effect and low energy events studied in the two previous sections would be barely detectable. A second possibility is the ionization yield. However, an estimation of the ionization yield with SRIM for 5.3 MeV alpha in the gas mixture shows a yield of 99.8%. A way too small amount of the energy is dissipated through phonon to explain this non-linearity. The third explanation is a screening effect during the avalanche process. For high enough energy events, with a large enough dispersion of the arrival of the primary electrons, the avalanche induced by the first electrons screens and reduce the electric field. Primary electrons that arrive later produce smaller avalanches, reducing the total amplitude

of the induced pulse. This effect can not be added to the simulation by ad-hoc parametrization. However, Fig 4.32 shows the simulation of different contaminations producing track events with rise times higher than 50 μs. Again, the background in this region is strongly dominated by the ^{210}Pb decay chain, especially by the decay of ^{210}Bi in the copper sphere bulk (orange).

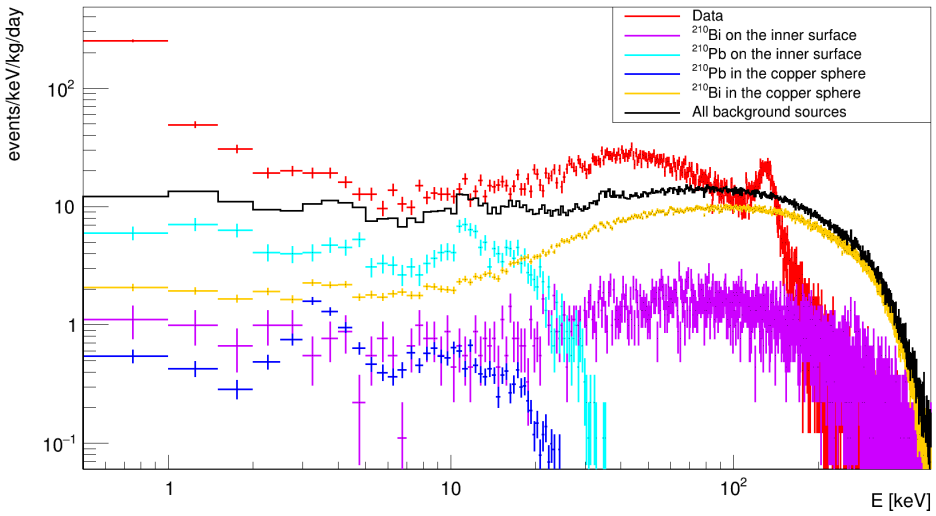

Figure 4.32: Comparison of track events data and simulation.

4.10 Conclusion and hypothesis on other background sources

Table 4.3 shows the event rate observed at all energies for the three regions of the rise time distribution. The simulation properly reproduces the rate for surface and track events but not for volume events.

	Rate data [mHz]	Rate simulation [mHz]
Volume	2.6	1.3
Surface	3.0	3.8
Track	9.3	10.1

Table 4.3: Events rate measured and simulated.

4.10.1 The rod

Although it is placed inside the sphere, due to its low mass (40 g) compared to the sphere, the background induced by the rod is negligible. Assuming the same contamination as the sphere, its contribution is hundreds of times lower. The simulations of the ^{238}U decay chain down to ^{210}Pb with the same contamination give 1.1×10^{-4} events/keV/kg/day between 500 eV and 1 keV from the rod and 0.036 events/keV/kg/day from the sphere, 1.2×10^{-4} from the rod and 0.053 for the ^{232}Th and 0.013 from the rod and 3.63 form the sphere for the ^{210}Pb decay chain.

4.10.2 ^{14}C on the inner surface of the sphere

Some evidence shows that all surfaces are covered by a carbonaceous contamination overlayer [76] 2 nm thick. The inner surface of the sphere being 1.13 m^2, the carbonaceous volume is about 4.5 $\times 10^{-3}$ cm^3. The density of carbonaceous compounds are of the order few g/cm^3 (2.93 g/cm^3 for Al_4C_2 and 3.16 g/cm^3 for SiC). Assuming half of the mass of the compound is made of carbon, the carbon quantity on the inner surface is roughly 7 $\times 10^{-3}$ g. Assuming this carbon to be in equilibrium with atmospheric ^{14}C production, its activity on the inner surface of the sphere is roughly 1.6 mBq (1.4×10^2nBq/cm^2). Figure 4.33 and 4.34 show a comparison of the data,

the simulation of ^{14}C on the inner surface of the detector and the sum of all other background simulations. Although this simulation suffers from a large uncertainty on the activity, we can conclude that the ^{14}C on the inner surface of the detector does not strongly contribute to the background of the volume events. However, this contamination could be a significant contribution to the surface background but giving the estimated contamination. The sum of ^{14}C and other contaminations seem to overestimate the total rate.

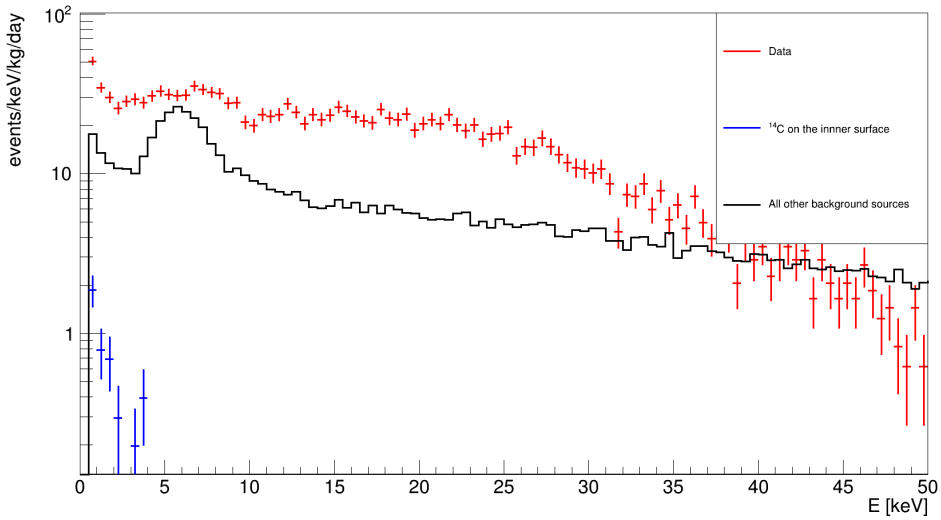

Figure 4.33: Comparison of ^{14}C simulation and data for volume events.

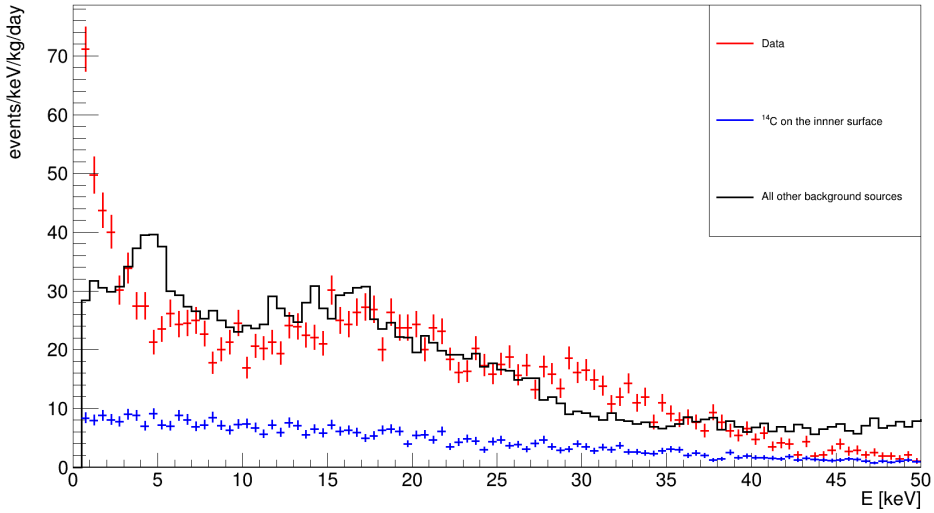

Figure 4.34: Comparison of ^{14}C simulation and data for surface events.

4.10.3 ^{3}H in the gas mixture

Exposure of neon to cosmic rays can result in the production of ^{3}H. The production rate was estimated to 228 ± 16 atoms / kg /day [77]. This activation is a problem for two reason. First the ^{3}H is a long-lived isotope with a half-life of 12.32 years. Second, ^{3}H decays by beta emission with a Q-value of 18.58 keV [78]. So, ^{3}H decay in the gas will produce events in the same region as dark matter signal: low energy events distributed in the volume. We do not know the history of the neon used for the WIMP search run. However, assuming the cylinder was exposed to cosmic ray for one year, given the production rate, the ^{3}H activity would be 0.14 ± 0.01mBq/kg. The ^{3}H in the sphere is then 0.04 ± 0.003mBq. Figure 4.35 shows a comparison of the simulation of ^{3}H decay within the gas volume and the data. We see that one year of exposure of the neon bottle is not enough to produce tritium in sufficient quantities to explain the observed background. However, this is true if you consider the neon

cylinder being free of tritium when it is produced, which is not necessary the case.

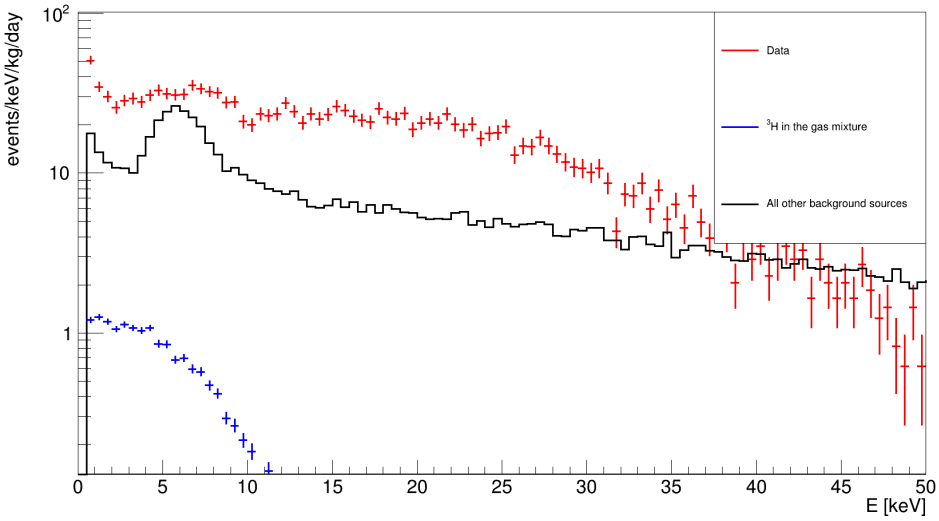

Figure 4.35: Comparison of ^{3}H simulation and data for volume events.

4.10.4 External gamma ray sources

The previous figures show that the event rate of the data (red) drops for energy deposition higher than 25 keV. The volume events being mostly induced by gamma rays, this pattern looks like a Compton edge induced by gamma ray of $\approx 120\,\text{keV}$. This hypothesis can be tested by simulating a point-like gamma source placed on the external surface of the sphere. Figure 4.36 shows the normalized spectrum of the volume events from data and point-like gamma ray source placed on the outer surface of the detector simulation.

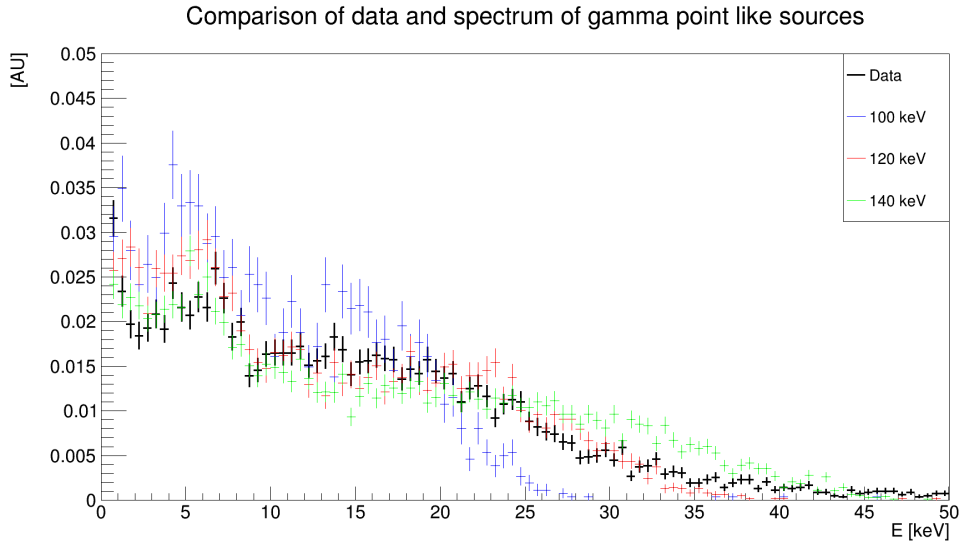

Figure 4.36: Volume event spectrum of simulated point like gamma ray sources with different energy.

An hypothesis for the missing 1.8 mHz of volume events is a 120 keV gamma source with an activity of 2.1 Bq. Figure 4.37 shows the effect of such a source on the background rate. The black curve shows the sum of all the other backgrounds, the blue crosses the background induced by the source and the orange curve shows the sum of both. Such a source allows for the reproduction of the rate at energies higher than 10 keV but strongly increases the emission of 8.1 keV fluorescence from the copper sphere. A 120 keV gamma ray source is a good candidate to explain the missing background but is not sufficient. We have not identified a source candidate for this radiation.

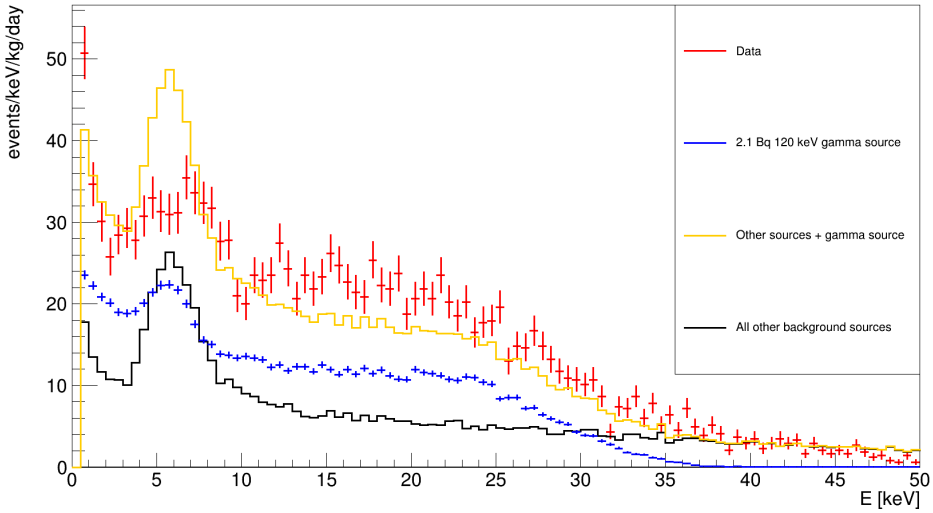

Figure 4.37: Spectrum of a 120 keV point like gamma source with an activity of 2.1 Bq

4.11 Discussion

The table 4.4 presents the main sources of background estimated for the SEDINE experiment.

This chapter presents a study of the background of the SEDINE detector. The main information is that the background is dominated by the presence of the ^{210}Pb decay chain on the surface and the bulk of the different material composing the detector and its shielding and particularly the contamination of the NOSV copper of the sphere. The analysis of this background run highlights several issues to be improved for the next-generation detector. The presence of an impurity in the gas causes electron attachment and degrades the signal. This effect can be estimated and parametrized but has to be reduced for the future experiment. The inhomogeneity of the electric field affects the signal; the use of a simple sensor limits the quality of the

	source	contamination / flux	Unit	Events rate [0.5;1] keV (events/keV/kg/day)	Events rate [1;5] keV (events/keV/kg/day)	Total rate (mHz)
Copper sphere	^{210}Pb	26	mBq/kg	1.03	2.0	0.13
	^{210}Bi	26	mBq/kg	2.6	2.1	0.11
	^{238}U	< 16	μBq/kg	0.036	0.042	0.0037
	^{232}Th	< 12	μBq/kg	0.053	0.045	0.0038
	^{40}K	< 110	μBq/kg	0.023	0.019	0.0013
	^{60}Co	41	μBq/kg	0.067	0.052	0.0051
	^{57}Co	23	μBq/kg	0.044	0.046	0.0026
Copper Shielding	^{210}Pbchain	26	mBq/kg	0.36	0.33	0.033
	^{238}U	< 16	μBq/kg	0.11	0.089	0.0096
	^{232}Th	< 12	μBq/kg	0.082	0.076	0.0088
	^{40}K	< 110	μBq/kg	0.038	0.035	0.0039
	^{60}Co	25	μBq/kg	0.16	0.12	0.016
Lead Shielding	^{210}Pb	37.4	Bq/kg	6.9	5.9	0.7
	^{238}U	79	μBq/kg	0.034	0.023	0.0028
	^{232}Th	9	μBq/kg	0.0047	0.0035	0.0008
	^{40}K	< 1.46	mBq/kg	0.0059	0.0048	0.0006
Gamma ray	1460 keV	0.125	$\gamma/cm^2/s$	0.53	0.47	0.059
	2614 keV	0.042	$\gamma/cm^2/s$	1.22	0.97	0.10
Inner Surface	^{210}Pb	1.8	mBq	3.42	0.77	0.039
	^{210}Bi	1.8	mBq	0.44	0.11	0.0040
	^{210}Po	1.8	mBq	0.22	0.014	0.0011
	^{214}Pb	0.2	mBq	0.074	0.003	0.0044
	^{214}Bi $+^{214}$ Po	0.2	mBq	0.05	0.02	0.0008
Total				17.5	13.2	1.2

Table 4.4: Summary of the main volume events background of SEDINE.

data. The development of better sensors inducing a homogeneous electric field and fast evacuation of positive ions is a crucial point for the future experiment. Finally, a better understanding of the background is essential. This can be achieved first with an accurate measurement of the activity of all the components of the detector and its shielding. Second, the main background is due to Compton interactions in the gas volume. It is planned for the next detector to take several other runs with different target gases with higher Z such as argon or xenon to increase sensitivity to gamma rays and improve the understanding of this background. The next chapter presents the estimation of the background of the NEWS-G detector at SNOLAB, and the last one presents the development of new sensors.

Chapter 5

NEWS-G at SNOLAB

5.1 Introduction

The next-generation SPC for dark matter searches is currently under construction. The aim is to extend the sensitivity of the detection method by using a bigger detector made of better material with a lower background level. In addition, new ways of calibration, gas purification and data analysis have been developed to ensure the best working condition and results extraction. This chapter presents the work done on the background optimization. Reducing the background involved several tasks. First, measuring the activity of the different contaminations. These measurements were done on several materials including copper and lead, and were done using different methods such as mass spectrometry and detection with high-purity germanium or alpha counters. Second, each background contribution was estimated by simulation using the software packages described in the previous chapter. This chapter will present the techniques used to reduce the main background contributions.

5.2 Detector description

Figure 5.1 shows the S140 detector and its shielding. The detector is a 1.4 m diameter shell made of C10100 commercially available copper. The thickness of the sphere is 10 mm and 0.5 mm of copper was plated on its inner surface. The sphere is enclosed in a 25 cm lead shell. The lead shielding is composed of two shells made of different types of lead. The main shell is made of commercially available lead. The high contamination of ^{210}Pb in such lead would create a tremendous amount of background. The detector is protected from this background source by a 3 cm thick shell of Roman lead with a much lower ^{210}Pb contamination. The lead shielding is enclosed in a 40 cm polyethylene shield to protect the detector from neutron radiation coming from the rock surrounding the cavern. A glove box is placed on top of the shielding. This box allows us to change the sensor without exposing the detector to the air in the laboratory. The copper sphere is not in contact with the lead shielding. To prevent background from the ^{222}Rn, the gap between the sphere and the shielding is filled with nitrogen.

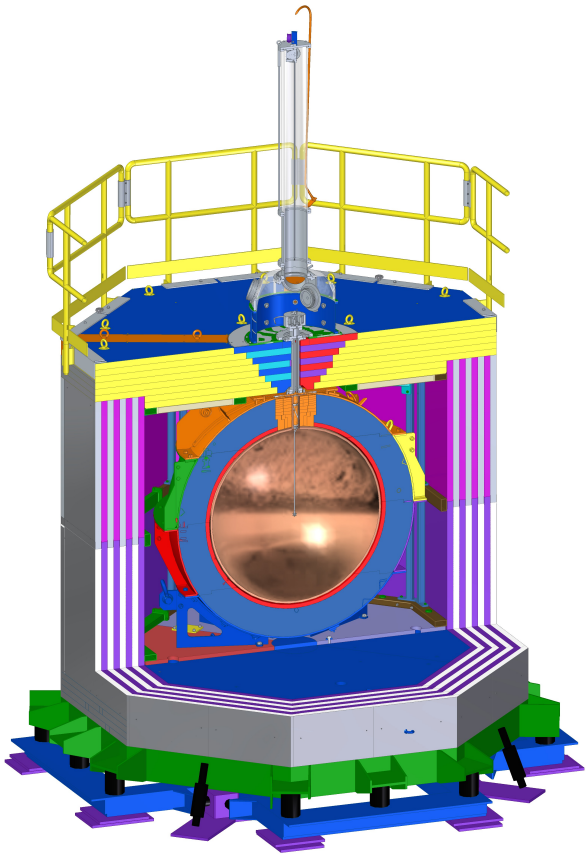

Figure 5.1: Schematic view of the S140 detector.

5.3 The gas mixture

5.3.1 ^{222}Rn decay chain in the gas mixture

The presence of ^{222}Rn within the gas mixture causes two problems. First the decay of ^{222}Rn and its daughters down to ^{210}Pb creates a background directly during the run being taken. Secondly the accumulation of ^{210}Pb with a long half-life of 22.3 years pollutes the detector for a long time. The decay of ^{222}Rn is not a problem by itself. The energy of the alpha emitted at 5.59 MeV is fully reconstructed and does not produce low energy events. After its decay, its daughter ^{218}Po is left charged and

drifts toward the inner surface of the sphere where it is plated. Then, its decay and daughters decay occur on the inner surface of the detector. Table 5.1 summarize the sub-keV background induced by ^{222}Rn daughters on the surface of the detector.

	events/keV/kg/day <1 keV / Bq of ^{222}Rn
^{214}Pb	323
^{214}Bi +^{214} Po	127
Total	450

Table 5.1: Background induced by ^{222}Rn daughters on the inner surface of the detector.

The total contributions of these contaminations bring 450 events/keV/kg/day below 1 keV per Bq of ^{222}Rn in the gas volume. To keep this contribution below 0.05 dru, the ^{222}Rn contamination of the gas mixture should not exceed 111 μBq.

5.3.2 ^{3}H decay chain in the gas mixture

During exposure to cosmic ray, ^{3}H is produced in neon cylinder. This activation is a problem for two reasons. First the ^{3}H is a long-lived isotope with a half-life of 12.32 years. Secondly, ^{3}H decays by beta emission with a Q-value of 18.58 keV [78]. The ^{3}H decay in the gas will populate the same region as the dark matter signal, low energy events distributed in gas volume.

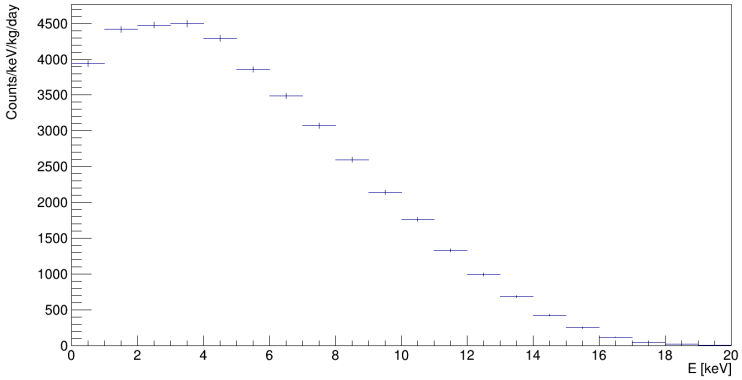

Figure 5.2: Simulation of tritium decay in 2 bars of neon + 10% CH_4 mixture, event rate expected for 1 Bq of ^{3}H in the gas volume.

Figure 5.2 shows the simulated spectrum of tritium decay within the gas volume. The event rate below 1 keV is 3940 dru / (Bq/kg). To keep this background contribution lower than 0.05 dru, the ^{3}H activity should not exceed 13 μBq/kg. With a production rate of 228 ± 16 atoms/kg/day of tritium in neon [77], and half-life of 12.32 years , this activity is reached after roughly 36 days of exposure of neon to cosmic rays at sea level.

5.4 The inner surface

5.4.1 ^{14}C

Assuming a similar contamination of a carbonaceous compound thick as in previous chapter with an activity of 1.4×10^2nBq/cm^2, the ^{14}C activity on inner surface of the detector would be roughly 8 mBq. Such contamination would bring an events rate of 7.7 dru for events with energy lower than 1 keV.

5.4.2 ^{210}Pb decay chain

^{210}Pb are deposited on surfaces exposed to air containing ^{222}Rn. With ^{210}Bi and with ^{210}Po in secular equilibrium with the ^{210}Pb, this decay chain would bring an event rate of 2 dru per mBq deposited on the surface for events with energy lower than 1 keV. Taking into account the volume, 1.3 m^3 of the sphere and the 123.3 Bq/m^3 of ^{222}Rn in the SNOLAB cavern [79], one hour of exposure of the volume of the sphere would bring a surface activity of 0.56 mBq, inducing an event rate of 1.12 dru for events with energy lower than 1 keV.

5.4.3 Surface cleaning and glove box

The two previous estimates show the importance of the cleaning of the inner surface of the detector. Although the ^{14}C and ^{210}Pb decay chain produce surface events that could be suppressed by a rise time cut, such backgrounds could strongly reduce the performances of the detector. Before its installation in its shielding, the inner surface of the sphere will be cleaned and passivated with a solution of hydrogen peroxide and sulphuric acid [80], protected under nitrogen atmosphere. The passivation will remove a few μm of copper from the surface bringing the contamination with solution. Once the passivation is done, the inner surface of the sphere should never be exposed to the air of the cavern to avoid any new deposition of ^{14}C or ^{210}Pb. A glove box will be installed on top the shielding to allow for changing the sensor without exposing the sphere to the air.

5.5 The copper sphere

5.5.1 Cosmogenic activation of the copper sphere

Time needed for material production, machining and transportation outside underground laboratories must be minimized to ensure the lowest background. The production rate R of an isotope by exposure to a flux ϕ of cosmic rays can be evaluated as:

$$R = N \int \sigma(E)\phi(E)dE \tag{5.1}$$

where σ is the production cross section and E is the energy of the incident particle, and N is the number of target nuclei. The production rate relies on two basic quantities: the flux of cosmic rays and the cross section for isotope production. The main hadronic component of cosmic rays is neutrons, so the production rate of isotope is then strongly related to the cosmic neutron flux. This flux has been estimated by several measurements of nucleon flux at sea level by Ziegler [81] and from several measurement of cosmic-ray-induced neutrons on the ground across the United States by Gordon et al. [82]. Figure 5.3 shows the differential neutron flux in New York city estimated from Ziegler and Gordon et al.'s parametrisation.

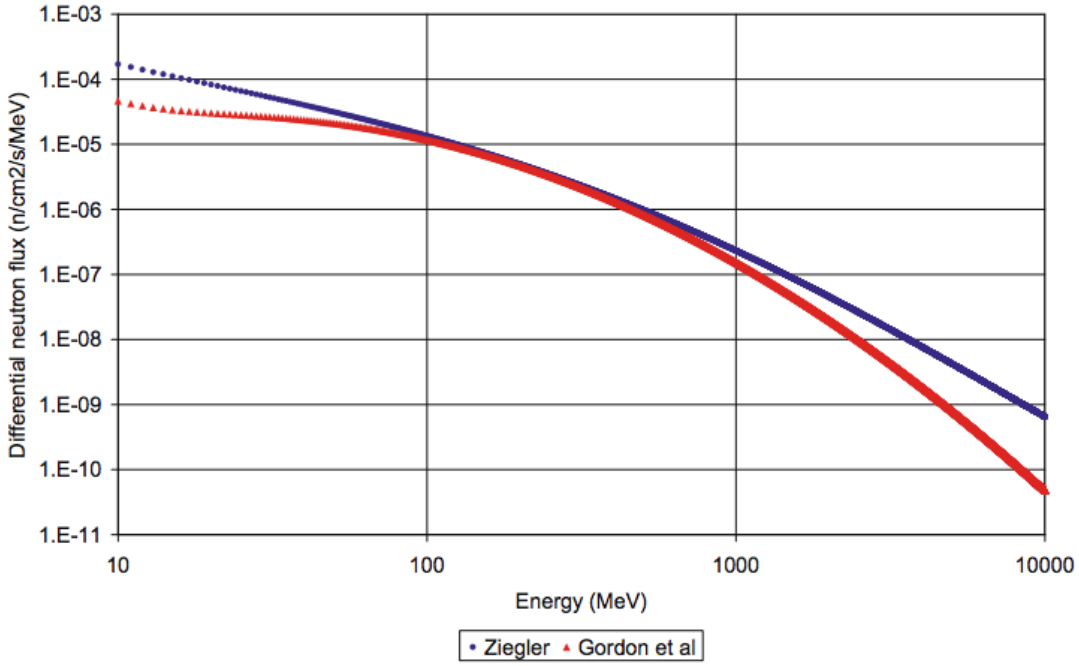

Figure 5.3: Differential neutron flux at sea level, [73]

The main radioactive isotopes produced in copper are ^{56}Co, ^{57}Co, ^{58}Co, ^{60}Co, ^{54}Mn, and ^{59}Fe. The excitation function for all these isotopes have been estimated with experimental data or by calculation. Experimental data was obtained using proton beams irradiating natural copper target from a few MeV to a few GeV and low energy ($\leq$ 100 MeV) neutron beams [73]. Calculated cross-sections are available from the MENDL libraries [83] and the semi-empirical Silberberg and Tsao formula using YIELDX code [84]. The figure 5.4 shows the excitation function of ^{60}Co in natural copper from different libraries.

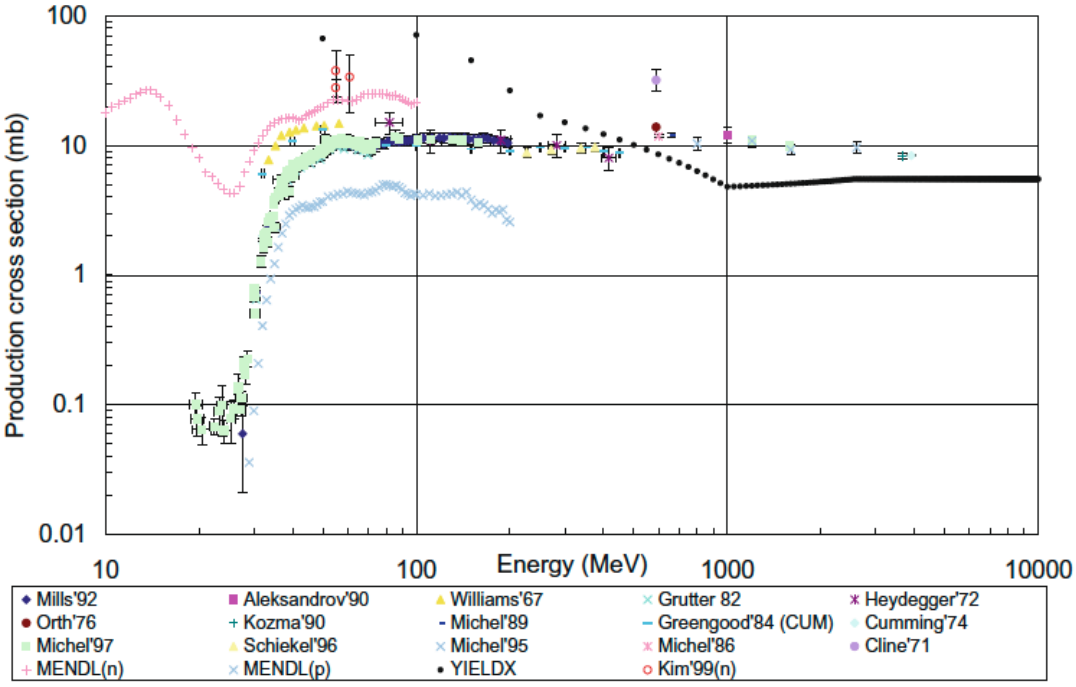

Figure 5.4: ^{60}Co excitation functions in natural copper [73].

The following table presents the half-lifes and production rates of isotopes in natural copper. The two different production rates are from the two neutron fluxes shown in Fig 5.3.

	Half life [days]	Production rate atoms/[days^{-1}]	
		Ziegler	Gordon et al
^{56}Co	77.2	22.9	20.0
^{57}Co	271.7	88.3	74.1
^{58}Co	70.9	159.6	123
^{60}Co	1898	97.4	55.4
^{54}Mn	312	32.5	27.7
^{59}Fe	44.6	6.5	4.9
^{46}Sc	83.79	3.8	2.7

Table 5.2: Half-life and production rate of isotopes in natural copper [73].

Due to their different half-lives, and production rates, the concentrations of these different isotopes will evolve differently. The following figures show the build-up activity with time and the evolution of the activity after 93 days of exposure to cosmic neutrons at sea level. These 93 days represents the estimated amount of time the copper will spend at sea level before being brought underground.

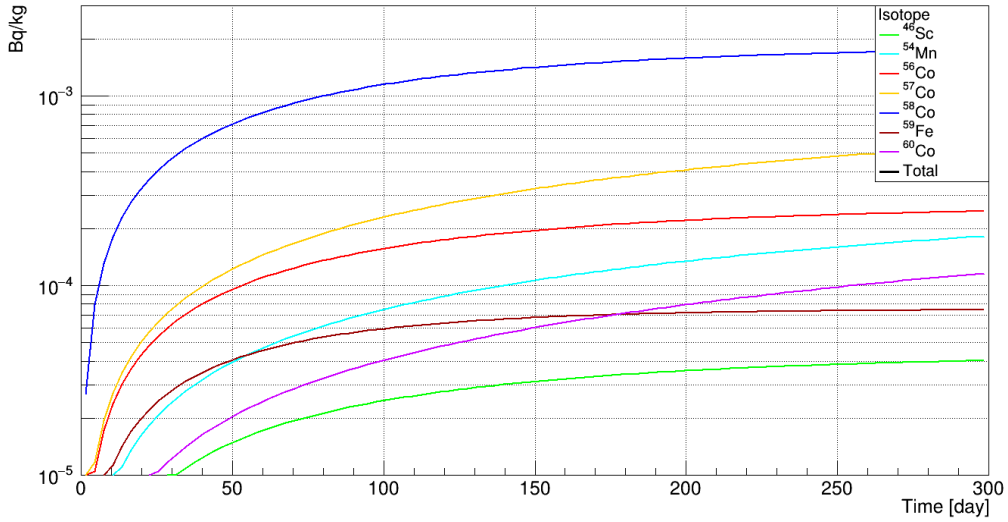

Figure 5.5: Activity of cosmogenically produced isotopes in natural copper.

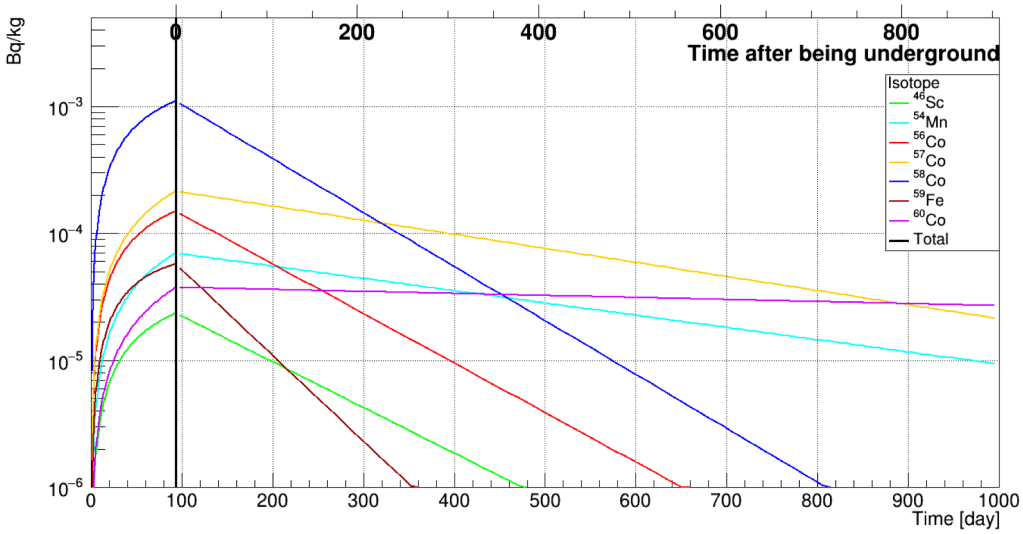

Figure 5.6: Activity of cosmogenically produced isotopes in natural copper after 3 months of exposure to cosmic ray at sea level.

The background induced by these seven isotopes was estimated by simulating decays of each isotope randomly distributed within the 10.5 mm of thickness of the

copper sphere. Knowing the half-life of the different isotopes, we can estimate the evolution of the background rate with time. Figure 5.7 shows the sub-keV background rate induced by each isotope and their sum. Starting around 3.5 events/kg/day for sub-keV events, the rate drops below 1 events/kg/day after approximately six months. Due to their short half-lives, the event rate is dominated by ^{56}Co and ^{58}Co. These two isotopes rapidly decay and after a long period of time, the background is dominated by the long-live isotope of ^{57}Co and ^{60}Co.

This section shows how much the exposure of material to the cosmic neutron flux is a critical aspect of the experiment. We choose to estimate the background after three months of exposure of the copper to cosmic neutron because it is approximately the time needed for welding of the two hemispheres, pressure certification, and transportation.

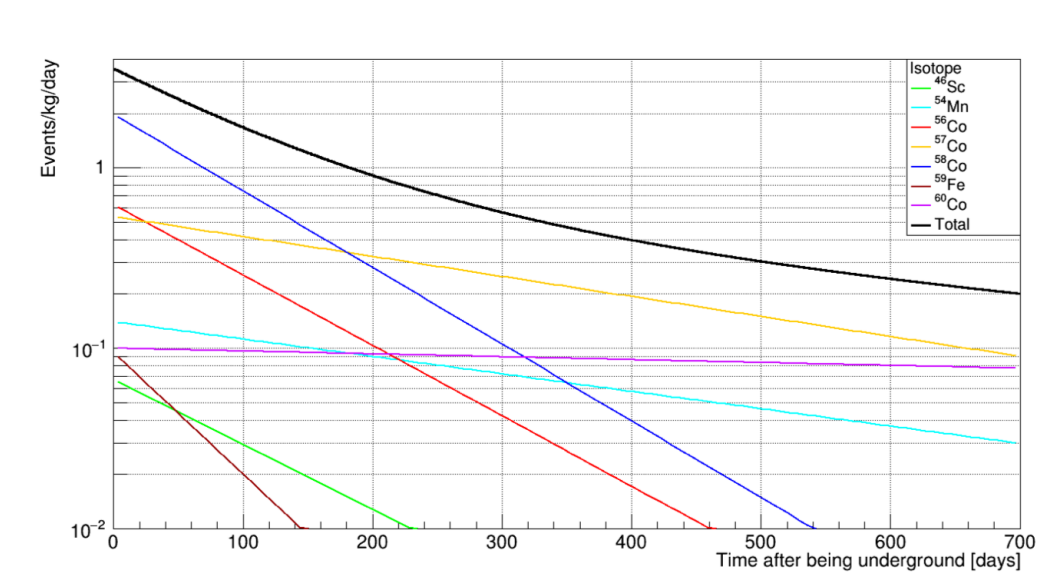

Figure 5.7: Sub-keV event rate of cosmogenic induced background in the copper sphere.

The neutron flux varies with altitude and is multiply by 1.8 at 795 m and 2.1

at 985 m [85]. The estimation of the isotope production and their backgrounds are underestimated. However, during its manufacturing, welding and machining the copper remained below an altitude of 200 m. So, this underestimation is much less than a factor 1.8.

5.5.2 ^{210}Pb decay chain, electro-plating

^{210}Pb is a long-lived isotope ($t_{1/2} = 22.2$ years) which is in the ^{238}U decay chain. Although the contamination of ^{238}U is expected in the range of few tens of μBq/kg the equilibrium is highly broken at the level of ^{210}Pb. The ^{210}Pb contamination in commercial copper has been estimated by the XMASS collaboration to be in the range of 17-40 mBq/kg using a low-background alpha particle counter [75]. A sample of the copper used to make the sphere was measured with this method and shows an activity of 28.5 ± 8.1 mBq/kg. ^{210}Pb decay is followed by de-excitation and decay of ^{210}Bi. All these processes can induce low energy events by emission of gamma rays, X-ray or Auger electrons. In particular, the β^- decay of ^{210}Bi produces a bremsstrahlung X-ray. Figure 5.8 shows the radial position of the decays within the copper thickness. As expected, due to their short range in copper the electron events originate within the few first hundred μm and gamma events are rapidly attenuated but can originate from the whole thickness of copper.

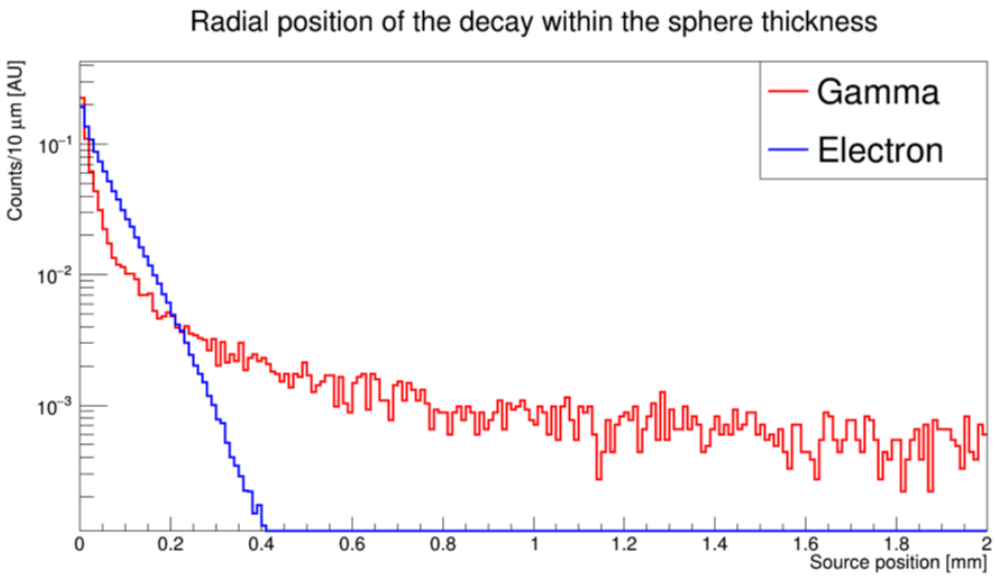

Figure 5.8: Position of the decays with the thickness of the copper sphere.

From the previous figure, we can deduce that most of the events are from decays within the innermost few hundred μm of the sphere. This background can be strongly reduced by plating pure copper on the inner surface of the detector. Figure 5.9 shows the effect of having a layer of pure copper. The event rate below 1 keV from gamma events distributed in the volume of the detector is reduced by respectively 62% and 70% with 500 μm and 1 mm of pure copper plated on the inner surface. Thus, we decided to electroplate 500 μm of pure copper on the two hemispheres before welding to form the sphere.

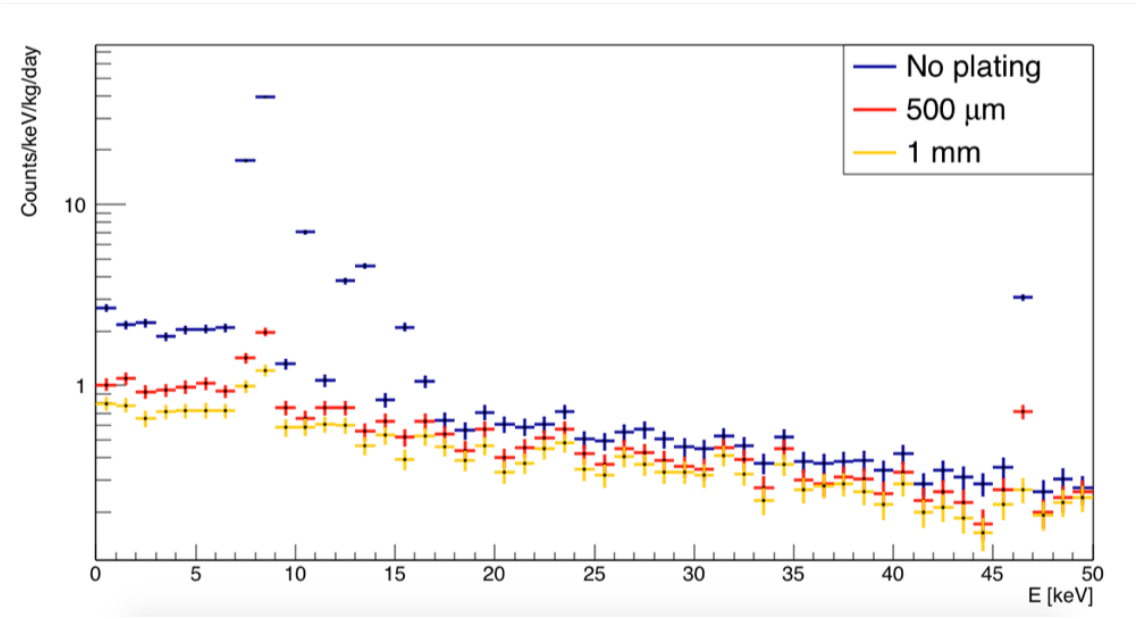

Figure 5.9: Effect of the electroplating pure copper on the inner surface of the detector.

The electroplating was performed at the Laboratoire souterrain de Modane in 2018. The process relies on oxidation and reduction reactions. The reaction is driven by an electric current. The current is passed from an inert anode through a liquid solution containing the metal so that the metal is deposited onto the cathode. For NEWS-G, the liquid solution is sulphuric acid (H_2SO_4) with copper from a mixture containing also $CuSO_4$. Under the electric current $CuSO_4$ splits to form Cu^{2+} and SO_4^{2-} that are respectively plated on the cathode and the anode. Figures 5.10 show a schematic and a picture of the setup used to do the electroplating. Copper has a high reduction potential of +0.34 V. All element with lower reduction potentials are left behind during the plating. Elements of interest in our case are Uranium, Thorium, and Lead with respectively reduction potentials of -1.64 V, -1.83 V and, -0.126 V are not plated [86] [87].

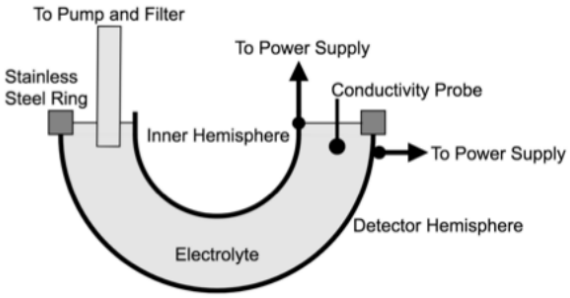

(a) Schematic of the plating process.

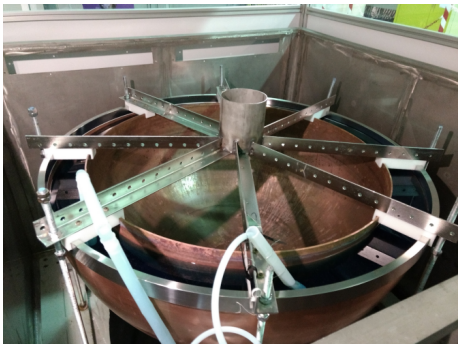

(b) Picture of the plating set-up.

Figure 5.10: Electroplating procedure

The mass of copper deposited onto the cathode is proportional to the charge delivered:

$$M = \frac{m_r \int I(t)dt}{zF} \tag{5.2}$$

where m_r is the molar mass of the element, $I(t)$ the current as a function of time, z the number of electrons transferred in reduction reaction (2 for Cu^{2+}) and F the Faraday constant.

After the process, the amount of pure copper plated on the inner surface was estimated to be $502.1 \pm 0.2\,\mu$m on the first hemisphere and $539.5 \pm 0.2\,\mu$m on the second. This amount of pure copper, in addition to a contamination of ^{210}Pb of 28.5 ± 8.1 mBq/kg will resulting an event rate of 1.04 ± 0.38 events/keV/kg/day below 1 keV, 1.01 ± 0.33 events/keV/kg/day between 1 and 5 keV.

5.5.3 ^{238}U and ^{232}Th decay chain

Uranium and thorium are present in the Earth's crust as a relic from its formation. Due to their long half-lives of 14.1 Gyr for ^{232}Th and 4.5 Gyr for ^{238}U, they are

currently present in rock even 4.5 Gyr after the formation of solar system. Both ^{232}Th and ^{238}U decay by α-emission and are the beginning of a long decay chains.

The half-lives of all daughter isotopes are much shorter than the Gyr range of ^{232}Th and ^{238}U, so the secular equilibrium of the chain is often assumed. We consider this for the ^{232}Th decay chain, both in the copper of the sphere and the lead around it. But, we do know that it is not true for ^{238}U. In both copper and lead, the equilibrium is broken at the level of the ^{210}Pb. So in this section, we will consider the whole decay chain of ^{232}Th and the decay chain of ^{238}U between ^{238}U and ^{210}Pb to be in equilibrium. The amount of ^{238}U and ^{232}Th in the copper was measured at the Pacific Northwest National Laboratory (PNNL) using an Inductively Coupled Plasma Mass Spectrometer (ICP-MS). Eleven samples of copper were cut from a test hemisphere with high-pressure water jet. The samples were cleaned to remove any oil or lubricant and etched in nitric acid to remove the exposed surface of copper, rinsed in de-mineralized water, and then were fully dissolved in nitric acid. Finally, the samples were analyzed on an Agilent 8800s ICP-MS and quantified using an isotope dilution mass spectrometric method. Table 5.3 summarize the activity of ^{232}Th and ^{238}U measured in eleven samples of copper.

		^{232}Th		^{238}U	
Sample ID	Cu dissolved [g]	μBq/kg	$\pm$	μBq/kg	$\pm$
News_Cu_1	2.0188	7.73	0.16	1.99	0.09
News_Cu_2	1.6628	27.5	0.3	5.60	0.18
News_Cu_3	2.2764	7.31	0.11	2.02	0.17
News_Cu_4	1.9258	12.8	0.1	2.70	0.11
News_Cu_5	2.9768	12.5	0.1	2.95	0.03
News_Cu_6	1.8886	7.08	0.05	1.85	0.09
News_Cu_7	4.5830	22.1	0.6	4.92	0.20
News_Cu_8	3.7314	10.0	0.1	2.30	0.11
News_Cu_9	5.8067	18.3	0.0	4.01	0.11
News_Cu_10	3.6778	13.3	0.2	3.57	0.10
News_Cu_11	3.6558	3.77	0.04	1.06	0.07
Mean		13	0.2	3	0.1

Table 5.3: Measure of ^{232}Th and ^{238}U activity in 11 copper samples.

The background rate of from these two contaminations was estimated by simulating the whole ^{232}Th decay chain and ^{238}U decay until ^{210}Pb. Decays were randomly distributed within the copper sphere with the innermost 500 μm layer free of any decays. These two simulations show for ^{232}Th, 0.075 ± 0.001 events/keV/kg/day below 1 keV and 0.069 ± 0.001 events/keV/kg/day between 1 and 5. For ^{238}U, 0.012 ± 0.0004 events/keV/kg/day below 1 keV, 0.011 ± 0.0004 events/keV/kg/day between 1 and 5 keV.

5.5.4 ^{40}K

The ^{40}K activity in the copper sphere was not estimated by our collaboration. However, C10100 copper is a commercial component used by several experiments. The NEXT-100 experiment, a double beta decay investigated the radiopurity of C10100 copper and found a contamination of 61 and 91 μBq/kg. A contamination of 91 μBq/kg gives an event rate of 0.0145 events/keV/kg/day below 1 keV, 0.0145 events/keV/kg/day between 1 and 5 keV.

5.6 The lead shield

The purpose of the lead shield is to protect the detector from backgrounds induced by gamma ray in the cavern around the experiment. This background will be discussed in the next section. The choice of lead as a shield material is because of its high Z value (82) making it particularly efficient for stopping gammas. Its own intrinsic radioactivity is a particular concern. Due to the presence of ^{238}U and its decay chain product in lead ores, the ^{210}Pb concentration is higher than 1 Bq/kg [88]. While refining raw lead metal, a ^{210}Pb concentration process is encountered. In fact, while other radioactive nuclides which are not chemically affine to lead are segregated from the slag, ^{210}Pb is concentrated. A large amount of ^{210}Pb such as 24 Bq/kg [89] would have a catastrophic impact on the background level of the experiment due to the bremsstrahlung radiation and X-rays from ^{210}Bi. The solution to this problem is to build the lead shield in two different shells; a first shell, 3 cm thick of Roman lead and a second shell 22 cm thick made of modern lead. The Roman lead is lead found in the sea, in a boat that sank roughly two thousands years ago. This time corresponds to hundreds of half-live of the ^{210}Pb and decreases its activity by a factor

2^{100}. The material is essentially free of ^{210}Pb. This section will be divided in two sections focusing first on the shell of Roman lead and second on the shell of modern lead.

5.6.1 The Roman lead shell

^{238}U and ^{232}Th decay chain

Similarly to the copper of the sphere, we measured the ^{238}U and ^{232}Th of the archaeological lead with ICP-MS at PNNL. Table 5.5 summarizes the activity measured in three samples of archaeological lead.

	^{232}Th		^{238}U	
Sample ID	μBq/kg	$\pm$	μBq/kg	$\pm$
News_rep1	13.6	0.3	66.7	8.4
News_rep2	5.2	1.7	29.1	6.0
News_rep3	8.4	1.2	37.9	8.6
Mean	9.1	1.8	44.5	7.7

Table 5.4: ^{232}Th and ^{238}U activity in 3 Roman lead samples.

In the same manner as for the copper sphere, the background rate from these two contaminations was estimated by simulating the whole of the ^{232}Th and ^{238}U chains until ^{210}Pb, with decays randomly distributed in a 3 cm shell of lead surrounding the detector. These two simulations show for ^{232}Th, 0.025 ± 0.005 events/keV/kg/day below 1 keV, and 0.0161 ± 0.003 events/keV/kg/day between 1 and 5 and for ^{238}U, 0.14 ± 0.02 events/keV/kg/day below 1 keV and 0.09 ± 0.02 events/keV/kg/day between 1 and 5 keV.

^{210}Pb chain

The archaeological lead is free of ^{210}Pb from decay products of ^{238}U chain originally present in the lead ore. However, the EDELWEISS collaboration which use the same Roman lead as us measured its ^{210}Pb activity and set an upper limit of 120 mBq/kg [89]. This result being an upper limit, it does not disagree with the assumption of a ^{210}Pb free lead. However, before being melted to form the shell for NEWS-G, the lead bricks were stored for several years at the LSM. LSM air contains ^{222}Rn, so deposition of ^{210}Pb occurs on the surface of the bricks. Although we cleaned the surfaces of the bricks before melting them, a contamination of a few tens of mBq/kg is possible. Simulation of ^{210}Pb randomly distributed in the lead volume is time consuming, getting a significant sample of events this way is infeasible. The solution is to first simulate decays of ^{210}Pb and look at the particles which cross the inner surface of the shield. Then we simulate this particle flux on the copper sphere. Figure 5.11 shows the spectrum of gamma rays and electrons crossing the inner surface of the Roman lead.

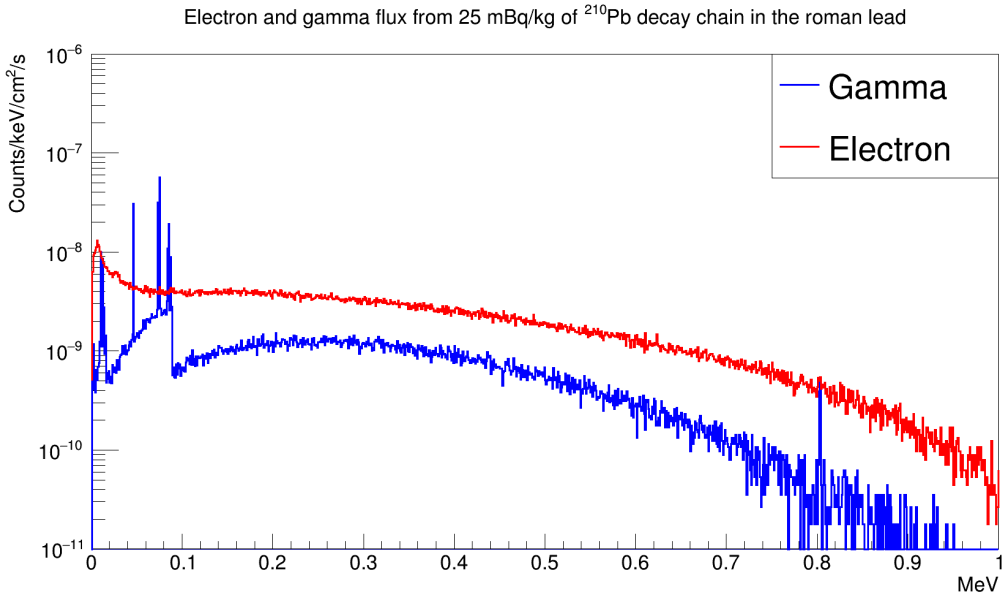

Figure 5.11: Spectrum of gamma rays and electrons crossing the inner surface of the Roman lead assuming 25 mBq/kg of ^{210}Pb.

Figure 5.12 shows the event rate estimated from the simulation of ^{210}Pb and its daughter distributed in the shell of lead (blue), electron (orange), and gammas ray (red), from the spectrum showed in Fig 5.11. We can first remark that although the electron flux from the lead is much higher than the gamma ray one, the contribution of those electrons to the detector background is negligible. The two methods show a good agreement. Finally, the expected background rate, with an upper limit on the contamination at 25 mBq/kg is 0.14 events/keV/kg/day below 1 keV and 0.12 events/keV/kg/day between 1 and 5 keV.

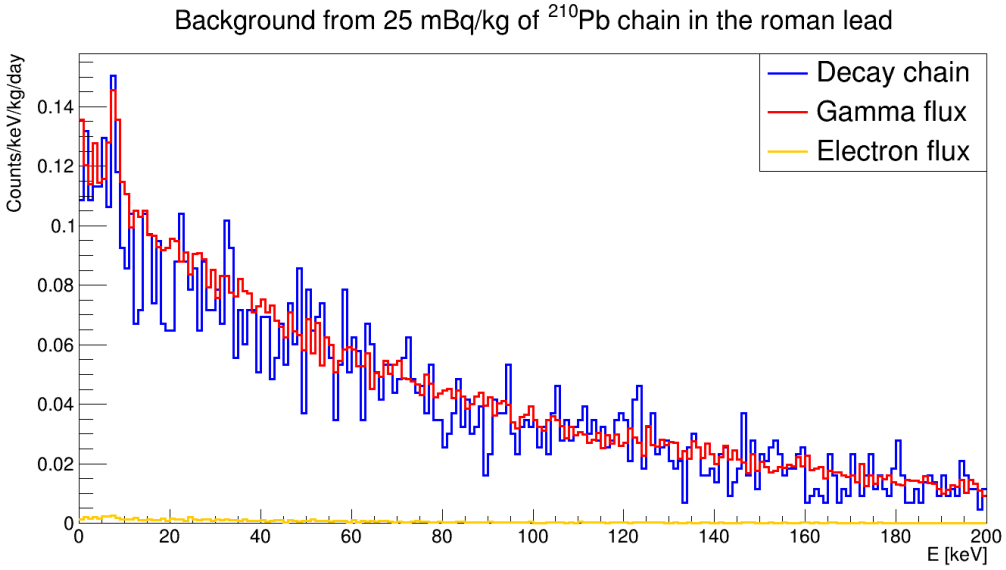

Figure 5.12: Comparison of the direct simulation of the ^{210}Pb decay chain in the Roman lead shell and simulation of gamma ray and electron flux crossing it's surface.

^{40}K

As for the copper sphere, we did not measure the amount of ^{40}K in the Roman lead. However, its activity was investigated by the EDELWEISS collaboration which set an upper limit of 1.3 mBq/kg [90]. From this we set an upper limit on the background induced by the ^{40}K in the Roman lead to 0.28 events/keV/kg/day below 1 keV and 0.23 events/keV/kg/day between 1 and 5 keV.

5.6.2 The modern lead shell

^{238}U and ^{232}Th decay chain

The amount of ^{238}U and ^{232}Th in the modern lead were measured with the same method as for the Roman lead, the results are shown in the following table.

	^{232}Th		^{238}U	
Sample ID	μBq/kg	$\pm$	μBq/kg	$\pm$
CNRS_rep1	2.9	0.5	177	20
CNRS_rep2	< 1.6		35	12
CNRS_rep3	22.6	3	24	10
Mean	9	2	79	14

Table 5.5: Measure of ^{232}Th and ^{238}U activity in 3 modern lead samples.

The simulation of the ^{232}Th decay chain shows 0.025 ± 0.005 events/keV/kg/day below 1 keV and 0.020 ± 0.04 and events/keV/kg/day between 1 and 5 keV. And the simulation of the ^{238}U chain until ^{210}Pb shows 0.17 ± 0.03 events/keV/kg/day below 1 keV and 0.13 ± 0.02 events/keV/kg/day between 1 and 5 keV.

^{210}Pb chain

The ^{210}Pb activity in the modern shield was measured at the LSM using a germanium counter. The data shows an activity of 4.6 ± 0.02 Bq/kg. Similarity to ^{210}Pb in the Roman lead, a simulation giving good enough statistic would take too much time. Instead we first simulate decays of ^{210}Pb and its daughters randomly distributed within the 22 cm shell of modern lead and record the flux of gamma ray reaching the surface of the Roman lead. The recorded flux is then propagated through the Roman lead, and the flux of gamma rays crossing its inner surface is recorded, to be propagated toward the copper sphere. Figure 5.13 shows the gamma ray flux reaching the outer surface and crossing the inner surface of the Roman lead shell.

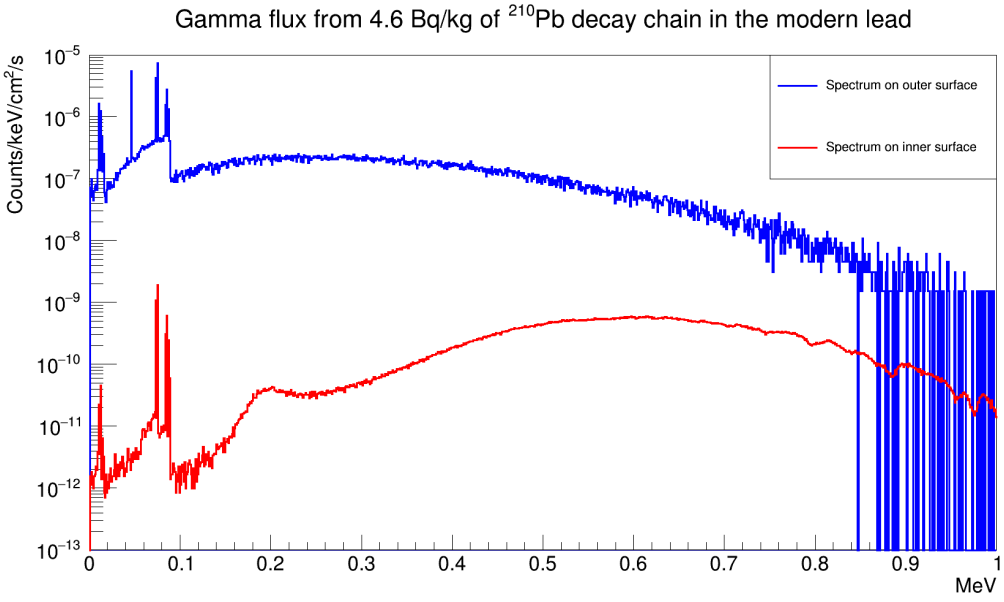

Figure 5.13: Gamma spectrum from the ^{210}Pb dacay chain in modern lead on the outer and inner surface the Roman lead shield.

The simulation of the flux from the inner surface of the Roman lead shell shows an event rate of 0.053 ± 0.0002 events/keV/kg/day below 1 keV and 0.055 ± 0.0002 events/keV/kg/day between 1 and 5 keV.

^{40}K

As for the copper sphere and the Roman lead, we did not measure the amount of ^{40}K in the modern lead. However, its activity was investigated by the XENON100 collaboration which set an upper limit of 1.46 mBq/kg [91]. This amount allows us to set an upper limit on the background induced by the ^{40}K in the Roman lead of 0.35 events/keV/kg/day below 1 keV and 0.26 events/keV/kg/day between 1 and 5 keV.

5.7 The cavern environment

The previous sections presented an estimation of the background induced by the material of the detector itself and shield surrounding it. The different layers of shield aim to protect the detector from the radiation present in the environment around it. Two kinds of radiation are coming from the rock of the Creighton mine: gamma rays and neutrons. Both these particles are produced by the decay of isotopes from the ^{238}U, ^{235}U, and ^{232}Th chains and from ^{40}K composing the rock. The neutron and gamma ray flux within the cavern and their impact on the background budget will be discussed in the first two sections. In addition to radiation from the rock, ^{222}Rn from the ^{238}U decay chain is gaseous and can escape the rock to fill the air of the cavern.

5.7.1 Gamma rays

The gamma ray flux within the cavern can be estimated from the activity of ^{238}U, ^{232}Th, and ^{40}K in the Norite rock surrounding SNOLAB. The rock contains 1.2% potassium, 1.3 ppm of ^{238}U and 3.3 ppm of ^{232}Th [79]. These concentrations represent 0.04 Bq/kg of ^{40}K, 13 Bq/kg of ^{238}U and 15 Bq/kg of ^{232}Th. The gamma flux within the cavern can be estimated by a simulation of these elements within a shell of concrete 10 m thick with a 20 m inner radius, and by looking at gamma rays crossing the surface of a 3 m radius sphere placed at the center of the cavity. Figure 5.14 and 5.15 represent the spectrum of gamma rays crossing the 3 m sphere and their zenith angle. In that case, the zenith angle is the angle between the direction of the momentum of the gamma when it crossed the surface and the vector normal to the sphere surface at the point where the gamma ray cross the surface.

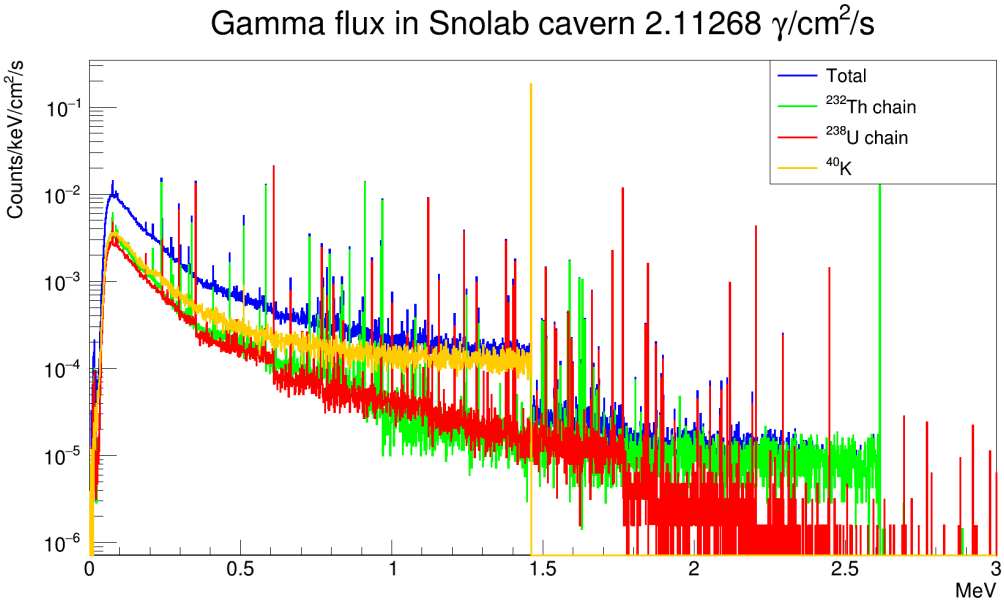

Figure 5.14: Gamma flux in the SNOLAB cavern.

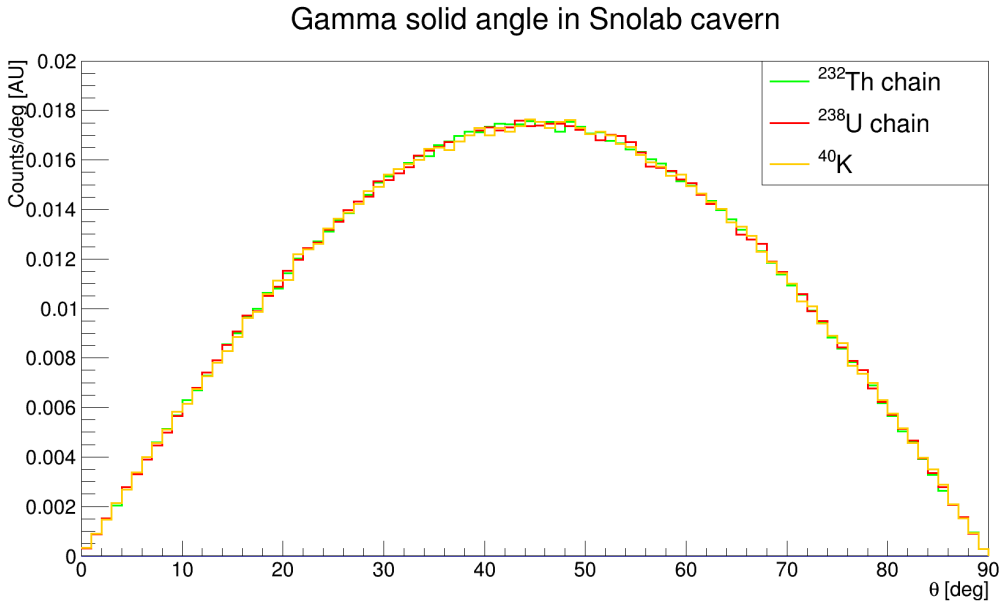

Figure 5.15: Zenith angle of momentum of gamma ray entering the volume of interest.

Due to the high interaction rate of gamma rays with lead, simulating directly this

gamma flux through the whole geometry and looking at the recorded events would take too much time. The solution is to first simulate the gamma flux trough the shield and record what crosses it and then simulate the attenuated spectrum onto the copper sphere. Figure 5.16 shows the effect of the shield surrounding the detector. The black curve represents the gamma flux in the cavern and the green curve shows the flux attenuated by the polyethylene and the iron shell, reaching the surface of the lead shield. This flux is propagated through 5 layers of lead, 5 cm each. The last spectrum, the dark blue one is the final one to be propagated on the copper sphere.

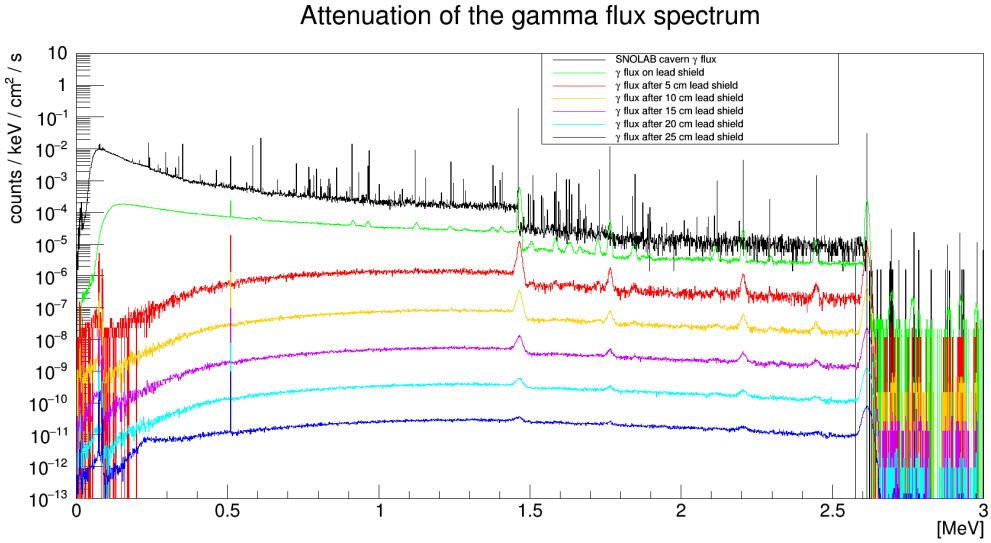

Figure 5.16: Attenuation of gamma flux through the shield.

The final simulation shows a sub-keV event rate of 0.0084 events/keV/kg/day and 0.0095 events/keV/kg/day between 1 and 5 keV.

5.7.2 Neutrons

Neutrons can be a source of background in two different ways. First, the elastic scattering of fast neutrons with target nuclei of the gas mixture can mimic WIMP

signals. Second, the interaction of neutrons (thermal and fast) with the materials of detector and the shield surrounding it can produce gamma rays which induce similar backgrounds to those listed in the previous sections. The main source of neutrons is the radioactivity of the cavern rock where neutrons are produced by (α, n) reaction and spontaneous fission. The flux of thermal neutron was estimated to be $4144.9 \pm 49.8 \pm 105.3\,\mathrm{neutrons/m^2/day}$ [92] and the fast neutron flux to be $4000\,\mathrm{neutrons/m^2/day}$ [79]. Similarly to the gamma ray spectrum, it takes too much CPU time to simulate the neutron spectrum through the whole shield surrounding the detector. The neutron spectrum is first propagated through the polyethylene shield and the attenuated flux is propagated on the lead shield.

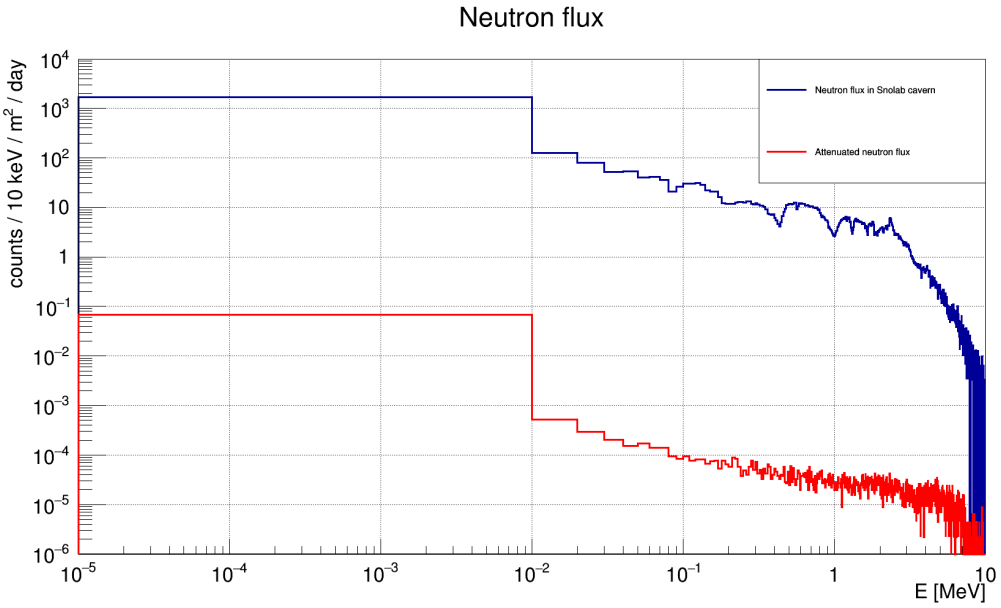

Figure 5.17: Blue, SNOLAB cavern neutron spectrum [93]. Red, spectrum reaching the lead shield surface.

The attenuated neutron flux is then propagated through the lead shield and the elastic scatterings are recorded. The gas mixture being made of neon and methane,

we need first to determine the quenching factor for the three elements Ne, C and H. Figure 5.18 shows the quenching factor of the H, C and Ne nuclei in the considered gas mixture determined with the SRIM software package [94].

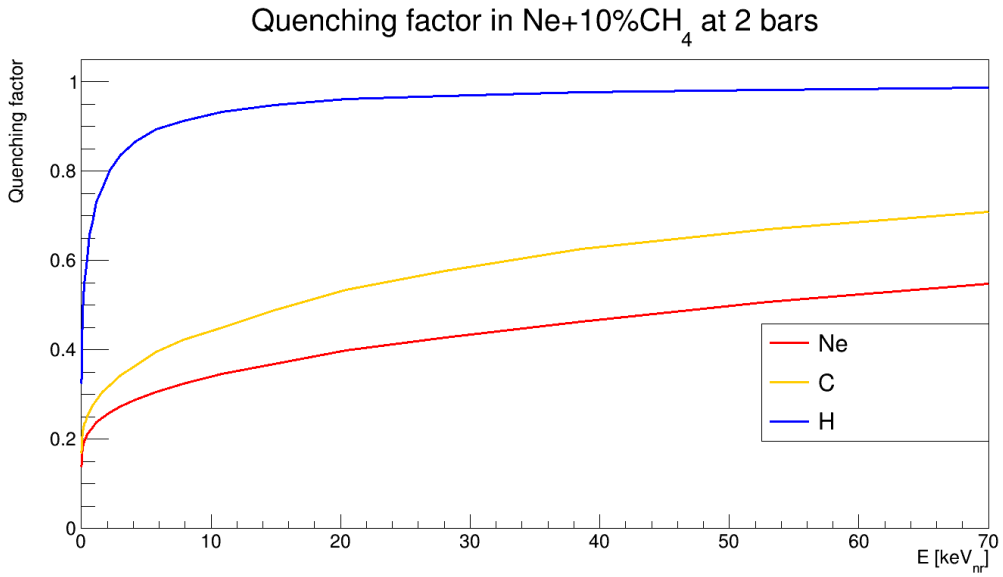

Figure 5.18: Quenching factor of Ne, C and H in a gas mixture made of Ne + 10 % CH_4 at 2 bars.

Figure 5.19 shows the expected event rate from the attenuated neutron flux from the SNOLAB cavern before (blue) and after (red) applying the quenching factor determined with SRIM. The expected event rate below one keV is 0.0043 events/keV/kg/day and 0.0004 events/keV/kg/day between 1 and 5 keV.

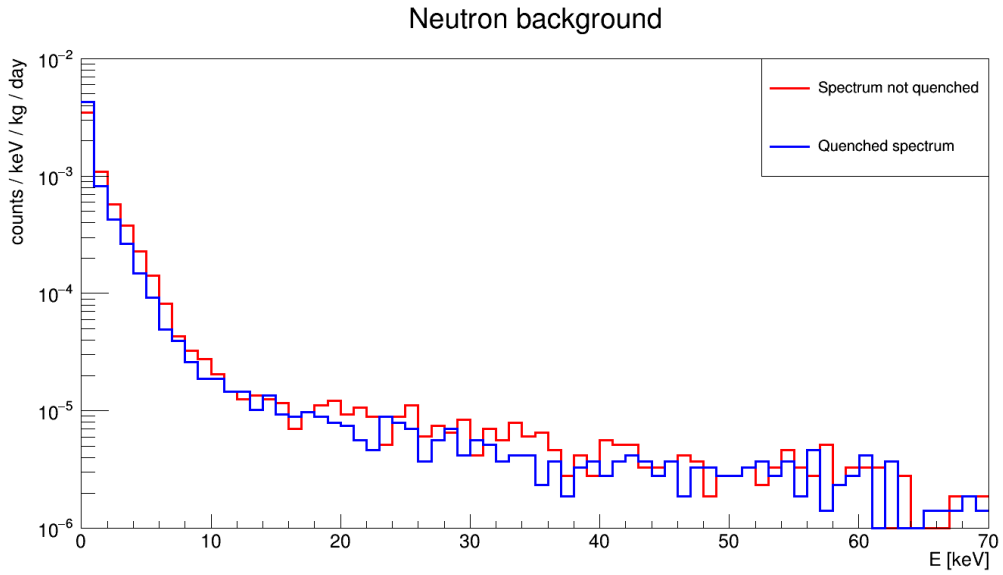

Figure 5.19: Neutron background with and without quenching factor applied.

5.7.3 ^{222}Rn

The ^{222}Rn in the cavern environment is a problem for two reasons. First the decay of short lived elements in its chain, (before ^{210}Pb) induces background events. Second, the deposition of long-lived ^{210}Pb on surfaces will be a long term source of backgrounds.

Decay between the copper sphere and the lead shell

The copper sphere is separated from the lead shell by a gap of 12 mm, corresponding to a volume of 0.072 m^3. The impact of the decay of ^{222}Rn followed by its daughters until ^{210}Pb was estimated by simulating one million decays of these isotopes randomly distributed in the gap. The ^{222}Rn concentration in the SNOLAB cavern is 123.3 ± 13.0Bq/m^3. The results of the simulation show the catastrophic impact of the ^{222}Rn: 30 ± 3 events/keV/kg/day of sub-keV events. To mitigate this, we inject

nitrogen in the space between the copper sphere and the lead shell. Typical activity of ^{222}Rn in nitrogen cylinder lies between 1 and 50 μBq/m^3 [95]. This amount is eight orders of magnitudes lower than the activity in SNOLAB air and makes this background negligible compared to all others.

^{210}Pb deposition on the outer surface

We need to estimate the background induced by the deposition of ^{210}Pb on the outer surface of the copper sphere and deduce a maximum allowed exposure time to the air of the SNOLAB cavern. This estimation was done by simulating ^{210}Pb and its daughters randomly distributed on the 59×10^3 cm^2 of the outer surface of the copper sphere. The simulations shows and sub-keV event rate of
1.5×10^{-6}(events/keV/kg/day)/(nBq/cm^2). We can estimate the amount of ^{210}Pb deposited on the outer surface of the copper sphere assuming that all ^{222}Rn decays in a shell 40 cm thick around the sphere will deposit their daughters on its surface. Taking into account the ^{222}Rn activity in the SNOLAB cavern, one day of exposure would bring a surface activity of 710 ± 75 nBq/cm^2, inducing an sub-keV event rate of 0.0011 ± 0.0001 events/keV/kg/day. Assuming the outer surface of the sphere will be cleaned upon its arrival at SNOLAB, the few days needed for its transportation in the cube hall and its installation in its shield before being covered by nitrogen will cause a negligible amount of background compared to others sources.

5.7.4 Cosmic rays muons

The muon flux in SNOLAB, attenuated by 6.011 km.w.e (kilometre equivalent water) is $0.27\mu/\mathrm{m}^2/\mathrm{day}$ [79] A parametrization of the energy distribution is defined by [96]:

$$\frac{dN}{dE_\mu} = Ae^{-bh(\gamma_\mu - 1)} \cdot \left(E_\mu + \epsilon_\mu \left(1 - e^{-bh}\right)\right)^{-\gamma_\mu} \tag{5.3}$$

Where $b = 0.4/\mathrm{km.w.e}$, γ_μ= 3.77 and ϵ_μ= 693 GeV, and h is the depth of the laboratory 6.011 ± 0.1 km.w.e.

The angular distribution is parametrized by:

$$I_{th}(h, \theta) = \left(I_1 e^{-h \cdot \sec(\theta)/\lambda_1} + I_2 e^{-h \cdot \sec(\theta)/\lambda_2}\right) \sec(\theta) \tag{5.4}$$

where I_1=$(8.60 \pm 0.53) \times 10^{-6}\mathrm{s}^{-1}\mathrm{cm}^{-2}\mathrm{sr}^{-1}$,

I_2=$(0.44 \pm 0.06) \times 10^{-6}\mathrm{s}^{-1}\mathrm{cm}^{-2}\mathrm{sr}^{-1}$,

λ_1=0.45 ± 0.01km.w.e and λ_2=0.87 ± 0.02 km.w.e.

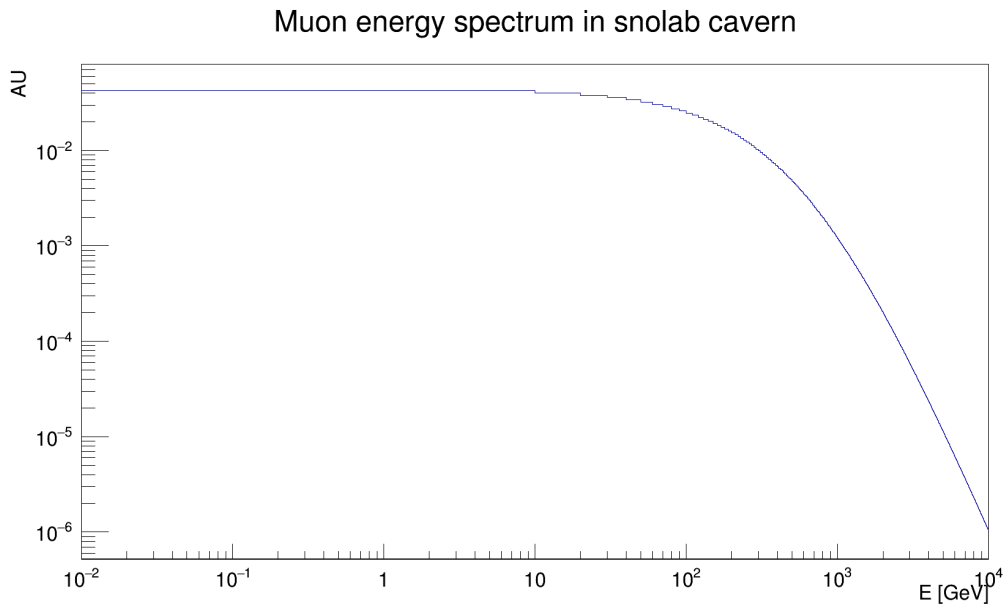

Figure 5.20: Muon energy spectrum in SNOLAB cavern

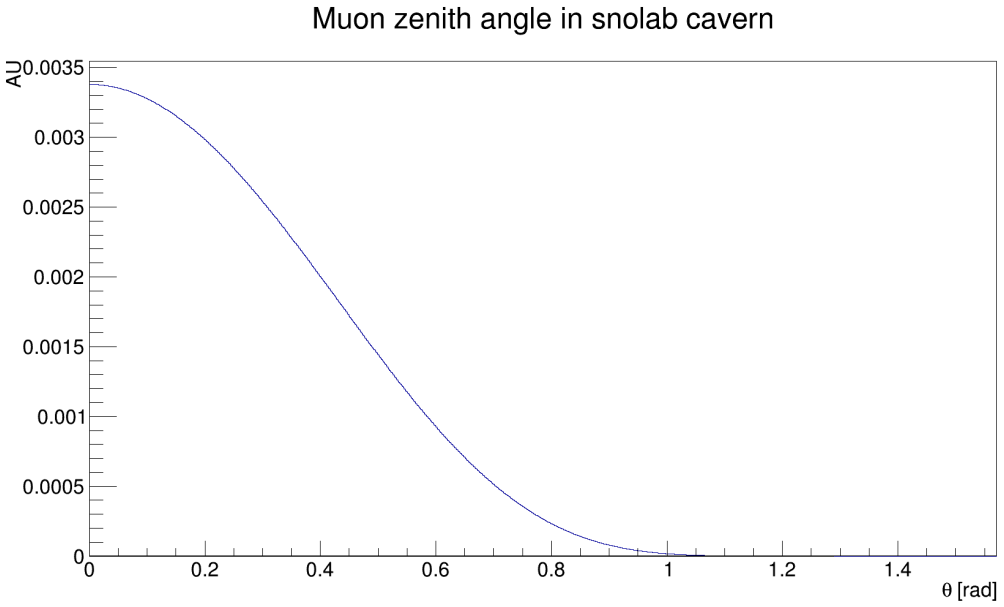

Figure 5.21: Muon zenith angle distribution in SNOLAB cavern

Figure 5.20 and 5.21 show the energy spectrum and zenith angle distribution of

cosmic muon in the SNOLAB cavern respectively. The simulation of all possible processes occurring during muon interactions is time-consuming. So first we ran a simulation of muons on a 4m × 4m square placed 2 metres above the sphere center. The recorded event rate is shown in figure 5.22.

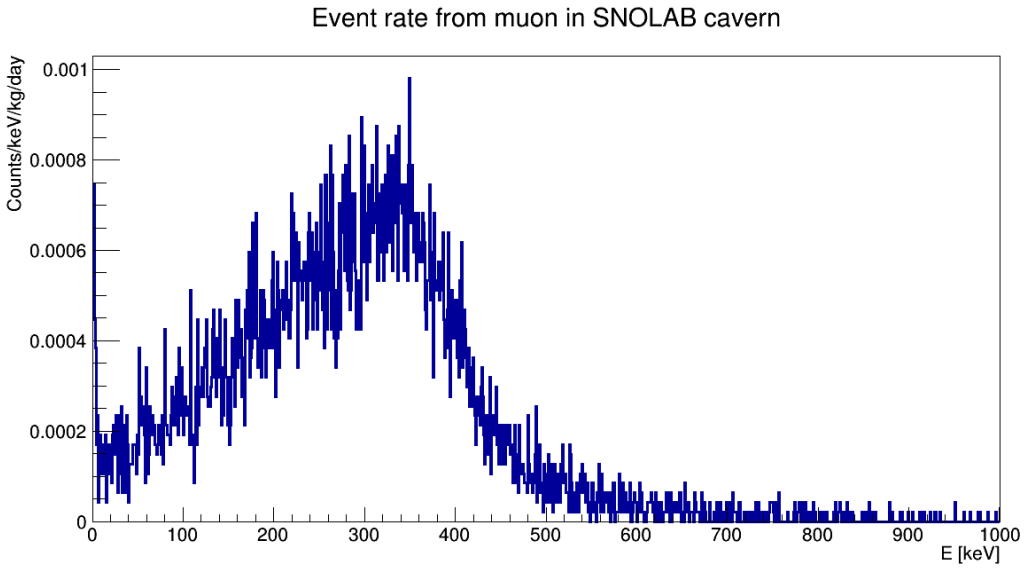

Figure 5.22: Muon event rate.

Although the number of recorded events is low, leading to a large uncertainty, the expected events rate is negligible compare to all other. We can expect $6.2 \pm 1.1 \times 10^{-4}$ events/keV/kg/day below 1 keV and $4.4 \pm 4.2 \times 10^{-4}$ events/keV/kg/day between 1 and 5 keV.

5.8 Conclusion

The table 5.6 summarize, the main backgrounds of NEWS-G at SNOLAB. The selection of low activity material in addition to the shielding surrounding the detector will reduce its background by at least one order of magnitude compared to the one

	Source	Contamination / flux	Unit	Events rate <1 keV [dru]	Events rate in [1;5] keV [dru]	Total rate [mHz]
Gas mixture	^{3}H	13	μBq/kg	0.05	0.06	0.005
	^{222}Rn	111	μBq/kg	0.05	0.04	0.2
Copper sphere 500 μm electrolyte	^{210}Pb	28.5	mBq/kg	1.04	1.01	0.86
	^{238}U	3	μBq/kg	0.0117	0.115	0.028
	^{232}Th	13	μBq/kg	0.0754	0.0692	0.163
	^{40}K	0.1	mBq/kg	0.0157	0.0186	0.0622
Roman lead	^{210}Pb	<25	mBq/kg	<0.14	<0.12	0.057
	^{238}U	44.5	μBq/kg	0.142	0.094	0.277
	^{232}Th	9.1	μBq/kg	0.0256	0.0161	0.0577
	^{40}K	<1.3	mBq/kg	<0.28	0.23	0.65
Low activity lead	^{210}Pb	4.6	Bq/kg	0.053	0.055	0.17
	^{238}U	79	μBq/kg	0.17	0.132	0.5
	^{232}Th	9	μBq/kg	0.0251	0.0201	0.075
	^{40}K	<1.46	mBq/kg	<0.35	0.26	0.67
Cavern	Gamma	4.87×10^{-8}	γ/cm^2/s	0.0084	0.0095	0.00464
	Neutron	4000	neutron/m^2/day	0.0044	0.0004	3.54×10^{-11}
	Muon	0.27	muon/m^2/day	0.00062	0.00044	5.04×10^{-8}
Total				1.67	1.54	2.4
Total + cosmogenic activation of the copper sphere				5.20	5.20	5.4
Total + cosmogenic activation of the copper sphere and 6 months of cooling				2.8	2.5	3.4
Total + cosmogenic activation of the copper sphere and 1 years of cooling				2.1	1.9	3.0
Total + cosmogenic activation of the copper sphere and 2 years of cooling				1.9	1.7	2.9

Table 5.6: Summary of the main background of NEWS-G at SNOLAB, without rise time selection. The upper limits of activities in the lead are not taking into account in the total.

observed with SEDINE. Figure 5.23 presents the sensitivity projection of NEWS-G at SNOLAB with the studied gas mixture. It was calculated with a model developed by D Durnford at Queen's University [62].The major question remains the rise of background observed with SEDINE at energy lower than 500 eV. Geant4 does not reproduce this background and if it appears, its understanding and reduction will be an intensive challenge for the future of the experiment. If the sub-keV background is at a level of 1.78 dru, NEWS-SNO will improve the sensitivity to WIMP-nucleon cross section for WIMP mass of 1 GeV/c^2 by more than two orders of magnitude and explore lower masses.

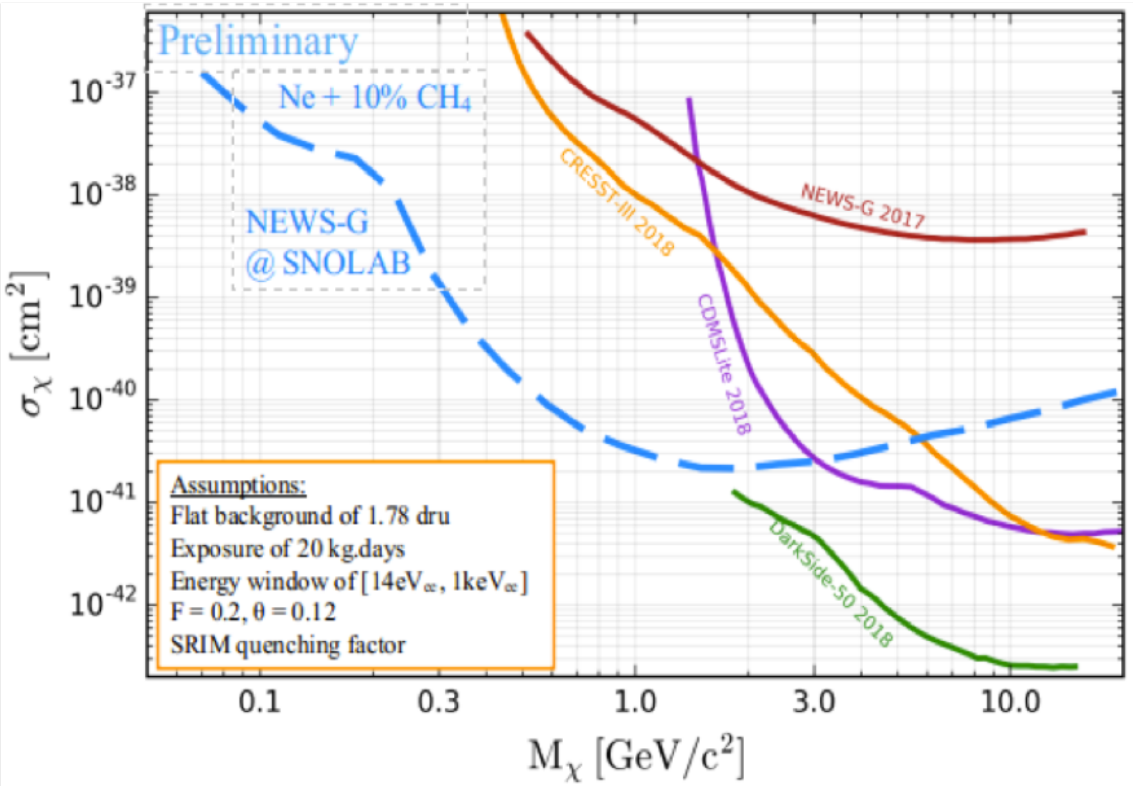

Figure 5.23: Projection of NEWS-G at SNOLAB

Chapter 6

Improving detector performance

6.1 Introduction

This chapter presents development done on the sensor. The goal of these studies is to solve some of the issues presented at the end of the chapter 3. Ideally, we want a sensor stable in time with a good resolution and a uniform gain. Two main sensors were developed and tested. A resistive umbrella sensor, the "bakelite sensor", was used to develop single electron calibration using a UV laser. The second sensor tested, Achinos sensor was developed for the big detector to ensure a strong enough drift field in the whole detector and high amplification.

6.2 Weakness of the single ball sensor

In real conditions, the ideal geometry of the electric field described in chapter 2 is broken by the presence of the grounded rod that supports the sensor at the center of the sphere. The rod implies two problems. First, the electric field symmetry is not spherical any more (Fig 3.22). Secondly, the non-homogeneity of the electric field within the first millimetre around the anode (Fig 3.23) where the amplification

of the signal is expected to occur leads to amplification factor that will depend on the precise point on the anode surface where the field line ends. This inhomogeneity in gain is magnified by the exponential dependence of the avalanche gain with the electric field. The simple, one voltage electrode, is unsuitable for application where an homogeneous response over the whole detector volume is required. These problems can be analysed and the detector performance improved by applying a second voltage close to the anode. Having a simple sensor also limits the voltage that can be applied on the anode before electric discharge occurs between the ball and the rod. A solution to these issues is the use of resistive material for a field corrector. The second voltage is applied on a so called "umbrella" supported by the rod. Several designs involving different materials have been tested.

6.3 The experimental set-up at Queen's University

6.3.1 Gas handling system

The studies at Queen's University have been done with a 30 cm sphere and gas handling system shown in Fig 6.1.

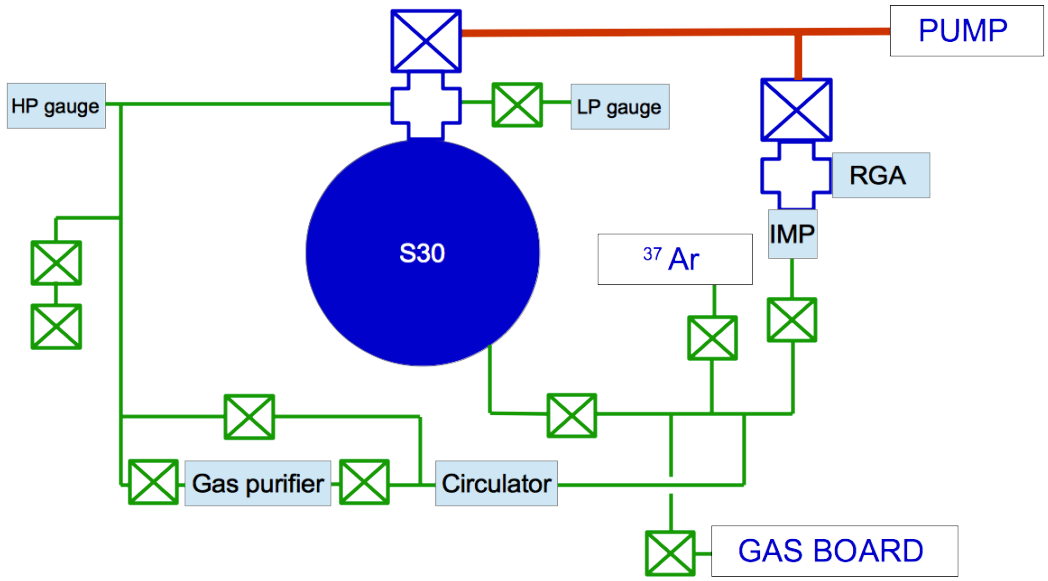

Figure 6.1: Gas handling system

The pumping is done with two pumps. The backing pump is used to carry out a primary vacuum in order of few 10^{-2} mbar. Then, the turbo pump starts and reaches a vacuum in a range of 10^{-5} mbar. A good vacuum is a sine qua non condition before injecting gas. It ensures a low level of impurity and a good working conditions. Different gas mixtures are used. They can come from pre-mixed bottles or from separate bottlse from which we make the desired mixture. The sphere is connected to two pressure gauges with different sensitivities. One low pressure gauge is used to measure the vacuum level after pumping and the leak rate. A high pressure gauge is used to read the pressure during and after filling the sphere with gas. As the gas

quality and the O_2 and H_2O level are critical conditions to ensure a good data taking, the sphere is connected to a Residual Gas Analyser (RGA) through an impedance. The RGA works at low pressure on the order of a few 10^{-4} mbar. It is connected to the pumping system with CF40 tubing. The RGA makes it possible to determine the composition of the gas within the sphere with a sensitivity of few ppm.

The gas can be continuously cleaned with a circulator and a gas purifier. The circulator is made of a small fan inserted in a machined cube. The gas purifier, is model MC1-902FV from micro-torr. It removes impurity such as O_2 or H_2O at a level lower than 100 ppt.

Two valves connected in series with the sphere make it possible to inject impurities such as air. This makes it possible to quantify the electronic attachment due to impurities and verify the efficiency of the purification system.

Finally a cylinder containing Ar^{37} is connected to the sphere through a valve.

6.3.2 Acquisition

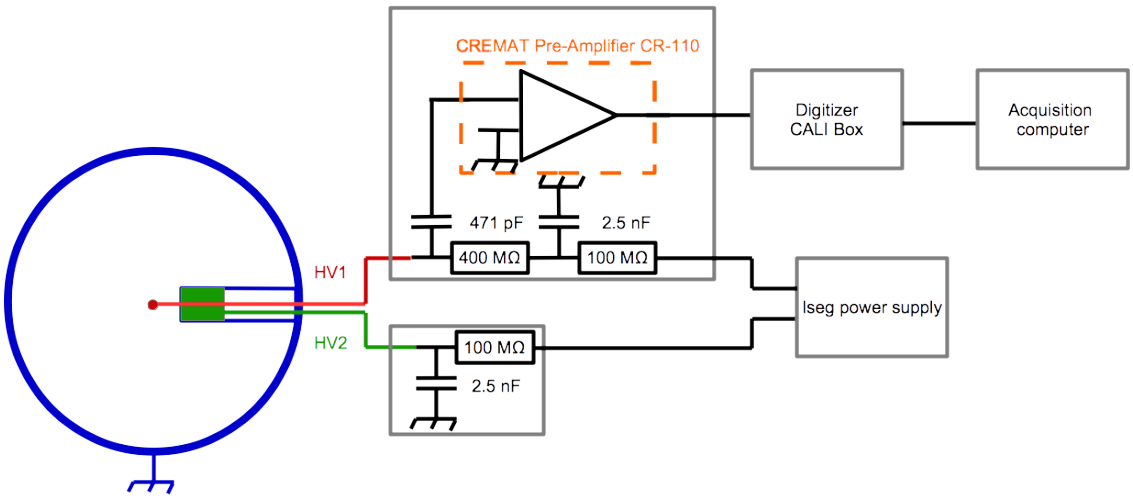

Figure 6.2: Power supply and electronic for acquisition

The anode and the umbrella are respectively linked to high voltages HV1 and HV2 (Fig 6.2) coming from a low noise power supply. They are both filtered by low pass filters with cutoff frequency f = 0.64 Hz. The signal from the anode is sent to a charge pre-amplifier through a decoupling capacitor of C = 471 pF. Then, the output signal from the charge pre-amplifier is sent to a digitizer and treated by an acquisition software. We will discuss in more detail the properties of the pre-amplifier and the digitizer so called "CALI box".

The pre-amplifier

The pre-amplifier amplifies the input signal to give an output signal proportional to the number of charges deposited on the anode. The pulses produced decrease with a time constant τ characteristic of each pre-amplifier. We used the CREMAT CR-110 charge sensitive pre-amplifier. Its decay time constant is $\tau = 140\,\mu$s and its gain is 1.4V/pC.

The digitizer

The amplified signal is digitized by a "CALI" box digitizer at the CEA in Saclay [72]. It works in a dynamic range of $\pm 1.25\,$V with a maximum sampling frequency of 5 MHz. It is possible to use different gain (x1, x2 or x4). The digitized signal is sent to a computer through ethernet cable.

6.4 Second electrode: Umbrella

6.4.1 Correction of the electric field

The goal of the umbrella is to apply a second voltage, close to the anode to correct the electric field around it. Two strategies depending of the geometry of the setup can be employed. The first one consist of applying null or positive voltage very close to the anode. The second possibility consist of applying negative voltage above the anode to avoid the avalanches on the north side of the ball where the field is disturbed by the wire.

6.4.2 Resistive material, Bakelite umbrella

The high voltage for the sensor is provided by a wire encased in a grounded supporting rod. This breaks the symmetry of the electric field. As shown on Fig:6.3 which represents the right side of the anode, the electric field is not isotropic. More precisely, the anisotropy of the electric field in the amplification region induces a dependence of the gain on the arrival angle of the primary electrons.

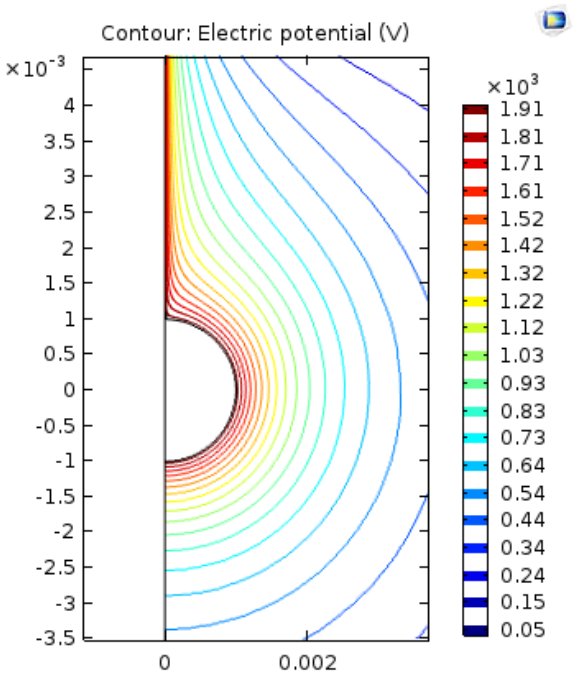

Figure 6.3: Electric potential in the amplification region around a 2 mm diameter anode.

The umbrella is installed between the ball and the rod to prevent electric discharge from the anode. A second voltage, HV2, can be applied on the umbrella to correct the effects of the anisotropy of the electric field. The umbrella is made of resistive material to allow the application of a voltage on its surface and prevent electric discharge with the anode. Figure 6.4 shows a bakelite umbrella. The resistivity of bakelite has

been measured to be on the order of $10^{12}\,\Omega \cdot cm$.

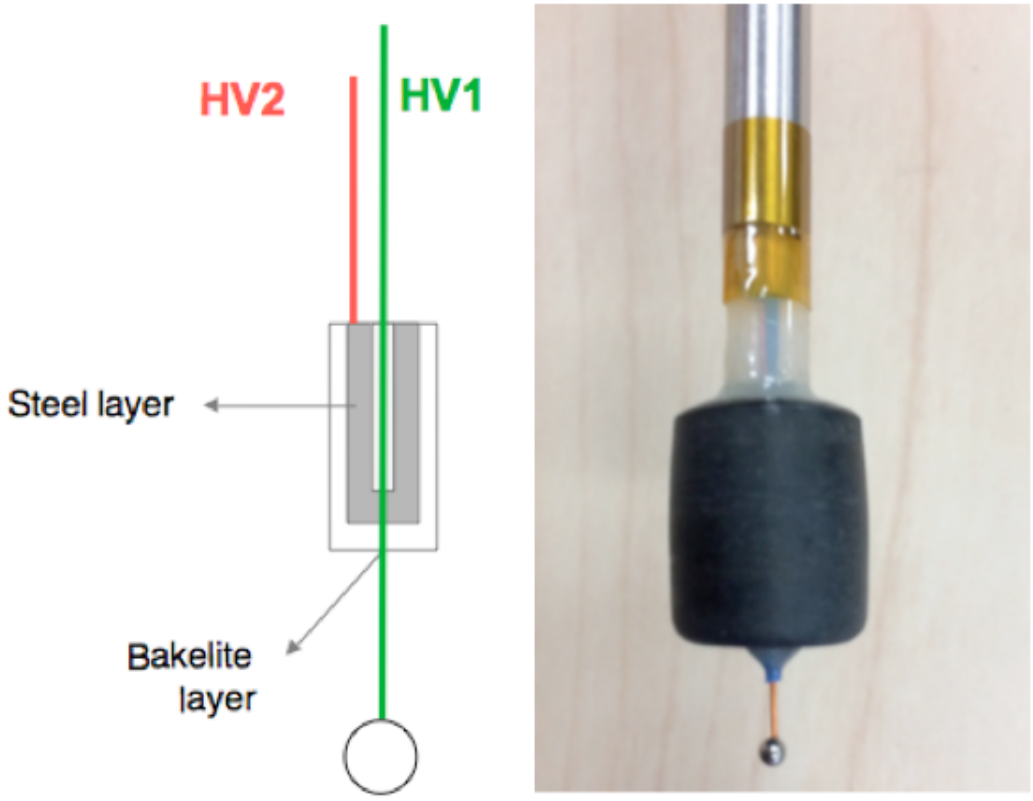

Figure 6.4: Left: Schematic view of the bakelite sensor with $HV1$ applied on the anode and $HV2$ on the a steel layer inside bakelite. Right: Picture of a $2\,mm$ diameter anode with bakelite umbrella used at Queen's university.

Figure 6.5 shows the electric field lines in the volume that ends on the lower half of the sensor with respect to the value of HV2. As we can see, applying a negative voltage on the umbrella forces the lines from a larger volume to end on the lower half of the sensor. This implies an improvement of the resolution of the detector. However, this method has a limit. For too low HV2, less than -10% of HV1, the direction of the field on the upper half of the sphere reverses. This volume would be lost because in the region, electron from primary ionization would drift toward the

sphere instead of the sensor.

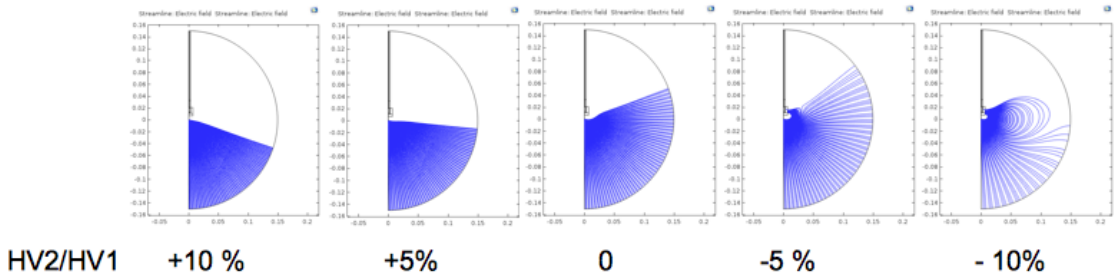

Figure 6.5: Electric field lines ending on the lower half of the sensor.

6.4.3 Experimental test

Figure 6.6 shows the effect of the voltage applied on the umbrella. These measurements were done with ^{37}Ar, a radioactive gas which decays by electron capture. Capture from the K-shell and L-shell release 2.82 keV and 270 eV X-rays respectively. This gaseous radioactive source is produced at the Royal Military College in Kingston by irradiating calcium-oxyde with the thermal neutron flux of a SLOWPOKE-2 nuclear reactor [97]. The sphere was filled with 500 mbar of gas mixture made of 98% of Ar and 2% of CH_4. The voltage HV1 applied on the anode was +2000 V and four voltages were tested on the umbrella.

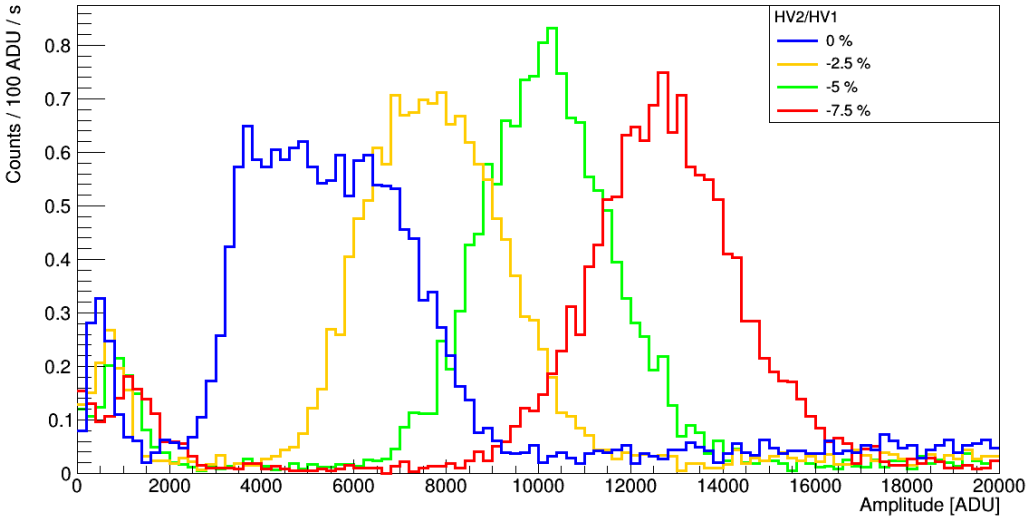

Figure 6.6: Effect of the second voltage applied on the umbrella. The voltage applied on the anode was kept constant at 2000 V. The peak is due to the decay of ^{37}Ar releasing 2.82 keV X-rays

When we decrease HV2, keeping HV1 constant, the peak due to capture from K-shell is shifted towards larger amplitude, showing an increase of the detector gain. This decrease of HV2 also improves the detector energy resolution. For HV2=0V, the recorded spectrum does not exhibit a gaussian shape. By applying a negative HV2, in order to obtain a ratio HV1/HV2 equal to -2.5%,-5% and -7.5% the gaussian fits on the yellow, green and red curves show a resolution of 18.5%, 14.2% and 12.7% respectively. These results confirm an improvement of the homogeneity of the gain of the detector for events distributed in its whole volume. Figure 6.7 shows the effect of HV2 on the detector resolution and the event rate. A reasonable negative value of HV2, higher than -8% of HV1, strongly improve the detector resolution with a very small loss of sensitive volume.

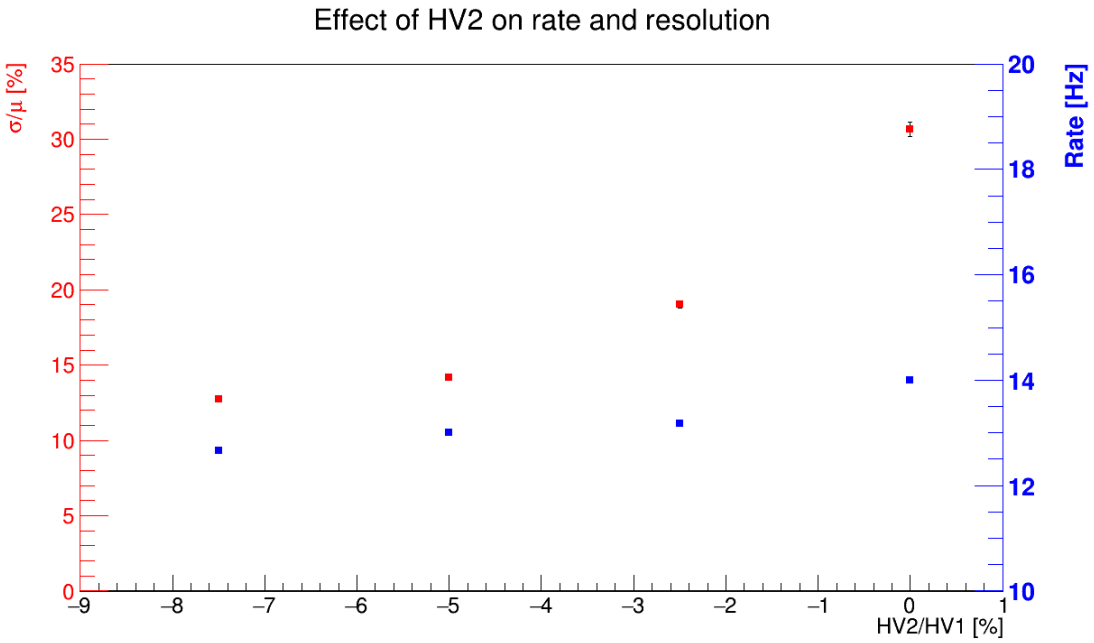

Figure 6.7: Effect of HV2 on the resolution (red) and rate (blue) of the 2.82 keV peak of ^{37}Ar. Applying a negative HV2 improves the resolution of the detector without significantly affecting the active volume the detector.

6.4.4 Performance, single electron calibration with a laser

The main goal of the single electron calibration is the parametrization of the theoretically motivated Polya distribution describing the gain of the detector. Specifically, it describes the number of ion-electron pairs produced by an avalanche induced by one electron.

$$P\left(\frac{n}{\overline{n}}\right) = \frac{(\theta+1)^{\theta+1}}{\Gamma(\theta+1)}\left(\frac{n}{\overline{n}}\right)^{\theta} e^{[-(\theta+1)n/\overline{n}]} \tag{6.1}$$

The detector response to single electrons has been studied using a solid state laser. The laser beam is split and sent through an optical fibre to a photo-detector and inside the sphere. Primary electrons are extracted from the sphere's inner surface by

the photoelectric effect. This method of calibration allows us to perform several measurement such as drift time, diffusion time and attachment rate of primary electrons. The laser is also used to monitor the stability of the detector with time. Figure 6.8 shows the setup used for laser calibration. The laser beam of wavelength 213 nm is sent through an optical fibre splitter to both a Photo Detector (PD) and to the SPC. This, along with the possibility of adjusting the current of the Laser pump from 100 A up to 150 A, provides a dynamic range of photo-electron extraction from single quanta up to a few hundred.

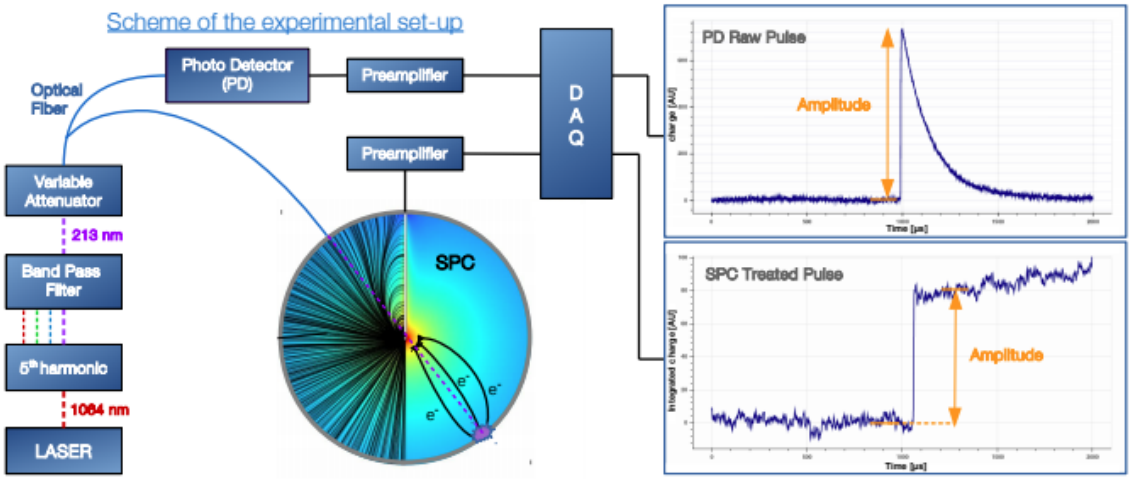

Figure 6.8: The 213 nm laser light is sent through an optical fibre splitter to both the PD (which triggers the acquisition) and the SPC to extract photo-electrons from the inner surface of the vessel. The two panels on the right show a typical PD signal (raw pulse on top panel) together with the resulting SPC signal (treated pulse on bottom panel) from a single electron reaching the sensor and undergoing an avalanche of average gain. The time delay between the SPC and the PD pulse corresponds to the drift time of the electron from the surface to the sensor [98].

Figure 6.9 presents the fit of laser data taken by triggering on the photo-detector.

With a strong enough attenuation of the light beam, the number of extracted electron follows a Poisson distribution with less than one electron expected. The recorded events are noise fluctuation when no primary electrons are extracted; this is the gaussian shape on the left of the spectrum centred at 0 ADU (Analogue-to-Digital-Unit). The tail at higher amplitude is the contribution of events with one or two primary electrons emitted. The fit of the recorded spectrum allows us to determine the mean number of primary electrons emitted ($\mu = 0.08$), the mean gain ($< \mathrm{G} >= 41.6\,\mathrm{ADU/e^-}$), and the baseline resolution ($\sigma = 4.3\,\mathrm{ADU}$). Sensitivity to single electrons allows us to determine the parameter of the θ parameter of the Polya distribution. For the tested conditions of gas and voltage, this parameter is close to 0.

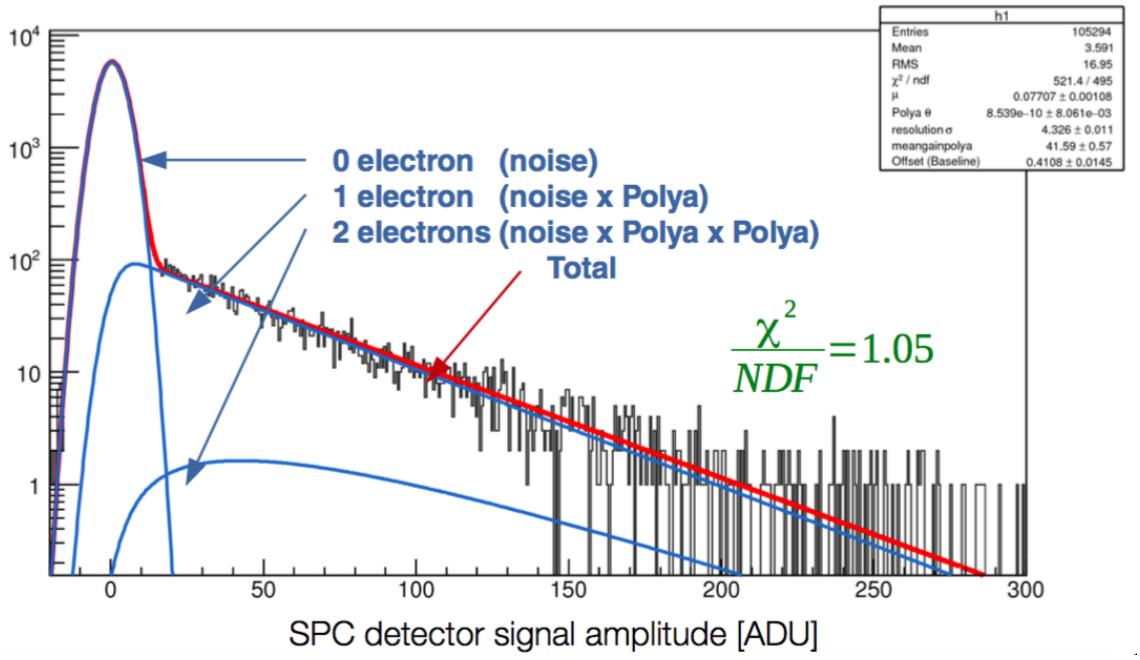

Figure 6.9: Data taken with solid state laser. The fit of the data (red) allows us to determine the mean number of primary electrons extracted from the sphere surface ($\mu = 0.08$). The blue curves represent the contribution of events for which 0, 1 or 2 primary electrons were extracted [98].

Figure 6.10 shows the mean number of primary electrons vs the amplitude of pulses recorded by the photo-detector. μ is the only parameter of the fit that depends on the intensity of the laser pulses. The linear relationship between these two variables demonstrates the accuracy of a Poisson distribution for the number of extracted primary electron.

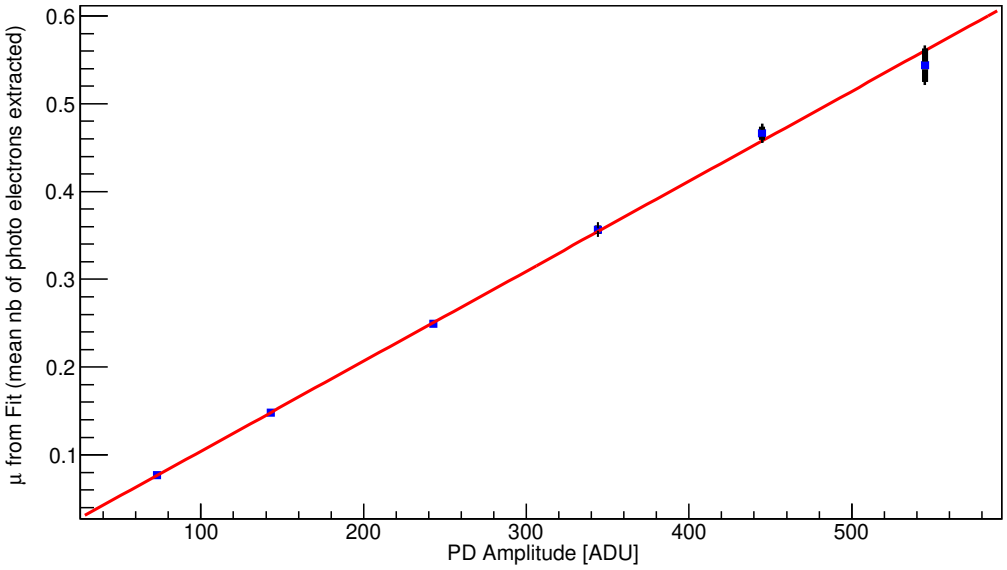

Figure 6.10: Mean number of primary electron extracted from the sphere surface [98].

In addition to laser events, we injected ^{37}Ar in the detector. Figure 6.11 shows the ^{37}Ar spectrum measured by a 30 cm detector filled with 1.5 bar of the Ne+2%CH_4 gas mixture. The spectrum clearly shows the 270 eV and 2822 eV lines of X-rays from electron capture in the L- and K-shell of ^{37}Ar, respectively. The energy scale is determined based on the position of the 2822 eV peak. The dashed line indicates the analysis threshold that was set at 100 eV. The solid red line indicates the fit of our model to the data. The relative abundance of 270 eV and 2822 eV events from

X-rays induced by electron capture from the L and K-shells was fixed to the expected ranching ratio L/K of 0:0987 [99]. The combination of both laser and ^{37}Ar events allows for measuring the W-value of the gas mixture. For that particular case, the measured value is W=27.6 $\pm$ 0.2eV

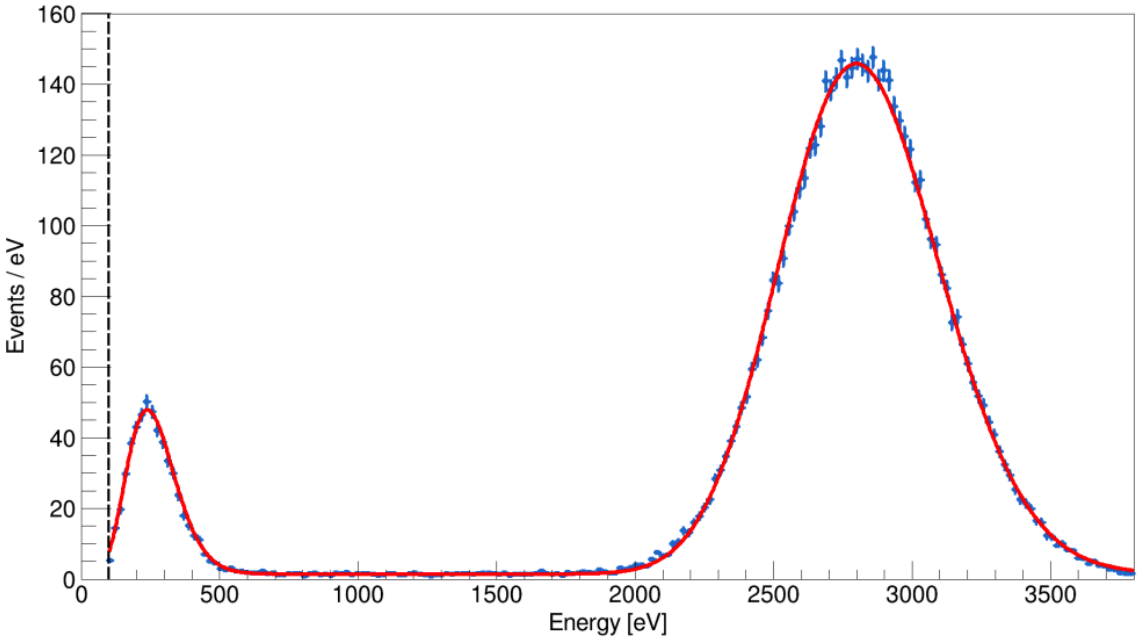

Figure 6.11: ^{37}Ar energy spectrum [98]

6.5 Novel sensor approach for large SPC, Achinos Sensor

Large future detectors will require new sensor technologies to allow for single electron detection. The size of the anode and the value of the high voltage need to reach a compromise between the amplification and the strength of the drift field. These two imperatives lead to a conflict for large scale detectors. To avoid electron attachment, a strong drift field is needed, requiring a large anode. On the other hand, the high gain needed for sub-keV threshold demands a small anode. In the case of spherical detector with a single ball sensor a limitation exists: the electric field, inversely proportional

to the radius of the ball, decreases very quickly at large distance, which accentuates the attachment or the recombination of drifting electrons. This phenomenon is even further accentuated in the case of a large sphere ($>$ 1 m diameter). To overcome this difficulty a new sensor concept called Achinos has been developed by the I. Giomataris group in CEA-Saclay [100]. The single ball is replaced by a structure made out of several balls at a fixed radius, the center forming an equipotential. The advantage of this technique is that at large distance the electric field is reinforced by more than one order of magnitude so it solves the problem of the weakness of the electric field at the volume of the sphere. In addition by reading one by one the ACHINOS balls the detector becomes a TPC with 3D tracking capability. The ACHINOS sensor consists of a set of anode balls uniformly distributed around a central sphere at an equal distance from the center of the detector (Fig 6.12). The anode balls are supported by insulated wires. These wires have a constant length and are fixed perpendicularly to the surface of the central sphere in such a way that all the anode balls are on a virtual sphere larger than the central sphere. The central sphere is made of either highly resistive material or a total insulator covered by a conducting surface, thus making it possible to apply HV2 on its surface (bias electrode). The value of HV2 is chosen to optimize the electric field configuration and improve the energy resolution of the detector.

Figure 6.12: Achinos sensor

The design of Achinos was studied with COMSOL. Figure 6.13 shows the electric field around an Achinos sensor made of 11 balls on the X-Y plane for Z=0 (center of the SPC). The effect of the ACHINOS module is visible, equipotential lines are formed similar to that of an anode with a diameter of 36 mm. Electrons liberated by ionization in the volume of the detector will drift under the influence of the electric field of the eleven balls equivalent to the case of single ball approximately 36 mm in diameter. Their drift will lead them close to an anode ball, where the electric field is increasing strongly and the charge multiplication will take place.

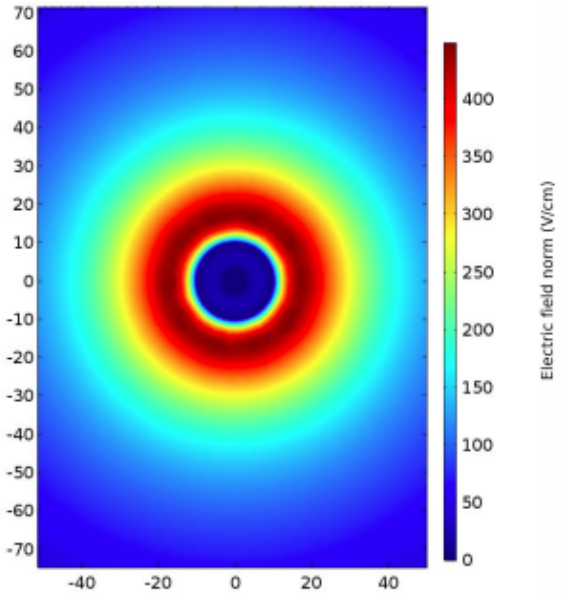

Figure 6.13: Electric field around an Achinos sensor [100]. The dimension are expressed in mm.

Several Achinos designs have been tested with an ^{55}Fe source placed inside the sphere. Figure 6.14 shows the recorded spectrum with an 11, 2 mm anode Achinos. The gas mixture was made of helium, argon, and methane with in respective proportion of respectively 80%, 11% and 9% at 650 mbar. The high voltage applied on each ball was 2015 V and -200 V on the central anode. The 5.9 keV x-ray of the ^{55}Fe is measured with a resolution of 12.4%.

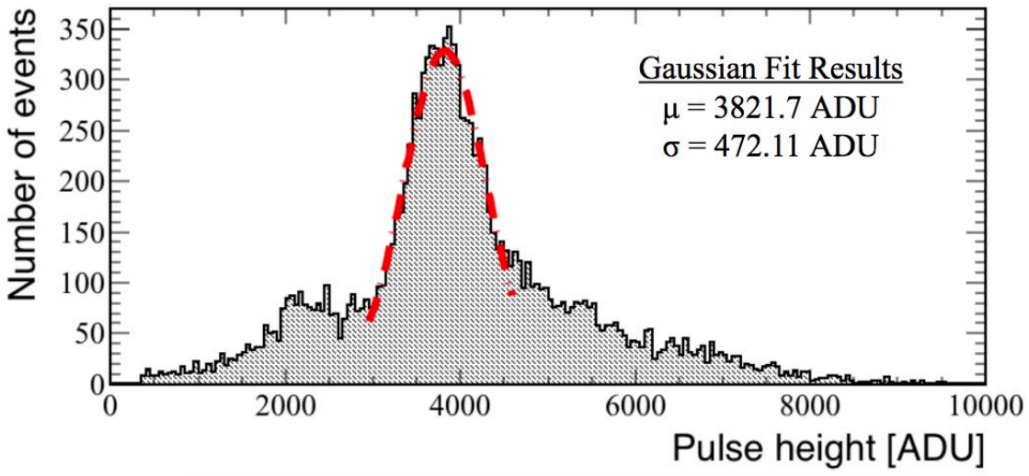

Figure 6.14: Pulse height distribution of the signal produced by the 5.9 keV X-ray line of an ^{55}Fe source. [100]

The observed large distribution is due to the precision of balls, of the solders and the positioning of the various components. New tools have been developed and a technical effort is under way to improve the precision of various elements. The Achinos sensor was tested during the commissioning run of the NEWS-G detector. The detector was filled with 135 mbar of pure CH_4. The performance of the detector where investigated with the same tools as at Queen's University, the combination of laser and ^{37}Ar calibration. The high voltage applied on each ball was 2020 V and the central anode was grounded. During an 11 days run, the stability of the detector was controlled using the laser at high power. Figure 6.15 shows the evolution of the ratio of the amplitude of the pulses recorded by the photo-detector and the pulse recorded by the sphere vs. the time in hour. We can remark that this ratio decreases over time and follows two patterns. A linear decreasing of $0.09 \pm 0.001\%$ per hour during the first 110 h (blue line) and $0.018 \pm 0.0005\%$ during the following 142 hours (yellow line). These slow decreases of the gain can be explained by several factors.

First the gas circulation and purification was not used during this run, so a slow diffusion of oxygen could be responsible for this decrease. Secondly, a degradation of the optical fibres could lead to the same result. The quality of optical fibres to be used at SNOLAB are under investigation at Queen's University. However, the absence of electric discharges show the suitability of such sensor for long term operation.

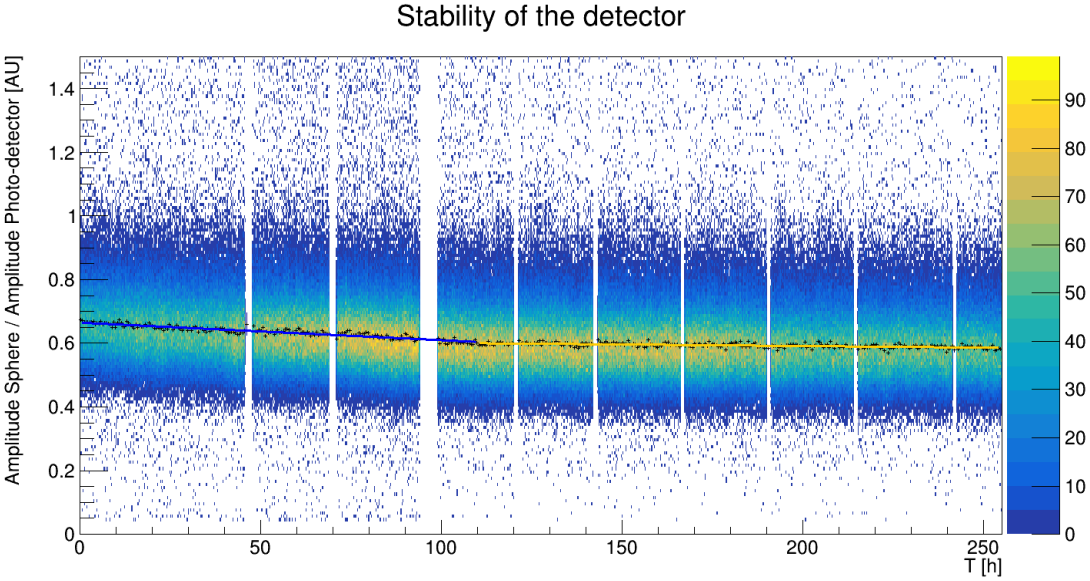

Figure 6.15: Stability of the achinos sensor during CH_4 run.

Following these 10 days of data acquisition, we injected ^{37}Ar in the detector. Figure 6.16 shows the rise time vs. amplitude distribution for the ^{37}Ar data. The 2.82 keV peak is clearly visible. We remark a correlation with lower amplitude for higher rise time. An oxygen contamination could be responsible for such correlation and shows the importance of using a gas purification system. Additionally, the lower part of the spectrum is polluted by electronic noise inducing events with a strong rise time vs. amplitude correlation.

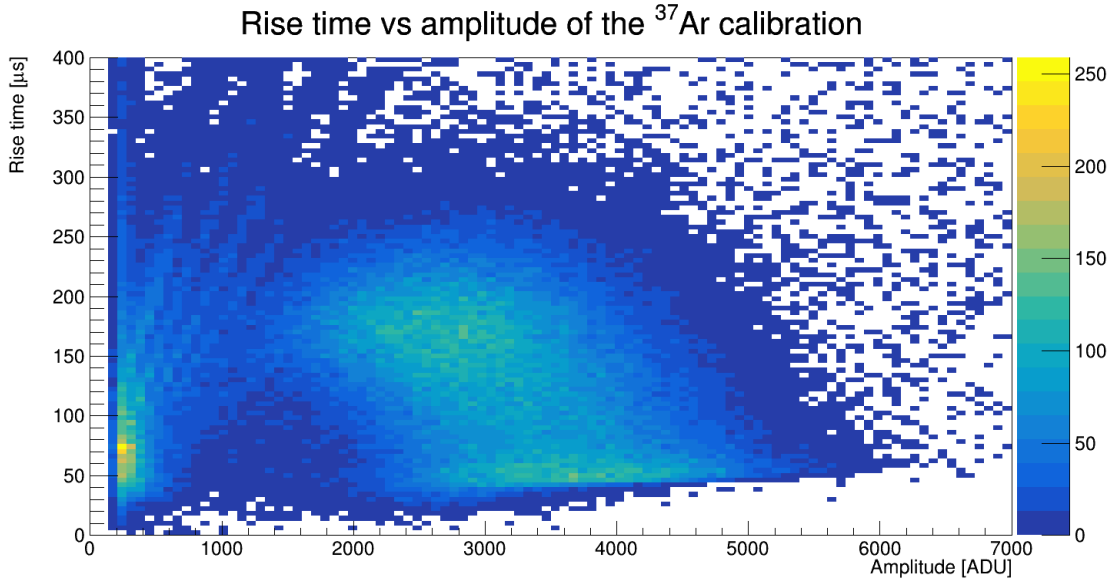

Figure 6.16: Rise time vs. amplitude distribution of the ^{37}Ar in 135 mbar of CH_4.

In addition to the high power laser and ^{37}Ar run, several runs with low power laser where taken to control the low energy response of detector. Figures 6.17 and 6.18 show the double deconvolved pulses of laser induced electrons where the arrival of one and three electrons respectively are clearly visible.

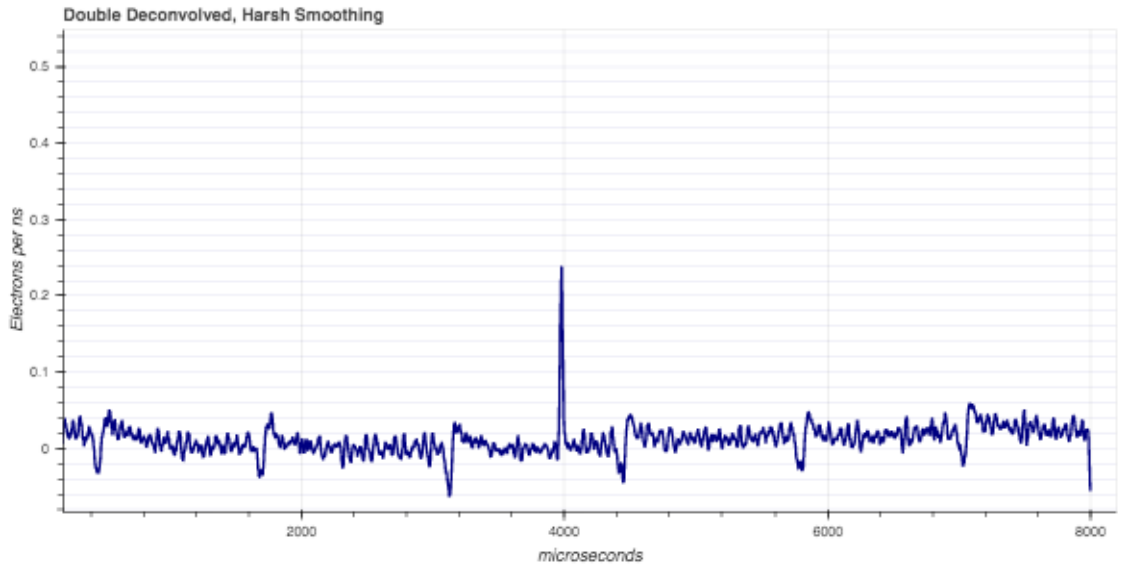

Figure 6.17: Double deconvolution of a laser induced pulse with one electron in 135 mbar of CH_4.

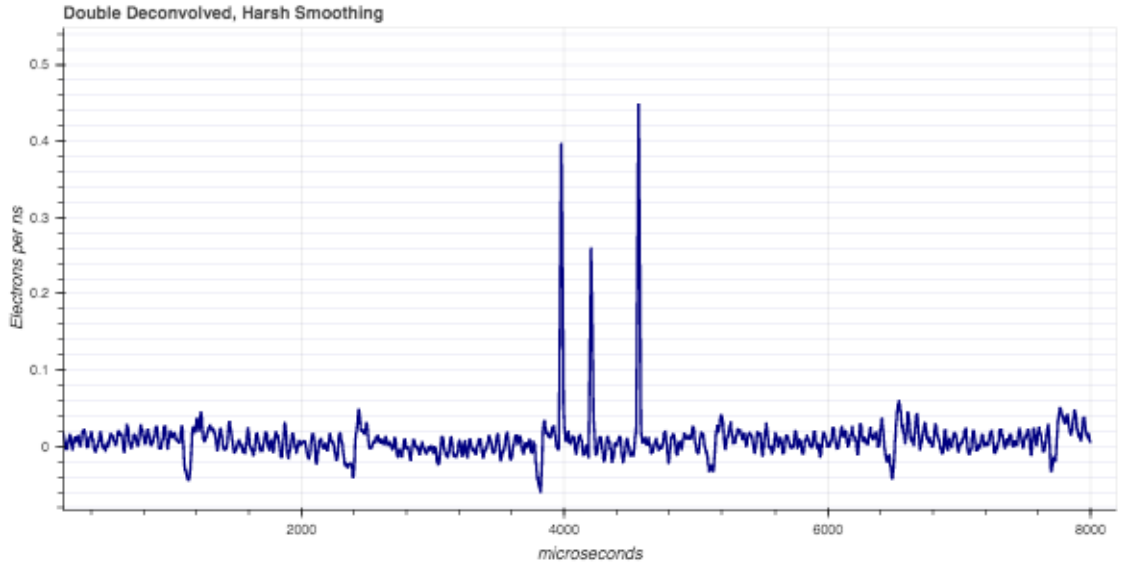

Figure 6.18: Double deconvolution of a laser induced pulse with three electron in 135 mbar of CH_4.

These first results show that the Achinos sensor provide good stability while giving

the low threshold to allow single electron detection.

6.6 Conclusion

SPCs have already shown their potential for dark matter detection with the SEDINE detector. New calibration methods confirm the ability of the detector to measure single electrons and recent sensor developments exhibit a stable behaviour for large detectors. The first commissioning runs show the potential of the achinos sensor and confirm the feasibility of single electron detection in a large detector. These first runs are under analysis and show the potential of the new detector. Its performance will be improved by the utilization of gas purification and intensive work on electronic noise reduction.

Chapter 7

Summary and Conclusions

The SEDINE detector, the first prototype SPC used to search for dark matter, showed the potential of such devices and allowed the collaboration to set a new limit on the dark-matter-nucleon cross section. This work was a step toward the completion of a new detector to be installed at SNOLAB in 2020. The study of the data taken with SEDINE shows the different aspects limiting the performance of the experiment. The study of the background of the experiment shows that it was strongly dominated by the presence of the ^{210}Pb decay chain on the surface and bulk of the detector and its shielding. The background induced by the copper sphere will be reduced in the new detector by the electroplating of 500 μm of pure copper on its inner surface. The shielding will be improved by using 25 cm of lead including an inner shell made of 3 cm of archaeological lead. This new shield will reduce both the background induced by gamma rays surrounding the experiment and the background from the shield itself. The background event rate observed with SEDINE was around 50 events/kg/keV/day between 0.5 and 1 keV. In the new detector this rate will be reduced down to 2 events/kg/keV/day after a year spent underground. Another improvement concerns the anode. The development of new sensors with resistive umbrellas shows that

the detector can be sensitive to single electron. The development of the achinos structure confirms this capability in large detectors. All these improvements will allow the experiment to set new constraints on WIMP-nucleon cross section three orders of magnitude better than the one set by SEDINE for WIMP masses of 0.6 GeV/c^2 and to explore lower masses. The background of the next detector will still be dominated by the presence of the ^{210}Pb decay chain at 28.5 mBq/kg. After two years of cooling underground the copper of the sphere will contribute almost 60% of the total background. The future of the collaboration relies on a new sphere made of 6N copper pure at 99.9999%. Such copper shows ^{210}Pb contamination below the limit of the current best detection method at 4.1 mBq/kg [75] . Fully electro-formed sphere in underground environment would constitute the ultimate low background detector, as ^{238}U and ^{232}Th contributions have been measured to be lower than in 6N copper and all cosmogenic contributions from handling copper at surface would be eliminated.

Bibliography

[1] G. Bertone, D. Hooper, and J. Silk, "Particle dark matter: Evidence, candidates and constraints," *Phys. Rept.*, vol. 405, pp. 279–390, 2005.

[2] G. Jungman, M. Kamionkowski, and K. Griest, "Supersymmetric dark matter," *Phys. Rept.*, vol. 267, pp. 195–373, 1996.

[3] J. Conrad, "Indirect Detection of WIMP Dark Matter: a compact review," in *Interplay between Particle and Astroparticle physics (IPA2014) London, United Kingdom, August 18-22, 2014*, 2014.

[4] B. Dutta, "Dark Matter Searches at Accelerator Facilities," in *Proceedings, 10th International Symposium on Cosmology and Particle Astrophysics (CosPA 2013): Honolulu, Hawaii, USA, November 12-15, 2013*, 2014.

[5] I. Giomataris, I. Irastorza, I. Savvidis, S. Andriamonje, S. Aune, M. Chapellier, P. Charvin, P. Colas, J. Derre, E. Ferrer, M. Gros, X. F. Navick, P. Salin, and J. D. Vergados, "A novel large-volume spherical detector with proportional amplification read-out," *Journal of Instrumentation*, vol. 3, no. 09, p. P09007, 2008.

[6] R. Adam *et al.*, "Planck 2015 results. I. Overview of products and scientific results," *Astron. Astrophys.*, vol. 594, p. A1, 2016.

[7] F. Zwicky, "Die Rotverschiebung von extragalaktischen Nebeln," *Helv. Phys. Acta*, vol. 6, pp. 110–127, 1933.

[8] K. G. Begeman, A. H. Broeils, and R. H. Sanders, "Extended rotation curves of spiral galaxies: Dark haloes and modified dynamics," *Mon. Not. Roy. Astron. Soc.*, vol. 249, p. 523, 1991.

[9] D. Clowe, M. Bradac, A. H. Gonzalez, M. Markevitch, S. W. Randall, C. Jones, and D. Zaritsky, "A direct empirical proof of the existence of dark matter," *Astrophys. J.*, vol. 648, pp. L109–L113, 2006.

[10] "Planck image gallery." `https://www.cosmos.esa.int/web/planck/picture-gallery`.

[11] P. A. R. Ade *et al.*, "Planck 2015 results. XIII. Cosmological parameters," *Astron. Astrophys.*, vol. 594, p. A13, 2016.

[12] M. Milgrom, "A modification of the Newtonian dynamics as a possible alternative to the hidden mass hypothesis," *apj*, vol. 270, pp. 365–370, July 1983.

[13] C. Alcock *et al.*, "The MACHO project: Microlensing results from 5.7 years of LMC observations," *Astrophys. J.*, vol. 542, pp. 281–307, 2000.

[14] S. Tara, "The standard model," *Philosophical Transactions of the Royal Society A: Mathematical, Physical and Engineering Sciences*.

[15] S. Chatrchyan *et al.*, "Observation of a New Boson at a Mass of 125 GeV with the CMS Experiment at the LHC," *Phys. Lett.*, vol. B716, pp. 30–61, 2012.

[16] G. Aad *et al.*, "Observation of a new particle in the search for the Standard Model Higgs boson with the ATLAS detector at the LHC," *Phys. Lett.*, vol. B716, pp. 1–29, 2012.

[17] M. e. a. Tanabashi, "Review of particle physics," *Phys. Rev. D*, vol. 98, p. 030001, Aug 2018.

[18] C. Patrignani *et al.*, "Review of Particle Physics," *Chin. Phys.*, vol. C40, no. 10, p. 100001, 2016.

[19] G. Bertone and D. Hooper, "History of dark matter," *Rev. Mod. Phys.*, vol. 90, no. 4, p. 045002, 2018.

[20] M. E. Peskin, "Supersymmetric dark matter in the harsh light of the large hadron collider," *Proceedings of the National Academy of Sciences*, vol. 112, no. 40, pp. 12256–12263, 2015.

[21] A. Boveia and C. Doglioni, "Dark Matter Searches at Colliders," *Ann. Rev. Nucl. Part. Sci.*, vol. 68, pp. 429–459, 2018.

[22] D. Hooper, "TASI Lectures on Indirect Searches For Dark Matter," 2018.

[23] A. Habig, "An Indirect search for WIMPs with Super-Kamiokande," in *27th International Cosmic Ray Conference (ICRC 2001) Hamburg, Germany, August 7-15, 2001*, p. 1558, 2001. [4,1558(2001)].

[24] M. G. Aartsen *et al.*, "Search for Neutrinos from Dark Matter Self-Annihilations in the center of the Milky Way with 3 years of IceCube/DeepCore," *Eur. Phys. J.*, vol. C77, no. 9, p. 627, 2017.

[25] M. Ackermann *et al.*, "Search for Gamma-ray Spectral Lines with the Fermi Large Area Telescope and Dark Matter Implications," *Phys. Rev.*, vol. D88, p. 082002, 2013.

[26] M. B. et al., "PAMELA and indirect dark matter searches," *New Journal of Physics*, vol. 11, p. 105023, oct 2009.

[27] F. Palmonari, V. Bindi, A. Contin, N. Masi, and L. Q. and, "Search for dark matter in cosmic rays with the AMS-02 space spectrometer," *Journal of Physics: Conference Series*, vol. 335, p. 012066, dec 2011.

[28] R. W. Schnee, "Introduction to dark matter experiments," in *Physics of the large and the small, TASI 09, proceedings of the Theoretical Advanced Study Institute in Elementary Particle Physics, Boulder, Colorado, USA, 1-26 June 2009*, pp. 775–829, 2011.

[29] C. e. a. Amole, "Dark matter search results from the pico-60 cf_3I bubble chamber," *Phys. Rev. D*, vol. 93, p. 052014, Mar 2016.

[30] M. Weber and W. de Boer, "Determination of the local dark matter density in our Galaxy," vol. 509, p. A25, Jan. 2010.

[31] N. Zhou, "Overview of dark matter direct detection experiments," 2014.

[32] B. Lehnert, "Backgrounds in the DEAP-3600 Dark Matter Experiment," in *15th International Conference on Topics in Astroparticle and Underground Physics (TAUP 2017) Sudbury, Ontario, Canada, July 24-28, 2017*, 2018.

[33] P. A. Amaudruz *et al.*, "First results from the DEAP-3600 dark matter search with argon at SNOLAB," *Phys. Rev. Lett.*, vol. 121, no. 7, p. 071801, 2018.

[34] R. Bernabei *et al.*, "First Model Independent Results from DAMA/LIBRA–Phase2," *Universe*, vol. 4, no. 11, p. 116, 2018. [Nucl. Phys. Atom. Energy19,no.4,307(2018)].

[35] G. Adhikari *et al.*, "Study of fast neutron detector for COSINE-100 experiment," *JINST*, vol. 13, no. 06, p. T06005, 2018.

[36] J. R. T. de Mello Neto *et al.*, "The DAMIC dark matter experiment," *PoS*, vol. ICRC2015, p. 1221, 2016.

[37] C. E. Aalseth *et al.*, "CoGeNT: A Search for Low-Mass Dark Matter using p-type Point Contact Germanium Detectors," *Phys. Rev.*, vol. D88, p. 012002, 2013.

[38] I. Giomataris, R. D. Oliveira, S. Andriamonje, S. Aune, G. Charpak, P. Colas, G. Fanourakis, E. Ferrer, A. Giganon, P. Rebourgeard, and P. Salin, "Micromegas in a bulk," *Nuclear Instruments and Methods in Physics Research Section A: Accelerators, Spectrometers, Detectors and Associated Equipment*, vol. 560, no. 2, pp. 405 – 408, 2006.

[39] F. Mayet, D. Santos, D. Santos, J. Billard, G. Bosson, J. Bouly, O. Bourrion, C. Fourel, O. Guillaudin, F. Mayet, and et al., "Mimac : A micro-tpc matrix for directional detection of dark matter," *European Astronomical Society Publications Series*, vol. 53, p. 25–31, 2012.

[40] F. Aznar *et al.*, "Status of the TREX-DM experiment at the Canfranc Underground Laboratory," in *15th International Conference on Topics in Astroparticle and Underground Physics (TAUP 2017) Sudbury, Ontario, Canada, July 24-28, 2017*, 2017.

[41] P. N. Luke, "Voltage-assisted calorimetric ionization detector," *Journal of Applied Physics*, vol. 64, no. 12, pp. 6858–6860, 1988.

[42] R. e. a. Agnese, "Improved wimp-search reach of the cdms ii germanium data," *Phys. Rev. D*, vol. 92, p. 072003, Oct 2015.

[43] E. A. et al., "Constraints on low-mass WIMPs from the EDELWEISS-III dark matter search," *Journal of Cosmology and Astroparticle Physics*, vol. 2016, pp. 019–019, may 2016.

[44] E. Aprile *et al.*, "The XENON1T Dark Matter Experiment," *Eur. Phys. J.*, vol. C77, no. 12, p. 881, 2017.

[45] X. Cui *et al.*, "Dark Matter Results From 54-Ton-Day Exposure of PandaX-II Experiment," *Phys. Rev. Lett.*, vol. 119, no. 18, p. 181302, 2017.

[46] F. Petricca *et al.*, "First results on low-mass dark matter from the CRESST-III experiment," in *15th International Conference on Topics in Astroparticle*

and Underground Physics (TAUP 2017) Sudbury, Ontario, Canada, July 24-28, 2017, 2017.

[47] Q. Arnaud *et al.*, "First results from the NEWS-G direct dark matter search experiment at the LSM," *Astropart. Phys.*, vol. 97, pp. 54–62, 2018.

[48] P. Agnes *et al.*, "Low-Mass Dark Matter Search with the DarkSide-50 Experiment," *Phys. Rev. Lett.*, vol. 121, no. 8, p. 081307, 2018.

[49] R. Agnese *et al.*, "Silicon Detector Dark Matter Results from the Final Exposure of CDMS II," *Phys. Rev. Lett.*, vol. 111, no. 25, p. 251301, 2013.

[50] R. Ernest and G. H, "An electrical method of counting the number of α-particles from radio-active substances," *Proc. R. Soc. Lond. A*.

[51] G. Knoll, *Radiation Detection and Measurement*. Wiley, 2000.

[52] F. Sauli, *Gaseous radiation detectors: fundamentals and applications*. Cambridge monographs on particle physics, nuclear physics and cosmology, Cambridge: Cambridge Univ. Press, 2014.

[53] W. Leo, *Techniques for Nuclear and Particle Physics Experiments: A How-to Approach*. Springer, 1994.

[54] J. M. D. S. P. S. O. Guillaudin, T. Lamy, "Comimac a low energy table top ion/electron facility for gaseous detector calibration and ionization quenching factor measurement," 2015.

[55] G. Cowan, *Statistical Data Analysis*. Oxford science publications, Clarendon Press, 1998.

[56] S. Agostinelli *et al.*, "GEANT4: A Simulation toolkit," *Nucl. Instrum. Meth.*, vol. A506, pp. 250–303, 2003.

[57] Author, "Shielding physics list." `http://geant4-userdoc.web.cern.ch/geant4-userdoc/UsersGuides/PhysicsListGuide/html/reference_PL/Shielding.html`.

[58] Author, "References," *Journal of the International Commission on Radiation Units and Measurements*, vol. 11, pp. 31–31, 04 2011.

[59] E. McDaniel and E. Mason, " The Mobility and Diffusion of Ions in Gases," 1973.

[60] W. Blum, W. Riegler, and L. Rolandi, *Particle detection with drift chambers; 2nd ed.* Berlin: Springer, 2008.

[61] G. Alkhazov, "Statistics of electron avalanches and ultimate resolution of proportional counters," *Nuclear Instruments and Methods*, vol. 89, pp. 155 – 165, 1970.

[62] D. Durnford, "Phenomenological studies and analysis techniques to search for light dark matter with News-G."

[63] Şahin, İ. Tapan, E. N. Özmutlu, and R. Veenhof, "Penning transfer in argon-based gas mixtures," *Journal of Instrumentation*, vol. 5, pp. P05002–P05002, may 2010.

[64] "Comsol muliphysics." `https://www.comsol.com/products`. Accessed: 2018-08-16.

[65] S. Biagi, "Monte carlo simulation of electron drift and diffusion in counting gases under the influence of electric and magnetic fields," *Nuclear Instruments and Methods in Physics Research Section A: Accelerators, Spectrometers, Detectors and Associated Equipment*, vol. 421, no. 1, pp. 234 – 240, 1999.

[66] J. Derré, "Pulse shape in the SPC prototype," 2007.

[67] B. W. Loo, F. S. Goulding, and D. Gao, "Ballistic deficits in pulse shaping amplifiers," *IEEE Transactions on Nuclear Science*, vol. 35, pp. 114–118, Feb 1988.

[68] F. V. de Sola, "Wimp and axion searches with news-g: Progress report. progress report," 2017.

[69] A. Hocker *et al.*, "TMVA - Toolkit for Multivariate Data Analysis," 2007.

[70] I. Katsioulas, "NEWS-G, Light dark matter search with a Spherical Proportional Counter, First results and Future prospects," in *53rd Rencontres de Moriond on Electroweak Interactions and Unified Theories (Moriond EW 2018) La Thuile, Italy, March 10-17, 2018*, 2018.

[71] M. Galan, "Table de radionucléides,"

[72] A. D. FARD, "Étude d'un détecteur sphérique gazeux pour la recherche d'événements rares à bas seuil en énergie," 2014.

[73] S. Cebrián, H. Gómez, G. Luzón, J. Morales, A. Tomás, and J. A. Villar, "Cosmogenic activation in germanium and copper for rare event searches," *Astroparticle Physics*, vol. 33, pp. 316–329, June 2010.

[74] "Identification of 210pb and 210po in the bulk of copper with low background alpha counter." `https://indico.ibs.re.kr/event/46/session/4/contribution/19/material/slides/0.pdf`.

[75] K. Abe *et al.*, "Identification of ^{210}Pb and ^{210}Po in the bulk of copper samples with a low-background alpha particle counter," *Nucl. Instrum. Meth.*, vol. A884, pp. 157–161, 2018.

[76] O. Dragoun, A. Spalek, A. Kovalıik, E. Yakushev, M. Rysavy, J. Frána, V. Brabec, A. Novgorodov, and D. Liljequist, "Scattering of 7.3 kev conversion electrons from a 57co source covered gradually by gold absorbers of various thicknesses," *Nuclear Instruments and Methods in Physics Research Section B: Beam Interactions with Materials and Atoms*, vol. 194, no. 2, pp. 112 – 122, 2002.

[77] J. Amare *et al.*, "Cosmogenic production of tritium in dark matter detectors," *Astropart. Phys.*, vol. 97, pp. 96–105, 2018.

[78] S. Nagy, T. Fritioff, M. Björkhage, I. Bergström, and R. Schuch, "On the q-value of the tritium β-decay," *Europhysics Letters (EPL)*, vol. 74, pp. 404–410, may 2006.

[79] "SNOLAB User's Handbook ," 2006.

[80] E. Hoppe, A. Seifert, C. Aalseth, P. Bachelor, A. Day, D. Edwards, T. Hossbach, K. Litke, J. McIntyre, H. Miley, S. Schulte, J. Smart, and G. Warren, "Cleaning and passivation of copper surfaces to remove surface radioactivity and prevent oxide formation," *Nuclear Instruments and Methods in Physics Research Section*

A: Accelerators, Spectrometers, Detectors and Associated Equipment, vol. 579, no. 1, pp. 486 – 489, 2007. Proceedings of the 11th Symposium on Radiation Measurements and Applications.

[81] J. F. Ziegler, "Terrestrial cosmic ray intensities," *IBM J. Res. Dev.*, vol. 42, pp. 117–139, Jan. 1998.

[82] M. S. Gordon, P. Goldhagen, K. P. Rodbell, T. H. Zabel, H. H. K. Tang, J. M. Clem, and P. Bailey, "Measurement of the flux and energy spectrum of cosmic-ray induced neutrons on the ground," *IEEE Transactions on Nuclear Science*, vol. 51, pp. 3427–3434, Dec 2004.

[83] Y. e. a. Shubin, "Cross-section data library mendl-2 to study activation and transmutation of materials irradiated by nucleons of intermediate energies, international atomic energy agency (iaea)," 1995.

[84] R. S. et al, "Updated partial cross sections of proton-nucleus reactions," 1998.

[85] L. Baudis, A. Kish, F. Piastra, and M. Schumann, "Cosmogenic activation of xenon and copper," *Eur. Phys. J.*, vol. C75, no. 10, p. 485, 2015.

[86] A. M. Suriano, S. M. Howard, C. D. Christofferson, I. J. Arnquist, and E. W. Hoppe, "Developing radiopure copper alloys for high strength low background applications," *AIP Conference Proceedings*, vol. 1921, no. 1, p. 080001, 2018.

[87] S. Glasstone, "The physical chemistry of electrolytic solutions (harned, herbert s.; owen, benton b.)," *Journal of Chemical Education*, vol. 21, no. 7, p. 363, 1944.

[88] L. Pattavina, J. W. Beeman, M. Clemenza, O. Cremonesi, E. Fiorini, L. Pagnanini, S. Pirro, C. Rusconi, and K. Schäffner, "Radiopurity of an archeological Roman Lead cryogenic detector," 2019.

[89] E. Armengaud *et al.*, "Background studies for the EDELWEISS dark matter experiment," *Astropart. Phys.*, vol. 47, pp. 1–9, 2013.

[90] V. Á. et al., "Radiopurity control in the NEXT-100 double beta decay experiment: procedures and initial measurements," *Journal of Instrumentation*, vol. 8, pp. T01002–T01002, jan 2013.

[91] E. A. et al., "Material screening and selection for xenon100," *Astroparticle Physics*, vol. 35, no. 2, pp. 43 – 49, 2011.

[92] M. C. Browne, *Preparation for deployment of the neutral current detectors*. PhD thesis, NORTH CAROLINA STATE UNIVERSITY, 1999.

[93] A. KAMAHA, *Improved Limits On The Existence Of Dark Matter. The Final Results From The PICASSO Experiment.* PhD thesis, Queen's University, 2015.

[94] J. F. Ziegler, M. D. Ziegler, and J. P. Biersack, "SRIM - The stopping and range of ions in matter (2010)," *Nuclear Instruments and Methods in Physics Research B*, vol. 268, pp. 1818–1823, Jun 2010.

[95] G. Zuzel, "Experience of gas purification and radon control in BOREXINO," in *American Institute of Physics Conference Series*, vol. 1921 of *American Institute of Physics Conference Series*, p. 050001, Jan. 2018.

[96] D. Mei and A. Hime, "Muon-induced background study for underground laboratories," *Phys. Rev.*, vol. D73, p. 053004, 2006.

[97] D. K. et al., "The facile production of ar-37 using a thermal neutron reactor flux," *Journal of Radioanalytical and Nuclear Chemistry*.

[98] Q. Arnaud *et al.*, "Precision laser-based measurements of the single electron response of spherical proportional counters for the NEWS-G light dark matter search experiment," *Phys. Rev.*, vol. D99, no. 10, p. 102003, 2019.

[99] D. A. Z. S. e. a. Barsanov, V.I., "Artificial neutrino source based on the 37ar isotope," *Phys. Atom. Nuclei (2007) 70: 300.*

[100] A. Giganon, I. Giomataris, M. Gros, I. Katsioulas, X. Navick, G. Tsiledakis, I. Savvidis, A. Dastgheibi-Fard, and A. Brossard, "A multiball read-out for the spherical proportional counter," *Journal of Instrumentation*, vol. 12, pp. P12031–P12031, dec 2017.

université PARIS-SACLAY

ÉCOLE DOCTORALE
Particules, hadrons, énergie et noyau: instrumentation, imagerie, cosmos et simulation (PHENIICS)

Titre : Optimisation du bruit de fond et de la réponse des détecteurs sphériques à gaz pour la recherche de matière noire légère.

Mots clés : matière noire, compteur proportionnelle sphérique, détecteur gazeux, bruit de fond

Résumé : Le premier prototype de compteur proportionnel sphérique SEDINE est déjà utilisé au Laboratoire souterrain de Modane, en France, pour la recherche de matière noire. La prochaine génération de détecteurs est en développement pour être installée à SNOLAB, au Canada, au printemps 2020. Le projet de recherche consiste en deux parties. La première est une étude des différents bruits de fond afin de les réduire au minimum. Ce travail est basé sur la simulation de la radioactivité des matériaux dont le détecteur est fait et l'estimation de l'épaisseur des blindages de différents matériaux afin de le protéger des radiations environnantes. La seconde partie consiste en l'étude du senseur. Placé au centre de la sphère, le senseur est l'un des points clés du détecteur. Ce développement est fait par l'analyse de données prises avec diverses sources radioactives et leur comparaison avec une simulation de la réponse du détecteur. Cette étude à pour but d'améliorer l'homogénéité de la réponse du détecteur et sa résolution.

Title : Optimization of spherical proportional counter backgrounds and response for low mass dark matter search.

Keywords : dark matter, spherical proportional counter, gas detector, background

Abstract : The first prototype Spherical Proportional Counter SEDINE is already in use at the Laboratoire souterrain de Modane, France, for dark matter research. The next generation of detector is under construction and will be installed at SNOLAB, Canada by spring 2020. The research project consists of two parts. The first component is a study of the different background signals that will inhibit dark matter sensitivity in order to reduce them as much as possible. This work is based on simulations of the radioactivity of materials from which the detector is made, and estimation of the thickness of shielding required to protect the experiment from radiation in the laboratory area. The second component consists of a study of the detector's sensor. Placed at the center of the sphere, the sensor is one of the most crucial components of the experiment. This study is based on data acquired with various radioactive sources and comparison with simulations of the detector's response. This study aims to improve the homogeneity of the detector response and its resolution.

Université Paris-Saclay
Espace Technologique / Immeuble Discovery
Route de l'Orme aux Merisiers RD 128 / 91190 Saint-Aubin, France